

# CHEMIA

# **STUDIA UNIVERSITATIS BABEȘ-BOLYAI CHEMIA**

**3/2024**

ISSN (print): 1224-7154;  
ISSN (online): 2065-9520; ISSN-L: 2065-9520

© STUDIA UBB CHEMIA

Published by Babeș-Bolyai University

# EDITORIAL BOARD OF STUDIA UNIVERSITATIS BABEȘ-BOLYAI CHEMIA

## **ONORARY EDITOR:**

IONEL HAIDUC – Member of the Romanian Academy

## **EDITOR-IN-CHIEF:**

LUMINIȚA SILAGHI-DUMITRESCU

## **EXECUTIVE EDITOR:**

CASTELIA CRISTEA

## **ASSOCIATE EDITOR:**

ALEXANDRU LUPAN

## **EDITORIAL BOARD:**

PAUL ȘERBAN AGACHI, Babeș-Bolyai University, Cluj-Napoca, Romania

LIVAIN BREAU, UQAM University of Quebec, Montreal, Canada

HANS JOACHIM BREUNIG, Institute of Inorganic and Physical Chemistry,

University of Bremen, Bremen, Germany

JEAN ESCUDIE, HFA, Paul Sabatier University, Toulouse, France

ION GROSU, Babeș-Bolyai University, Cluj-Napoca, Romania

EVAMARIE HEY-HAWKINS, University of Leipzig, Leipzig, Germany

FLORIN DAN IRIMIE, Babeș-Bolyai University, Cluj-Napoca, Romania

FERENC KILAR, University of Pecs, Pecs, Hungary

BRUCE KING, University of Georgia, Athens, Georgia, USA

ANTONIO LAGUNA, Department of Inorganic Chemistry, ICMA, University of

Zaragoza, Zaragoza, Spain

JURGEN LIEBSCHER, Humboldt University, Berlin, Germany

KIERAN MOLLOY, University of Bath, Bath, UK

IONEL CĂTĂLIN POPESCU, Babeș-Bolyai University, Cluj-Napoca,  
Romania

CRISTIAN SILVESTRU, Babeș-Bolyai University, Cluj-Napoca, Romania

**YEAR**  
**MONTH**  
**ISSUE**

**Volume 69 (LXIX) 2024**  
**September**  
**3**

---

PUBLISHED ONLINE: 2024-09-30  
PUBLISHED PRINT: 2024-09-30  
ISSUE DOI: 10.24193/subbchem.2024.3

---

# **S T U D I A**

## **UNIVERSITATIS BABEȘ–BOLYAI**

### **CHEMIA**

**3**

#### **CONTENT/ SOMMAIRE/ INHALT/ CUPRINS**

Noemi DEAK, Meryem IDBOUMLIK, Albert SORAN, Mohammed LACHKAR, Brahim EL BALI, Gabriela NEMES, Investigation of the Catalytic Activity of Hybrid Decavanadate Materials.....	7
Azhar ATCHABAROVA, Dinara ABDUAKHYTOVA, Khaïsa AVCHUKIR, Graziella Liana TURDEAN, Saken ABDIMOMYN, Rustam TOKPAYEV, Tamina KHAVAZA, Mikhail NAURYZBAYEV, Study of Kazakhstan's Shungite as Electrocatalyst Substrate in Hydrogen Evolution Reaction in Acidic Media.....	25
Ioana ROMAN, Claudia-Andreea MOLDOVEANU, Ștefan DRAGAN, Julia BAUMLI, Claudia CIMPOIU, Vlad-Alexandru TOMA, Neurotrophic Effects of Iridoid Glycosides from <i>Lamium Album</i> L. as Natural GLP1-R Modulators in Repeated Restraint Stress .....	35
Dan-Alexandru TATARU, Maria OLINIC, Călin HOMORODEAN, Mihai-Claudiu OBER, Florin-Leontin LAZAR, Andrada URDA-CIMPEAN, Dan-Mircea OLINIC, Correlations Between Oxidative Stress Markers and Coronary Anatomy in Percutaneously Treated Patients with Acute ST-elevation Myocardial Infarction .....	55

Călin G. FLOARE, Adrian PÎRNĂU, Mihaela MIC, Elena MATEI, An Exploration of Human $\gamma$ D-crystallin Affinity for Potential Aggregation Inhibitors: A Molecular Docking Investigation .....	67
Dau B. THIN, Truong T. V. HOA, Bui B. THINH, Essential Oil from <i>Knema Elegans</i> Warb.: Chemical Composition, Antioxidant and Anti-acetylcholinesterase Activities .....	93
Sathish Raam RAVICHANDRAN, Chitra Devi VENKATACHALAM, Mothil SENGOTTIAN, Catalytic and Solvent Hydrothermal Liquefaction of Microalgae: A Strategy for Recovering Fine Chemicals .....	109
Mihaela NICOLAE (TITA), Ion ONUTU, Daniel TITA, Timur CHIS, Bogdan DOICIN, Contributions to Assessment and Remediation of Acid Tars Lagoons .....	131
Javier E. VILASÓ-CADRE, Iván A. REYES-DOMÍNGUEZ, Juan J. PIÑA, A Procedure for the Gravimetric Quantification of Total Organic Carbon and Carbonates in Natural Rocks Focused on Mineral and Coal Processing.....	147
Ioan-Alexandru UDREA, Valentin ORDODI, Cristina PAUL, Mircea DAN, Ana-Maria PANĂ, Cristian STĂNESE, Dumitru Daniel BONCIOG, Luca DORU-ALEXANDRU, Narcis-Grațian CRĂCIUN, Nicolae VASZILCSIN, Effects of Audio Frequency Electric Fields on the Esterification Reactions of Acetic Acid with C4-C8 Branched Alcohols.....	167
Gabriele-Mario BOGDAN, Marian Iosif FRÎNCU, Sorin-Aurel DORNEANU, Use of Electrodialysis to Produce and Recycle On-site Raw Materials for Waste Printed Circuit Board Recycling Process. I. HBr and KOH Electrosyntheses.....	177
Róbert SZABÓ, Csaba Pál RÁCZ, Norbert MUNTEAN, Francisc Vasile DULF, Antioxidant Activity Enhancement of Icariside II Through Complexation with Whey Protein Concentrate .....	193
Claudia MAXIM, Adriana TRIFAN, Daniela SUTEU, Obtaining and Characterization of Propanediol Phytoextracts from <i>Acmella Oleracea</i> .....	203
István SZÉKELY-SZENTMIKLÓSI, Emőke Margit RÉDAI, Robert-Alexandru VLAD, Zoltán SZABÓ, Béla KOVÁCS, Attila-Levente GERGELY, Csilla ALBERT, Blanka SZÉKELY-SZENTMIKLÓSI, Emese SIPOS, Microencapsulation of <i>Salvia Officinalis</i> L. Essential Oil by Complex Coacervation Technology.....	221

Studia Universitatis Babes-Bolyai Chemia has been selected for coverage in Thomson Reuters products and custom information services. Beginning with V. 53 (1) 2008, this publication is indexed and abstracted in the following:

- Science Citation Index Expanded (also known as SciSearch®)
- Chemistry Citation Index®
- Journal Citation Reports/Science Edition



## INVESTIGATION OF THE CATALYTIC ACTIVITY OF HYBRID DECAVANADATE MATERIALS

Noemi DEAK<sup>a#</sup>, Meryem IDBOUMLIK<sup>ab#</sup>, Albert SORAN<sup>a</sup>,  
Mohammed LACHKAR<sup>b</sup>, Brahim EL BALI<sup>c</sup>, Gabriela NEMES<sup>a\*</sup>

**ABSTRACT.** Three decavanadate ( $V_{10}O_{28}$ )<sup>6-</sup> containing compounds were used to test their catalytic activity in the sulfoxidation reaction of diphenyl sulfide using environmentally friendly conditions (low temperature, non-toxic solvent). The compounds of interest for our study,  $(NH_4)_2(H_2en)_2\{V_{10}O_{28}\}\cdot 4H_2O$ ,  $(H_2en)_3\{V_{10}O_{28}\}\cdot 6H_2O$  and  $\{Li_2(H_2O)_{10}\}(V_{10}O_{28})(NH_4)_4$ , were evaluated, showing good activity in sulfoxidation reaction and leading to complete conversion of the sulfide even after three runs. The tetraammonium decaaqualithium decavanadate, with the formula  $\{Li_2(H_2O)_{10}\}(V_{10}O_{28})(NH_4)_4$  was obtained through a modified literature method and its structure re-determined and investigated, giving similar results as previously described and confirming the structure of the used material.

**Keywords:** *decavanadate derivatives, catalytic sulfoxidation, green and sustainable chemistry*

### INTRODUCTION

Sulfinyl ( $-SO-$ ) and sulfonyl ( $-SO_2-$ ) functional groups can be found in numerous compounds, [1,2] applied in many fields, such as biologically relevant derivatives, [2,3,4,5,6] fine chemicals, [7] pharmaceuticals, [2,8,9] ligands in catalyst structures, [10,11,12] etc. Because of these, their synthesis

<sup>a</sup> Babeş-Bolyai University, Faculty of Chemistry and Chemical Engineering, 11 Arany Janos RO-400028 Cluj-Napoca, Romania.

<sup>b</sup> Engineering Laboratory of Organometallic, Molecular Materials, and Environment (LIMOME), Faculty of Sciences, Sidi Mohamed Ben Abdellah University, Po. Box 1796 (Atlas), 30000, Fez, Morocco.

<sup>c</sup> Independent Scientist, Oujda, Morocco.

\* Corresponding author: [gabriela.nemes@ubbcluj.ro](mailto:gabriela.nemes@ubbcluj.ro)

# These authors contributed equally.





presents an interest in the scientific community. There are several different methods known in the literature for the synthesis of sulfoxides or sulfones. [1, 13, 14] Among the most commonly used methods for obtaining sulfoxides or sulfones is to oxidize the corresponding sulfide. [1, 15] Different oxidation procedures are known, for example employing meta-chloro-perbenzoic acid (mCPBA),  $\text{HIO}_4$ , oxone,  $\text{H}_2\text{O}_2$  as oxidizing agents. [14, 16, 17] In these cases, the central issue is represented by the formation of both the sulfone and the sulfoxide, which requires a laborious separation process to purify the desired products. Thus, the selective synthesis of the sulfoxide or sulfone represents a constant challenge. It is intensely studied to find easy, cheap, and sustainable methods for oxidizing sulfides to sulfoxide or sulfone, respectively. [14, 16] In this context, different homogeneous and heterogeneous systems are used as catalysts, [14, 17, 18] mainly based on tungsten, vanadium, titanium. [6, 17, 18] Since vanadium containing compounds are well known in catalytic oxidation reactions, [19, 20] among these the oxidation of sulfides, [21, 22, 23] hence for testing the catalytic activity of the decavanadates, the choice fell on this process.

Sulfoxidation reactions represent an interest in our research group as well, since one of our research areas has been focused on studying ligands that contain sulfinyl and sulfonyl groups. In the last few years, pincer-type ligands that contained such moieties were designed, synthesized then used. [24, 25, 26, 27] For example, pincer ligands containing two sulfonyl groups, [27] or a sulfonyl group and a sulfinyl one [25] were used to obtain germylene and stannylene systems, [24, 25, 27, 28] transition metal complexes [29] or p-block element containing compounds. [30] Furthermore, a ligand containing two sulfinyl groups in ortho position was also obtained, and it was used as ligand for obtaining phosphorus and silicon containing derivatives. [26] Our promising results in synthesizing such derivatives made us work on finding new methods for obtaining sulfoxides that are easy, cheap and more sustainable.

Examples of different polyoxometalates can also be found among the catalysts used for sulfide oxidation, [31] for example polyoxovanadates, among which are decavanadates. Decavanadate anion ( $\text{V}_{10}\text{O}_{28}$ )<sup>6-</sup> containing compounds became frequently investigated in the scientific community for their diverse applications, [32] in materials chemistry, [33, 34, 35] energy conversion and storage, [35] catalytic [36] or biological activity. [37, 38, 39] Their properties can be tuned by selecting the appropriate charge balancing counter cations, [40] constructing structures with various application possibilities. They can be encountered in the role of catalyst in different processes as well. [19] However, using decavanadate-based materials for sulfide oxidation processes is not as standard. Some examples are known where ( $\text{V}_{10}\text{O}_{28}$ )<sup>6-</sup> anion-containing materials were tested as catalyst for such processes, having different charge

balancing counter cations like organic phosphonium- or ammonium-salts [41,42], Mn-decavanadate clusters, [43] imidazole-decorated transition metal hybrid decavanadates, [44] aryl sulfonium moieties. [45]

In the present work, we aimed to present the catalytic activity of the decavanadate-based materials obtained and studied in our research groups. [38,39] These compounds presented varied structural features and were tested for their antimicrobial, antioxidant, or corrosion-inhibiting activity. [38,39] Given the ease of the synthetic procedure through which these materials could be obtained and investigated, we also decided to evaluate their role as catalyst. This determination was prompted by the general knowledge that cheap and easily obtained catalysts are needed to achieve sustainable synthetic procedures.

## RESULTS AND DISCUSSIONS

Three different decavanadate-based materials were used as catalysts to test their activity in sulfide oxidation reactions: diethylenediammonium diammonium decavanadate tetrahydrat  $(\text{NH}_4)_2(\text{H}_2\text{en})_2\{\text{V}_{10}\text{O}_{28}\}\cdot 4\text{H}_2\text{O}$  [38] (**Cat1**), triethylenediammonium decavanadate hexahydrated  $(\text{H}_2\text{en})_3\{\text{V}_{10}\text{O}_{28}\}\cdot 6\text{H}_2\text{O}$  [39] (**Cat2**) and tetraammonium decaaqualithium decavanadate, with the formula  $\{\text{Li}_2(\text{H}_2\text{O})_{10}\}(\text{V}_{10}\text{O}_{28})(\text{NH}_4)_4$  (**Cat3**) (**Table 1**).

**Table 1.** Formula and abbreviation of the tested decavanadate catalysts.

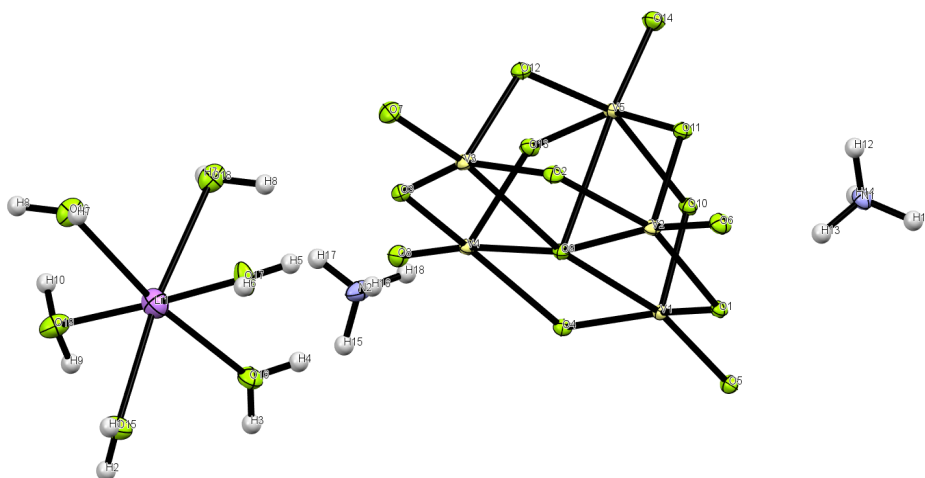
Formula	Abbreviation
$(\text{NH}_4)_2(\text{H}_2\text{en})_2\{\text{V}_{10}\text{O}_{28}\}\cdot 4\text{H}_2\text{O}$	<b>Cat1</b>
$(\text{H}_2\text{en})_3\{\text{V}_{10}\text{O}_{28}\}\cdot 6\text{H}_2\text{O}$	<b>Cat2</b>
$\{\text{Li}_2(\text{H}_2\text{O})_{10}\}(\text{V}_{10}\text{O}_{28})(\text{NH}_4)_4$	<b>Cat3</b>

The derivatives tested as catalysts were selected taking into account their facile synthesis, following the sustainability guidelines. [46] Vanadium-containing polyoxometalates seemed like a good starting point because of their already proven use in sulfoxidation reactions, as detailed in the introduction. Furthermore, none of the elements on which these materials were based are critical from the availability point of view. [47] The materials were prepared in an aqueous solution, using straightforward and readily available reagents.

As described in the previous papers of the research groups, both **Cat1** [38] and **Cat2** [39] were synthesized via wet chemistry, using ammonium metavanadates and ethylenediamine as structure-directing agents under acidic conditions, leading to the protonation of the organic moieties within the structure,

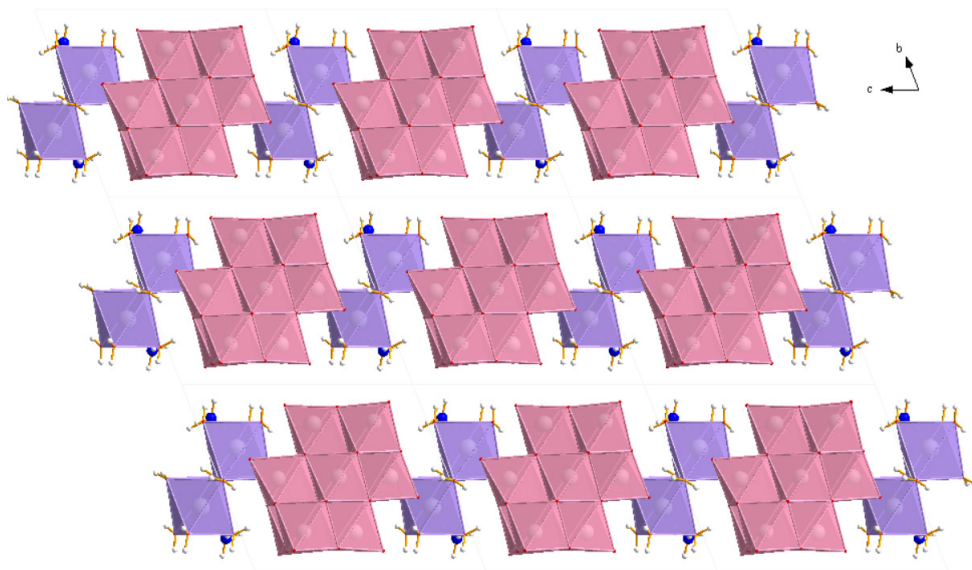
then the crystals were obtained via slow evaporation. Single-crystal X-ray diffraction analysis showed that the structural integrity of **Cat1** was maintained by hydrogen bonds involving nitrogen and oxygen atoms among ammonium ions, ethylenediamine, water, and decavanadates. In contrast, the structure of **Cat2** was stabilized by similar hydrogen bonds but with no presence of ammonium ions. [38,39] The promising results obtained in these studies encouraged us to continue their investigation and to test these materials for their catalytic role in sulfoxidation reactions.

Besides these derivatives, we aimed to obtain new decavanadate materials as well, containing lithium counterions. Using straightforward, easy synthesis, we aimed to evaluate the effect of starting materials and synthetic conditions in forming such new decavanadates. For this, ammonium metavanadate ( $\text{NH}_4\text{VO}_3$ ) was dissolved in nitric acid, then a solution of lithium hydroxide ( $\text{LiOH}$ , 10 % solution) was added until the pH was adjusted to 5, the solution was then maintained under stirring at 50 °C. Single crystals of **Cat3** suitable for crystallographic studies were obtained after filtration and gradual evaporation at ambient temperature. The analysis of the crystals through single-crystal X-ray diffraction showed that the structure of the compound we obtained is identical to one described previously in the literature. [48,49] The X-ray diffraction analysis on a single crystal of the compound revealed the existence of four ammonium cations, a decaaquadilithium cation  $[\text{Li}_2(\text{H}_2\text{O})_{10}]^{2+}$  and the arrangement is surrounded by decavanadate cluster anion  $[\text{V}_{10}\text{O}_{28}]^{6-}$ . The solid-state structure is shown in **Figure 1**.



**Figure 1.** The ORTEP image of the asymmetric unit of **Cat3** with non-hydrogen atom displacement ellipsoids drawn at a 60% probability level.

The X-ray measurement was performed at low temperature ( $T = 100 \text{ K}$ ), this leading to better results in the structure analysis. The study of the structure revealed that the V–V distances within the decavanadate cluster anion  $[\text{V}_{10}\text{O}_{28}]^{6-}$  range from 3.0631(3) to 3.1195(3) Å, (**Table 4** in Experimental Section), which is consistent with those found in comparable structures containing such anions. [50] The average V–O distances within the decavanadate entity also have values similar to those observed in known structures. [37,39,50,51,52,53] The dication  $[\text{Li}_2(\text{H}_2\text{O})_{10}]^{2+}$  consists of Li atoms surrounded by six water molecules, two of which act as a bridge between the two neighbouring  $[\text{LiO}_6]$ , with a Li–Li distances of 3.228(5) Å. Decavanadate, decaaqualithium and ammonium cations are all linked via N–H...O and O–H...O as hydrogen bonds, which are the primary basis of the structural cohesion of the system. The interaction between ammonium cations, decaaquated lithium cations, and decavanadate anions, all connected by a network of hydrogen bonds, defines the architecture of this compound's crystal structure. The system's structural backbone and basic building components are the decavanadate anions. The decaaqualithium cations are arranged in a superposition pattern around these anions. (**Figure 2**)

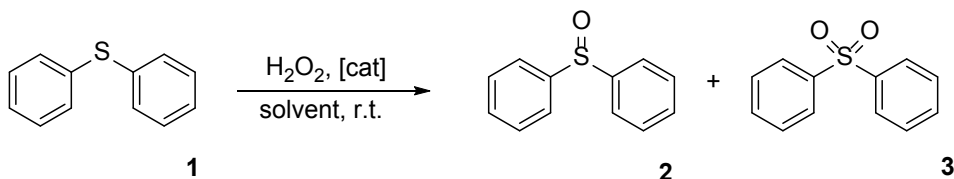


**Figure 2.** Illustration of the compound **Cat3** along the *a* axis, with decavanadate polyhedra = old rose, decaaqualithium polyhedra = lavender.

The obtained **Cat3** was analyzed through FT-IR (Fourier transformed IR) and thermal analysis, showing similar characteristics to those previously presented in the literature. [48,49] For example bands at 984-950  $\text{cm}^{-1}$  and 840-733  $\text{cm}^{-1}$  for  $\nu(\text{V}=\text{O})$  and  $\nu(\text{O}-\text{V}-\text{O})$  vibrations, bands at 3180  $\text{cm}^{-1}$  and 1418  $\text{cm}^{-1}$  for N-H and H-N-H vibrations, and vibrations  $\delta(\text{OH})$  and  $\nu(\text{OH})$  in the range of 3450–3560  $\text{cm}^{-1}$  and 1620  $\text{cm}^{-1}$  in the infrared spectrum confirm the presence of all the moieties in the structure of **Cat3**.

### Investigation of catalytic activity

In the present work, decavanadates **Cat1 - 3** were tested for their catalytic activity in a sulfoxidation process on a model substrate, namely diphenyl-sulphide. (**Scheme 1**)

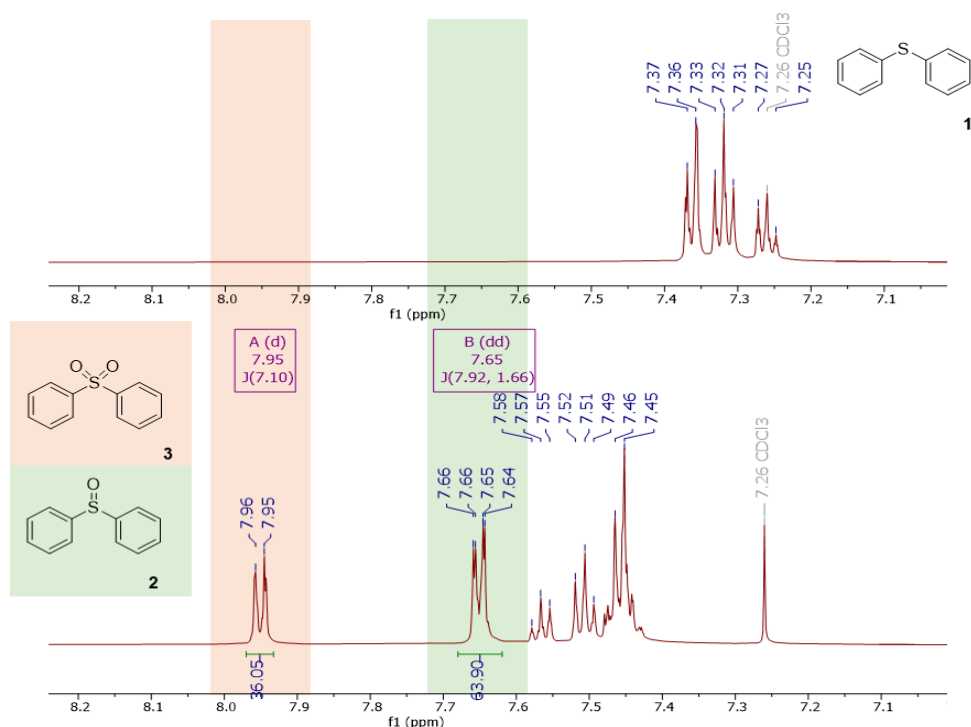


**Scheme 1.** Oxidation of diphenyl-sulphide.

For the catalytic test in the selection of the reaction conditions, the following criteria were taken into consideration: the reaction should take place at room temperature ( $22\text{ }^\circ\text{C} \pm 2$ ), the reaction time should be as short as possible, the oxidant should be easily handled, the solvents should be easily accessible and with low toxicity.

For the selection of solvents, first the guidelines of green and sustainable chemistry were followed, [54,55] that consider different safety, health and environment related criteria. All the solvent guides rank water, ethanol, 2-propanol and ethyl acetate as recommended solvents. In contrast, solvents like methanol, ethylene glycol, acetone, cyclohexanone, benzyl alcohol, tert-butyl alcohol are recommended with some warnings. Furthermore, literature data was also considered, following examples of catalytic sulfoxidation reactions, where solvents like methanol, [56] water, etc. were successfully employed. Thus, all three catalysts **Cat1 - 3** (**Table 1**) were tested in five different solvents, namely methanol (MeOH), ethylene-glycol (EG), water, ethanol (EtOH), 2-propanol (*i*-PrOH). An excess of hydrogen-peroxide was used as oxidant (35% solution), this being one of the most atom-economical next to molecular oxygen, but easier to handle.

The reactions were followed through  $^1\text{H}$  NMR spectroscopy, where both the diphenyl sulfoxide **2** ( $(\text{C}_6\text{H}_5)_2\text{SO}$ ) and diphenyl sulfone **3** ( $(\text{C}_6\text{H}_5)_2\text{SO}_2$ ) present characteristic signals. In the  $^1\text{H}$  NMR spectra the conversion and the percentage of compounds **2** and **3** could be easily calculated and followed (**Figure 3**). In the  $^1\text{H}$  NMR spectra sulfone **3** gives a doublet signal at 7.95 ppm, while sulfoxide **2** gives a doublet of doublets at 7.65 ppm (both in  $\text{CDCl}_3$ ), and neither overlaps with other signals; thus, following the progress of the oxidation, conversion and the ratio between the two products could be possible.



**Figure 3.** Use of  $^1\text{H}$  NMR spectroscopy for following the oxidation process.

The data obtained from the investigation of the three decavanadate based materials **Cat1 - 3** in the oxidation reaction are presented in **Table 2**, showing conversion and the percentage of the obtained compound **2** and **3**.

In the chosen catalytic conditions, in most cases all three catalyst **Cat1 - 3** had similar performance. Full conversion of difenyl-sulfide was observed in MeOH, EtOH, *i*-PrOH, while in EG and  $\text{H}_2\text{O}$  lower conversion was obtained. (**Table 2**)

**Table 2.** Oxidation results.

Catalyst	Solvent	Conversion* (%)	Compound <b>2*</b> (%)	Compound <b>3*</b> (%)
none <sup>a</sup>	MeOH	13	100	0
<b>Cat1<sup>b</sup></b> (no H <sub>2</sub> O <sub>2</sub> )	MeOH	0	0	0
<b>Cat1</b>	MeOH	100	64	36
	EG	100	27	73
	H <sub>2</sub> O	52	68	32
	EtOH	100	16	84
	<i>i</i> -PrOH	100	42	58
<b>Cat2</b>	MeOH	100	22	78
	EG	81	28	72
	H <sub>2</sub> O	100	11	89
	EtOH	100	24	76
	<i>i</i> -PrOH	100	32	68
<b>Cat3</b>	MeOH	100	13	84
	EG	52	53	47
	H <sub>2</sub> O	100	34	66
	EtOH	100	10	90
	<i>i</i> -PrOH	100	40	60
Reaction conditions: diphenyl-sulfide (0.27 mmol), solvent (3 mL), 1 mL H <sub>2</sub> O <sub>2</sub> , catalyst (1.5 mol%), room temperature, 2h. <sup>a</sup> no catalyst was used. <sup>b</sup> no H <sub>2</sub> O <sub>2</sub> was used. *without separation from reaction mixture, calculated from <sup>1</sup> H NMR measurements. Methanol (MeOH), ethylene-glycol (EG), water (H <sub>2</sub> O), ethanol (EtOH), 2-propanol ( <i>i</i> -PrOH).				

In the case of **Cat2** and **Cat3** selectivity towards the sulfoxide **2** was better when using *i*-PrOH, then MeOH or EtOH (32-40% vs. 10-24%), while for **Cat1** selectivity towards sulfoxide was better in the case of MeOH (64%). However, when using EtOH, better selectivity towards sulfone **3** could be noted (>76%). No 100% selectivity towards sulfoxide **2** could be achieved, higher selectivity towards the corresponding sulfone **3** was predominant in most cases. However, in the case of **Cat1**, higher selectivity towards the sulfoxide could be observed when using MeOH or H<sub>2</sub>O (>60%). Interesting to note, that high selectivity (90%) towards sulfone **3** could be observed in case of **Cat3** in EtOH.

For further assessing the properties of the catalytic system, up-scaling and catalyst recycling test were realized as well. The activity of **Cat3** was tested on 0.5 g substrate, using *i*-PrOH as solvent. The catalyst was then re-used in two more runs. Realizing the experiment on a larger scale (0.5 g substrate) led to full conversion, as seen in the screening test previously, however, in this case selectivity towards sulfone **3** was observed. It is noteworthy that even after the 3<sup>rd</sup> run the catalyst **Cat3** led to complete conversion of the diphenyl-sulfide in 2 hours. It is interesting the fact that after the 2<sup>nd</sup> run, the selectivity of the process was different then after the 1<sup>st</sup> and 3<sup>rd</sup> runs, leading to 64% of sulfoxide **2** in the product mixture.

These results reveal that the tested catalytic systems can be easily tuned to obtain a fast, environmentally friendly process towards obtaining sulfones. To note, that the catalyst **Cat3** led to complete conversion even after the 3<sup>rd</sup> run.

## CONCLUSIONS

In this work we investigated the catalytic activity of three decavanadate species  $(\text{NH}_4)_2(\text{H}_2\text{en})_2\{\text{V}_{10}\text{O}_{28}\}\cdot 4\text{H}_2\text{O}$  (**Cat1**),  $(\text{H}_2\text{en})_3\{\text{V}_{10}\text{O}_{28}\}\cdot 6\text{H}_2\text{O}$  (**Cat2**) and  $\{\text{Li}_2(\text{H}_2\text{O})_{10}\}(\text{V}_{10}\text{O}_{28})(\text{NH}_4)_4$  (**Cat3**), in sulfoxidation reactions. Compound **Cat3** was obtained through a modified literature procedure, then structurally investigated as well, in order to determine its structural features. The data obtained was in agreement with those previously reported in the literature, more than that, the single crystal X-ray diffraction analysis provided a solid-state structure with improved characteristics. In the case of all three catalysts **Cat1-3**, full conversion of the diphenyl-sulfide substrate was observed in a short reaction time (2h), in most solvents (MeOH, EtOH, *i*-PrOH), with low catalyst loading (1.5 mol%), however with no selectivity towards the sulfoxide or sulfone. Moreover, **Cat3** showed good results in the recyclability test, giving full conversion of the substrate even after three runs. Even though the selectivity of the chosen reaction condition was not as envisioned beforehand, it provides a quick and easy way to obtain sulfonyl and sulfinyl group containing compounds. In perspective, further adjustments will be made in the structure of the decavanadates and the reaction conditions in order to obtain a catalytic system with a cheap, simple catalyst in mild and environmentally favorable reaction conditions.



## EXPERIMENTAL SECTION

### Synthesis and crystallization of decavanadate derivatives

Catalysts were prepared according to literature procedures, as follows: **Cat1** and **Cat2** were prepared according to the procedures described in the literature [37,39], while **Cat3** was obtained using a modified literature procedure. [48,49]

$(\text{NH}_4)_2(\text{H}_2\text{en})_2\{\text{V}_{10}\text{O}_{28}\}\cdot 4\text{H}_2\text{O}$ , **Cat1** – obtained using the previously described method [38].

Ammonium metavanadate  $(\text{NH}_4)\text{VO}_3$  (300 mg, 2.5 mmol) was dissolved in 20 mL distilled water at 90 °C under continuous stirring. The obtained light-yellow solution was allowed to cool to 50 °C, then copper(II) chloride tetrahydrate  $(\text{CuCl}_2\cdot 4\text{H}_2\text{O})$ , 80 mg, 0.4 mmol) and ethylenediamine (30 mg, 0.5 mmol) were added, obtaining a brown colored solution. The pH of this solution was adjusted to pH 5 by adding nitric acid ( $\text{HNO}_3$ , 3M solution) dropwise. The mixture was further stirred for 30 minutes then filtered and kept at room temperature until the apparition of an orange colored, crystalline solid.

$(\text{H}_2\text{en})_3\{\text{V}_{10}\text{O}_{28}\}\cdot 6\text{H}_2\text{O}$ , **Cat2** – obtained using the previously described method [39]

Ammonium metavanadate (300 mg, 2.5 mmol) was dissolved in 20 mL distilled water at 95 °C. The light-yellow colored solution was then cooled to 50 °C and ethylenediamine (30 mg, 0.5 mmol) was added before adjusting the orange-colored solution to pH 4 by adding  $\text{HNO}_3$ . The resulting brown solution was filtered and slowly evaporated at room temperature to give orange crystals, which were separated, washed and dried in air.

$\{\text{Li}_2(\text{H}_2\text{O})_{10}\}\{\text{V}_{10}\text{O}_{28}\}(\text{NH}_4)_4$ , **Cat3** – obtained using modified literature procedure [48,49]

Ammonium metavanadate  $(\text{NH}_4)\text{VO}_3$ , 300 mg, 2.5 mmol) was dissolved in nitric acid (10 ml, 3 M), yielding a measured pH of 2. Subsequently, a solution of lithium hydroxide (LiOH, 10 %) was added dropwise until the pH was adjusted to 5. The mixture was then stirred at moderate temperature (50 °C) for 30 min, filtered and cooled to room temperature. By gradual evaporation at ambient temperature, coral-like single crystals, suitable for crystallographic studies, were obtained after 3 days. It's important to note that this structure has been previously published, with its characterization conducted at room temperature resulting in a higher R-factor of 3%. However, through the redetermination at 100 K in the present work, a lower R-factor was achieved, leading to a more stabilized structure and a refined understanding of its configuration. [24,25].

### General procedure

In a typical experiment 50 mg (0.27 mmol) diphenyl-sulphide, 3 mL solvent, 1 mL H<sub>2</sub>O<sub>2</sub> 35% solution, 5 mg catalyst (1.5 mol%) were added in a round bottom flask and stirred at room temperature for 120 minutes. Water and ethyl-acetate were added, the phases separated, the organic phase washed with water, then dried under vacuum and analysed by <sup>1</sup>H NMR spectroscopy. NMR was registered in CDCl<sub>3</sub>.

### General considerations

All chemicals were purchased from usual chemical suppliers and used as received. NMR spectra were recorded in deuterated chloroform on Bruker Avance 400 (operating frequency of 400.13 MHz for <sup>1</sup>H) as well as Bruker Avance 600 (frequencies of 600.13 MHz for <sup>1</sup>H) spectrometers. The chemical shifts are given in ppm relative to the solvent residual peak for the <sup>1</sup>H NMR spectra.

### X-ray crystal structure re-determination of Cat3

The measurement was performed at low temperature (T= 100 K) using a Bruker D8 Venture diffractometer equipped with a CCD detector and a molybdenum (Mo) radiation source with Mo-K $\alpha$  ( $\lambda$ = 0.71073 Å) at 100 K in the range of  $3.0^\circ < \theta < 28.3^\circ$  to perform a single-crystal X-ray diffraction measurement. Processing of the acquired data was performed using SHELXL software. [57]. Data reduction was carried out using SAINT [58] and the data was corrected for Lorentz polarisation and absorption effects using the SADABS program. [59] Refinement was carried out using APEX 3 software. [60] The structure was refined with anisotropic thermal parameters for non-H atoms. Hydrogen atoms were placed in fixed and idealized positions and refined with a driving model and a mutual isotropic thermal parameter. The drawings of the molecular structures were created with the DIAMOND [61] and MERCURY [62] programs. **Table 3** presents the crystallographic data and experimental details of the data collection and structure refinements.

The use of single-crystal X-ray analysis allowed the thorough examination of the obtained material **Cat3**. It crystallizes in the triclinic space group  $P\bar{1}$ , with  $a = 8.4427(2)$  Å,  $b = 10.1475(2)$  Å,  $c = 11.0738(3)$  Å,  $\alpha = 68.445(1)^\circ$ ,  $\beta = 86.957(1)^\circ$ ,  $\gamma = 67.637(1)^\circ$ , and  $Z = 1$ . The structure has been refined to an R-factor of 1.5%. Hydrogen bonding interactions (O-H $\cdots$ O and N-H $\cdots$ O) tie water molecules and inorganic structures. Fourier-transform infrared spectroscopy results reveal distinct bands associated with water molecules, decavanadate, and ammonium cations, aligning with the crystalline structure.

**Table 3.** Structure refinement, data collection and crystal data for **1**.

Chemical formula	O <sub>28</sub> V <sub>10</sub> ·10(H <sub>2</sub> O)·4(H <sub>4</sub> N)·2(Li)
Mr	1223.61
Crystal system, space group	Triclinic, P $\bar{1}$
Temperature (K)	100
a, b, c (Å)	8.4427 (2), 10.1475 (2), 11.0738 (3)
$\alpha, \beta, \gamma$ (°)	68.445 (1), 86.957 (1), 67.637 (1)
V (Å <sup>3</sup> )	811.85 (3)
Z	1
F(000)	604
Radiation type / $\lambda$ Å	Mo K / 0.71073
D <sub>x</sub> (Mg,m <sup>-3</sup> )	2.503
R <sub>(int)</sub>	0.020
No. measured reflections	27842
No. independent reflections	4010
reflections with I > 2 $\sigma$ (I)	3916
$\theta_{max}, \theta_{min}$	28.3°, 3.0°
Reciprocal space	h = -11→11 k = -13→11 l = -14→14
R[F <sup>2</sup> > 2 $\sigma$ (F <sup>2</sup> )]/ wR(F <sup>2</sup> )/ S	0.015/0.041/1.12

The crystal structure reveals the existence of four ammonium cations, a decaaquadilithium cation [Li<sub>2</sub>(H<sub>2</sub>O)<sub>10</sub>]<sup>2+</sup>. The arrangement is surrounded by decavanadate cluster anion. [V<sub>10</sub>O<sub>28</sub>]<sup>6-</sup>. With ten edges and ten corners shared by each [VO<sub>6</sub>] octahedra, the decavanadate anion has a cage-like structure.

Sharing edges, six octahedra are organized in a 2 x 3 equatorial plane; the other four octahedra are positioned above and below the equatorial plane, linked by inclined edges shared with the six octahedra in front. The average <V-O> distances within the decavanadate entity have the values shown in **Table 4**, which are similar to those observed in other structures comprising such oxoanions.[37,52,63,64,65]

As shown in **Table 5**, BVS calculations, using the I. D. Brown and D. Altermatt approach, [66] revealed that all vanadium atoms have valence sums ranging from 4.96 to 5.01, with an overall average of 4.98, close to the ideal value of 5 for V (V). The bond valences of the oxygen atoms range from 1.62 to 2.06, indicating that our structure contains a cluster of deprotonated decavanadate (**Table 6**).

The dication [Li<sub>2</sub>(H<sub>2</sub>O)<sub>10</sub>]<sup>2+</sup> consists of two edge-shared [LiO<sub>6</sub>] octahedra. Each Li atom is surrounded by six water molecules, two of which act as a bridge between the two [LiO<sub>6</sub>]. The distance between Li1 – Li1<sup>ii</sup> ions within the cationic structure is of 3.228(5) Å. The oxygen atom O18, located precisely between the two lithium atoms making up the metal cation,

therefore has the highest Li-O distance in this context. Cations and anions alternate in structure, forming an arrangement sequence, as illustrated explicitly in **Figure 1** along the *a* axis.

**Table 4.** Angles and distances selected in  $\{V_{10}O_{28}\}^{6-}$  of **Cat3**.

$\{V_{10}O_{28}\}^{6-}$			
Distances (Å)		Angles (°)	
V1—O5	1.6869(8)	O1—V1—V3 <sup>i</sup>	90.23(2)
V1—O10	1.6994(8)	O5—V1—O9 <sup>i</sup>	166.20(4)
V1—O1	1.9091(8)	O10—V1—O1	96.99(4)
V1—O4	1.9240(8)	O5—V1—O4	97.07(4)
V1—O9	2.0914(8)	O10—V1—O4	96.59(4)
V1—O9 <sup>i</sup>	2.1115(8)	O1—V1—O4	156.34(3)
V2—O6	1.6155(8)	O6—V2—O11	104.06(4)
V2—O2	1.8178(8)	O2—V2—O11	94.58(4)
V2—O11	1.8288(8)	O6—V2—O4 <sup>i</sup>	98.47(4)
V2—O4 <sup>i</sup>	1.9948(8)	O2—V2—O4 <sup>i</sup>	90.14(4)
V2—O1	1.9954(8)	O11—V2—O1	89.71(4)
V2—O9 <sup>i</sup>	2.2458(8)	O4 <sup>i</sup> —V2—O1	76.43(3)
V3—O7	1.6038(9)	O14—V5—O13	102.96(4)
V3—O12	1.8250(8)	O12—V5—O13	89.45(4)
V3—O2	1.8685(8)	O11—V5—O13	153.21(4)
V3—O3	1.8895(8)	O14—V5—O10	100.68(4)
V3—O5 <sup>i</sup>	2.0566(8)	O12—V5—O10	154.43(4)
V3—O9 <sup>i</sup>	2.2908(8)	O11—V5—O10	84.75(3)
V4—O8	1.6267(8)	O7—V3—O5 <sup>i</sup>	97.51(4)
V4—O13	1.7994(8)	O12—V3—O5 <sup>i</sup>	157.42(4)
V4—O3	1.8117(8)	O2—V3—O5 <sup>i</sup>	83.94(3)
V4—O4	1.9946(8)	O3—V3—O5 <sup>i</sup>	82.83(3)
V4—O1 <sup>i</sup>	2.0358(8)	O7—V3—O9 <sup>i</sup>	171.80(4)
V4—O9 <sup>i</sup>	2.2196(8)	O12—V3—O9 <sup>i</sup>	83.11(3)
V5—O14	1.5982(8)	O13—V4—O4	91.33(4)
V5—O12	1.8522(8)	O3—V4—O4	154.84(4)
V5—O11	1.8543(8)	O8—V4—O1 <sup>i</sup>	98.68(4)
V5—O13	1.9054(8)	O13—V4—O1 <sup>i</sup>	155.89(4)
V5—O10	2.0218(8)	O3—V4—O1 <sup>i</sup>	88.71(3)
V5—O9 <sup>i</sup>	2.3580(8)	O4—V4—O1 <sup>i</sup>	75.53(3)

**Table 5.** BVS per Vanadium atoms of **1**.

Octahedral	V1O <sub>6</sub>	V2O <sub>6</sub>	V3O <sub>6</sub>	V4O <sub>6</sub>	V5O <sub>6</sub>
<b>BVS</b>	5.00	4.98	5.01	4.99	5.02

**Table 6.** BVS per Oxygen atoms of **1**.

Atome	$\Sigma s$	Atome	$\Sigma s$
<b>O1</b>	1.853	<b>O8</b>	1.787
<b>O2</b>	1.825	<b>O9</b>	1.683
<b>O3</b>	1.826	<b>O10</b>	1.728
<b>O4</b>	1.789	<b>O11</b>	1.735
<b>O5</b>	1.732	<b>O12</b>	1.778
<b>O6</b>	2.051	<b>O13</b>	1.699
<b>O(7)</b>	1.764	<b>O(14)</b>	1.693

Decavanadate, decaaqualithium and ammonium cations are all linked via N-H...O and O-H...O as hydrogen bonds, which are the main basis of the structural cohesion of the system. The overall stability and order of these molecular arrangements is essentially maintained by the hydrogen bonds that make them up.

The structural configuration reveals the presence of multiple hydrogen bonds, uniformly characterized by their weak nature, with an average bond length of 2.99 Å. Refer to **Table 7** for a full list of these important interactions, where many of the hydrogen bonding details are carefully documented.

**Table 7.** Bond number (s) calculations for all the oxygen atoms in the  $\{V_{10}O_{28}\}^{6-}$  anion in **Cat3**.

<i>D—H...A</i>	<i>D...A</i> (Å)	<i>D—H...A</i> (°)
<b>O17-H5...O3</b>	2.78(17)	165.930(2604)
<b>O16-H4...O8</b>	2.92(18)	152.198(2337)
<b>N2-H16...O8</b>	2.85(16)	171.372(1978)
<b>N1-H13...O11</b>	3.06(16)	108.549(1904)
<b>N1-H14...O10</b>	3.01(19)	109.344(1600)
<b>N1-H13...O1</b>	2.89(17)	173.282(2341)

## ACKNOWLEDGMENTS

N.D. thanks for the financial support received from a Grant for Young Researchers (SRG-UBB 32934/22.06.2023) funded by the Babeş-Bolyai University.

## REFERENCES

- 1 S. Patai, Z. Rappoport, C. J. M. Stirling, *The Chemistry of Sulphones and Sulphoxides*, Wiley, New York, **1988**.
- 2 M. Wang, X. Jiang, *ACS Sustainable Chem. Eng.*, **2022**, *10* (2), 671–677.
- 3 A. J. Waldman, T. L. Ng, P. Wang, E. P. Balskus, *Chem. Rev.*, **2017**, *117* (8), 5784–5863.
- 4 G. Yu, Q. Wang, S. Liu, X. Zhang, Q. Che, G. Zhang, T. Zhu, Q. Gu, D. Li, *J. Nat. Prod.*, **2019**, *82* (4), 998–1001.
- 5 G. Errante, G. La Motta, C. Lagana, V. Wittebolle, M.-É. Sarciron, R. Barret, *Eur. J. Med. Chem.*, **2006**, *41*, 773–778.
- 6 J. Legros, J. R. Dehli, C. Bolm, *Adv. Synth. Catal.*, **2005**, *347*, 19 – 31.
- 7 P. Devendar, G.-F. Yang, *Top. Curr. Chem. (Z)*, **2017**, *375*, article no. 82.
- 8 I. Fernandez, N. Khiar, *Chem. Rev.*, **2003**, *103* (9), 3651–3706.
- 9 N. Wang, P. Saidhareddy, X. Jiang, *Nat. Prod. Rep.*, **2020**, *37*, 246-275.
- 10 S. Otocka, M. Kwiatkowska, L. Madalinska, P. Kielbasinski, *Chem. Rev.*, **2017**, *117* (5), 4147–4181.
- 11 G. Sipos, E.E. Drinkel, R. Dorta, *Chem. Soc. Rev.*, **2015**, *44*, 3834–3860.
- 12 B. M. Trost, M. Rao, *Angew. Chem. Int. Ed.*, **2015**, *54*, 5026 – 5043.
- 13 E. Wojaczynska, J. Wojaczynski, *Chem. Rev.*, **2010**, *110*, 4303–4356.
- 14 N.-W. Liu , S. Liang , G. Manolikakes, *Synthesis*, **2016**, *48* (13), 1939-1973.
- 15 S. Liang, K. Hofman, M. Friedrich, J. Keller, G. Manolikakes, *ChemSusChem*, **2021**, *14*, 4878–4902.
- 16 K.A. Stingl, S.B. Tsogoeva, *Tetrahedron: Asymmetry*, **2010**, *21*, 1055–1074.
- 17 J.-E. Bäckvall, *Modern Oxidation Methods*, Wiley-VCH, Weinheim, **2004**.
- 18 K.P. Volcho, N.F. Salakhutdinov, A.G. Tolstikov, *Russ. J. Org. Chem.*, **2003**, *39* (11), 1537-1552.
- 19 M. Sutradhar, A.J. L. Pombeiro, J.A.L. da Silva, *Vanadium Catalysis*, The Royal Society of Chemistry, **2020**.
- 20 R. R. Langeslay, D. M. Kaphan, C. L. Marshall, P. C. Stair, A.P. Sattelberger, M. Delferro, *Chem. Rev.*, **2019**, *119*, 2128–2191.
- 21 A. Galindo, A. Pastor, F. Montilla, and M. del Mar Conejo, in *Vanadium Catalysis*, ed. M. Sutradhar, A. J. L. Pombeiro, and J. A. L. da Silva, The Royal Society of Chemistry, **2020**, ch. 10, pp. 205-240.
- 22 R. R. Langeslay, D. M. Kaphan, C. L. Marshall, P. C. Stair, A. P. Sattelberger, M. Delferro, *Chem. Rev.*, **2019**, *119* (4), 2128–2191.
- 23 J.K. Li, C.P. Wei, Y.Y. Wang, M. Zhang, X.R. Lv, C.W. Hu, *Inorg. Chem. Commun.*, **2018**, *87*, 5–7.
- 24 N. Deak, D.Madec, G. Nemes, *Eur. J. Inorg. Chem*, **2020**, 2769-2790.
- 25 N. Deak, O. Thillaye du Boullay, I.-T. Moraru, S. Mallet-Ladeira, D.Madec, G. Nemes, *Dalton Trans.*, **2019**, *48*, 2399-2406.
- 26 N. Deak, O. Thillaye du Boullay, S. Mallet-Ladeira, I.-T. Moraru, D. Madec, G. Nemes, *Eur. J. Inorg. Chem*, **2020**, 3729-3737.


- 27 N. Deak, P. M. Petrar, S. Mallet-Ladeira, L. Silaghi-Dumitrescu, G. Nemeş, D. Madec, *Chem. Eur. J.*, **2016**, 22, 1349-1354.
- 28 N. Deak, I.-T. Moraru, N. Saffon-Merceron, D. Madec, G. Nemes, *Eur. J. Inorg. Chem.*, **2017**, 4214-4220.
- 29 N. Deak, R. Septelean, I.-T. Moraru, S. Mallet-Ladeira, D. Madec, G. Nemes, *Studia UBB Chemia*, **2018**, LXIII (2), 105-115.
- 30 N. Deak, S. Mallet-Ladeira, L. Silaghi-Dumitrescu, D. Madec, G. Nemes, *Studia UBB Chemia*, **2017**, LXII (4), Tom II, 411-420.
- 31 S.-S. Wang, G.-Y. Yang, *Chem. Rev.*, **2015**, 115, 4893-4962.
- 32 K.Y. Monakhov, W. Bensch, P. Kögerler, *Chem. Soc. Rev.*, **2015**, 44, 8443-8483.
- 33 T. Zhou, L.-L. Xie, Y. Niu, H.-R. Xiao, Y.-J. Li, Q. Han, X.-J. Qiu, X.-L. Yang, X.-Y. Wu, L.-M. Zhu, H. Pang, X.-Y. Cao, *Rare Met.*, **2023**, 42 (5), 1431-1445.
- 34 M. Ghosh, D. Sorsche, R. B. Ahmed, M. Anjass, *ChemSusChem*, **2023**, 16, article no. e2023006.
- 35 M. Anjass, G.A. Lowe, C. Streb, *Angew. Chem. Int. Ed.*, **2021**, 60, 7522-7532.
- 36 Q. Liang, Z. Peng, J. Liang, J., Song, Y., Jia, W., & Mao, *Fibers. Polym.*, **2022**, 23, 3380-3385.
- 37 M. Aureliano, C. André Ohlin, *J. Inorg. Biochem.*, **2014**, 137, 123-130.
- 38 M. Idboumlik, M. Kadiri, N. Hamdi, M. Driouch, A.F.I. Ngopoh, I. Lakkab, E-E. Bendeif, M. Sfaira, B. El Bali, M. Lachkar, A. Zarrouk, *Mater. Chem. Phys.*, **2022**, 287, article no. 126211.
- 39 M. Idboumlik, I. Lakkab, S. Erraouan, N. Hamdi, M. Lachkar, M. Dusek, V. Eigner, B. El Bali, *J. Mol. Struct.*, **2024**, 1312, article no. 138551.
- 40 A. Misra, K. Kozma, C. Streb, M. Nyman, *Angew. Chem. Int. Ed.* **2020**, 59, 596-612.
- 41 N. Tang, Y. Zhang, F. Lin, H. Lu, Z. Jiang, C. Li, *Chem. Commun.*, **2012**, 48, 11647-11649.
- 42 C. Li, N. Mizuno, K. Murata, K. Ishii, T. Suenobu, K. Yamaguchi, K. Suzuki, *Green Chem.*, **2020**, 22, 3896-3905.
- 43 J.-K. Li, C.-P. Wei, Y.-Y. Wang, M. Zhang, X.-R. Lv, C.-W. Hu, *Inorg. Chem. Commun.*, **2018**, 87, 5-7
- 44 X. Huang, X. Gu, Y. Qi, Y. Zhang, G. Shen, B. Yang, W. Duan, S. Gong, Z. Xue, Y. Chen, *Chin. J. Chem.*, **2021**, 39, 2495-2503.
- 45 K. Routh, C.P. Pradeep, *Inorg. Chem.*, **2023**, 62, 13775-13792.
- 46 P. T. Anastas and J. C. Warner, *Green Chemistry: Theory and Practice*, Oxford University Press, **1998**.
- 47 A. J. Hunt, Ed., *Element Recovery and Sustainability*, RSC Publishing, **2013**.
- 48 R. Ksiksi, M. Graia, A. Driss, T. Jouini, *Acta Cryst. E*, **2004**, E60, i105-i107.
- 49 R. Ksiksi, Z. Abdelkafi-Koubaa, S. Mlayah-Bellalouna, D. Aissaoui, N. Marrakchi, N. Srairi-Abid, M. Faouzi Zid, M. Graia, *J. Mol. Struct.*, **2021**, 1229, article no. 129492
- 50 G.-B. Li, S.-H. Yang, M. Xiong, J.-H. Lin, *Acta Cryst. C*, **2004**, C60, m612-m614.
- 51 J.L. Ferreira da Silva, M.F. Minas da Piedade, M.T. Duarte, *Inorganica Chim. Acta*, **2003**, 356, 222-242.

- 52 A.-A. Mamdouh, A.B.M. Ibrahim, N. El-Houda A. Reyad, T.R. Elsayed, I. Cordeiro Santos, A. Paulo d, R. M. Mahfouz, *J. Mol. Struct*, **2022**, 1253, article no. 132247.
- 53 M. Louati, R. Ksiksi, I. Elbini-Dhouib, S. Mlayah-Bellalouna, R. Doghri, N. Srairi-Abid, M.-F. Zid, *J. Mol. Struct*, **2021**, 1242, article no. 130711.
- 54 D. Prat, A. Wells, J. Hayler, H. Sneddon, C.R. McElroy, S. Abou-Shehadad, P. J. Dunn, *Green Chem.*, **2016**, 18, 288-296.
- 55 D. Prat, J. Hayler, A. Wells, *Green Chem.*, **2014**, 16, 4546-4551.
- 56 X. Wang, T. Zhang, Y. Li, J. Lin, H. Li, X.-L. Wang, *Inorg. Chem.*, **2020**, 59, 17583–17590.
- 57 G. M. Sheldrick, *Acta Cryst.*, **2015**, C71, 3-8.
- 58 BrukerSAINT 6.45, Bruker AXS Inc., Madison, Wisconsin, USA, **2001**.
- 59 BrukerSADABS 2.10, Bruker AXS Inc., Madison, Wisconsin, USA, **2001**.
- 60 BrukerAPEX3 2019.11-0, Bruker AXS Inc., Madison, Wisconsin, USA, **2019**.
- 61 Brandenburg, K.; Putz, H. DIAMOND Version 3; Crystal Impact GbR: Bonn, Germany, **2005**.
- 62 C. F. Macrae, I. Sovago, S. J. Cottrell, P. T. A. Galek, P. McCabe, E. Pidcock, M. Platings, G. P. Shields, J. S. Stevens, M. Towler, P. A. Wood, *J. Appl. Cryst.*, **2020**, 53, 226-235.
- 63 J.L. Ferreira da Silva, M.F. Minas da Piedade, M.T. Duarte, *Inorganica Chim. Acta*, **2003**, 356, 222-242.
- 64 G.-B. Li, S.-H. Yang, M. Xiong, J.-H.Lin, *Acta Cryst.*, **2004**, C60, m612-m614.
- 65 M. Louati, R. Ksiksi, I. Elbini-Dhouib, S. Mlayah-Bellalouna, R. Doghri, N. Srairi-Abid, M.-F. Zid, *J. Mol. Struct*, **2021**, 1242, article no. 130711.
- 66 I.D. Brown, D. Altermatt, *Acta Cryst. B*, **1985**, B41, 244-247.





# STUDY OF KAZAKHSTAN'S SHUNGITE AS ELECTROCATALYST SUBSTRATE IN HYDROGEN EVOLUTION REACTION IN ACIDIC MEDIA

Azhar ATCHABAROVA<sup>a</sup> , Dinara ABDUAKHYTOVA<sup>a\*</sup> ,  
Khaisa AVCHUKIR<sup>a</sup> , Graziella Liana TURDEAN<sup>b,c\*</sup> ,  
Saken ABDIMOMYN<sup>a</sup> , Rustam TOKPAYEV<sup>a</sup> ,  
Tamina KHAVAZA<sup>a</sup> , Mikhail NAURYZBAYEV<sup>a</sup> 

**ABSTRACT.** The most efficient method to produce hydrogen is by electrolysis of water, and scientist's current research is focused on developing inexpensive catalysts for this process. The article aims to study a carbon material (CM) obtained from shungite raw materials as electrocatalyst support in hydrogen evolution reaction (HER). The obtained activated CM has a multi-layered lamellar morphology with a specific surface area 356.40 m<sup>2</sup>/g. Electrocatalytical properties of the activated carbon material are the following: overpotential ( $\eta$ ) at 10 mA/cm<sup>2</sup> of 0.515 V vs. RHE with a Tafel slope of 172.5 mV/dec and good stability in acidic media. The obtained results show that activated CM from shungite raw material can be used as an electrocatalyst for obtaining hydrogen.

**Keywords:** *hydrogen, carbon material, shungite, electrocatalyst, hydrogen evolution reaction.*

## INTRODUCTION

Hydrogen is actively studied as an alternative to fossil fuel, due to its high heat value and the environmentally friendly final product, *i.e.*, water [1, 2]. One of

---

<sup>a</sup> Center of Physical Chemical Methods of Research and Analysis, Al-Farabi Kazakh National University, Almaty, Kazakhstan

<sup>b</sup> Babeş-Bolyai University, Faculty of Chemistry and Chemical Engineering, Research Center of Electrochemistry and Non-Conventional Materials, 11 Arany Janos str., RO-400028, Cluj-Napoca, Romania

<sup>c</sup> Interdisciplinary Research Institute on Bio-Nano-Sciences, 42 Treboniu Laurian St., RO-400271, Cluj-Napoca, Romania

\* Corresponding authors: [abduakhytova@mail.ru](mailto:abduakhytova@mail.ru), [graziella.turdean@ubbcluj.ro](mailto:graziella.turdean@ubbcluj.ro)



the ways of obtaining hydrogen is water electrolysis, which is easy, available equipment-wise, and provides high purity of hydrogen without toxic waste. Hydrogen evolution reaction (HER) is the main reaction in water electrolysis and is widely studied with various metals, alloys, and composite materials. Noble metals are considered to be the best options for HER [3,4], due to the low stress of hydrogen. Among those, platinum is considered the best catalyst for the electrochemical production of hydrogen, but economic reasons limit its wider use in HER [5,6]. Palladium can be an electrocatalyst in HER alongside with Pt. As known, nowadays Pd and its alloys are widely used in hydrogen storage.

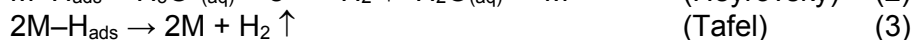
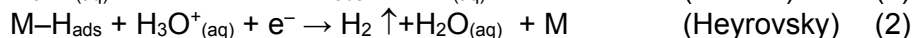
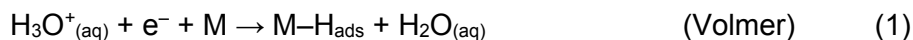
In terms of economic efficiency, several transition metal oxides (Ni, Co, Mn, Fe, etc.) have been extensively studied in HER [7-9]. The main obstacles to the use of metal oxides as electrocatalysts are the interface complexity of the hybrid structures, relatively high resistance, low selectivity and durability, and susceptibility to gas intoxication followed by negative environmental impact. In addition, most metal oxides are semiconductors or dielectrics.

Carbon materials are known to be widely used as electrodes in electrochemical processes. This is due to the fact that carbon has good thermal stability, controlled surface chemical properties, and corrosion resistance against acids and bases. The literature has reported investigations on carbon-based materials such as carbon nanotubes, carbon nanofibers, graphene, activated carbon, and extrinsic carbon structures, as electrodes. [10]. Among all the carbon materials mentioned above, activated carbon is the most prominent due to its cheap and easy production technology, using different available materials (plant-based or carbon-mineral-based), large active surface area, porous structure, and high conductivity, as in the case of metals [11].

The aim of this article is the study of the electrocatalytic activity of carbon materials obtained from shungite solids - waste materials from the processing of polymetallic ores in Kazakhstan [12], for the hydrogen evolution reaction.

## RESULTS AND DISCUSSION

In acidic solutions, HER occurs at the surface of the electrode following a multi-step electrochemical reaction:



where: M is a vacant surface site of the electrocatalyst, and the M-H<sub>ads</sub> is the absorbed hydrogen atoms.

STUDY OF KAZAKHSTAN'S SHUNGITE AS ELECTROCATALYST SUBSTRATE  
IN HYDROGEN EVOLUTION REACTION IN ACIDIC MEDIA

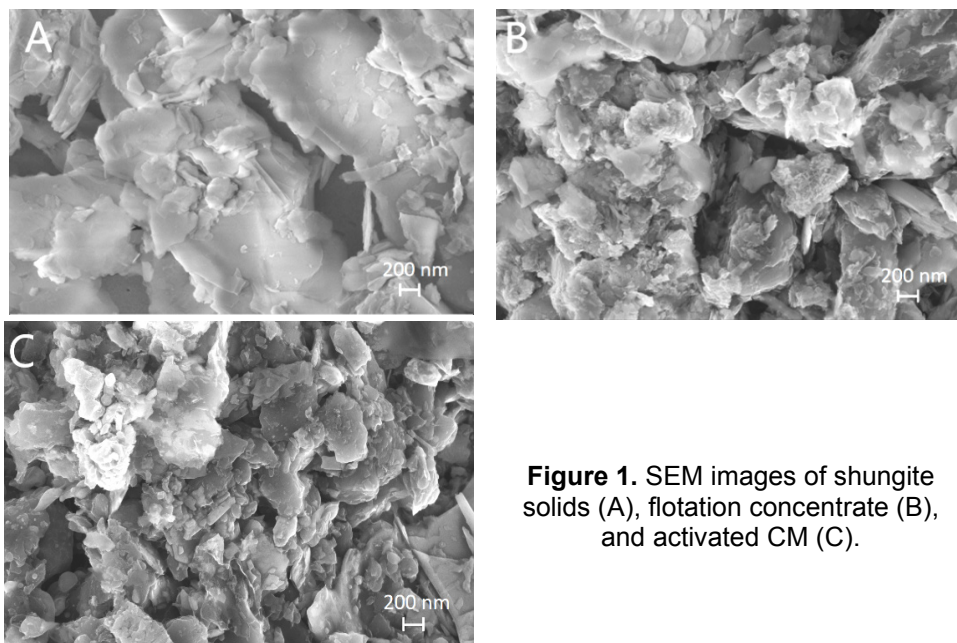
Briefly, the process consists of an initial discharge of the hydronium ions and the formation of an adsorbed hydrogen intermediates (*i.e.*,  $M-H_{ads}$ , Volmer reaction 1), followed by the formation of  $H_2$  either in Heyrovsky reaction 2, or in Tafel reaction 3 [13-16].

Three types of materials - shungite solids, flotation concentrate, and activated CM - were selected to investigate the HER, in acidic media. The content of the various elements in these materials is shown in Table 1. It can be seen that after the enrichment process by carbonization and activation, the impurity content decreased significantly.

**Table 1.** X-ray diffraction element analysis of carbon materials.

Carbon materials	Element's content, %							
	Mg	Si	P	S	K	Mn	Fe	Al
Shungite solids	0.897	26.375	0.063	0.254	3.675	0.141	8.837	10.812
Flotation concentrate	0.552	15.106	0.042	4.055	3.19	0.082	8.87	8.199
Activated CM	0.201	0.00	0.099	0.030	2.241	0.046	0.417	0.00

The SEM images of the carbon-based materials (Fig 1) show the shungite solids have a layered lamellar structure, but after the flotation and carbonization processes its surface loses this characteristic layering, becoming noticeably rougher.

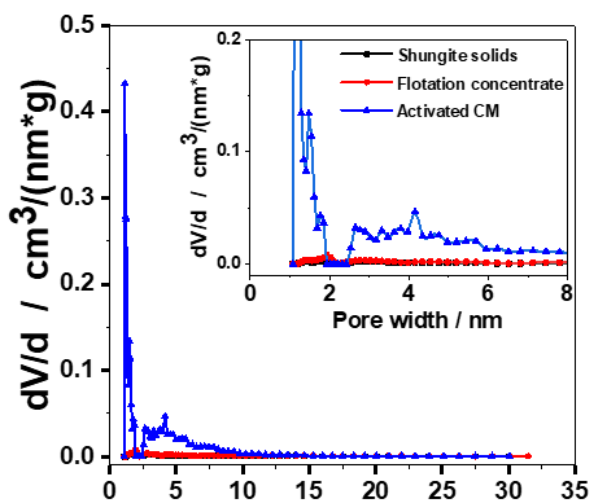


**Figure 1.** SEM images of shungite solids (A), flotation concentrate (B), and activated CM (C).

As can be seen from the pore distribution curve (Figure 2), after the carbonization and activation step, the porosity of the carbon material increases, and the material is mainly formed by micropores. Table 2 provides the numerical values of the specific surface area and pore volume for the studied carbon materials. In the case of the activated carbon material, the specific surface area (356.4 m<sup>2</sup>/g) and the pore numbers (0.5 cm<sup>3</sup>/g) have maximum values.

**Table 2.** Porosity of carbon materials.

Carbon materials	Carbon content, %	Specific surface area (S <sub>BET</sub> ), m <sup>2</sup> /g	Total pore volume, (V <sub>tot</sub> ), cm <sup>3</sup> /g	Micropores, %
Shungite solids	≥10	9.38	0.03	70.37
Flotation concentrate	25	16.30	0.05	71.74
Activated CM	51	356.40	0.50	89.40



**Figure 2.** Pore size distribution curve.

The electrochemical activity of carbon materials was studied in an acidic environment of 0.5 M H<sub>2</sub>SO<sub>4</sub> at 25°C, by recording linear voltammograms at a scan rate of 10 mV/s. In the HER polarization curves presented in Fig 3, the potential values recorded *versus* Ag|AgCl electrode were converted into potential values expressed *versus* reversible hydrogen electrode (RHE) using the following equation 4 [17]:

$$E_{\text{RHE}} = E_{\text{Ag/AgCl}} + E^0_{\text{Ag/AgCl}} + 0,059 \times \text{pH} \quad (4)$$

It is worth mentioning that, in order to be an ideal catalyst for the HER process, the studied material should provide a high current density value for a low overpotential value, as well as a low value of HER onset potential (*i.e.*, on the recorded  $j - E$  diagrams, the potential value where the  $H_2$  evolution behavior will be initially observed) [17]. From a practical point of view, the electrocatalytical activity of any material in HER is estimated by comparing the overpotential ( $\eta_{HER}$ ) values, recorded at  $10 \text{ mA/cm}^2$ .

As seen in Fig 3A, the bare glassy carbon electrode (GCE) has negligible electrocatalytic activity towards HER, while the different studied carbon materials show enhanced electroactivity in HER, probably due to the presence of the active sites in their structure. Also, the values summarized in Table 3 show that the onset potential increases in the following order:  $-0.8 \text{ V vs. RHE}$  (at GCE)  $< -0.351 \text{ V vs. RHE}$  (at Flotation concentrate/GCE)  $< -0.298 \text{ V vs. RHE}$  (at Activated CM/GCE)  $< 0.03 \text{ V vs. RHE}$  (at (Pt/C(10%))/GCE), respectively. At the same time, the studied carbon materials have the following increasing overpotential order, at  $10 \text{ mA/cm}^2$ :  $-0.052 \text{ V vs. RHE}$  (at (Pt/C(10%))/GCE)  $< -0.515 \text{ V vs. RHE}$  (at Activated CM/GCE)  $< -0.602 \text{ V vs. RHE}$  (at Flotation concentrate/GCE), respectively. It must be underlined that the HER overpotential at  $10 \text{ mA/cm}^2$  has the lowest value at commercial Pt/C(10%), *i.e.*,  $-0.052 \text{ V vs. RHE}$ , which is comparable to the value reported in the literature for similar electrocatalysts (*e.g.*,  $-0.040 \text{ V vs. RHE}$  at Pt/C(20%)) [17]).

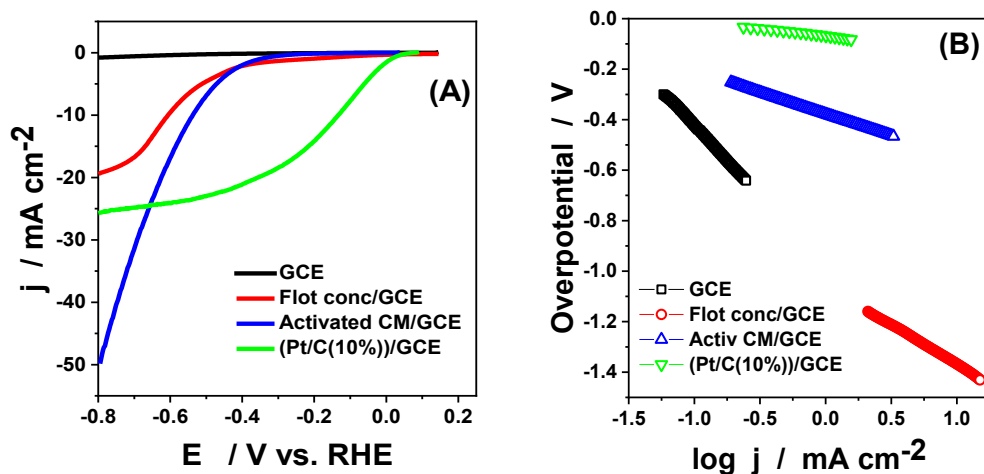
**Table 3.** Electrocatalytic properties of studied carbon materials.

Carbon materials	Onset potential, V vs. RHE	$\eta_{HER}$ recorded at $10 \text{ mA/cm}^2$ , V vs. RHE	Tafel slope, mV/dec
GCE	-0.8	-	561.5
Flotation concentrate/GCE	-0.351	-0.602	312.9
Activated CM/GCE	-0.298	-0.515	172.5
(Pt/C(10%))/GCE	0.03	-0.052	59.3

In order to obtain information about the kinetic mechanism of the hydrogen evolution reaction at various electrocatalytic materials, Tafel plots are necessary to be represented (equation 5) [14]:

$$\eta = a + b \times \log |j| \quad (5)$$

where:  $\eta$  is the overpotential,  $b$  is the Tafel slope,  $j$  is the current density.



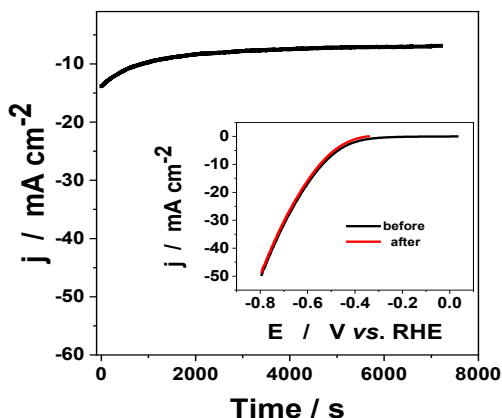
**Figure 3.** Linear polarization curves (A) and the corresponding Tafel plots (B) for HER at bare GCE (black), flotation concentrate/GCE (red), activated CM/GCE (blue), and Pt/C(10%)/GCE (green) modified electrodes. Experimental conditions: electrolyte, 0,5 M H<sub>2</sub>SO<sub>4</sub>; scan rate, 10 mV/s; starting potential, 0.1 V vs. RHE.

Thus, the slopes of the linear portions of the low overpotential values of the LSV polarization curves are estimated and compared.

Moreover, Tafel slope values depend on the overpotential ( $\eta$ ) and the surface coverage with M-H<sub>ads</sub> species for various rate-determining steps of HER [13, 16]. In our case, for Pt-C(10%) the Tafel slope is 59.3 mV/dec, as reported in the literature for similar electrocatalyst (*i.e.*, 34.4 mV/dec at Pt-C(20%) [17]). Also, the Tafel slopes of 172.5 mV/dec (at activated CM) and 312.9 mV/dec (at flotation concentrate), indicate that the activated CM having the lowest value of the slope has a higher HER activity compared with the flotation concentrate material [17]. Moreover, it can be concluded that the kinetic of HER follows steps in which the hydrogen adsorption and desorption occur in consecutive Volmer- Heyrovsky reactions [16, 17] and that the initial proton adsorption (*i.e.*, Volmer reaction 1) is the rate-determining step of the whole HER process [18].

The material's long-term stability is an essential parameter to be estimated for a HER electrocatalyst. Thus, by chronoamperometry at an applied potential of -0.5 V vs. RHE, for a period of 3 hrs, the stability of activated CM was researched. As presented in Figure 4, the activated CM shows acceptable stability; the current density decrease from the initial value was ~30%. Moreover, the linear polarization curves recorded before and after chronoamperometry measurements (Figure 4, inset) showed that there are no significant changes from the initial curve, which suggests good stability of the activated CM material.

STUDY OF KAZAKHSTAN'S SHUNGITE AS ELECTROCATALYST SUBSTRATE  
IN HYDROGEN EVOLUTION REACTION IN ACIDIC MEDIA



**Figure 4.** Chronoamperometry curve of activated CM and comparative linear polarization curves of activated CM before and after chronoamperometry measurements (inset).

## CONCLUSIONS

Two types of activated carbon materials - flotation concentrate and activated CM - were obtained from shungite solids by froth floatation, followed by carbonization and activation steps. Morphological and structural characteristics of the materials were presented. The electrochemical activity in hydrogen evolution reaction in acidic media was investigated by linear polarization curves, and chronoamperometry. The Tafel slopes showed that the activated CM having the lowest value of the Tafel slope (*i.e.*,  $172.5 \text{ mV/dec}$ ) has a higher HER activity compared with the flotation concentrate material. The long-term stability estimated from LSV before and after chronoamperometric measurements showed good stability of the activated CM material. According to the obtained results, the activated CM made from shungite raw material can be employed as an electrocatalyst to produce hydrogen.

## EXPERIMENTAL SECTION

### Reagents

The following reagents were used in the present study: shungite solids (from Bakyrchik deposit, East Kazakhstan region), Flotol flotation agent (from KhimProm), kerosene (TC-1 from RPG), Nafion<sup>®</sup> (5% in ethanol, from Sigma



Aldrich), ethanol (95.0 %, from Sigma Aldrich), 0.5 M H<sub>2</sub>SO<sub>4</sub> (State Standard 14262-78) and Pt/C (10%) (from Sigma Aldrich).

### **Preparation of activated CM**

The shungite solids having a low content of carbon were enriched by different methods. Shortly, shungite rock was preliminarily crushed, until the final particle size was  $\leq 300 \mu\text{m}$ . The composition of the initial samples for enrichment was averaged and selected by the quartering method. Shungite materials were ground to  $100 \mu\text{m}$  and enriched in carbon content using froth floatation with two-step rewashing, utilizing Flotol floatation agent and kerosene to obtain floatation concentrate samples. In order to obtain activated CM samples and to increase the porosity of the material, the shungite floatation concentrate was treated by carbonization at  $700 - 750 \text{ }^\circ\text{C}$ , followed by steam-gas activation at  $800 - 850 \text{ }^\circ\text{C}$ .

### **Methods of investigation**

The morphology of the obtained carbon-based samples was investigated using scanning electron microscopy. Micrographs were obtained using an Ultra-high Resolution Scanning Electron Microscope (UHR FE-SEM Hitachi SU8020). It was equipped with secondary electron detectors, four-quadrant electron backscatter photodiode detector.

The porous characteristics of the materials were obtained using N<sub>2</sub> - sorption experiments, which were carried out using Quadrasorb evo device for volumetric gas sorption. Before analysis, the samples were degassed at  $250 \text{ }^\circ\text{C}$  and a pressure of  $1 \cdot 10^{-6}$  bar for 12 hours. Specific surface area ( $S_{\text{Specific}}$ ) was determined using the BET equation (Brunauer-Emmett-Teller). The total pore volume ( $V_{\text{tot}}$ ) was calculated based on the nitrogen amount adsorbed at the highest relative pressure.

Electrochemical measurements were performed in a three-electrode cell, equipped with the modified electrode as the working electrode, the Ag|AgCl reference electrode, and a platinum grid as an auxiliary electrode, respectively. The electrolyte was a 0.5 M H<sub>2</sub>SO<sub>4</sub> solution. All measurements were carried out using a computer-controlled AUTOLAB (type PGSTAT302N, Methrom, The Netherlands) potentiostat/galvanostat.

### **Electrode preparation**

Modified electrodes based on the immobilization of carbon-based materials in a polymeric matrix were prepared by the drop-casting method.

Thus, 50 mg of carbon-based material were dispersed in 100  $\mu\text{L}$  of Nafion<sup>®</sup> solution (5%) and 50  $\mu\text{L}$  of ethanol (95.0%). The obtained dispersion was ultrasonicated for 30 min. Then, a volume of 10  $\mu\text{L}$  of dispersion was dropped onto the mirror-polished glassy carbon electrode surface (6 mm diameter) and left to dry, at room temperature. The obtained electrodes (symbolized as: flotation concentrate/GCE, activated CM/GCE, (Pt/C)/GCE) were then used for the study of the electrocatalytical activity of the activated carbon material for HER. In order to compare the obtained material's properties, electrodes with commercial catalyst Pt/C (10%) were also prepared.

## ACKNOWLEDGMENTS

This research was funded by the Science Committee of the Ministry of Education and Science of the Republic of Kazakhstan (Grant No. AP09563184).

## REFERENCES

1. M. Sastri; *Int. J. Hydrogen Energy*, **1980**, *5*, 365 – 367. doi:10.1016/0360-3199(80)90017-8.
2. L. Tianze; D. Yuanyuan; Zh. Jianjiao; W. Lixue; D. Fangzheng; W. Dandan; Z. Hong; *Int. J. Hydrogen Energy*, **2024**, *77*, 359 – 372. doi:10.1016/j.ijhydene.2024.06.185.
3. H.-E. Cheng; W.-L. Li; Z.-P. Yang; *Int. J. Hydrogen Energy*, **2019**, *44*, 30141 – 30150. doi:10.1016/j.ijhydene.2019.09.188.
4. M. Molla; M. Sarker; A. Kibria; *Bangladesh J. Sci. Ind. Res.*, **2008**, *43*, 103 – 116. doi:10.3329/bjsir.v43i1.861.
5. Z. Wang; X. Ren; Y. Luo; L. Wang; G. Cui; F. Xie; X. Sun; *Nanoscale*, **2018**, *10*, 12302 – 12307. doi:10.1039/c8nr02071j.
6. J. Benson; M. Li; S. Wang; P. Wang; P. Papakonstantinou; *ACS Appl. Mater. Interfaces*, **2015**, *7*, 14113 – 14122. doi:10.1021/acsami.5b03399.
7. X. Qian; T. Hang; S. Shanmugam; M. Li; *ACS Appl. Mater. Interfaces*, **2015**, *7*, 15716 – 15725. doi:10.1021/acsami.5b00679.
8. V. Vij; S. Sultan; A. M. Harzandi; A. Meena; J. N. Tiwari; W.-G. Lee; K. S. Kim; *ACS Catalysis*, **2017**, *7*, 7196 – 7225. doi:10.1021/acscatal.7b01800.
9. C. Lo Vecchio; A. S. Arico; G. Monforte; V. Baglio; *Renew. Energy*, **2018**, *120*, 342 – 349. doi:10.1016/j.renene.2017.12.084.
10. J. Zhang; Z. Xia; L. Dai; *Science Adv.*, **2015**, *1*, e1500564. doi:10.1126/sciadv.1500564.
11. R. Paul; Q. Dai; C. Hu; L. Dai; *Carbon Energy*, **2019**, *1*, 19 – 31. doi:10.1002/cey2.5.

12. S. A. Efremov; Production technology of carbon-mineral materials on the basis of shungite rocks: PhD thesis, 05.17.01, Almaty, **2010**, p. 240.
13. B. E. Conway; B. V. Tilak; *Electrochim Acta*, **2002**, *47*, 3571 – 3594. doi: 10.1016/S0013-4686(02)00329-8.
14. T. Shinagawa; A. T. Garcia-Esparza; K. Takanabe; *Scientific Rep*, **2015**, *5*, 13801. doi: 10.1038/srep13801.
15. F. Bao; E. Kemppainen; I. Dorbandt; R. Bors; F. Xi; R. Schlatmann; R. van de Krol; S. Calnan; *ChemElectroChem* **2021**, *8*, 195 – 208. doi: 10.1002/celec.202001436.
16. H. Prats; K. Chan; *Phys. Chem. Chem. Phys.*, **2021**, *23*, 27150 – 27158. doi: 10.1039/d1cp04134g.
17. R. S. A. Saravanan; N. Prabu; M. Sasidharan; G. Maduraiveeran; *Appl. Surf. Sci.*, **2019**, *489*, 725 – 733. doi:10.1016/j.japsusc.2019.06.040.
18. Y. Zheng; Y. Jiao; L. H. Li; T. Xing; Y. Chen; M. Jaroniec; S. Z. Qiao; *ACS Nano*, **2014**, *8*, 5290 – 5296. doi: 10.1021/nn501434a.

## NEUROTROPHIC EFFECTS OF IRIDOID GLYCOSIDES FROM *LAMIUM ALBUM* L. AS NATURAL GLP1-R MODULATORS IN REPEATED RESTRAINT STRESS

Ioana ROMAN<sup>a</sup>, Claudia-Andreea MOLDOVEANU<sup>b,a</sup>,  
Ștefan DRĂGAN<sup>b</sup>, Julia BAUMLI<sup>c</sup>, Claudia CIMPOIU<sup>c,d</sup>  
and Vlad-Alexandru TOMA<sup>b,a\*</sup>

**ABSTRACT.** The pleiotropic effects of *Lamium* species are extensively utilized for treating urinary bladder injuries and infections and addressing blood hypertension or liver toxicities. Despite widespread *Lamium* consumption in animals and humans, its impact on brain biochemical parameters remains unexplored. In our study, we demonstrated the regenerative effect of *L. album* L. in a rat model of restraint stress, commonly employed to investigate neuropsychological stress. Following extract administration, there was a reduction in stress hormones (corticosterone, adrenaline), inflammation (TNF $\alpha$ ), and oxidative stress. These neuroregenerative effects may be attributed to *Lamium*'s phytochemical composition, particularly its iridoids and luteolin content, which appear to mimic the action of glucagon-like peptide 1 (GLP-1). These findings suggest the potential use of *L. album* as a neuroregenerative adjuvant.

**Keywords:** *iridoids, Lamium album, GLP1*

---

<sup>a</sup> Department of Experimental Biology and Biochemistry, Institute of Biological Research, & Cluj-Napoca, Branch of NIRDBS, Bucharest, Romania

<sup>b</sup> Department of Molecular Biology and Biotechnology, Faculty of Biology and Geology, & Centre for Systems Biology, Biodiversity and Bioresources "3B" Babes-Bolyai University, RO-400006 Cluj-Napoca, Romania

<sup>c</sup> Babes-Bolyai University, Faculty of Chemistry and Chemical Engineering, Cluj-Napoca, Romania

<sup>d</sup> Research Center for Advanced Chemical Analysis, Instrumentation and Chemometrics, Cluj-Napoca, Romania

\* Corresponding author: vlad.toma@ubbcluj.ro



## INTRODUCTION

*Lamium* species are utilized in traditional medicine for treating infections, hypertension, as well as uterine and vaginal bleeding. Extracts of these species also exhibit anti-hypoxic, anti-inflammatory, and antioxidant activities [1-3] owing to their biologically active compounds, including flavonoids, iridoids, phenolic acids, amino acids, carotenoids, sterol derivatives, trigonelline, ursolic, and oleanolic acids [4-6].

The primary compounds found in *L. album* herbs include verbascoside, isoverbascoside, and various derivatives of isoscutelareine. Minor compounds such as apigenin-7-O-glucoside, luteolin-7-O-glucoside, apigenin-7-O-rutinoside, and naringenin-7-O-rutinoside have also been identified [3,7]. These plant extracts demonstrate antioxidant effects due to their phytochemicals. Furthermore, certain genera-specific compounds from the iridoids class exhibit a wide range of beneficial properties, including anticancer, antioxidant, antibacterial, antiviral, anti-inflammatory, antiarthritic, immunomodulatory, neuroprotective, and wound healing properties [8]. Among these, 6-shanzhiside methyl ester and 8-acetylshanzhiside methyl ester have been identified as the main effective iridoid glycosides (IGs) in the *Lamiaceae* group [9]. They have been shown to block TNF- $\alpha$ -induced nuclear factor- $\kappa$ B (NF- $\kappa$ B) and I $\kappa$ B- $\alpha$  phosphorylation while increasing Akt phosphorylation in hypoxic neuronal environments [10-12].

These features of *L. album* highlight its therapeutic potential in inflammatory and oxidative stress disorders such as toxic hepatitis, xenobiotic-induced kidney failure, and brain hypoxic impairments. Brain hypoxia is associated with neuropsychological stress, brain traumatic injuries, aging, or disturbances in oxygen delivery (e.g., anemia, hemoglobin dysfunctions, -SH depletion, hypoxic environments) [13-16]. Various experimental studies have utilized repeated restraint stress, which correlates with physical and psychological stress, to investigate brain hypoxia and its effects in rodents [17].

Restraint stress induces hypoxia and imbalance in the HPA axis (activation of the hippocampus-hypothalamus-adrenal axis (HHPA) stimulus), leading to increased neuronal damage and elevation of stress hormone concentrations, including corticotropin-releasing hormone, ACTH, adrenaline, noradrenaline, and glucocorticoids [17, 18, 19-29]. In stress conditions, the CA3 field of the hippocampus plays a specific role in coping mechanisms, as noticed in our previously published work [30], by developing a balancing function in the input-output relationship of stress signals according to large literature shreds of evidence [24, 25, 31-34]. Repeated restraint stress profoundly affects the nervous system endocrine glands, digestive system, and kidneys [23, 24, 35-38]. Both acute (3-7 days) and chronic HHPA stimulation (14-22 days) lead to increased glucocorticoid levels [32, 35, 38], which act synergistically with

excitatory amino acids to cause concentration-dependent hippocampal neuronal damage [37-41] during prolonged exposure to repeated restraint stress (> 5 days, 3 hours of stress per day).

Iridoids, as GLP-1R agonists [42], determine endogenous regulation of the HPA axis by their stimulatory action on GLP-1 receptors. This stimulatory effect of the shanzhiside-methyl esters is accompanied by decreases in corticosterone and adrenaline and structural improvement of the dentate gyrus by modulating granular and subgranular cell regeneration and distribution.

On the other hand, the same authors [42] mentioned that GLP-1 agonists enhanced stress-induced corticosterone release. These studies have shown that recruitment of central GLP-1 receptors potently activates the HPA axis in both humans and rodents, resulting in increased ACTH and corticosterone concentrations in the blood. Importantly, central administration of exendin-4, a GLP-1 agonist, leads to an increase in corticosterone concentration in rodents, suggesting the involvement of central GLP-1 receptors possibly expressed on CRH-expressing neurons in the hypothalamus. Central blockade of CRH receptors blocks exendin-4-induced increases in ACTH and corticosterone, establishing a role for central GLP-1 receptors in HPA axis regulation. For example, in a study focusing on the role of GLP-1 in cocaine addiction, GLP-1 neurons were found to be activated by an injection of corticosterone into the fourth ventricle. Fourth ventricle corticosterone administration reduced cocaine self-administration, and this reduction was blocked by GLP-1 receptor antagonists in the ventral tegmental area. These data suggest that not only does central GLP-1 activate the HPA axis, but corticosterone in turn activates the central GLP-1 system.

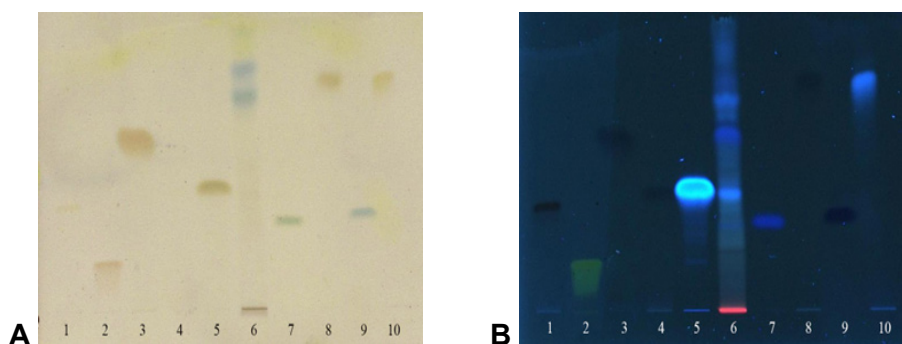
Our study aimed to investigate whether shanzhiside derivatives modulate the activity and plasticity of the hippocampus in response to repeated restraint stress and induce cellular regeneration associated with reducing oxidative stress and corticosterone concentration. This research hypothesis was based on the anti-hypoxic, anti-inflammatory, and GLP-1R regulatory properties of iridoids found in *L. album*, such as 6-shanzhiside methyl ester and 8-acetyl shanzhiside methyl ester.

## RESULTS AND DISCUSSION

### Phytochemistry of the *L. album* extract

The content of phytochemical compounds, namely iridoids, flavonoids, and phenolics in the *L. album* extract, was determined using spectrophotometric assays. The results showed that phenolics are present in the highest amount

( $1.082 \pm 0.055$  mg/mL gallic acid equivalents), followed by iridoids ( $158.84 \pm 1.92$   $\mu$ g/mL aucubin equivalents), with flavonoids being present in the smallest amount ( $70.13 \pm 0.02$   $\mu$ g/mL rutin equivalents). The *in vitro* antioxidant capacity of the *L. album* extract was determined using two widely used assays: 2,2'-azino-bis (3-ethylbenzthiazoline-6-sulfonic acid radical cation (ABTS<sup>•+</sup>) and 2,2-diphenyl-1-picrylhydrazyl radical (DPPH<sup>•</sup>). The antioxidant capacity determined using the DPPH assay ( $2.40 \pm 0.14$   $\mu$ mol/mL Trolox equivalents) was higher than that determined using the ABTS method ( $0.84 \pm 0.01$   $\mu$ mol/mL Trolox equivalents). The High-Performance Thin-Layer Chromatography (HPTLC) method was optimized and employed for the screening of phytochemical compounds, particularly iridoids, which are of particular interest in the extract. HPTLC screening of the *L. album* extract confirmed the presence of iridoids through derivatization with a specific reagent (p-dimethylamine benzaldehyde), as well as certain specific phenolic compounds (**Figure 1A-B**). The presence of iridoids is confirmed by the blue spots on a cream/beige background.

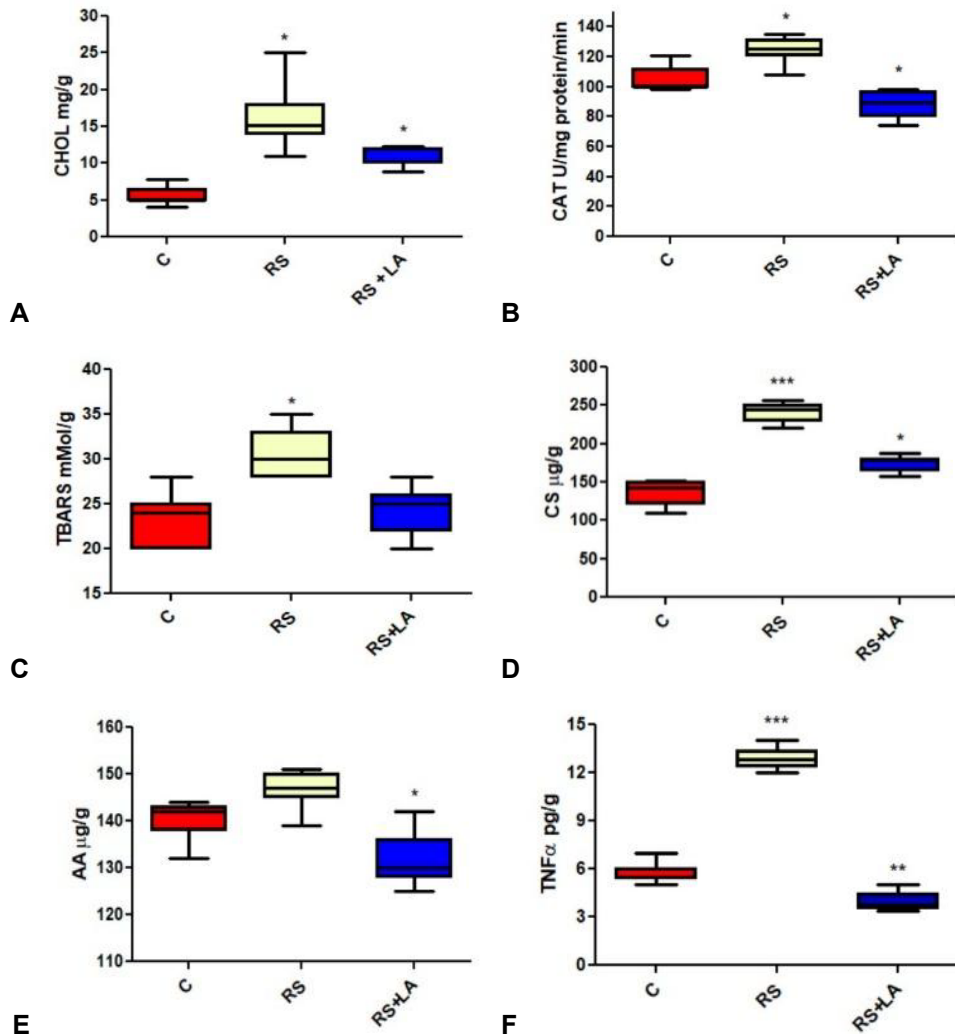


**Figure 1.** HPTLC separation on RP-18 F254s with acetonitrile – 0.1% formic acid (5:5, v/v) as the mobile phase. **(A)** Visible light after derivatization with p-dimethylaminobenzaldehyde. **(B)** UV 366 nm. Tracks: 1 – rutin; 2 – quercetin; 3 – procatechuic; 4 – vanillic acid; 5 – caffeic acid; 6 – *L. album* extract; 7 – ferulic acid; 8 – gallic acid; 9 – p-coumaric acid; 10 – chlorogenic acid.

### Biochemical analyses

Brain biochemical spectrum reactions (**Figure 2A - F**) demonstrated a particular biochemical behavior in the hippocampus under stress conditions. Cholesterol concentration in the C group was  $4.34 \pm 0.19$  mg/g, and stress exposure exhibited a significant increase ( $17.78 \pm 0.33$  mg/g,  $p < 0.001$ ) in hippocampal cholesterol levels, while the administration of *L. album* significantly decreased the cholesterol concentration ( $10.5 \pm 0.28$  mg/g,  $p < 0.001$ , **Figure 2A**).

NEUROTROPHIC EFFECTS OF IRIDOID GLYCOSIDES FROM *LAMIUM ALBUM* L.  
AS NATURAL GLP1-R MODULATORS IN REPEATED RESTRAINT STRESS



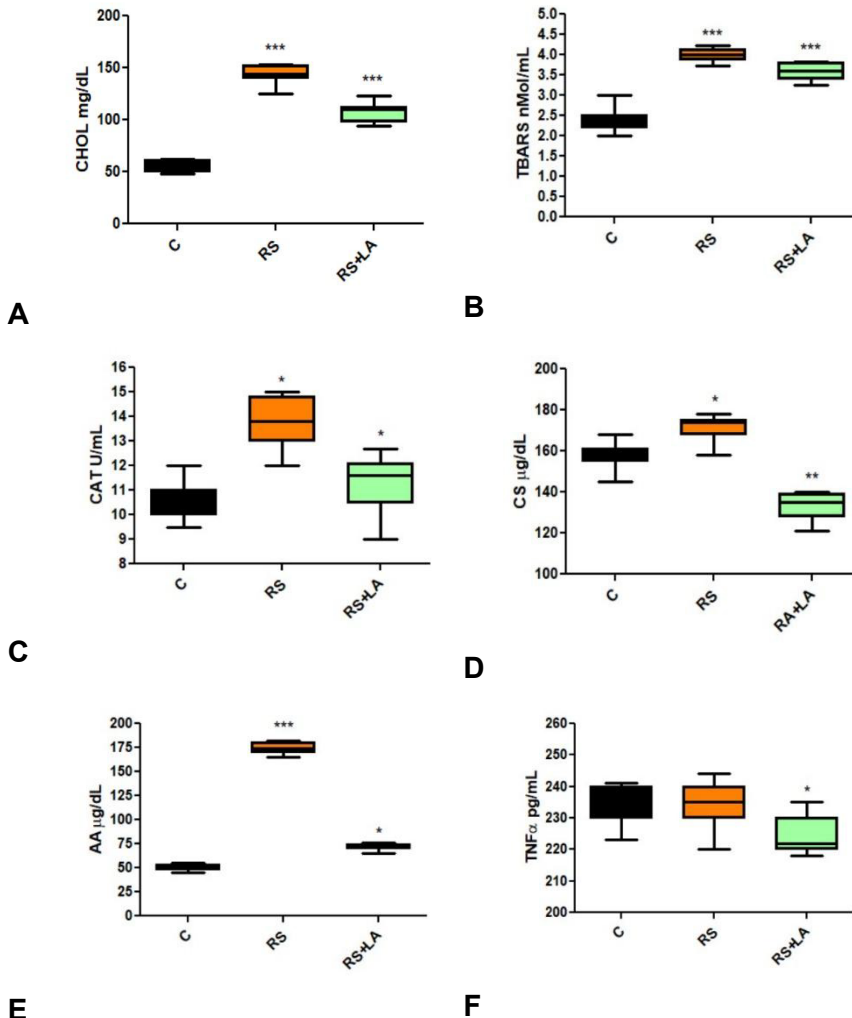
**Figure 2.** Biochemical markers in brain homogenates. An increase in cholesterol (A) was noted to be correlated with reactions in the oxidative microenvironment, based on levels of catalase (B) and TBARS (C). Administration of *L. album* resulted in a decrease or normalization of oxidative stress indicators ( $p < 0.05$ ). Stress-related hormones, corticosterone (D) and adrenaline (E), increased the RS group. At the same time, the extract significantly reduced these hormone levels ( $p < 0.05$ ), similar to the variations in TNF $\alpha$  (F) levels in hippocampal homogenates. The values are expressed as mean in the Q1-Q3 quartile range and the error bars show the non-outlier range.



Repeated restraint stress determined a prominent increase in oxidative stress markers in the hippocampus. In stressed animals, CAT (**Figure 2B**) was  $115.8 \pm 2.3$  U/mL ( $p < 0.01$ ), and TBARS (**Figure 2C**) was  $33.0 \pm 0.6$  nMol/g ( $p < 0.01$ ), suggesting the activation of the HPA axis associated with redox imbalance. Additionally, such an imbalance generates ROS/NOS, commonly related to oxidative stress-associated pathologies (e.g., hypertension, diabetes, mental disorders). Treatment with *L. album* extract significantly counteracted the oxidative stress level compared with stressed animals (CAT,  $81.1 \pm 17.9$  U/mg of protein/min, and  $p < 0.05$ ; TBARS,  $24.9 \pm 0.8$  nMol/g,  $p < 0.05$ ). However, the increased oxidative stress markers are not sufficient to confirm the activation of the HPA axis; therefore, a strong link with hormones (corticosterone, testosterone, adrenaline, renin, etc.) and cytokines (IL-8, IL-9, IL-12, TNF $\alpha$ ) signaling is mandatory. Stressed rats expressed a high level of corticosterone ( $263 \pm 3.64$   $\mu$ g/g, **Figure 2D**) and adrenaline ( $162 \pm 2.41$   $\mu$ g/g, **Figure 2E**) in the hippocampus as well as in the blood, where CS was  $164.5 \pm 3.63$   $\mu$ g/dL (**Figure 3A**) and AA was  $55 \pm 0.96$   $\mu$ g/mL (**Figure 3B**). Consequently, stressed rats that expressed a high hippocampal level of CS (**Figure 2D**) marked a decreased corticosterone concentration after *L. album* administration (RS + LA,  $168 \pm 1.75$   $\mu$ g/dL,  $p < 0.001$ , **Figure 2D**). In addition, blood CS was slightly decreased (**Figure 2A**) in RS + LA ( $112.4 \pm 2.63$   $\mu$ g/dL), which approaches the C value ( $152.3 \pm 3.11$   $\mu$ g/dL,  $p < 0.001$ ).

Alongside, repeated restraint stress determined an increase in TNF $\alpha$  concentration in the hippocampus (**Figure 2F**) ( $12.28$  pg/mg protein,  $p < 0.01$ ) after stress exposure versus the C group ( $6.26$  pg/mg protein), and *L. album* administration significantly decreased hippocampal TNF $\alpha$  concentration ( $4.25$  pg/mg protein,  $p < 0.001$ , **Figure 2F**). In addition, hippocampal adrenaline (**Figure 2E**) follows the same dynamics as corticosterone variations. During stress conditions, AA plays a key role in stress habituation [31], the reason why slight increases were noticed in stressed groups ( $171 \pm 11.2$   $\mu$ g/g,  $p > 0.05$ ). Nevertheless, the hippocampal AA concentration in group C ( $161.6 \pm 1.6$   $\mu$ g/g) closely resembled that of the RS group, underscoring the absence of a connection between long-term exposure to restraint stress and stimulation of the sympathetic nervous system. In this context, the actions of an *L. album*-antioxidant-rich diet on stressed animals seemed to lead to high autonomic nervous system resistance reflected by a low concentration of hippocampal AA ( $121.4 \pm 16.5$ ,  $\mu$ g/g,  $p < 0.05$ ) compared to C and RS groups. Concerning the blood biochemistry, the cholesterol concentrations (**Figure 3C**), and oxidative stress parameters (CAT, TBARS - **Figure 3D** and **Figure 3E** respectively) in the Control and experimental groups suggest that restraint stress generates hypercholesterolemia and blood redox imbalance. Our study points out that the serum level of cholesterol (**Figure 3C**) is significantly increased ( $190.7 \pm 0.7$  mg/dL,  $p < 0.001$ ) in the RS group, which was a specific alteration during acute restraint stress conditions.

NEUROTROPHIC EFFECTS OF IRIDOID GLYCOSIDES FROM *LAMIUM ALBUM* L.  
AS NATURAL GLP1-R MODULATORS IN REPEATED RESTRAINT STRESS



**Figure 3.** Serum biochemical markers variations. An increase in serum concentrations of cholesterol (A) was noted, along with changes in oxidative status indicated by TBARS (B) and catalase (C) levels. Plant extract administration led to a slight decrease in catalase whereas cholesterol and TBARS were unchanged. The stress effects were more pronounced in the blood compared to the hippocampus. Following extract treatment, corticosterone (D) and adrenaline (E) levels decreased significantly ( $p < 0.05$ ), as did TNF $\alpha$  (F) levels ( $p < 0.05$ ). The values are expressed as mean in the Q1-Q3 quartile range and the error bars show the non-outlier range.

On the other hand, *L. album* extract protects the metabolism by an emphatic decrease in cholesterol concentration, as seen in the RS + LA group ( $67.7 \pm 8.6$  mg/dL,  $p < 0.001$ , **Figure 3C**). In the context of restraint stress-induced redox unbalancing, the increased TBARS level is closely related to the high CAT activity during repeated stress conditions, which marks an elevated oxidative status in the blood. Blood oxidative stress in the RS + LA group did not present remarkable changes. Therefore, in the RS + LA group, CAT activity ( $12.8 \pm 1.23$  U/mL) and TBARS concentration ( $3.4 \pm 0.16$  nMol/mL) were decreased compared to the RS group which had CAT:  $15.0 \pm 1.56$  U/mL and TBARS:  $4.0 \pm 0.18$  nMol/mL ( $p < 0.05$  for CAT and  $p > 0.05$  for TBARS) but remained elevated compared with the Control group.

### Molecular Docking of GLP1-Like Iridoids with GLP1 Receptor

The interactions between the 6-O-acetyl shanzhiside methyl ester and 8-O-acetyl shanzhiside methyl ester found in *L. album* and their GLP1 mimetic actions were evaluated through molecular docking tests using the HDOCK server using exendin-4, a GLP1-R agonist with 39 amino acids and an incretin analog (PDB doi: <https://doi.org/10.2210/pdb1JRJ/pdb>) as positive control and GLP-1R Antagonist 1 (7-(4-chlorophenyl)-1,3-dimethyl-5,5-bis(trifluoromethyl)-8H-pyrimido[4,5-d]-pyrimidine-2,4-dione) as negative control molecules (HDOCK server, Huang Laboratory, School of Physics, Huazhong University of Science and Technology, 1037 Luoyu Rd, Wuhan, Hubei 430074, P.R. China).

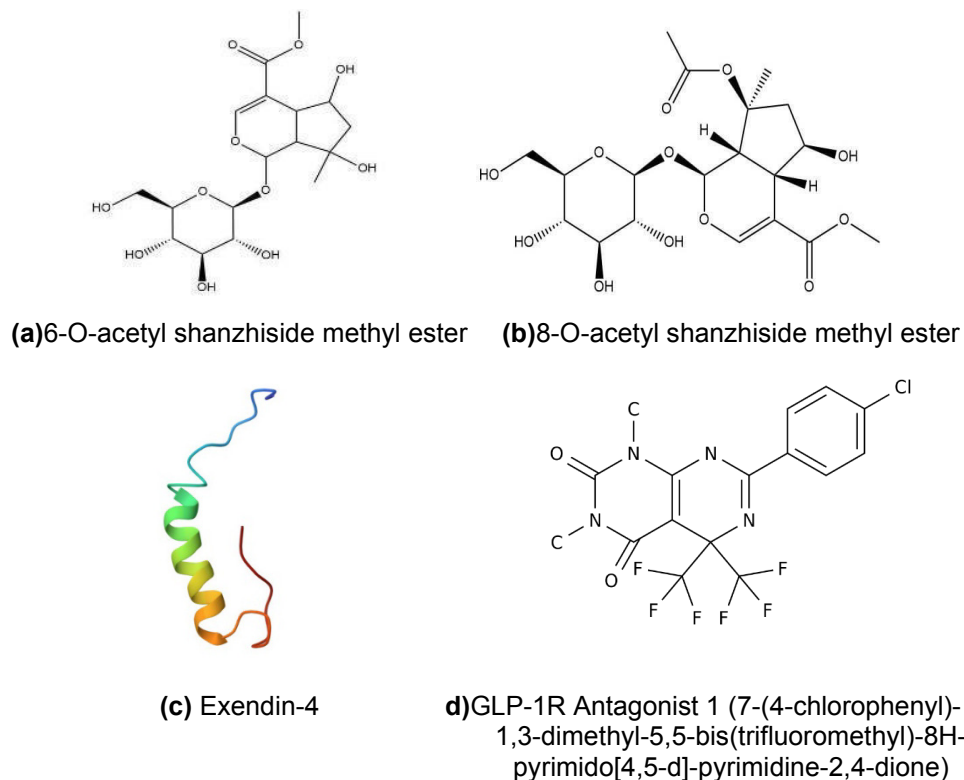
Given that the protein-protein/RNA/DNA complexes in the Protein Data Bank typically have a docking score of around -200 or better, the docking was empirically related to a docking confidence score to indicate the likelihood of binding between two molecules as follows:

$$\text{Confidence score} = 1.0 / [1.0 + e^{0.02x (\text{Docking\_Score} + 150)}]$$

Roughly, when the confidence score was above 0.7, the two molecules would be very likely to bind; when the confidence score was between 0.5 and 0.7, the two molecules would be possibly binding, and a confidence score below 0.5, indicated that the molecules would be unlikely to bind. Nevertheless, the confidence score here should be used carefully due to its empirical nature.

The docking scores, as indicated by the confidence score, show that 8-ASME have a confidence score slightly above 0.7, suggesting that 8-ASME can bind to GLP1-R more probable than 6-ASME with a potentiation effect as was described by GLP1-R-ligands geometry. Exendin-4 and GLP1-R antagonist 1 were in opposite docking values which confirm their agonistic and antagonistic behavior regarding GLP1-R.

NEUROTROPHIC EFFECTS OF IRIDOID GLYCOSIDES FROM *LAMIUM ALBUM* L.  
AS NATURAL GLP1-R MODULATORS IN REPEATED RESTRAINT STRESS

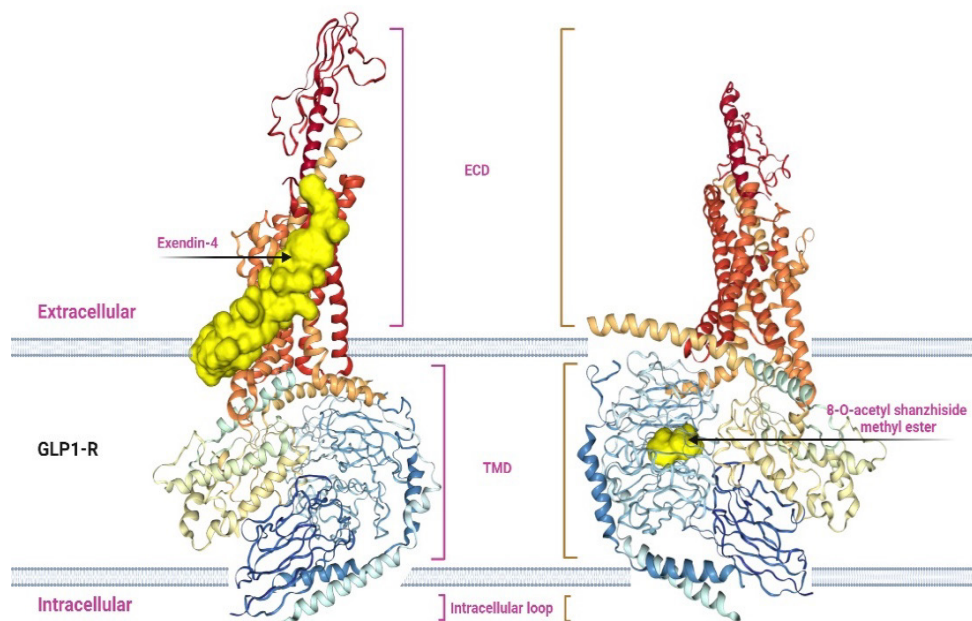


**Figure 4.** Perspective formulas of (a) 6-O-acetyl shanzhiside methyl ester and (b) 8-O-acetyl shanzhiside methyl ester found in *Lamium* species. The structures depicted in (c) Exendin-4 and (d) GLI-1R antagonists represent positive and negative docking controls.

**Table 1.** Docking scores of the two interaction models between GLP1-R and iridoid glycosides 6-ASME (6-O-acetyl shanzhiside methyl ester), 8-ASME (8-O-acetyl shanzhiside methyl ester), GLP1-R agonist exendin-4 and antagonist molecule as GLP1-R antagonist 1.

Molecular interactions		Model 1	Model 2
GLP1-R + Exendin-4	DK Score	-270.18	-260.71
	Conf. Score	0.91	0.90
GLP1-R + 6-ASME	DK Score	-186.89	-176.29
	Conf. Score	0.67	0.62
GLP1-R + 8-ASME	DK Score	-214.78	-212.38
	Conf. Score	0.78	0.77
GLP1-R+GLP-1R Antagonist 1	DK Score	-186.89	-176.29
	Conf. Score	0.67	0.62

The interaction modeling was simulated between ligands: exendin-4 as standard GLP1-R agonist, 6-O-acetyl shanzhiside methyl ester, 8-O-acetyl shanzhiside methyl ester, and the GLP1 receptor (GLP1-R) as was depicted in **Figure 5**.



**Figure 5.** GLP1-R geometry and interaction models with exendin-4 and 8-O-acetyl shanzhiside methyl ester (8-ASME). The tested compound was selected based on the docking and the confidence scores given by HDock simulations. Compared to 6-ASME, 8-ASME was described as the compound with the highest probability of docking with GLP1-R.

**Figure 5** depicts new aspects of 8-ASME, a representative iridoid glycoside from *Lamium*, and its interaction with the receptor's binding pocket compared to exendin-4. The agonist binds to the ECD of the receptor, while 8-ASME binds to the TMD, based on steric constraints and probably its membrane solubility. If the receptor's binding pocket is not occupied by 8-ASME, these findings suggest that the receptor can be stimulated by exendin-4. Based on these interactions, the iridoid glycoside 8-ASME acts as a GLP1-R modulator in the presence of the agonist, and iridoid glycosides can function as potent receptor molecules, not only as agonists. Further studies with multimolecular systems will elucidate these assumptions. However, our experimental data strongly support these processes. An interesting interaction

between GLP1-R and GLP1-R antagonist 1 was noticed after HDOCK simulation. The antagonist also binds to the TMD like 8-ASME, but the docking score was very low, as noted in **Table 1**. The docking scores (DK) were calculated using the knowledge-based iterative scoring functions IT Score PP or IT Score PR. A more negative docking score indicates a more probable binding model. However, the score should not be regarded as the true binding affinity of the two molecules since it has not been calibrated to experimental data (**Table 1**).

Following previous studies [3-5, 7], we also report the complex composition of the *L. album* extract. Phytochemical analysis confirmed the presence of polyphenols, iridoids, and flavonoids, which justify the observed biological effects of this plant's extracts on various diseases. The composition of the extract and the ratio of its bioactive compounds determines its biological particularities. Jiang et al. [10] found that 8-ASME increased the expression of VEGF, Ang 1, and the phosphorylation of Tie2 and Akt in an *in vitro* model. They also noted a decrease in TNF $\alpha$ -induced nuclear factor  $\kappa\beta$  (NF- $\kappa\beta$ ) and I $\kappa$ B- $\alpha$  phosphorylation due to 8-O-acetyl shanzhiside methyl ester, confirming our experimental data. Furthermore, in 2010, the same author [11] demonstrated that 6-ASME protected the brain against injury in a rat model of ischemia and reperfusion.

Phytochemical analysis revealed that iridoids are among the major bioactive compounds in *L. album*. The iridoids are characteristic chemical features of the *Lamiaceae* family compared to other plant families [1, 3, 12]. These bioactive compounds provide a brain-protective effect in the context of experimental brain hypoxia or inflammatory events induced by restraint stress [13]. Moreover, hippocampal cellular changes are a response to hypoxia as well as corticosteroid signaling, which negatively affect neuronal function according to McEwen [33], marked by lower connectivity, axonal edema, IL-1 upregulation, and behavioral changes. Previously published studies indicate a tandem stress reaction of these structures related to corticosterone signaling as well as excitatory mediation [32, 34, 37]. Consistent with our results, increasing concentrations of corticosterone induced by restraint stress are linked to ROS generation [43]. Additionally, Richard-Jane et al. [44] reported that chronic stress, but not acute stress, significantly increased plasma cholesterol concentration. We have noticed that the serum level of cholesterol significantly increased, and this elevation is associated with acute restraint stress. These data demonstrate that both acute and chronic restraint stress induces high cholesterol concentration in the blood and brain. Oxidative stress, as a side effect of restraining, is known to cause inactivation of membrane receptors, impairments of membrane permeability, and disruption of membrane structure [45]. As shown by our results, the increased TBARS levels in the blood and hippocampus are closely related to high CAT activity, reflecting pressure on the antioxidant defense system according to Novozhilov et al. (2013) [46].

In search of a relationship between corticosterone via ROS/NOS, cytokine generation [34], and the neurotrophic actions of *Lamium* iridoids, we found that GLP-1 signaling impairments act as a mediator between the detrimental effects of restraint stress and the neurotrophic actions of 6- and 8-ASME [46]. GLP-1, somatostatin, substance P, neuropeptide Y, and enkephalin are molecules that modulate the HHPA axis in stress response areas such as the hypothalamic nuclei, the pituitary gland, hippocampal formation, and the frontal cortex [45]. GLP-1+ neurons project to multiple brain areas, including regions critical for the regulation of the HHPA axis stress response. Furthermore, GLP-1R is widely distributed throughout the CNS, with GLP-1R mRNA expression observed in the olfactory bulb, the basal portion of the frontal cortex, the nucleus accumbens, the amygdala, and the dorsal portion of the hippocampus [43].

We hypothesize that the administration of *L. album* in animals exposed to restraint stress contributes to hippocampal regeneration due to the effect of shanzhiside-methyl esters, which are recognized as natural agonists for GLP-1R. Our data suggested that shanzhiside-methyl esters serve as agonists according to the literature [12], or based on our new findings, these compounds can be agonist-like or GLP-1R potentiator molecules for glucagon-like peptide 1 (GLP-1) receptors. Other results indicated that shanzhiside-methyl esters inhibit the release of TNF $\alpha$ , NF $\kappa$  $\beta$ , I $\kappa$  $\beta$ , Ang1, and VEGF, and microglial  $\beta$ -endorphin, while also acting as agonistic molecules on GLP-1R [47,48].

Restraint stress disrupts the HPA axis, cholesterol metabolism, adrenaline levels, and oxidative stress parameters. However, administration of *L. album* hydroalcoholic extract normalizes and improves the biochemical steady-state in the blood and hippocampus. The presence of other antioxidants, such as polyphenols and flavonoids, contributes to the pleiotropic effects of the *L. album* extract, marked by decreased lipid peroxidation, reduced catalase activity, and lower cholesterol concentration. Iridoids, acting as GLP-1R agonists or GLP-1R agonist analogs, can regulate the HPA axis endogenously through their stimulatory action on GLP-1 receptors. Previously published research [49] demonstrated that HPA axis activation and variations in corticosterone levels are time-dependent processes. Our data demonstrate that GLP-1R agonists/agonist analogs from *L. album* reduce HPA axis activation and corticosterone concentration after five days of repeated stress exposure.

Some studies have mentioned that GLP-1 agonist (exenatide-4) injection decreased corticosterone concentration after two weeks of exposure. Exenatide-4 at 10  $\mu$ g/kg and liraglutide at 1200  $\mu$ g/kg were effective [50-52]. Our doses of 6-shanzhiside methyl ester were 1807  $\mu$ g/kg and 8-acetyl shanzhiside methyl ester were 2226  $\mu$ g/kg. Daily oral administration of these doses also exerted an inhibitory effect on corticosterone release after five days of repeated exposure to restraint stress, demonstrating a possible plant-based modulated response of GLP-1R in restraint stress.

## CONCLUSIONS

The results of the current study suggest that bioactive compounds from *L. album* have protective and regenerative actions on the hippocampus exposed to repeated restraint stress. This is achieved by modulating the oxidative-inflammatory status and GLP1-R stimulation to regulate the stress response via HPA axis modulation through the GLP1 agonist or more probably, GLP1-R potentiator effects of *L. album* iridoids. These actions could serve as a link between stress effects on the nervous system and digestive function, which are often impaired by various stressors. Given the obtained results, this encourages further studies in this direction, specifically regarding the role of iridoids such as 8-acetylshanzhiside methyl ester in neuroprotection and brain-digestion relationship improvement.

## EXPERIMENTAL SECTION

### Plant material and extract preparation

A hydro-alcoholic extract of *L. album* leaves and flowers was prepared. *L. album* was collected from the Brasov depression area, Romania, in June 2021. The extract was prepared using a 70% v/v ethanol solution. The plants were dried at room temperature (+22°C) and ground into a powder. 2.5 g of *L. album* powder was mixed with 100 mL of 70% v/v ethanol in a water bath at +80°C for 90 minutes, followed by filtration. This resulted in the creation of the stock extract.

### Phytochemical analysis

Phytochemical characterization of the *Lamium album* extract involved determining the levels of iridoid, flavonoid, and phenolic compounds and assessing its antioxidant capacity. The total iridoid content (TIC) was determined using the Trim-Hill reaction. To achieve this, 0.4 mL of the extract was mixed with 4 mL of Trim-Hill reagent (consisting of acetic acid, 0.2% CuSO<sub>4</sub>, and concentrated HCl in a ratio of 10:1:0.5). Subsequently, absorbance was measured at 609 nm, with the presence of iridoids indicated by blue color. The iridoid amount was quantified using a calibration curve with aucubin (ranging from 0.1 to 1 mg/mL). Results were averaged from three replicates [42]. Total flavonoid content (TFC) was estimated using the aluminum chloride reagent. Initially, 1.2 mL of the extract was mixed with 0.6 mL of NaNO<sub>2</sub> (5%), followed by adding 1.2 mL of AlCl<sub>3</sub> (10%) after 5 minutes. Subsequently, 2 mL of NaOH



0.1 M was added, and absorbance was measured at 430 nm after another 10 minutes. A calibration curve with a standard solution of rutin (ranging from 10 to 125  $\mu\text{g/mL}$ ) was used, and results were expressed in  $\mu\text{g}$  of rutin/mL of *Lamium album* extract [53]. The total phenolic content (TPC) was determined using the Folin-Ciocalteu method. Initially, 0.3 mL of the extract was mixed with 1.5 mL of Folin-Ciocalteu reagent, followed by adding 1.2 mL of sodium carbonate 0.7 M after 5 minutes. The mixture was then incubated at room temperature in a dark place for 2 hours, and absorbance was measured at 760 nm. Results were expressed in  $\mu\text{g}$  of gallic acid/mL of *L. album* extract based on a calibration curve obtained using a standard solution of gallic acid (ranging from 10 to 250  $\mu\text{g/mL}$ ) [53].

The antioxidant capacity of the extract was evaluated using the DPPH and ABTS assays [53,54]. Chromatographic analysis was performed on RP-18 F254s HPTLC plates developed with acetonitrile – 0.1% formic acid (in a ratio of 5:5, v/v) as the mobile phase. Aliquots of 10  $\mu\text{l}$  of the plant extract and 5  $\mu\text{l}$  of the standard solutions were applied to the plate as 8 mm bands using a Linomat 5 device (Camag, Muttenz, Switzerland). Polyphenols and flavonoids were visualized under UV light at 366 nm, while iridoids were detected as blue/red-violet spots after derivatization with p-dimethylamine benzaldehyde.

### **Chemicals for biological assays**

Malondialdehyde standard solution and thiobarbituric acid were obtained from Sigma Chemical Company, St. Louis, MO, USA. For the determination of plasma catalase activity, a Catalase Assay Kit from Abcam, Cambridge, UK, was employed. Adrenaline, corticosterone, and TNF $\alpha$  were assayed using ELISA kits provided by Bio Vision Inc., Milpitas, CA 95035, USA. The Folin-Ciocalteu reagent was obtained from Merck Millipore, Darmstadt, Germany. A standard for the adrenaline was obtained from Terapia-Ranbaxy, Cluj-Napoca, Romania. For cholesterol determinations, the reagent was purchased from Bio Maxima, Lublin, Poland. All other chemicals and solvents used in the study were of analytical grade and were obtained from Chemical-Company, Iasi, Romania.

### **Animals and ethics**

The experiment was conducted on adult female Wistar rats (8 weeks old), weighing  $150 \pm 20$  g. The rats were procured and housed in the zoobase of the University of Veterinary Medicine in Cluj-Napoca, Romania, under standard conditions (12/12 light-dark cycle, humidity 30-70%, temperature 20-26°C), and provided with standard food and water *ad libitum*. All experimental procedures

described in this study adhered to the Directive 2010/63/EU and Romanian National Legislation (Law no. 43/2014). The experiments were approved by the Scientific Council and Ethical Committee of Babes-Bolyai University (Ethical Statement no. 2012/03.02.2022).

### **Experimental design**

The animals were randomly divided into three experimental groups, each consisting of 6 animals: (I) negative Control group (C), (II) Restraint Stress group (RS), exposed to 3 hours of restraint per day for 5 consecutive days, and (III) Restraint Stress + *L. album* extract group (RS + LA). The experiment lasted for five days. The extract was administered before immobilization via intragastric gavage, in a dose of 100 mg of dry substance/kg of body weight daily, which was equivalent with approximately 1800 µg/kg 6-shanzhiside methyl ester and 2200 µg/kg of 8-acetyl shanzhiside methyl ester according to literature which described the ratio of the different iridoids in *Lamium*, following OECD guidelines for volume and dosage selection [43, 55-57]. Restraint stress was induced by immobilizing the rats in 20 cm × 7 cm plastic tubes for 3 hours per day for 5 days, with several 3 mm holes at the far end of the tubes to allow for breathing while restricting movement. Control and experimental animals were euthanized under isoflurane anesthesia one day after treatment and stress immobilization (on the 6<sup>th</sup> day). The experiment was designed to assess the regenerative effect of iridoids, specifically 6-shanzhiside methyl ester and 8-acetylshanzhiside methyl ester, derived from the *L. album*.

### **Brain and blood preparations for biochemical assays**

Immediately after euthanasia, the hippocampal formation was extracted and homogenized with a lysis buffer (PBS 100 mM, Triton X 0.5%, and protease inhibitor cocktail from Sigma-Aldrich, USA). The homogenate was then centrifuged at 10000 x g, +4°C, for 15 minutes, and the resulting supernatant was utilized for biochemical assays. Blood was collected in a plain vacutainer for biochemical analyses and allowed to clot for 30 minutes at room temperature. The serum was separated by centrifugation at 1200 x g for 10 minutes and subsequently stored at -80°C. The serum was utilized for determining catalase activity (CAT), thiobarbituric acid reactive substances (TBARS), cholesterol, corticosterone (CS), and adrenaline (AA) concentrations. Corticosterone and adrenaline levels in the blood were measured using ELISA methods (Bio Vision, CA), along with CAT activity (Abbexa, UK). ELISA plates were analyzed with a Biotek Synergy microplate reader (Biotek Instruments Inc., Winooski, VT, USA), following the manufacturer's instructions.

## Molecular docking

The molecular docking was performed using the HDOCK online software. The main steps of the analysis involved preparing the structures, docking, scoring, clustering, ranking, and refinement of the results. Preparation: The structures of GLP1-R involved in the complex were prepared to ensure that the protein is in the correct format and contains all necessary information. Docking: HDOCK employs a hybrid docking algorithm that combines global docking with local refinement. Initially, a large number of initial docked poses are generated using a global docking approach. This involves sampling a wide range of possible orientations and conformations for the proteins in the complex. Scoring: Each generated pose is then scored based on various criteria, including shape complementarity, electrostatics, and desolvation energy between iridoid glycosides and GLP1-R. Clustering: The generated poses are clustered based on their structural similarity. Clustering identifies distinct groups of poses that represent similar binding modes. Ranking: The clustered poses are ranked based on their scores, with the top-ranking poses considered the most likely representations of the protein complex. Refinement: Finally, the top-ranking poses undergo local refinement to improve their accuracy and resolution further. This refinement step typically involves optimizing the side-chain conformations and fine-tuning the intermolecular interactions within the GLP1-R-iridoid glycosides complex.

## Statistical analysis

All data are expressed as mean in Q1-Q3 quartile range and the error bars show the non-outlier range. The Gaussian distribution was assessed using the Shapiro-Wilk normality test. One-way analysis of variance (ANOVA) followed by post hoc Dunnett's range test procedures was conducted. Statistical significance was set at  $p < 0.05$  (95% confidence interval). Statistical analyses were performed using GraphPad Prism version 5.0 for Windows (GraphPad Software, Boston, MA 02110, USA).

**Abbreviations:** AA, adrenaline; Akt, protein kinase B; Ang1, angiopoietin 1; CA, *Cornus ammonis*; CAT, catalase; CS, corticosterone; DG, dentate gyrus; GLP-1, glucagon-like peptide 1; GLP-1R, glucagon-like peptide 1 receptor; HHPA axis, hippocampal-hypothalamic-pituitary-adrenal axis; H&E, hematoxylin-eosin staining; HPLC, high-performance liquid chromatography; I $\kappa$ B- $\alpha$ , nuclear factor of kappa light polypeptide gene enhancer in B-cells inhibitor-alpha; *L. album*, LA; NF- $\kappa$ B, nuclear factor  $\kappa$ B; PBS, phosphate buffer saline; RNS, reactive nitrogen species; ROS, reactive oxygen species; RS, restraint stress; MDA, malondialdehyde; TBARS, thiobarbituric acid reactive substances; Tie2,

tyrosine kinase receptor for angiopoietin 1; TLC, thin layer chromatography; TNF $\alpha$ , tumor necrosis factor  $\alpha$ ; VEGF, vascular endothelial growth factor.

**Ethics Approval:** All experimental procedures outlined in this study were conducted following the European Communities Council Directive 2010/63/EU and Romanian National Legislation (Law no. 43/2014). The experiments received approval from the Scientific Council and Ethical Committee of Babeş-Bolyai University (Ethical Statement no. 2012/03.02.2016).

## ACKNOWLEDGMENTS

I.R., C.A.M., and V.A.T. were sustained by the Ministry of Research, Innovation, and Digitization through the Core Project BioClimpact no. 7/30.12.2022, code 23020401. V.A.T. and C.A.M. were sustained by the Babeş-Bolyai University Research Grant SRG-UBB 32939/22.06.2023.

## REFERENCES

1. F.N. Yalçın; D. Kaya; *FABAD J Pharm Sci.*, **2006**, *31*, 43-52.
2. F.N. Yalçın; D. Kaya; E. Kiliç; M. Özalp; T. Ersöz; İ. Çaliş; *Hacettepe Univ. J. Pharm.*, **2007**, *27*, 11-22.
3. O.R. Pereira; R.I.R. Macias; M.J. Perez; J.J.G. Marin; S.M. Cardoso; *J. Funct. Food.*, **2013**, *5*, 1170-1179.
4. K.V. Wood; C.C. Bonham; D. Miles; A.P. Rothwell; G. Peel; B.C. Wood, D. Rhodes; *Phytochemistry*, **2002**, *59*, 759-765.
5. M. Wójciak-Kosiora; I. Sowa; R. Kocjan; R. Nowak; *Ind. Crop. and Prod.*, **2013**, *44*, 373-377.
6. N. Ito; T. Nihei; R. Kakuda; Y. Yaoita; M. Kikuchi; *Chem. Pharm. Bull.*, **2006**, *54*, 1705-1708.
7. O.R. Pereira; M.R.M. Domingues; A.M.S. Silva; S.M. Cardoso; *Food Res. In.*, **2012**, *48*, 330-335.
8. B. Ghule; S. Palve; L. Rath; P. Yeole; *J. Planar Chromat.*, **2012**, *25*, 426-432.
9. D. Zhang; Y. Gao; S. Jiang; Y. Chen; Y. Zhang; Z. Pan; *R.S.C. Adv.*, **2018**, *8*, 2459-2468.
10. W.L. Jiang; S.P. Zhang; H.B. Zhu; J. Hou; *Basic Clin. Pharmacol. Toxicol.*, **2011**, *108*, 21-27.
11. W. Jiang; S. Zhang; F. Fu; H. Zhu; J. Hou; *J. Neuroinflam.*, **2010**, *7*, 55.
12. H. Fan; T.F. Li; N. Gong; Y.X. Wang; *Neuropharmacology*, **2016**, *101*, 98-109.
13. E. Şahin; S. Gümüşlü; *Behav. Brain Res.*, **2004**, *155*, 241-248.
14. E. Şahin; S. Gümüşlü; *Comp. Biochem. Phys.*, **2007**, *144*, 342-347.

15. V. Toma; A. Farcaș; I. Roman; B. Sevastre; D. Hathazi; F. Scurtu; G. Damian; R. Silaghi-Dumitrescu; *PLoS ONE.*, **2016**, *11.4*, e0153909.
16. J.L. Madrigal; R. Olivenza; M.A. Moro; I. Lizasoain; P. Lorenzo; J. Rodrigo; J.C. Leza; *Neuropsychopharmacol.*, **2001**, *24*, 420-9.
17. T. Buynitsky;DI Mostofsky;*Neurosci Biobehav R.*,**2009**,*33*, 1089-1098.
18. X. Wang; T. Mori; T. Sumii; E.H. Lo; *J. Am. Heart. Assoc.*, **2002**, *33*, 1882-1888.
19. S. Castellani; A. Ungar; G. Cava; C. Cantini; C. Stefanile; A. Camaiti; G. Masotti; *J. Lab. Clin. Med.*, **1997**, *129*, 462-469.
20. A. Marcilhac; M. Faudon; G. Anglade; F. Hery; P. Siaud; *Pharmacol. Biochem. Behav.*, **1999**, *63*, 599-605.
21. I. Roman; V.A. Toma; A.D. Farcaș; *Studia Univ. V.G., S.S.V.*,**2015**, *25*, 207-214.
22. J. Simoni; G. Simoni; A. Hartsell; M. Feola; *A.S.A.I.O. J.*, **1997**, *43*, 714-725.
23. B.S. McEwen; T. Seeman; Ann. N.Y.; *Acad. Sci.*, **1999**, *896*, 30-47.
24. S.M. Jacob; *Crit. Care.*, **2002**, *6*, 306-312.
25. B.S. McEwen; *Neurobiol. Aging*, **2002**, *23*, 921-939.
26. H. Ito; I. Kanno; J. Hatazawa; S. Miura; *Ann. Nuclear Med.*, **2003**, *17*, 381-386.
27. Z.C. Liu; T.M.S. Chang; *Artif. Cell. Blood Substit. Immobil. Biotechnol.*, **2008**, *36*, 513-524.
28. T.L. Mollan; A. Alayash; *Antioxid. Redox Signal*, **2013**, *18*, 2251-2253.
29. V. Stojanovic; N. Vuckovic; N. Barisic; A. Doronjski; *Stress Health*, **2011**, *27.3*, e195-e198.
30. V.A. Toma; A. Farcaș; M. Parvu; R. Silaghi-Dumitrescu; I. Roman; *Brain Res. Bull.*, **2017**, *130*, 10-17.
31. A.K. Nayanatara; Y. Tripathi; H.S. Nagaraja; P.S. Jeganathan; *Res. J. Pharmacol. Biol. Chem. Sci.*, **2012**, *3*, 34-42.
32. N. Grissom; S. Bhatnagar; *Neurobiol. Learn Mem.*, **2009**, *92*, 215-224.
33. B.S. McEwen; *Brain Res.*, **2000**, *886*, 172-189.
34. B.S. McEwen; A.M. Magarinos; *Hum. Psychopharmacol. Clin. Exp.*, **2001**, *16*, 7-19.
35. N. Spruston; C. McBain; P. Andersen, R. Morris, D. Amaral, T. Bliss, J. O'Keefe Eds.; *Oxford University Press*, **2006**, *5*, 133-202.
36. K. Alkadhi; *I.S.R.N.*, **2013**, I.D.806104, 1-23.
37. R. Sapolsky; *Prog. Brain Res.*, **1990**, *86*, 13-23.
38. J. Drljača; A.T. Vejnović; D.M. Miljković; M.J. Popović; D.B. Rakić; S.R. Sekulić; I.D. Čapo; B.B. Petković; *Arch. Biol. Sci.*, **2020**, *72*, 5-11.
39. Y. Watanabe; E. Gould; *Hippocampus*, **1992**, *2*, 431-436.
40. F. Ohl; T. Michaelis; G.K. Vollmann-Honsdorf; C. Kirschbaum; E. Fuchs; *Psychoneuroendocrinology*, **2000**, *25*, 357-363.
41. H.C. Abercrombie; N.H. Kalin; M.E. Thurow; M.A. Rosenkranz; R.J. Davidson; *Behav. Neurosci.*, **2003**, *17*, 505-516.
42. M.K. Holt; S. Trapp; *Cogent. Biol.*, **2016**, *2*, ID: 1229086, 1-9.
43. H. Sato; T. Takahashi; K. Sumitani; H. Takatsu; S. Urano; *J. Clin. Biochem. Nutrl.*, **2010**, *47*, 224-232.
44. D. Richard-Jane; V. Rodriguez-Sureda; A. Benavides; J. Peinado-Onsurbe; M.D. Lopez-Tejero; M. Llobera; *Metabolism*, **2002**, *51*, 925-931.
45. S. Ghosal; B. Myers; J.P. Herman; *Physiology & Behavior*, **2013**, *122*, 201-207.

NEUROTROPHIC EFFECTS OF IRIDOID GLYCOSIDES FROM *LAMIUM ALBUM* L.  
AS NATURAL GLP1-R MODULATORS IN REPEATED RESTRAINT STRESS

46. A.V. Novozhilov; T.V. Tavrovskaya; V.A. Ivanov; V.I. Morozov; *Bull. Exp. Biol. Med.*, **2013**, 155, 447-450.
47. R.R.K. Kearns; R.I. Spencer; *Physiology & Behavior*, **2013**, 122, 193-200.
48. S.C. Cork; J.E. Richards; M.K. Holt; F.M. Gribble; F. Reinan; S. Trapp; *Molec. Metab.*, **2015**, 4, 718-731.
49. H.D. Schmidt; E.G. Miettlicki-Baase; K.Y. Ige; J.J. Maurer; D.J. Reiner; D.J. Zimmer; D.S. Van Nest; L.A. Guercio; M.E. Wimmer; D.R. Olivos; B.C. De Jonghe; M.R. Hayes; *Neuropsychopharmacology*, **2016**, 41, 1917-1928.
50. J.L. Lachey; D.A. D'Alessio; L. Rinaman; J.K. Elmquist; D.J. Drucker; R.J. Seeley; *Endocrinology*, **2005**, 146, 458-462.
51. V. Volke; K. Rünkorg; M. Krass; *Endocrine Abstracts*, **2012**, 29, P705.
52. Y. Jia; N. Gong; T.F. Li; B. Zhu; Y.X. Wang; *Pharmacol. Res.*, **2015**, 102, 276-285.
53. A. Hosu; V. Avram-Floare; D.A. Magdas; I. Feher; M. Inceu; C. Cimpoiu; *J. Anal. Methods Chem.*, **2016**, ID 4172187, 1-10.
54. R. Re; N. Pellegrini; A. Proteggente; A. Pannala; M. Yang; C. Rice-Evans; *Free Radic. Biol. Med.*, **1999**, 26, 1231-1237.
55. E. K. Akkol; F. N., Yalçın; D. Kaya; İ. Çalış; E. Yesilada; T. Ersöz; *J. Ethnopharmacol.*, **2008**, 118(1), 166-172.
56. C. Bubueanu; R. Iuksel; M. Panteli; *Acta Pharm.*, **2019**, 69(3), 443-449.
57. K. Alipieva; T. Kokubun; R. Taskova; L. Evstatieva; N. Handjieva; *Biochem. Syst. Ecol.*, **2007**, 35(1), 17-22.



## CORRELATIONS BETWEEN OXIDATIVE STRESS MARKERS AND CORONARY ANATOMY IN PERCUTANEOUSLY TREATED PATIENTS WITH ACUTE ST-ELEVATION MYOCARDIAL INFARCTION

Dan-Alexandru TĂTARU<sup>a,b</sup> , Maria OLINIC<sup>a,b\*</sup> ,  
Călin HOMORODEAN<sup>a,b</sup> , Mihai-Claudiu OBER<sup>b</sup> ,  
Florin-Leontin LAZĂR<sup>a</sup> , Andrada URDĂ-CÎMPEAN<sup>a</sup> ,  
Dan-Mircea OLINIC<sup>a,b</sup> 

**ABSTRACT.** Understanding biochemical mechanisms involved in acute myocardial infarction is crucial for future treatments. The current study analyzed the oxidative stress markers in patients with percutaneously treated acute ST-elevation myocardial infarction and correlated the findings to coronary anatomy and Syntax II score (SS-II). Blood samples were obtained before coronary re-perfusion, after one and 24 hours. The following markers of oxidative stress were determined: malondialdehyde (MDA), reduced glutathione to oxidized glutathione ratio (GSH/GSSG) and total antioxidant capacity (TAC). Thirty-seven consecutive patients were included. The patients were divided into groups according to the infarct-related artery: left anterior descending artery (LAD-group) vs non-LAD group, and according to the calculated SS-II, SS-II ≤ 34 vs. SS-II > 34. MDA concentration and GSH/GSSG ratio showed non-significant differences between LAD vs non-LAD groups at all time frames. Patients with LAD as the infarct-related artery had a significantly lower TAC 24 hours after re-perfusion: 30.22 ± 9.78 % inhibition in the LAD group vs. 35.7 ± 5.78 % inhibition in the non-LAD group, p=0.013. The oxidative stress markers were similar between patients regardless of the SS-II value, and neither the culprit vessel nor the SS-II significantly influenced the dynamics of oxidative stress markers.

**Keywords:** oxidative stress, myocardial infarction, Syntax Score.

<sup>a</sup> "Iuliu Hațieganu" University of Medicine and Pharmacy, Faculty of General Medicine, 8 Victor Babeș street, RO-400012, Cluj-Napoca, Romania.

<sup>b</sup> Cluj County Emergency Hospital, Interventional Cardiology Department, 3-5 Clinicilor street, RO-400006, Cluj-Napoca, Romania.

\* Corresponding author: maria\_olnic@yahoo.com





## INTRODUCTION

Cardiovascular diseases are the leading cause of death and illness worldwide [1]. Acute ST-elevation myocardial infarction (STEMI) occurs when a coronary artery is completely occluded, leading to myocardial necrosis. According to current evidence-based guidelines, primary percutaneous coronary intervention (pPCI) is the most effective method of opening the infarct-related artery [2]. However, sudden restoration of blood supply to an ischemic tissue creates the premises for reactive oxygen species (ROS) formation, which increases oxidative stress, leading to myocardial reperfusion injury (MRI) and microvascular obstruction (MVO) [3].

The mechanism involved in MRI has yet to be fully understood. Oxidative stress, lipid peroxidation, inflammation, MVO, and excessive catecholamine release are all responsible for the increase in infarct size [3].

Reactive oxygen species break down polyunsaturated lipids, producing malondialdehyde (MDA). This stable lipid peroxidation end-product is frequently used as a marker of oxidative stress [4].

Reduced glutathione (GSH) is an essential antioxidant and an electron donor, preventing damage to cellular components caused by ROS. Oxidized glutathione, also known as glutathione disulphide (GSSG), is a compound that gives information about the usage of GSH during oxidative stress reactions. In a resting cell, the molar GSH/GSSG ratio exceeds 100:1, while in various models of oxidative stress, this ratio could decrease to 10:1 and even 1:1 [5].

Total antioxidant capacity (TAC) is a measurement used to assess the antioxidant status of biological samples. It can evaluate the antioxidant response against the free radicals produced in a given disease [6].

The pathophysiology of acute myocardial infarction is very complex. Independent of the vessel involved, numerous biochemical pathways can severely influence post-infarction prognosis, leading to MRI and MVO. Evidence suggests that infarct size is not sufficient to explain differences in major adverse cardiac events (MACE) and mortality [7].

As the burden of coronary artery disease remains high after an acute coronary event, risk stratification is essential for effective treatment and reduction of mortality [8,9]. Myocardial infarction associated with the occlusion of the left anterior descending artery (LAD) is associated with an increased risk for MACE [10].

Thus, for adequate short- and long-term risk stratification in post-STEMI patients, the Syntax-II Score (SS-II) was validated, independent of other factors influencing post-infarction mortality [11]. The SS-II integrates, in addition to anatomic coronary characteristics, relevant clinical variables such as age, gender, left ventricular ejection fraction (LVEF), renal impairment, chronic obstructive pulmonary disease (COPD) and peripheral artery disease (PAD).

According to current evidence, the SS-II is a faithful predictor of MACE and mortality in STEMI patients treated by pPCI. A SS-II>34 cut-off is associated with the highest rate of MACE and the highest short-term cardiovascular mortality [12].

This work aimed to identify correlations between the infarct-related artery, the SS-II, and oxidative stress markers in patients with STEMI treated by pPCI.

## RESULTS AND DISCUSSION

In the present study, 37 consecutive patients were included for statistical analysis.

The culprit vessels were the LAD in 18 patients (LAD group), the circumflex artery (Cx) in 10 patients and the right coronary artery (RCA) in 9 patients (Cx and RCA (19 patients) - non-LAD group). The clinical characteristics of the groups are presented in Table 1. Hospital stay was significantly longer in the LAD group ( $p=0.003$ ).

**Table 1.** Clinical characteristics of the LAD and non-LAD groups; LAD - left anterior descending artery; SD - standard deviation; LVEF - left ventricular ejection fraction.

Group name	LAD group	non-LAD group
Age (years), mean $\pm$ SD	64.7 $\pm$ 11.1	62.2 $\pm$ 12.4
Male patients (%)	55	73
Total ischemia time (hours), mean $\pm$ SD	6.22 $\pm$ 3.29	6.47 $\pm$ 4.01
LVEF (%), mean $\pm$ SD	44.44 $\pm$ 7.25	46.66 $\pm$ 6.85
Hospital stay (days), mean $\pm$ SD	6.44 $\pm$ 4.23	3.47 $\pm$ 1.21

In the LAD group, the mean MDA was  $2.9 \pm 0.86$  nmol/ml at P0 vs.  $2.67 \pm 0.85$  nmol/ml, at P1 ( $p=0.098$ ) vs.  $2.18 \pm 0.94$  nmol/ml at P24 ( $p=0.002$ ). At P0, the median value of the GSH/GSSG ratio was 3.30 (2.02-4.77) vs. 2.18 (1.3-2.98) at P1 ( $p=0.02$ ) vs. 1.98 (1.49-2.75) at P24 ( $p=0.004$ ). TAC had no significant variations from baseline,  $p=0.334$ .

In the non-LAD group, the mean MDA was  $3.28 \pm 1.04$  nmol/ml at P0 vs.  $2.68 \pm 0.78$  nmol/ml at P1 ( $p<0.001$ ) vs.  $2.12 \pm 0.96$  nmol/ml at P24 ( $p<0.001$ ). The GSH/GSSG ratio was 2.94 (2.18-5.35) at P0 vs. 2.34 (1.88-2.98) at P1,  $p=0.002$  vs. 1.79 (1.25-3.12) at P24,  $p=0.001$ . TAC had no significant variations,  $p=0.437$ .

Table 2 depicts the values of the oxidative stress parameters according to the culprit vessel.

**Table 2.** Oxidative stress markers at P0, P1 and P24 between the LAD and non-LAD groups (Mann-Whitney U test); P0 - baseline before reperfusion; P1 - one hour after reperfusion; P24 - 24 hours after reperfusion; LAD - left anterior descending artery; MDA - malondialdehyde; GSH - reduced glutathione; GSSG - oxidized glutathione; TAC - total antioxidant capacity; Normally distributed data is presented as mean  $\pm$  standard deviation; Data without normal distribution is presented as median (interquartile range).

Group name	LAD	non-LAD	
			<b>p-value</b>
<b>P0</b>			
MDA (nmol/ml)	2.9 $\pm$ 0.86	3.28 $\pm$ 1.04	0.214
GSH ( $\mu$ mol/ml)	4.9 (3.04-6.67)	4.91 (3.53-6.3)	0.967
GSSG ( $\mu$ mol/ml)	1.82 (1.03-2.33)	1.58 (1.22-2.49)	0.928
GSH / GSSG	3.30 (2.02-4.77)	2.94 (2.18-5.35)	0.919
TAC (inhibition %)	31.64 $\pm$ 5.22	33.69 $\pm$ 4.39	0.157
<b>P1</b>			
MDA (nmol/ml)	2.67 $\pm$ 0,85	2.68 $\pm$ 0.78	0.976
GSH ( $\mu$ mol/ml)	4.25 (2.58-7.51)	3.96 (2.99-6.55)	0.714
GSSG ( $\mu$ mol/ml)	1.97 (1.69-2.34)	2 (1.5-2.74)	0.932
GSH / GSSG	2.18 (1.3-2.98)	2.34 (1.88-2.98)	0.529
TAC (inhibition %)	29.97 $\pm$ 7.11	34.07 $\pm$ 5.10	<b>0.019</b>
<b>P24</b>			
MDA (nmol/ml)	2.18 $\pm$ 0.94	2.12 $\pm$ 0.96	0.854
GSH ( $\mu$ mol/ml)	3.81 (2.98-5.62)	4.91 (4.04-6.41)	0.102
GSSG ( $\mu$ mol/ml)	2.15 (1.64-2.51)	2.7 (1.72-4.24)	0.136
GSH / GSSG	1.98 (1.49-2.75)	1.79 (1.25-3.12)	0.601
TAC (inhibition %)	30.22 $\pm$ 9.78	35.7 $\pm$ 5.78	<b>0.013</b>

Only TAC had different dynamics between the two groups: P0, 31.64  $\pm$  5.22 % of inhibition in the LAD group vs. 33.69  $\pm$  4.39 % of inhibition in the non-LAD group, p=0.154; P1, 29.97  $\pm$  7.11 % inhibition in the LAD group vs.

34.07 ± 5.10 % of inhibition in the non-LAD group, p=0.019; P24, 30.22 ± 9.78 % inhibition in the LAD group vs. 35.7 ± 5.78 % inhibition in the non-LAD group, p=0.013.

For all 37 patients, the median value of SS-II was 28.1 (20.65-41.1). The clinical characteristics of the SS-II≤34 and SS-II>34 are presented in Table 3. In the SS-II>34 group LVEF was notably lower (p=0.058) and hospital stay was significantly longer (p=0.005), compared to the SS-II≤34 group.

**Table 3.** Clinical characteristics of the SS-II≤34 and SS-II>34 groups; SD - standard deviation; LAD - left anterior descending artery; LVEF - left ventricular ejection fraction.

Syntax-II Score	≤34	>34
Number of patients	23	14
Age (years), mean ± SD	58.3 ± 8.5	72.1 ± 9.8
Male patients (%)	87	28.5
LAD infarct-related artery (%)	34.8	71.5
Total ischemia time (hours), mean ± SD	6.26 ± 3.67	6.51 ± 3.71
LVEF (%), mean ± SD	47.8 ± 3.3	41.7 ± 8.4
Hospital stay (days), mean ± SD	3.56 ± 1.23	7.14 ± 4.53

Table 4 shows the values of the oxidative stress markers between the two SS-II groups. The SS-II did not influence the dynamics of the markers determined in this study.

In the SS-II≤34 group, MDA had significant variations: P0, 3.21 ± 1.08 nmol/ml; P1, 2.77 ± 0.79 nmol/ml, p=0.001; P24), 2.27 ± 0.96 nmol/ml, p<0.001. Also, the GSH/GSSG ratio had significant changes: P0, 3.1 (2.18–5.02; P1, 2.02 (1.54-2.62), p<0.001; P24; 1.98 (1.49-2.75), p<0.001. TAC had no significant variations in this group of patients.

In the SS-II>34 group, MDA decreased significantly after re-perfusion: P0, 2.91 ± 0.72 nmol/ml; P1, 2.52 ± 0.83 nmol/ml, p=0.032; P24, 1.93 ± 0.91 nmol/ml, p=0.004. Moreover, GSH/GSSG ratio decreased significantly: P0, 3.69 (2.02-6.00); P1, 2.48 (1.35-4.10), p=0.074; P24, 2.3 (1.43-3.25), p=0.011. TAC had no significant changes.

The present study aimed to establish a connection between oxidative stress markers and coronary anatomy in STEMI patients. Both short-term and long-term prognoses are more severe for patients with STEMI and multi-vessel coronary artery disease compared to patients with single-vessel disease

[13]. Also, significant evidence suggests that RCA occlusion is linked to better post-infarction survival, whereas LAD occlusion is associated with the highest mortality after STEMI [14]. This study showed that the LAD was the main vessel responsible for infarction (almost three-quarters of patients) in patients with high SS-II. Other authors have reported similar results [14].

**Table 4.** Oxidative stress markers at P0, P1 and P24 between the SS-II $\leq$ 34 and SS-II $>$ 34 groups (Mann-Whitney U test); P0 - baseline before reperfusion; P1 - one hour after reperfusion; P24 - 24 hours after reperfusion; LAD - left anterior descending artery; MDA - malondialdehyde; GSH - reduced glutathione; GSSG - oxidized glutathione; TAC - total antioxidant capacity; Normally distributed data is presented as mean  $\pm$  standard deviation; Data without normal distribution is presented as median (interquartile range).

Syntax-II Score	$\leq 34$	$> 34$	
			<b>p-value</b>
<b>P0</b>			
MDA (nmol/ml)	3.21 $\pm$ 1.08	2.91 $\pm$ 0.72	0.352
GSH ( $\mu$ mol/ml)	4.95 (3.47-7.6)	4.58 (3.64-6.67)	0.715
GSSG ( $\mu$ mol/ml)	1.94 (1.22-2.58)	1.55 (0.8-2.09)	0.164
GSH / GSSG	3.1 (2.18-5.02)	3.69 (2.02-6.00)	0.528
TAC (inhibition %)	31.66 $\pm$ 4.64	34.39 $\pm$ 4.88	0.119
<b>P1</b>			
MDA (nmol/ml)	2.77 $\pm$ 0.79	2.52 $\pm$ 0.83	0.312
GSH ( $\mu$ mol/ml)	4.95 (2.77-7.3)	3.98 (2.68-7.72)	0.937
GSSG ( $\mu$ mol/ml)	2 (1.5-3.09)	1.97 (1.5-2.32)	0.484
GSH / GSSG	2.02 (1.54-2.62)	2.48 (1.35-4.10)	0.411
TAC (inhibition %)	31.94 $\pm$ 5.32	32.30 $\pm$ 8.13	0.824
<b>P24</b>			
MDA (nmol/ml)	2.27 $\pm$ 0.96	1.93 $\pm$ 0.90	0.283
GSH ( $\mu$ mol/ml)	4.91 (3.73-5.5)	3.89 (3.05-7.1)	0.503
GSSG ( $\mu$ mol/ml)	2.66 (1.74-3.34)	2.15 (1.5-2.45)	0.274
GSH / GSSG	1.98 (1.49-2.75)	1.79 (1.25-3.12)	0.368
TAC (inhibition %)	32.97 $\pm$ 6.85	33.14 $\pm$ 10.63	0.821

Regardless of the time frame, MDA, GSH, GSSG, and the GSH/GSSG ratio exhibited similar values in the LAD and non-LAD groups. TAC had comparable values at baseline but was significantly lower in the LAD group after reperfusion. This fact suggests increased oxidative stress and a depletion of the antioxidative mechanism in the LAD group. The larger myocardial mass involved in LAD-related myocardial infarction can lead to the formation of numerous reactive oxygen species on the first day after reperfusion [15,16]. In addition to acute heart failure, mortality is related to life-incompatible malignant arrhythmias. Evidence shows that LAD involvement predisposes to ventricular arrhythmias [17], and increased oxidative stress can induce these devastating phenomena [18]. A low TAC value indicates a large amount of reactive oxygen species and could explain the molecular mechanisms that more frequently induce life-threatening arrhythmias in LAD-related myocardial infarction. These observations may explain the higher mortality present in patients suffering from an anterior STEMI.

Evidence shows that vascular territories not involved in infarction also suffer from acute ischemia through mechanisms such as MVO or arteriolar spasm [19]. However, no significant differences were noticed between the oxidative stress markers in patients from the SS-II $\leq$ 34 vs. SS-II $>$ 34 groups. It seems that co-morbidities such as COPD, PAD and renal impairment do not have a direct impact on short-term oxidative stress dynamics.

Several published works have shown a significant decrease in MDA after pPCI in the clinical context of STEMI treated by pPCI [15,16,20]. In this study, MDA decreased significantly in all patient subgroups, and this change was not influenced by the infarct-related artery or by the severity of the coronary disease indicated by the SS-II. Moreover, in the present paper, the GSH/GSSG ratio decreased significantly in all patient groups. Other studies with similar protocols have also reported similar results [15,21].

TAC did not vary significantly in the first 24 hours, regardless of the culprit vessel or SS-II. Literature data suggest TAC has specific dynamics after coronary re-perfusion [15]. Although simple to perform, the 2,2-diphenyl-1-picrylhydrazyl (DPPH) method has the drawback of non-linear response to plasma volume. This facet points to the need for careful comparisons of results obtained under non-identical conditions. However, it does not invalidate the possibility of monitoring the trend in changes of TAC within one protocol [22].

The results of this study suggest that the production of free radicals, in the context of STEMI, depends not only on the myocardium involved but also on the body's ability to counter and control the production of reactive oxygen species.

This study's major limitations include the small number of patients and the early loss of follow-up, which prevented data on MACE from being obtained.

## CONCLUSIONS

This study found that patients with LAD-related STEMI had a significantly lower TAC 24 hours after reperfusion than patients with STEMI due to another artery occlusion.

The specific culprit vessel did not influence plasma levels of MDA or the GSH/GSSG ratio. Additionally, the study determined that the oxidative stress markers were similar between patients, regardless of the calculated SS-II.

Neither the culprit vessel nor the SS-II significantly influenced the dynamics of oxidative stress markers.

## EXPERIMENTAL SECTION

The research was conducted following the Declaration of Helsinki [23]. Written consent was obtained from each patient before the procedure. Consecutive STEMI patients treated by pPCI were included in the study. The inclusion criteria were as follows: electrocardiographic evidence of ST elevation of  $\geq 1$  mV in two or more standard limb leads or  $\geq 2$  mV in two or more precordial leads; typical chest pain lasting more than 20 minutes; presentation within 12 hours since symptom onset; successful pPCI of the culprit vessel.

Two physicians with experience in interventional cardiology analyzed the angiographic images for each patient and independently calculated the SS-II using the algorithm available online at <https://syntaxscore.org> [11]. The patients were divided into groups as follows: patients with the LAD as the infarct-related artery (LAD group) vs. patients with the Cx or the RCA as the culprit (non-LAD group); patients with low SS-II $\leq 34$  vs. high SS-II $>34$ .

Peripheral venous blood samples were obtained from each patient immediately before pPCI (P0), one hour after reperfusion (P1), and after 24 hours (P24). Blood samples were collected into plastic tubes with ethylenediaminetetraacetic acid (EDTA) and centrifuged at 1500 rpm for 15 minutes. The resulting plasma was stored at  $-30^{\circ}\text{C}$  until analysis. The following oxidative stress markers were determined at each harvest: MDA, GSH, GSSG, GSH/GSSG ratio and TAC. The dynamics of these markers were compared according to the previously mentioned patient groups.

MDA was measured using the method outlined by Conti et al. [24]. Initially, 50  $\mu$ l of plasma was boiled with 1 mL of 10 mmol/L 1,3-diethylthiobarbituric acid (DETBA) reagent in phosphate buffer (0.1 mol/L, pH =3). After a 60-minute incubation, the resulting DETBA-MDA product was extracted using 5 ml of n-butanol. The solution was centrifuged at 1500 rpm for 15 minutes. The fluorescence of the supernatant was then assessed at an emission wavelength of 534 nm using a spectrofluorometer (Lambda 35, Perkin Elmer, USA) with a synchronous fluorescence technique at a 14 nm difference between the excitation and emission wavelengths ( $\Delta\lambda$ ). MDA concentration was determined using a standard solution incorporating different MDA concentrations (62.5 to 250 pmol of MDA per 50  $\mu$ l), employing the same measurement technique. The MDA levels were reported in nmol/ml.

GSH was determined after a method proposed by Hu [25]. First, 500  $\mu$ l of plasma was mixed with 500  $\mu$ l of cold 10% trichloroacetic acid (TCA). After 10 minutes in ice, the mixture was centrifuged at 3000 rpm for 15 minutes. After that, 200  $\mu$ l of the supernatant was mixed with 1.7 ml of sodium phosphate 0.1 M / EDTA 5 mM buffer, pH=8 and 0.1 ml of o-phthalaldehyde (1 mg/ml in absolute methanol). Using a spectrofluorometer (Lambda 35, Perkin Elmer, USA), the fluorescence at 350 nm excitation and 420 nm emission was read against a blank that contained deionized water to replace plasma.

GSSG was estimated using Vats' method [26]. Initially, 250  $\mu$ l of the plasma sample was incubated with 0.1 ml of 40 nM N-ethylmaleimide for 30 minutes, followed by an addition of 0.65 ml of 0.1 M NaOH. After that, the same procedure was followed for fluorescence development as in GSH measurement, except 0.1 M NaOH was put instead of the buffer. The GSH and GSSG values were calculated from standard curves and were expressed in  $\mu$ mol/ml.

TAC was determined according to Janaszewska et al. [22]. The reduction assay was performed by adding 20  $\mu$ l of plasma to 400  $\mu$ l of 0.1 mM methanol solution of DPPH and a phosphate buffer, pH=7.4. After a 30-minute incubation at ambient temperature, the absorbance of the samples at 520 nm was measured with a spectrofluorometer (Lambda 35, Perkin Elmer, USA) and compared with that of a control sample containing only DPPH and a phosphate buffer. TAC was measured in inhibition per cent (%) as  $[(\text{control extinction} - \text{serum extinction}) / \text{control extinction}] \times 100$ .

All the reagents supplied by Sigma (Deisenhofen, Germany) were of analytical grade and were used without further purification. All the water used was doubly distilled.

The statistical analysis was conducted using SPSS software v25 (IBM, USA). The Shapiro-Wilk test was used to assess for normal distribution [27]. Quantitative data without normal distribution was described using box plots,



median and Q1-Q3, where Q1-Q3 (interquartile range) stands for the range between the 25th percentile (Q1) and the 75th percentile (Q3). Normally distributed data was presented as mean  $\pm$  standard deviation.

The non-parametric Mann-Whitney U test was used to compare samples from unpaired samples [28], and the Wilcoxon Signed Ranks test was used to analyze oxidative stress parameters within the same group [29]. For normally distributed samples, the paired samples t-test was used [28]. The threshold of statistical significance was set at  $p \leq 0.05$ .

## REFERENCES

1. D.A. Tătaru, M. Olinic, C. Homorodean, M.C. Ober, M. Spînu, F.L. Lazăr, L. Onea, D.M. Olinic, *J Clin Med*, **2024**, 13, 517.
2. B. Ibanez and the ESC Taskforce, *Eur Heart J*, **2017**, 00, 1.
3. D. Yellon, D. Hausenloy, *N Engl J Med*, **2007**, 357, 1121.
4. Y. Chai, S. Ashraf, K. Rokutan, R. Johnston, J. Thomas, *Arch Biochem Biophys*, **1994**, 310, 273.
5. B. Owen, D.A. Butterfield, *Methods Mol Biol*, **2010**, 648, 269.
6. S.B. Kedare, R.P. Singh, *J Food Sci Technol*, **2011**, 48, 412.
7. G. Fuernau, K. Fengler, S. Desch, I. Eitel, F.J. Neumann, H.G. Olbrich, A. de Waha, S. de Waha, G. Richardt, M. Hennersdorf, K. Empen, H. Hambrecht, C. Jung, M. Böhm, J. Pöss, R.H. Strasser, S. Schneider, T. Ouarrak, G. Schuler, K. Werdan, U. Zeymer, H. Thiele, *Clin Res Cardiol*, **2016**, 105, 1030.
8. S.C. Smith, A. Collins, R. Ferrari, D.R. Holmes, S. Logstrup, D.V. McGhie, J. Ralston, R.L. Sacco, H. Stam, K. Taubert, D.A. Wood, W.A. Zoghbi, *Circulation*, **2012**, 126, 2769.
9. M. Olinic, F.L. Lazar, H.L. Onea, C. Homorodean, M. Ober, D. Tataru, M. Spinu, A. Achim, D.M. Olinic. *Life (Basel)*, **2024**, 14, 333.
10. P. Trzeciak, M. Gierlotka, M. Gąsior, A. Lekston, K. Wilczek, G. Słonka, Z. Kalarus, M. Zembala, B. Hudzik, L. Poloński L, *In J Cardiol*, **2017**, 193.
11. A.B. Cid Alvarez, F. Gomez-Peña, A. Redondo-Dieguez, A. Avila, D. López, X. Sanmartin, J.R. González-Juanatey, R. Trillo-Nouche, *EuroIntervention*, **2019**, 15, e796.
12. S.A. Hirji, S.R. Stevens, L.K. Shaw, E.C. Campbell, C.B. Granger, M.R. Patel, M.H. Sketch, T.Y. Wang, E.M. Ohman, E.D. Peterson, J.M. Brennan, *Am Heart J*, **2017**, 116.
13. S.J. Backhaus, J.T. Kowallick, T. Stiermaier, T. Lange, A. Koschalka, J.L. Navarra, J. Lotz, S. Kutty, B. Bigalke, M. Gutberlet, H.J. Feistritz, G. Hasenfuß, H. Thiele, A. Schuster, I. Eitel, *Clin Res Cardiol*, **2020**, 109, 339.
14. Y. Song, Z. Gao, X. Tang, Y. Ma, P. Jiang, J. Xu, Y. Yao, X. Zhao, S. Qiao, Y. Yang, R. Gao, B. Xu, J. Yuan. *Catheter Cardiovasc Interv*, **2018**, 92, 40.
15. E. Sedláková, O. Rácz, E. Lovásová, R. Beňačka, M. Kurpas, A. Chmelárová, J. Sedlák, M. Studenčan, *Cent Eur J Med*, **2009**, 4, 26.

CORRELATIONS BETWEEN OXIDATIVE STRESS MARKERS AND CORONARY ANATOMY IN PERCUTANEOUSLY TREATED PATIENTS WITH ACUTE ST-ELEVATION MYOCARDIAL INFARCTION

- 16.D. Tataru, D. Olinic, A. Urda, M. Olinic, R. Orasan, *Studia UBB Chemia*, **2018**, 3, 117.
- 17.L.C. Godoy, P.R. Lawler, M.E. Farkouh, B. Hersen, J.C. Nicolau, V. Rao, *Can J Cardiol*, **2019**, 35, 993.
- 18.M. Neri, I. Riezzo, N. Pascale, C. Pomara, E. Turillazzi. *Mediators Inflamm*, **2017**, 7018393.
- 19.N.W. an der Hoeven, G.N. Janssens, G.A. de Waard, H. Everaars, C.J. Broyd, C.W.H. Beijnk, P.M. van de Ven, R. Nijveldt, C.M. Cook, R. Petraco, T. Ten Cate, C. von Birgelen, J. Escaned, J.E. Davies, M.A.H. van Leeuwen, N. van Royen, *JAMA Cardiol*, **2019**, 4, 736.
- 20.K.A. Olsson, J. Harnek, A.K. Ohlin, N. Pavlidis, B. Thorvinger, H. Ohlin, *Scand Cardiovasc J*, **2002**, 36, 237.
- 21.A.M. Tavares, A.S. da Rosa Araujo, S. Liesuy, N. Khaper, L.E. Rohde, N. Clausell, A. Belló-Klein, *Exp Clin Cardiol*, **2012**, 17, 263.
- 22.A. Janaszewska, G. Bartosz, *Scand J Clin Lab Invest*, **2002**, 62, 231.
- 23.World Medical Association, *JAMA*, **2013**, 310, 2191.
- 24.M. Conti, P.C. Morand, P. Levillain, A. Lemonnier, *Clin Chem*, **1991**, 37, 1273.
- 25.M.L. Hu, *Methods Enzymol*, **1994**, 233, 380.
- 26.P. Vats, V.K. Singh, S.S. Sing, *Aviat Space Environ Med*, **2008**, 79, 1106.
- 27.S.S. Shapiro, M.B. Wilk, *Biometrika*, **1965**, 3, 591.
- 28.M.P. Fay, M.A. Proschan, *Stat Surv*, **2010**, 4, 1.
- 29.F. Wilcoxon, *Biometrics Bull*, **1945**, 1, 80.



# AN EXPLORATION OF HUMAN $\gamma$ D-CRYSTALLIN AFFINITY FOR POTENTIAL AGGREGATION INHIBITORS: A MOLECULAR DOCKING INVESTIGATION

Călin G. FLOARE<sup>a\*</sup> , Adrian PÎRNĂU<sup>a</sup> , Mihaela MIC<sup>a</sup> ,  
Elena MATEI<sup>a\*</sup> 

**ABSTRACT.** Cataract, the leading cause of blindness worldwide, is characterized by the presence of a cloudy area in the eye lens resulting in a loss of transparency. A number of mechanisms contribute to the longevity and transparency of the human lens, a reducing and oxygen deficient environment, the presence of UV-filters, and most importantly a unique supramolecular organization of its structural proteins, the  $\alpha$ -,  $\beta$ - and  $\gamma$ -crystallins. With advancing age, progressively, or due to some mutations, this fragile equilibrium can be perturbed, causing  $\gamma$ -crystallin insolubilization, misfolding, fragmentation and aggregation.

In this study, we performed a comparative molecular docking analysis of several experimentally investigated molecules of natural origin, that might protect  $\gamma$ -crystallins from destabilization and aggregation. Our specific protein targets are wild-type human  $\gamma$ D-crystallin, and its mutant P23T  $\gamma$ D-crystallin, associated with congenital cataract. Thirteen phytochemicals were investigated as potential inhibitors of  $\gamma$ D-crystallin aggregation, and we compared their binding energies with those of lanosterol, an ingredient present in over-the-counter eye products, to prevent cataracts. We performed a detailed comparative molecular docking analysis and we found that the binding energies of lanosterol outcompete those of all the other investigated potential natural inhibitors.

**Keywords:**  $\gamma$ -crystallins, aggregation inhibitors, molecular docking

---

<sup>a</sup> National Institute for Research and Development of Isotopic and Molecular Technologies, 67-103 Donat Street, 400293 Cluj-Napoca, Romania.

\* Corresponding authors: [calin.floare@itim-cj.ro](mailto:calin.floare@itim-cj.ro), [elena.matei@itim-cj.ro](mailto:elena.matei@itim-cj.ro)



## INTRODUCTION

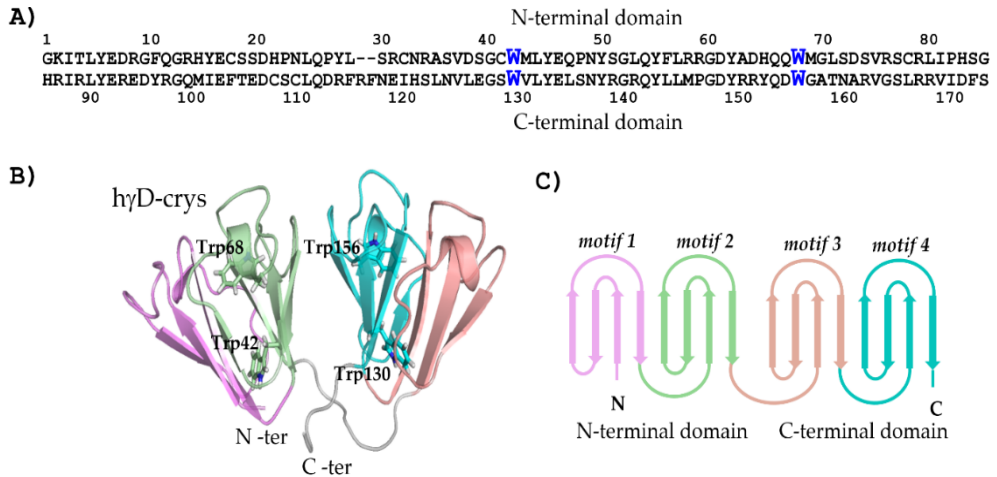
Crystallins, the predominant structural proteins in the eye lens, are the major contributors to the optimal refractive index necessary to focus light correctly into the retina. They must remain stable and soluble at very high concentrations throughout the entire life of the organism, to avoid the formation of light scattering aggregates [1, 2]. There are three major classes of crystallins in mammals,  $\alpha$ -,  $\beta$ - and  $\gamma$ -crystallins.  $\alpha$ -Crystallins ( $\alpha$ A and  $\alpha$ B) are members of the small heat-shock proteins superfamily [3-5] and are found in many cells and organs outside the lens. For instance,  $\alpha$ B-crystallin was found to be expressed in the retina, heart, skeletal muscles, skin, brain and other tissues and to be overexpressed in several neurological disorders and in other cells known to be involved in many diseases, or in stressed cell lines. The small heat-shock  $\alpha$ -crystallins suppress thermally induced aggregation of various enzymes and proteins, including that of  $\beta$ - and  $\gamma$ -crystallins, and represent ~40% of the eye lens proteins [6]. They are larger and polydisperse, multimeric proteins, that tend to form high molecular weight oligomers with sizes between 0.5 and 1MDa [7]. The  $\beta$ - and  $\gamma$ -crystallins are evolutionarily related and belong to the  $\beta\gamma$ -crystallin superfamily, which also contains nonlens members in both prokaryotes and eukaryotes [8-10]. They contain aromatic and sulfur-rich residues with very compact intramolecular packing and have two homologous domains connected by a linker peptide [11].  $\beta$ -Crystallins associate to form dimers up to octamers, and  $\gamma$ -crystallins, which range from 20-22 kDa, are monomers in solution [12].  $\gamma$ -Crystallins are located in the central lens nucleus, and are one of the longest-lived proteins in the human body, without protein turnover, and can reach very high concentrations (~400 mg/ml in mammalian eye, and ~1000 mg/ml in some fish lenses).

Cataract affects a great majority of people and its incidence increases with age. It was estimated that more than 150 million people have impaired vision due to cataract [13]. Of these, more than 17 million people are blind, and approximately 28000 new cases are reported daily worldwide [14]. Even if good vision can be restored with an intraocular lens implant, posterior subcapsular opacification can occur in 10% of cases [15]. Therefore, identifying more robust and natural ways to prevent cataracts, is highly desirable.

The extraordinary transparency and longevity of the mammalian lens are due to the quasi-anoxic and reducing environment with antioxidant defenses and high glutathione levels [16], the presence of UV filters [17] and, most importantly, the particular composition and organization of its structural proteins,  $\alpha$ -,  $\beta$ - and  $\gamma$ -crystallins. In the central part of the lens, the concentration of  $\gamma$ -crystallins can reach ~400 mg/ml [18], which over time or due to some congenital or external factors may locally increase and  $\gamma$ -crystallins aggregate.

AN EXPLORATION OF HUMAN  $\gamma$ D-CRYSTALLIN AFFINITY FOR POTENTIAL AGGREGATION INHIBITORS: A MOLECULAR DOCKING INVESTIGATION

Their delicate supramolecular equilibrium is maintained and the aggregation is additionally prevented by  $\alpha$ -crystallins, which act as chaperones.



**Figure 1.** Human  $\gamma$ D-crystallin structure. A) Amino acid sequence of human  $\gamma$ D-crystallin, in the upper part N-terminal domain (N-ter) and in the lower part, C-terminal domain (C-ter). Tryptophan residues which contribute to the packing of the hydrophobic core and strongly quench the UV fluorescence are highlighted in blue. B) A ribbon representation of human  $\gamma$ D-crystallin. The four tryptophan residues are shown in stick representation. C) The complex topology of the  $\gamma$ D-crystallin domain constructed from four intercalated antiparallel  $\beta$ -sheet Greek key motifs, separated into two domains, joined by a short loop. Each motif is colored differently.

The human  $\gamma$ D-crystallin protein (h $\gamma$ D-Crys), represented in Figure 1, is the third most abundant  $\gamma$ -crystallin in the lens and a significant component of the age-onset cataracts. It is a highly soluble monomeric protein composed of 173 amino acids arranged in two structurally homologous domains. Each domain is composed of two  $\beta$ -sheet Greek key motifs (see Figure 1C), a characteristic structural feature of the  $\gamma$ -crystallin family. The domains are connected by a linker peptide and form a highly conserved hydrophobic interface that plays a crucial role in determining long-term stability. In mammals, each domain of  $\gamma$ -crystallin contains a pair of conserved Trp residues, which contribute to the packing of the hydrophobic core and strongly quench UV fluorescence [19, 20]. The balance of interactions required to maintain short-range order between the constituent proteins of the eye lens is delicate, and it has been demonstrated that the  $\gamma$ D-crystallin protein can undergo irreversible

phase separation. In particular, the mutant protein P23T  $\gamma$ D-crystallin (h $\gamma$ D-P23T) in which the amino acid proline at position 23 is replaced by a threonine, is associated with congenital cataracts [21]. Biochemical analyses of this mutant protein demonstrated that the solubility of h $\gamma$ D-P23T, is dramatically lower than that of the wild-type h $\gamma$ D-crystallin (h $\gamma$ D-WT) protein, due to self-association into higher molecular weight amorphous aggregates under native conditions (neutral pH=7, 37°C) [13, 22-24]. These amorphous-looking deposits have a high degree of structural homogeneity at the atomic level retaining a native-like conformation, as revealed by solid-state NMR [21]. The Pro23 to Thr mutation has been associated with a number of known cataract phenotypes. Additionally, the h $\gamma$ D-P23T mutant protein exhibit an inverse dependence of its solubility with temperature. The protein aggregates melt as the temperature of the solution decreases [24]. This particular behavior is similar to that we previously observed in a system containing cyclodextrins, methylated pyridines and some water, which presented a liquid-to-solid reentrant phase transition upon heating [25].

Structure-based docking screening is common in early drug discovery and molecular docking is a fast way to identify the prevailing binding modes of a ligand to a protein and of their particular interactions at the atomic level. Due to its facility of use, speed and cost-effective exploration of vast chemical space to identify a subset of potential hits for a target, it is currently routinely used by researchers to supplement the experimental studies. However, in too many cases, too harsh or inappropriate approximations are used, which results in undersampling of possible configurations which materializes into inaccurate predictions of the lowest binding energies. This reality prevents trustable comparisons between docking results obtained by different groups even if they are performed with practically the same software and complicates the situation even more if different software is used. The likelihood of obtaining valuable results from molecular docking simulations is directly related to the establishment of good practices and controls prior to undertaking a large-scale prospective screen. A good description of the major challenges is presented in a recent contribution [26]. The present research was initiated due to these identified limitations and our aim was to develop a detailed workflow and, ultimately, a database containing carefully performed simulations. This database contains detailed information about the crystallographic molecular structures of the proteins or macromolecules used and their structural pre-processing before the simulations, simulation parameters and the number of runs. We aim to standardize molecular docking simulations or at least to establish a good protocol in order to obtain reproducible and trustworthy results, in agreement with Aci-Sèche *et al.* [27]. In this article, we gathered and we present such a workflow, particularly exploring the molecular association between human

$\gamma$ D-crystallin and a series of potential natural inhibitors of its aggregation, compared with that of lanosterol, an ingredient which is present in over-the-counter eye products used to prevent cataracts. In all our simulations performed to identify the most stable complexes between ligands and the h $\gamma$ D-WT and h $\gamma$ D-P23T crystallin proteins, we used AutoDock software. A comparative and trustworthy analysis, of the specific molecular interactions between  $\gamma$ D-crystallin proteins and small ligands can then provide valuable information, even at this level of theory, that contributes to the understanding and possibly to the control of the biochemical and biophysical interactions between these exceptional proteins constituting the eye lens. Consequently, in this study, we only present in detail the extended molecular docking analysis. Comprehensive *in vitro* aggregation suppression assays of h $\gamma$ D-WT and h $\gamma$ D-P23T are still underway and will be independently reported when completed.

## RESULTS

### Lanosterol

We initiated this study by thoroughly analyzing of the interaction between lanosterol and h $\gamma$ D-WT and h $\gamma$ D-P23T mutant. The tetracyclic triterpenoid lanosterol, from which animal and fungal steroids are derived, has been identified as an important component for maintaining the clarity of the eye lens [28]. Additionally, during a preclinical study lanosterol was identified as a possible agent for cataract remediation and prevention. Lanosterol, an amphipathic molecule present in the ocular lens, is synthesized by lanosterol synthase in a cyclization reaction of the cholesterol synthesis pathway. *In vivo* experiments in dogs have shown significant improvement in cataracts within 6 weeks of lanosterol injection [29]. In 2018, lanosterol was shown to improve lens clarity in cells with lens opacities due to aging or physical stressors [30]. A later study found positive results against lens opacification in cataract mice [31]. Lanosterol is currently used as an ingredient in over-the-counter eye products to prevent cataracts. However, because the solubility and bioavailability of lanosterol do not favor aqueous formulations, some researchers doubt its effectiveness [32]. Nevertheless, Heliostatix Biotechnology claims to have a method of solubilizing lanosterol for use in aqueous products and they already sell LumenPro, a vision eye care drop for animals with cataracts, that combines lanosterol and N-acetylcarnosine [33]. We consequently considered lanosterol, at this early stage of our analysis, as a point of reference. As we will see throughout the paper, this initial study was then followed by a comparative investigation of another 13 natural compounds with the potential

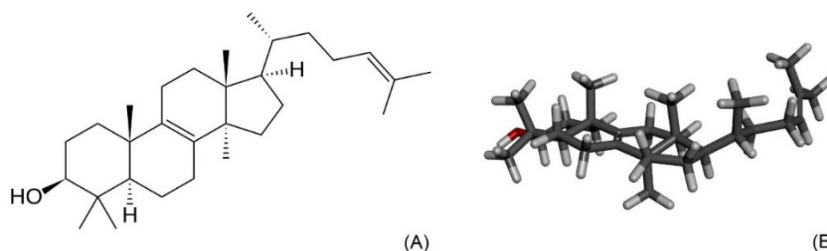


to counteract  $\gamma$ -crystallins misfolding and aggregation. This comparative theoretical analysis practically constitutes the subject of the actual paper. We performed this study as a necessary step before a thorough investigation of a more exhaustive search of potential inhibitors spanning the ZINC database [34, 35]. As mentioned above, our aim was to more closely evaluate the performance/precision for compound screening and to establish controls and a detailed workflow to further determine the reliability of the results.

In this study we performed an *in silico* ligand-protein molecular docking analysis which is currently a key tool in structural molecular biology and computer-assisted drug design. The goal is to predict the most likely binding mode(s) of a ligand to a protein with a known three-dimensional structure.

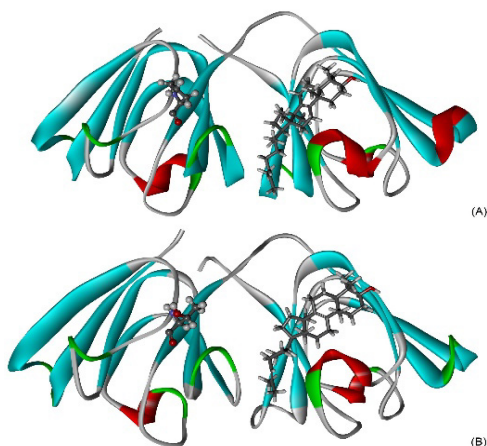
Prior to the actual docking calculations, we performed *first-principles* optimizations of the three-dimensional molecular structure of the ligands, to ensure that the three-dimensional molecular structure and the relative position of all atoms of the ligand were appropriate and correct from a chemical point of view. During the actual docking procedure, only the torsional angles of the bonds within the ligand are modified, following a Monte Carlo algorithm. Then, the molecule is docked to the protein, and this conformation is optimized through an energy minimization. The distances between the atoms of the ligand remain practically the same as those in the initial optimized conformation. As we also specified previously, the three-dimensional molecular structure of lanosterol was optimized using Gaussian 16 software [36] with the meta-GGA M06-2X hybrid functional and the 6-311++G(d,p) basis set. The same molecular conformation optimization was performed for all the molecules investigated in this study. As a result of the calculations, no imaginary vibrational frequencies were obtained, which proves that the optimized structure corresponds to a minimum of the potential energy surface (PES) and is not a transition state.

The chemical structure of lanosterol and the three-dimensional optimized conformation are shown in Figure 2. This was the molecular structure of the ligand used, on the following, by the docking algorithm.



**Figure 2.** Lanosterol structure. (A) Lanosterol,  $C_{30}H_{50}O$ , molecular weight 426.7 g/mol (B) Molecular optimized structure of lanosterol using Gaussian 16 software with the meta-GGA M06-2X hybrid functional and the 6-311++G(d,p) basis set.

The conformations of the proteins were obtained from the structures deposited in the RCSB database, from the crystallographic one for h $\gamma$ D-WT (PDB ID: 1HK0 [37]), and from the NMR determined solution structure for the h $\gamma$ D-P23T mutant (2KFB [38]). To adapt them to the molecular docking process all the water molecules were removed. The docking procedure input files were generated using AutodockTools v. 1.5.6 [39, 40], the flexibility of the ligand was taken into account considering five torsion angles around the single bonds that were automatically detected in AutoDock, while the h $\gamma$ D-crystallin conformations were kept rigid. AutoGrid software was used to generate interaction energy maps of the different types of atoms before actually performing the docking procedure. The maximum grid size was set to 126x126x126 points with a grid point spacing of 0.475 Å and the h $\gamma$ D-crystallin conformations were fully included in the protein-centered cubic search volume. With the aim of obtaining good statistics and clustering distributions, as mentioned previously, we performed the highest number of runs accessible in AutoDock, 2000.

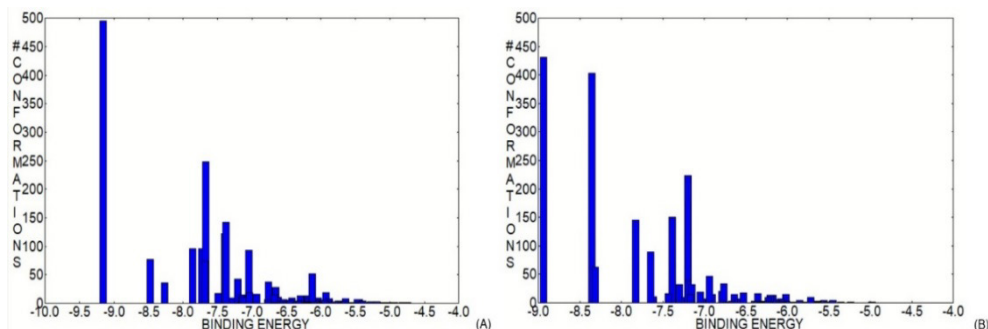


**Figure 3.** The lowest binding energies molecular docking conformations of lanosterol to (A) wild-type h $\gamma$ D-WT and (B) the h $\gamma$ D-P23T mutant. We also highlighted the amino acids at position 23 of polypeptidic chain.

Figure 3 shows the conformations with the lowest binding energies for the complex formed by lanosterol, and h $\gamma$ D-WT and the h $\gamma$ D-P23T variant, respectively.

The binding energies of these conformations are: -9.16 kcal/mol for the complex with h $\gamma$ D-WT and -8.94 kcal/mol for the complex with h $\gamma$ D-P23T. From the results obtained in the calculations, the binding of lanosterol to the h $\gamma$ D-P23T mutant is less favorable, by approximately 0.22 kcal/mol, than that obtained for h $\gamma$ D-WT. To better understand this difference, we mention that

after performing the 2000 runs, the obtained conformations were classified into families of similar conformations, denoted as “clusters” in Autodock and on the following. In Figure 4 we plot the histograms of the binding energy distributions of all the clusters identified during the analysis of docked conformations.

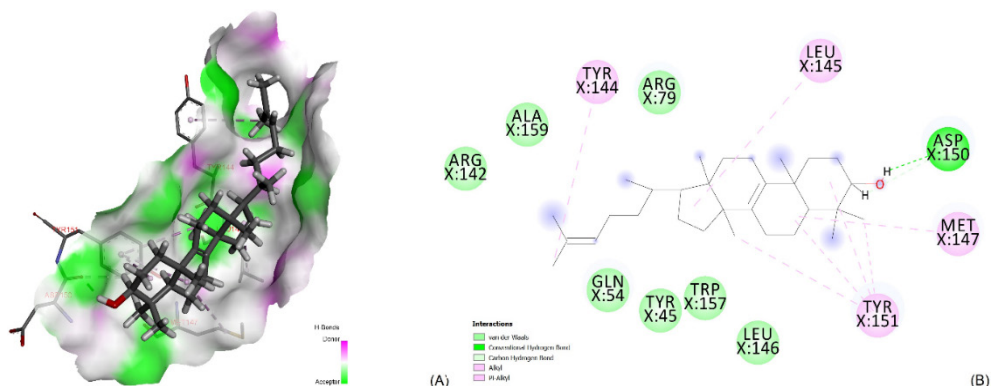


**Figure 4.** Histograms of the clusters of binding energies of lanosterol to hγD-crystallin: (A) hγD-WT and (B) the hγD-P23T mutant.

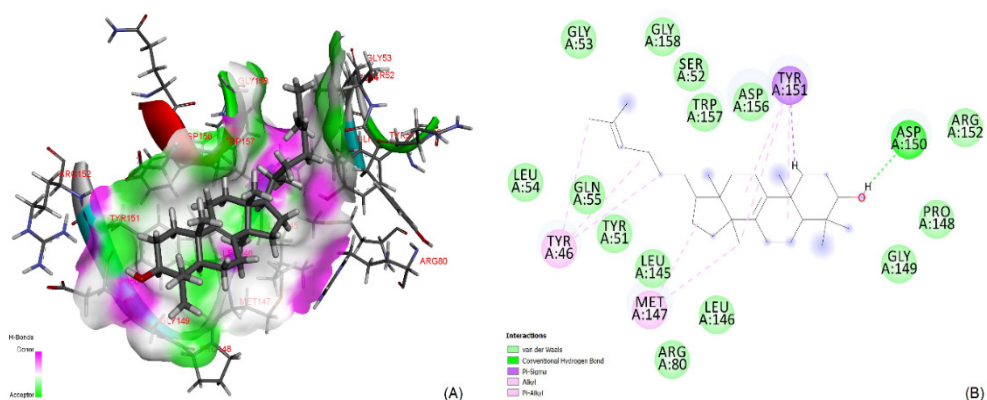
To properly grasp the meaning of these representations, we specify that the position of each cluster on the binding energy axis is determined only by the member with the lowest value of the binding energy of the cluster. In addition to the binding energy, another significant information is the frequency with which each binding conformation is identified, represented as the intensity in the histograms. As the number of members in a group/cluster increases, that particular binding conformation is more favored or has been identified more often. Other useful information, which can provide additional insight, is the range of binding energies of the members of each group, or at least the average binding energy of the group. With these specifications in mind, if we now analyze the results represented in Figure 4 we observe that the conformations with the lowest values of the binding energies also have the highest number of members in both cases, 495 for hγD-WT vs 431 in the case of the hγD-P23T mutant; the binding energy range of the members of these clusters is 3.45 vs 2.96 kcal/mol and the average binding energy is -8.0 vs -8.02 kcal/mol. This analysis demonstrated that these binding configurations were predominant and, as we can see, differed only slightly for the two proteins. In our opinion, these results prove that the method is reliable and stable, but still within a margin of error.

In Figures 5 and 6, we present a detailed analysis of the intermolecular interactions from the binding sites.

AN EXPLORATION OF HUMAN  $\gamma$ D-CRYSTALLIN AFFINITY FOR POTENTIAL AGGREGATION INHIBITORS: A MOLECULAR DOCKING INVESTIGATION



**Figure 5.** Proximity interactions within the binding site (A) and corresponding two-dimensional maps (B) between lanosterol and h $\gamma$ D-WT.



**Figure 6.** Proximity interactions within the binding site (A) and the corresponding two-dimensional maps (B) between lanosterol and the h $\gamma$ D-P23T mutant.

As shown in Figure 3, the two conformations are quite similar, and the hydroxyl group of the lanosterol molecule interacts in both cases with the amino acids Asp150 and Tyr151 which are nearby. The lanosterol molecule seems to be only slightly displaced. During our analysis we noted that, in the PDB file containing the wild-type crystallographic h $\gamma$ D-WT structure with RCSB ID: 1HK0, seems to be a numbering problem. Effectively, the amino acid number 86 does not exist, and we only have Gly85 and Ser87; however, in the 2KFB file, we have one additional glutamine residue from the His-tag tail at the N-terminus. In the file containing the h $\gamma$ D-WT structure, the amino

acid glutamine does not appear, and the amino acid sequence starts normally with glycine (Gly1). We specify these inconsistencies because, in Figures 5 and 6, the amino acid numbering of the two proteins differs below position 85, due to these specific differences, after which the amino acid numbering becomes identical. We conclude this initial analysis by observing that molecular docking simulations successfully revealed the fact that lanosterol binds to a hydrophobic interfacial region near residues 135–165 on the C-terminal domain, a region that is crucial for h $\gamma$ D-Crys domain-swapping dimerization. This finding indicates that lanosterol binding likely disrupts the h $\gamma$ D-Crys dimerization and was also previously put in evidence by molecular dynamics simulations [41]. With all these theoretical predictions success, the binding of lanosterol to the C-terminal should, in practice, outcompete self-aggregation to be effective, and because lanosterol is poorly soluble in water, its effectiveness is uncertain [32]. The race for a better inhibitor is still on.

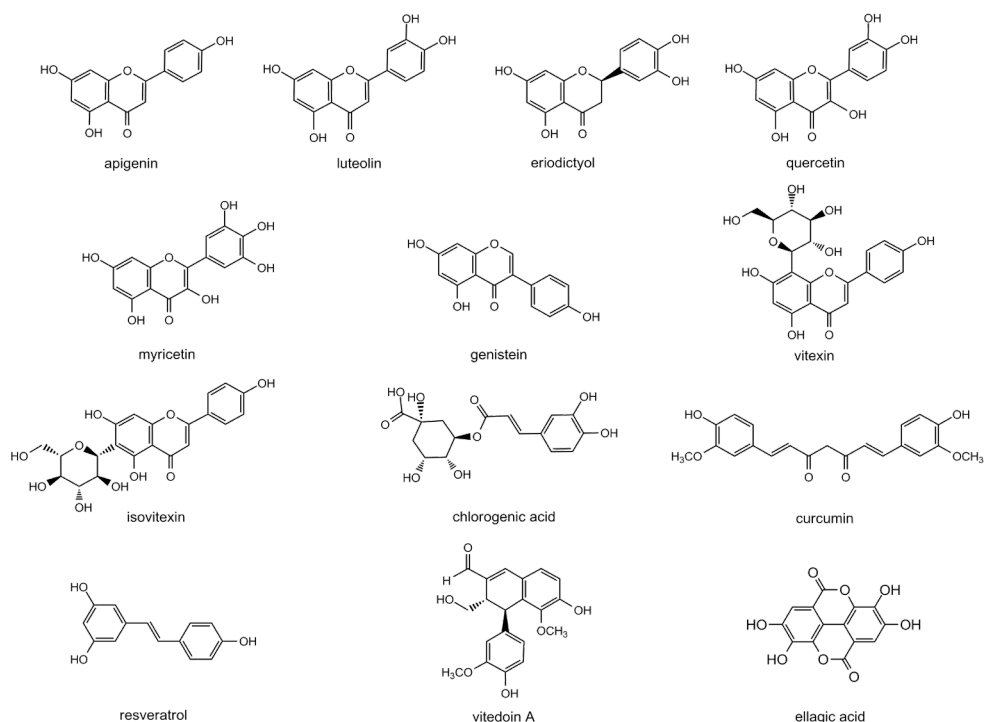
### **Potential natural inhibitors of h $\gamma$ D-crystallin aggregation**

Finding an effective inhibitor to prevent or hopefully reverse of cataracts is a difficult endeavor. However, researchers do not give up hope and many theoretical and experimental studies have been conducted. There is an urgent need for inexpensive, nonsurgical approaches for the treatment of cataract for the reasons we extensively mentioned in the Introduction. High throughput theoretical [42] and experimental [6] studies have even been attempted. Given that considerable attention has been devoted to the search for phytochemical therapeutics, in this research we decided to focus on and comparatively investigate mainly flavonoids. This decision to investigate this class of polyphenols is based on the observation that several pharmacological actions of flavonoids may operate in the prevention of both age-related and diabetic cataracts. Flavonoids can affect multiple mechanisms or etiological factors responsible for the development of sight threatening ocular diseases including oxidative stress, nonenzymatic glycation and the polyol pathway and numerous studies have been conducted [43-52]. The interest in the other phytochemicals included in our study has been raised because a potential anti-cataract activity has been previously identified or studied: chlorogenic acid [53], curcumin [54-60], resveratrol [61-63], vitexin A [43, 64], and ellagic acid [65, 66]. As shown in Table 1 and Figure 7, we list and graphically represent all 2D chemical structures of the investigated natural potential  $\gamma$ -crystallin aggregation inhibitors in this work.

AN EXPLORATION OF HUMAN  $\gamma$ D-CRYSTALLIN AFFINITY FOR POTENTIAL AGGREGATION INHIBITORS: A MOLECULAR DOCKING INVESTIGATION

**Table 1.** Investigated natural compounds with the potential to protect  $\gamma$ -crystallins from misfolding and aggregation.

Natural compounds	Plant	ZINC code
Apigenin	<i>Origanum vulgare</i>	ZINC000003871576
Luteolin	<i>Olea europaea</i>	ZINC000018185774
Eriodictyol	<i>Thymus vulgaris</i>	ZINC000000058117
Quercetin	<i>Allium cepa</i>	ZINC000003869685
Myricetin	<i>Spinacia oleracea</i>	ZINC000003874317
Genistein	<i>Fabaceae (Glycine max)</i>	ZINC000018825330
Vitexin	<i>Crataegus pinnatifida</i>	ZINC000004245684
Isovitexin	<i>Crataegus pinnatifida</i>	ZINC000004095704
Chlorogenic acid	<i>Vaccinium angustifolium</i>	ZINC000006482465
Curcumin	<i>Curcuma longa</i>	ZINC000100067274
Resveratrol	<i>Vitis vinifera</i>	ZINC000000006787
Vitedoin A	<i>Vitex negundo</i>	ZINC000014883365
Ellagic acid	<i>Rubus fruticosus</i>	ZINC000003872446



**Figure 7.** Chemical structures of natural compounds analyzed as potential cataract inhibitors.

We present the results obtained after performing docking calculations identical to those for lanosterol for all potential natural inhibitors specified and represented in Figure 7. All of them were docked on the same h<sub>y</sub>D-WT and h<sub>y</sub>D-P23T proteins with RCSB IDs: 1HK0 and 2KFB, respectively, using the same calculation parameters. Our aim was not only to theoretically identify a potential natural inhibitor of h<sub>y</sub>D-crystallin aggregation with improved properties compared with lanosterol but also, as mentioned, to test the reliability of the molecular docking procedure for this particular case.

In Table 2 we present the results obtained for the leading conformations of all the potential natural inhibitors investigated in interaction with both, h<sub>y</sub>D-WT and h<sub>y</sub>D-P23T proteins. We specify for each one, the binding energy of the best docked conformation, the mean binding energy of the members in its cluster and also the number of the members of the cluster to which this conformation belongs. As shown in the table, for genistein, resveratrol and curcumin, we specified two entries. When both genistein and resveratrol were docked to the h<sub>y</sub>D-P23T mutant protein we identified two lowest binding energy conformations. We mention them because, for genistein, both structures had the exact lowest binding energy but are docked to two different binding sites.

**Table 2.** Binding energies of the best docked conformations of investigated natural compounds to the h<sub>y</sub>D-WT (RCSB ID: 1HK0) and the h<sub>y</sub>D-P23T mutant (RCSB ID: 2KFB).

Compound	Lowest	Mean	Number	Lowest	Mean	Number
	Binding Energy	Binding Energy	in Cluster	Binding Energy	Binding Energy	in Cluster
	wild-type h <sub>y</sub> D-WT - 1HK0			mutant h <sub>y</sub> D-P23T - 2KFB		
Apigenin	-8.15	-7.20	275	-6.27	-5.99	214
Luteolin	-8.23	-7.17	157	-6.50	-5.88	395
Eriodictyol	-7.53	-6.48	53	-6.68	-6.35	786
Quercetin	-8.32	-7.15	192	-6.37	-5.71	403
Myricetin	-8.34	-6.92	118	-6.24	-5.56	355
Genistein	-8.90	-8.02	314	-6.19	-5.83	36
				-6.19	-5.79	194
Vitexin	-7.22	-6.22	92	-6.18	-4.77	206
Isovitexin	-7.08	-5.50	52	-6.50	-5.58	1452
Chlorogenic Acid	-6.81	-5.14	18	-6.13	-4.68	76
Curcumin enol-keto	-7.69	-6.67	7	-7.36	-5.94	210
Curcumin diketo	-8.95	-6.33	11	-7.16	-5.88	217
Resveratrol	-7.80	-6.98	77	-5.97	-5.47	165
				-5.93	-5.44	472
Vitedoin A	-6.71	-5.85	16	-6.16	-5.01	240
Ellagic Acid	-7.89	-7.31	477	-7.66	-7.30	109

For resveratrol, we again specified two most probable docking conformations, because the difference in energy between them was small enough. For curcumin we performed the calculation for both known curcumin tautomers: enol-keto and diketo. We considered both conformations relevant to be specified also to underline and point out the uncertainties of the molecular docking method on which we will further elaborate in the following.

By analyzing the results presented in this table, we observed that the values of the binding energies with the h $\gamma$ D-WT protein are generally lower than with the h $\gamma$ D-P23T mutant. For all the molecules investigated, we computed a mean of approximately -7.8 kcal/mol versus -6.5 kcal/mol, suggesting a stronger binding of all investigated compounds with h $\gamma$ D-WT. This finding is opposite to what we initially expected to provide evidence and we observed this behavior during the initial calculation of lanosterol docking, as well. We specify here that we have not yet measured, experimentally, how a particular inhibitor interacts comparatively with the h $\gamma$ D-WT protein versus the h $\gamma$ D-P23T mutant and we did not find or know of a previous study to use it as a comparison. However, we know that the h $\gamma$ D-P23T mutant aggregates at significantly lower concentrations than does h $\gamma$ D-WT [21, 67]. This is what effectively motivated us to initiate this study to try also to understand how a single point mutation can have a drastic effect on the affinity and statistical equilibrium between these proteins and how this equilibrium can be influenced.

Even if a more precise investigation is necessary to clarify this theoretical result, we presume that the higher affinity obtained for all the molecules investigated for h $\gamma$ D-WT could essentially be caused by the fact that the two protein structures were not determined under the same experimental conditions. The structure of h $\gamma$ D-WT was solved by X-ray crystallography, while the structure of h $\gamma$ D-P23T was solved using NMR in solution, and all atoms belonging to proteins were kept rigid during the calculations. We also emphasize here that we analyzed the affinity between several small potential inhibitors and h $\gamma$ D-P23T as a monomer, without considering any details regarding the protein-protein interactions causing aggregation of this mutant. After this important preliminary observation, we will now continue our analysis since much relevant information is still hidden in the details of the best docking conformations. In the following, we will refer, to the lowest binding energies values specified in Table 2 and to the practical docking conformations that, for a better comparison, are all represented in Figure 8. With the exception of vitexin, all flavonoids here prefer docking in the same pocket created between the C-terminal tail and the linker between the N- and C- terminal domains, when interacting with h $\gamma$ D-WT. Additionally, with the exception of genistein and vitexin, all the flavonoids preferentially dock in the same pocket belonging to C-terminal domain, when interacting with h $\gamma$ D-P23T mutant protein. This comparative result suggested that protein pockets can accommodate molecules of various dimensions, with different affinities. If, between flavonoids, for the



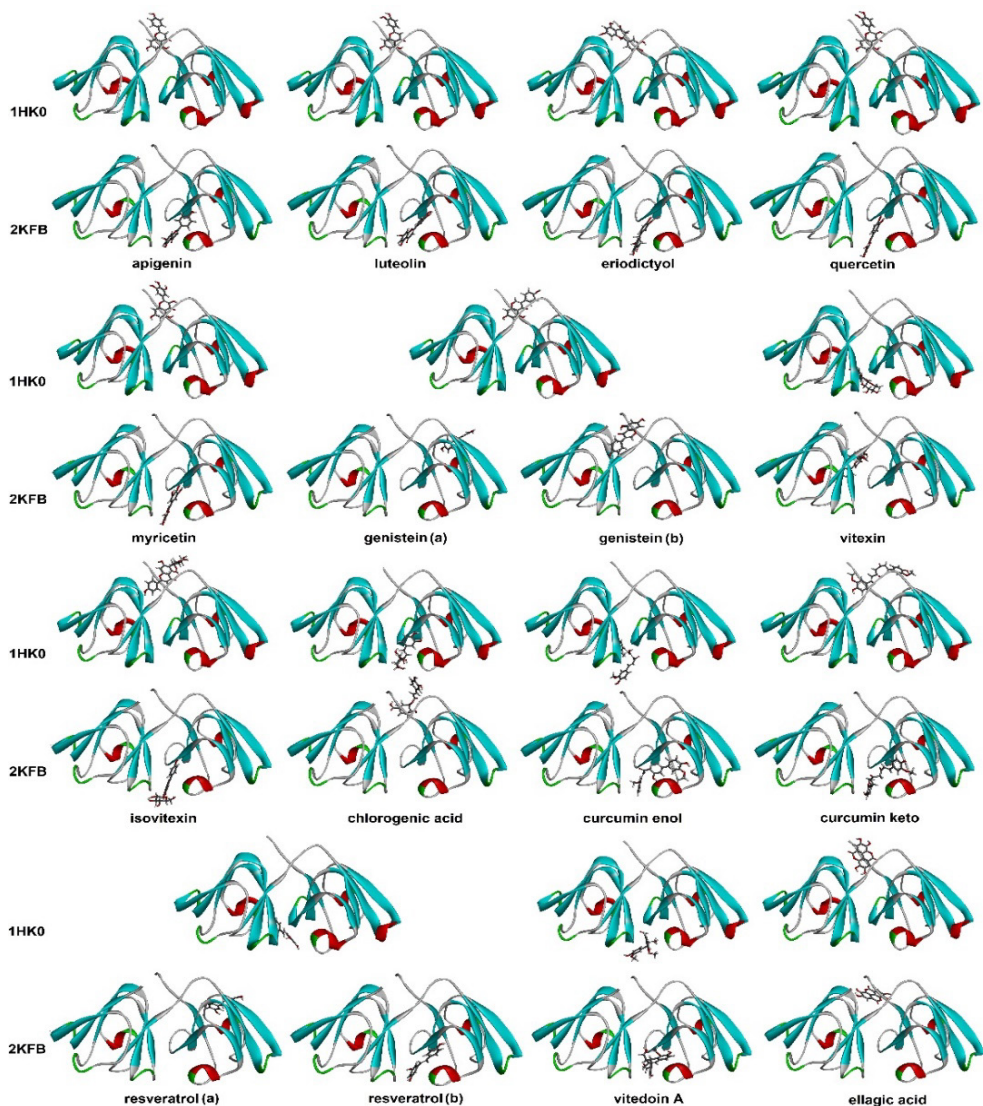
hyD-WT, genistein leads with a binding energy of -8.9 kcal/mol, to the hyD-P23T mutant protein it is eriodictyol which has the lowest binding energy of -6.68 kcal/mol, and genistein does not have a high affinity for the mutant protein. We remark here also that the binding energies differ only by a maximum of 0.5 kcal/mol, vitexin having a binding energy of -6.18 kcal/mol.

When we compared the binding energies of all investigated molecules to the hyD-P23T mutant we observed that resveratrol, as a result of our calculations, was the least bound molecule. For resveratrol, we chose to present here two configurations bound to the hyD-P23T mutant with very close binding energies of -5.97 kcal/mol and of -5.93 kcal/mol. We represent this additional structure, because it was identified with preference (its cluster has 492 members versus 165 for the leading conformation) and because, as we can see in Figure 8, it binds in the same pocket belonging to C-terminal domain which extends in the space between N- and C- terminal domains, as the majority of flavonoids.

In Figure S17 from the Supplementary Material, we additionally present the histograms of the clusters of binding energies for all investigated potential natural inhibitors. In practical analysis, histograms are of crucial importance. Besides the fact that histograms aid in the identification of protein binding sites and of most stable configuration they also provide a practical, ordered and interactive view, inside AutoDockTools, of the identified clusters of conformations.

As an example, for genistein, if we look at the histogram representation for the interaction with hyD-P23T mutant protein, we observe that we obtained two clusters of conformations superposed at the lowest value of the binding energy, one with 36 members and another with 194. This is the reason why we both specified in Table 2 and Figure 8, as mentioned above, genistein (a), the leading conformation of the cluster having 36 members and genistein (b) the leading conformation of the cluster with 194 members. For resveratrol, as shown in Figure 8, the conformation named resveratrol (a) has the binding energy -5.97 kcal/mol and belongs to the cluster with 165 members only. After analyzing the favorite binding pockets for the hyD-WT and hyD-P23T mutant more generally, in Figure 8, we observe that those preferred by the majority of flavonoids are also “popular” for other molecules too, with some particular exceptions. We remarked here that vitexin, which is bulkier and has a greater lateral dimension and probably does not fit into the pocket created between the C-terminus and the linker between the N- and C- terminal domains, ultimately binds to the space between the N- and C- terminal domains. Isovitexin, on the other hand, respect the trend of preferred binding sites of the majority of flavonoids to both proteins even though it was slightly less stable than vitexin for the hyD-WT protein and more stable than vitexin when docked to the hyD-P23T mutant. Chlorogenic acid which binds in a somewhat reversed

AN EXPLORATION OF HUMAN  $\gamma$ D-CRYSTALLIN AFFINITY FOR POTENTIAL AGGREGATION INHIBITORS: A MOLECULAR DOCKING INVESTIGATION



**Figure 8.** Lowest binding energies molecular docking conformations for all potential natural aggregation inhibitors to h $\gamma$ D-WT (RCSB ID: 1HK0) and h $\gamma$ D-P23T mutant (RCSB IDs: 2KFB) investigated in this work, ordered horizontally. To facilitate comparisons between these conformations, we represented them together. We kept the same order of the molecules investigated in this work, as previously specified in Figure 2. Proximity interactions within the binding site and their corresponding two-dimensional interaction maps are presented in Figures S1-S16 from the Supplementary Material.

manner to the abovementioned trend created by the majority of flavonoids, but has a relatively low binding energy to both proteins if we compare it with the other investigated molecules. Another surprising behavior is that of curcumin, for which we calculated the docking of both well-known tautomers enol-keto and diketo. We observe here that diketo tautomer, with a binding energy of -8.95 kcal/mol, is the leader of all natural compounds investigated, followed by genistein with an energy of -8.9 kcal/mol when docked to h<sub>y</sub>D-WT. The diketo conformer of curcumin is also between the most bound molecules to the h<sub>y</sub>D-P23T mutant, with a binding energy of -7.16 kcal/mol, which is slightly higher than that of curcumin-enol, -7.36 kcal/mol, and of ellagic acid, -7.66 kcal/mol. The binding of diketo curcumin tautomer follows also the abovementioned trend created by the majority of flavonoids, and the same mentioned pockets are preferentially chosen for both proteins. The bindings of Vitedoin A and ellagic acid, which are bulkier, are not consistent with the trend observed for the majority of flavonoids. Vitedoin A did not show a good binding ability because it is the least bound molecule to the h<sub>y</sub>D-WT protein, and is close to the value obtained for resveratrol, when docked to the h<sub>y</sub>D-P23T mutant. Conversely, ellagic acid is the leading molecule when docked to the h<sub>y</sub>D-P23T mutant, for which the lowest value of the binding energy is -7.66 kcal/mol. If we now compare the binding energies of the leader molecules for both h<sub>y</sub>D-WT and h<sub>y</sub>D-P23T, -8.95 kcal/mol for curcumin diketo and that of ellagic acid, with the values obtained initially for lanosterol, -9.16 kcal/mol for the complex with h<sub>y</sub>D-WT and -8.94 kcal/mol for the complex with the h<sub>y</sub>D-P23T mutant, we observe that lanosterol is clearly the leader.

These binding energy values correspond to an estimated dissociation constant ( $K_d$ ), which ranges from ~2.4  $\mu$ M to ~30  $\mu$ M for h<sub>y</sub>D-P23T mutant, with exception of resveratrol with an estimated  $K_d$  of ~45  $\mu$ M. In the case of h<sub>y</sub>D-WT protein the estimated dissociation constant ranges from ~0.3  $\mu$ M to ~12  $\mu$ M. These are reasonable  $K_d$  values, indicating potential binding inhibitors. However, the binding energies computed by molecular docking are only theoretical estimations of the possibility of complex formation, and a more accurate affinity constant can be determined experimentally by Isothermal titration calorimetry (ITC), or Nuclear Magnetic Resonance (NMR).

## DISCUSSION

The results obtained in this study showed that the interaction of all potential inhibitors investigated and also that of lanosterol is more favorable with h<sub>y</sub>D-WT than with the h<sub>y</sub>D-P23T mutant. For instance, for lanosterol, the difference in binding energy to the wild-type and mutant protein is relatively small (approximately 0.22 kcal/mol); however, for genistein isoflavone, the difference

in binding energy is  $\sim 2.7$  kcal/mol. For ellagic acid, the difference is again only 0.23 kcal/mol, and for all the other investigated molecules, the difference varies within these two values. We mentioned that this behavior can be caused by the fact that we used two different protein structures obtained independently by different groups, one crystallographically determined and the other in solution, and not being perfectly similar in sequence of aminoacids. Additionally, there are numerous cases in the literature in which mutants have reduced affinity for ligands compared to the wild-type protein. For instance, previous studies have shown that mutations in the Cyanovirin-N lectin completely abolish the carbohydrate binding site either on domain A, or domain B, rendering those mutants devoid of antiviral activity [68].

On the other hand, although molecular docking simulations are generally reliable and fast compared to other simulation methods, they use many approximations. Thus, the presence of a solvent, water or buffer solution, plays a fundamental role, but in traditional molecular docking simulations, water molecules are not taken into account and protein conformations are kept rigid. In reality, interactions with water molecules and hydrogen bond formation, or conversely, the presence of hydrophobic groups in the composition of the molecule, determine the functional, packed conformations of proteins, as well as the particular interactions with ligands and the value of the stability constants of their complexes in water. As a result of interactions with the solvent molecules, protein-ligand interactions adapt, and the amino acids in the interaction area can change their position to a certain extent. In fact, the conformation of the ligand adapts slightly as a result of interactions with the protein but also due to the presence of water molecules. It is therefore expected, following these approximations, that the results have a certain margin of error. In our study we did not intend to neglect the advances in molecular docking simulations where the receptor flexibility [69] and the explicit hydration can be taken into account by modifying the force field to model explicit water molecules [70] or through the use of physics-based endpoint approximation methods, such as the Molecular Mechanics Poisson-Boltzmann Surface Area (MM-PBSA) and Molecular Mechanics Generalized Born Surface Area (MM-GBSA). The main reason for our classic approach is that even if the accuracies of these advanced methods are usually higher than those of empirical scoring methods, the correlation between estimated and experimental binding free energies varies from system to system [71]. This is probably because the presence of other similar proteins in the immediate vicinity also plays an essential role in the more accurate description of the interactions involved. Temperature and pH are also critical parameters that influence interactions. Molecular dynamics simulations explicitly consider the presence of solvent molecules and can consider multiple proteins in the system but involve an incomparably greater computational effort [72].

Despite these, our calculations showed that lanosterol preferentially binds to a potential dimerization interface in the C-terminal domain of h $\gamma$ D-Crys, which may provide protection from aggregation and cataract formation and this was also shown via molecular dynamics and free energy profile (FEP) calculations [41]. The fact that its binding energy is higher than that of all other investigated potential natural inhibitors must not be considered as a drawback also, but rather attributed to the particular structure of lanosterol and its specific binding mode. The out-of-plane methyl groups provide the molecule with an enlarged hydrophobic surface, leading to an enhanced binding affinity at the hydrophobic interface. Additionally, as the binding is mostly vdW-driven it seems that the hydrocarbon branches anchor to the hydrophobic site, reducing the mobility of the ligand and enhancing its binding stability.

Among the natural inhibitors studied, genistein, curcumin and ellagic acid had the lowest binding energies to h $\gamma$ D-crys. We are actually extending these calculations to other potential inhibitors, and we plan experimental tests.

The comparative investigation presented in this article revealed that the *in silico* screening of inhibitors against the aggregation of h $\gamma$ D-crystallin is not a simple task and requires considerable time and quite significant computing power. The system whose behavior we analyze at the molecular level is complex. Since only the analysis of a single inhibitor requires considerable time on the order of an entire day on a single workstation for a well performed molecular docking simulation or several days to calculate a long enough molecular dynamics trajectory on a high-performance parallel computer, it is somehow illusory to aim for an exhaustive analysis of hundreds, thousands or millions of compounds available in the ZINC organic molecular compound database. High-throughput screening of the ZINC database on moderately sized computer clusters requires not much more than 1 s/molecule/core (1 ms/configuration) [26] but this can result in undersampling of possible configurations. Even if large scale docking can be attempted with the recently developed AutoDock-GPU [73], targeting a subset of the ZINC database is a more feasible approach. This was our initial motivation when we chose to analyze, as carefully possible at this level of the theory, the docking of flavonoids in this study. A substantial effort must be consequently dedicated to the most rational and documented determination of this subset based on the knowledge of the possible interactions involved, as well as the identification and analysis of the interaction surface between the h $\gamma$ D-P23T mutant aggregating protein ensemble. A more promising strategy could be to infer the structure of a potential inhibitor by analyzing the interaction domains between the monomers and understanding how the Pro23Thr mutation favors this interaction. This can be investigated within relatively short nonequilibrium molecular dynamics simulations and the simulations can also be performed at various temperatures. From a personal experience during molecular dynamics studies of the liquid-solid reentrant

phase transition upon heating in methylated pyridines containing cyclodextrins, temperature plays an important role in the stability of the system [25]. Similar simulations were recently performed and reported by Brudar and Hribar-Lee [74] and Zhou *et al.* [41, 75].

The identification of a non-surgical cataract remedy remains a real challenge to which we are committed and new contributions from our group will follow.

## CONCLUSIONS

In this study, the affinities of h $\gamma$ D-crystallin, the wild-type and the P23T mutant were explored using the lanosterol molecule as a reference. We performed molecular docking calculations for 13 phytochemicals identified as molecules potentially inhibiting h $\gamma$ D-crystallin aggregation that were previously studied experimentally and reported in the literature, and we compared their binding energies with that of lanosterol. Initially, we observed that all the investigated molecules had a greater affinity for h $\gamma$ D-WT than for the h $\gamma$ D-P23T mutant. Even if this result must be checked using more precise methods for binding energy estimation or experimentally, we most likely associated this result with the particular h $\gamma$ D-crystallin molecular structures determined, one by X-ray crystallography and the other using liquid NMR, which were kept rigid during our calculations. The second observation was that the binding energies of the lanosterol, which was used as a reference, outcompeted those of all the other investigated potential natural inhibitors. This result, however, must not be taken as a drawback of this study but rather attributed to the particular structure of lanosterol and to its specific binding mode to a hydrophobic interfacial region near the C-terminal domain, a region crucial for h $\gamma$ D-Crys domain-swapping dimerization. This binding mode is similar to that previously identified by more accurate molecular dynamics simulations [41] and proves the reliability of molecular docking simulations as initial binding mode approximation. According to the comparative analysis of all 13 phytochemicals investigated, genistein, curcumin and ellagic acid had the lowest binding energies to h $\gamma$ D-crystallins but still higher than that of lanosterol. Ongoing efforts are underway to improve and extend these calculations to other potential inhibitors following the new and innovative ideas.

## COMPUTATIONAL DETAILS

Screening for inhibitors of h $\gamma$ D-P23T mutant aggregation is a real challenge and requires considerable time and resources. The architecture of structural eye lens proteins is complex and, in this study, we explored drug

affinity of the human  $\gamma$ D-crystallin protein, which has been proven to be a significant component of the age-onset cataracts.

Because the analysis of hundreds or thousands of compounds needs the availability of a large computing cluster and an exhaustive analysis of millions compounds available in the ZINC database is practically impossible, in this first approach, we theoretically analyzed a relatively small subset of thirteen potential natural inhibitors we identified in the literature. Lanosterol was used as a reference. Prior to the actual docking calculations, the molecular structures of all potential h $\gamma$ D-crystallin aggregation inhibitors were optimized with Gaussian 16 software [36] using the meta-GGA M06-2X hybrid functional and the 6-311++G(d,p) basis set and no imaginary frequencies were obtained. The molecular conformations of h $\gamma$ D-WT and the h $\gamma$ D-P23T mutant were identified in the RCSB database (PDB ID: 1HK0 [37] and 2KFB [38]) and the three-dimensional molecular structures used in our calculations were extracted from these conformations. Computational molecular docking with the aim of obtaining the most feasible interaction conformations between the chosen potential aggregation inhibitors and h $\gamma$ D-crystallin was then performed using the Monte Carlo simulated annealing search implemented in AutoDock v4.2 [39].

AutoDockTools v 1.5.6 [39, 40] was used to prepare the input docking files and pdbqt files, which include the atomic coordinates (PDB), partial charges (Q) and atom types (T) in one file. We initially added all the hydrogens to both molecules. Following the AutoDock standard docking procedure, all nonpolar hydrogen atoms and their charges were then automatically merged with their parent carbon atom. Atomic charges were calculated using the Gasteiger-Marsili method [76].

The flexibility of all natural potential inhibitors has been taken into account by setting up torsion angles around the rotatable bonds, automatically detected by the AutoDock ligand input procedure. All atoms of both h $\gamma$ D-crystallin proteins were kept rigid. Prior to the actual docking run, AutoGrid was used to precalculate grid maps of the interaction energies of various atom types. The grid size was set to 126 $\times$ 126 $\times$ 126 points with 0.475 Å grid point spacing, and the cubic search box was centered on the h $\gamma$ D-crystallin protein and surrounding it.

The Lamarckian genetic algorithm [77, 78], which iteratively generates and optimizes a population of ligand conformations, was used to search for the best conformers, the global search space being mainly sampled. The default parameters, automatically set up by AutoDockTools, which are also mentioned in detail in our previous contributions [79-81], were used: the initial population of random individuals had a population size of 150 individuals, the maximum number of energy evaluations per run was 2,500,000, maximum

number of generations was 27,000, with a rate of gene mutation of 0.02, a crossover rate of 0.8 and the cluster tolerance was 2 Å. To obtain good statistics and clustering, 2000 runs were performed, each starting with a different random generation seed. Visualization and analysis of the docking results were performed using Biovia Discovery Studio Visualizer v20.1 and Chimera v1.14 [82].

## ACKNOWLEDGMENTS

This work was supported by the Romanian Ministry of Research, Innovation and Digitization (MCID), CNCS/CCCDI-UEFISCDI, Grant number PN-III-P4-PCE-2021-0316 and by the MCID through the “Nucleu” Program within the National Plan for Research, Development and Innovation 2022–2027, Project PN 23 24 01 05, and through the Installations and Special Objectives of National Interest (IOSIN), IZOSTAB. The computing resources used were provided by the High-Performance Computing Data Center of INCDTIM, Cluj-Napoca.

The authors declare that they have no conflicts of interest.

Supplementary material: Supplementary file and molecular docking simulations were uploaded on the Zenodo website and are available at the link <https://zenodo.org/records/13691397> (DOI: 10.5281/zenodo.13691397)

## REFERENCES

1. G.J. Wistow, J. Piatigorsky, *Annu. Rev. Biochem.*, **1988**, *57*, 479-504.
2. H. Bloemendal, W. de Jong, R. Jaenicke, N.H. Lubsen, C. Slingsby, A. Tardieu, *Progress in Biophysics and Molecular Biology*, **2004**, *86*(3), 407-485.
3. W.W. Dejong, J.A.M. Leunissen, C.E.M. Voorter, *Mol. Biol. Evol.*, **1993**, *10*(1), 103-126.
4. J. Horwitz, *Exp. Eye Res.*, **2009**, *88*(2), 190-194.
5. J. Horwitz, M.P. Bova, L.L. Ding, D.A. Haley, P.L. Stewart, *Eye*, **1999**, *13*, 403-408.
6. S. Islam, M.T. Do, B.S. Frank, G.L. Hom, S. Wheeler, H. Fujioka, B. Wang, G. Minocha, D.R. Sell, X. Fan, K.J. Lampi, V.M. Monnier, *J. Biol. Chem.*, **2022**, *298*(10), 102417.
7. S. Bassnett, Y.R. Shi, G.F.J.M. Vrensen, *Philos. Tans. Roy. Soc. B*, **2011**, *366*(1568), 1250-1264.
8. N.H. Lubsen, H.J.M. Aarts, J.G.G. Schoenmakers, *Prog. Biophys. Mol. Bio.*, **1988**, *51*(1), 47-76.



9. G. Wistow, *Molecular Biology and Evolution of Crystallins: Gene Recruitment and Multifunctional Proteins in the Eye Lens*, Springer, R.G. Landes Co., Austin, TX., **1995**.
10. M.E. Ray, G. Wistow, Y.A. Su, P.S. Meltzer, J.M. Trent, *Prog. Nat. Acad. Sci. USA*, **1997**, *94*(7), 3229-3234.
11. A. Laganowsky, J.L.P. Benesch, M. Landau, L.L. Ding, M.R. Sawaya, D. Cascio, Q.L. Huang, C.V. Robinson, J. Horwitz, D. Eisenberg, *Protein Sci.*, **2010**, *19*(5), 1031-1043.
12. C. Slingsby, G.J. Wistow, A.R. Clark, *Protein Sci.*, **2013**, *22*(4), 367-380.
13. J.I. Clark, J.M. Clark, *Int. Rev. Cytology*, **1999**, *192*, 171-187.
14. Z. Kyselova, M. Stefek, V. Bauer, *J. Diabetes Complicat.*, **2004**, *18*(2), 129-140.
15. J. Konopinska, M. Mlynarczyk, D.A. Dmuchowska, I. Obuchowska, *J. Clin. Med.*, **2021**, *10*(13), 2847.
16. X.J. Fan, V.M. Monnier, J. Whitson, *Exp. Eye Res.*, **2017**, *156*, 103-111.
17. A.M. Wood, R.J.W. Truscott, *Exp. Eye Res.*, **1993**, *56*(3), 317-325.
18. V.P.R. Vendra, I. Khan, S. Chandani, A. Muniyandi, D. Balasubramanian, *Biochim. Biophys. Acta - Gen. Subjects*, **2016**, *1860*(1), 333-343.
19. M.S. Kosinski-Collins, S.L. Flaugh, J. King, *Protein Sci*, **2004**, *13*(8), 2223-2235.
20. J. Chen, P.R. Callis, J. King, *Biochemistry*, **2009**, *48*(17), 3708-3716.
21. J.C. Boatz, M.J. Whitley, M. Li, A.M. Gronenborn, P.C.A. van der Wel, *Nature Commun.*, **2017**, *8*(1), 15137.
22. P. Evans, K. Wyatt, G.J. Wistow, O.A. Bateman, B.A. Wallace, C. Slingsby, *J. Mol. Biol.*, **2004**, *343*(2), 435-444.
23. A. Basak, O. Bateman, C. Slingsby, A. Pande, N. Asherie, O. Ogun, G.B. Benedek, J. Pande, *J. Mol. Biol.*, **2003**, *328*(5), 1137-1147.
24. A. Pande, O. Annunziata, N. Asherie, O. Ogun, G.B. Benedek, J. Pande, *Biochemistry*, **2005**, *44*(7), 2491-2500.
25. M. Plazanet, C. Floare, M.R. Johnson, R. Schweins, H.P. Trommsdorff, *J. Chem. Phys.*, **2004**, *121*(11), 5031-5034.
26. B.J. Bender, S. Gahbauer, A. Lutten, J.K. Lyu, C.M. Webb, R.M. Stein, E.A. Fink, T.E. Balius, J. Carlsson, J.J. Irwin, B.K. Shoichet, *Nat. Protoc.*, **2021**, *16*(10), 4799-4832.
27. S. Aci-Sèche, S. Bourg, P. Bonnet, J. Rebehmed, A.G. de Brevern, J. Diharce, *Data Brief*, **2023**, *49*, 109386.
28. M.W. Huff, D.E. Telford, *Trends in Pharmacological Sciences*, **2005**, *26*(7), 335-340.
29. L. Zhao, X.-J. Chen, J. Zhu, Y.-B. Xi, X. Yang, L.-D. Hu, H. Ouyang, S.H. Patel, X. Jin, D. Lin, F. Wu, K. Flagg, H. Cai, G. Li, G. Cao, Y. Lin, D. Chen, C. Wen, C. Chung, Y. Wang, A. Qiu, E. Yeh, W. Wang, X. Hu, S. Grob, R. Abagyan, Z. Su, H.C. Tjondro, X.-J. Zhao, H. Luo, R. Hou, J. Jefferson, P. Perry, W. Gao, I. Kozak, D. Granet, Y. Li, X. Sun, J. Wang, L. Zhang, Y. Liu, Y.-B. Yan, K. Zhang, *Nature*, **2015**, *523*(7562), 607-611.
30. X. Shen, M. Zhu, L. Kang, Y. Tu, L. Li, R. Zhang, B. Qin, M. Yang, H. Guan, *J. Ophthalmol.*, **2018**, *2018*, 1-9.

31. K. Wang, M. Hoshino, K. Uesugi, N. Yagi, B.K. Pierscionek, U.P. Andley, *Investigative Ophthalmol. & Visual Sci.*, **2022**, 63(5), 15.
32. D.M. Daszynski, P. Santhoshkumar, A.S. Phadte, K.K. Sharma, H.A. Zhong, M.F. Lou, P.F. Kador, *Sci. Rep.*, **2019**, 9(1).
33. *Heliostatix Biotechnology*, **2023**. <https://Heliostatix.org>. (accessed 1st November 2023 2023).
34. J. Irwin, *Abstr. of Papers of Am. Chem. Soc.*, **2017**, 253.
35. J.J. Irwin, K.G. Tang, J. Young, C. Dandarchuluun, B.R. Wong, M. Khurelbaatar, Y.S. Moroz, J. Mayfield, R.A. Sayle, *J. Chem. Inf. Model.*, **2020**, 60(12), 6065-6073.
36. M. J. Frisch, G. W. Trucks, H. B. Schlegel, G. E. Scuseria, M. A. Robb, J. R. Cheeseman, G. Scalmani, V. Barone, G. A. Petersson, H. Nakatsuji, X. Li, M. Caricato, A. V. Marenich, J. Bloino, B. G. Janesko, R. Gomperts, B. Mennucci, H. P. Hratchian, J. V. Ortiz, A. F. Izmaylov, J. L. Sonnenberg, D. Williams-Young, F. Ding, F. Lipparini, F. Egidi, J. Goings, B. Peng, A. Petrone, T. Henderson, D. Ranasinghe, V. G. Zakrzewski, J. Gao, N. Rega, G. Zheng, W. Liang, M. Hada, M. Ehara, K. Toyota, R. Fukuda, J. Hasegawa, M. Ishida, T. Nakajima, Y. Honda, O. Kitao, H. Nakai, T. Vreven, K. Throssell, J. J. A. Montgomery, J. E. Peralta, F. Ogliaro, M. J. Bearpark, J. J. Heyd, E. N. Brothers, K. N. Kudin, V. N. Staroverov, T. A. Keith, R. Kobayashi, J. Normand, K. Raghavachari, A. P. Rendell, J. C. Burant, S. S. Iyengar, J. Tomasi, M. Cossi, J. M. Millam, M. Klene, C. Adamo, R. Cammi, W. Ochterski, R. L. Martin, K. Morokuma, O. Farkas, J. B. Foresman, D.J. Fox, *Gaussian 16, Revision C.02*, Gaussian Inc., Wallingford CT: **2016**.
37. A. Basak, O. Bateman, C. Slingsby, A. Pande, N. Asherie, O. Ogun, G.B. Benedek, J. Pande, *J. Mol. Biol.*, **2003**, 328(5), 1137-1147.
38. J. Jung, I.-J.L. Byeon, Y. Wang, J. King, A.M. Gronenborn, *Biochemistry*, **2009**, 48(12), 2597-2609.
39. G.M. Morris, R. Huey, W. Lindstrom, M.F. Sanner, R.K. Belew, D.S. Goodsell, A.J. Olson, *J. Comput. Chem.*, **2009**, 30(16), 2785-2791.
40. O. Trott, A.J. Olson, *J. Comput. Chem.*, **2009**, 31(2), 455–461.
41. H.S. Kang, Z.X. Yang, R.H. Zhou, *J. Am. Chem. Soc.*, **2018**, 140(27), 8479-8486.
42. F. Olawale, O. Iwaloye, I.M. Folorunso, S. Shityakov, *J. Comput. Biophys. and Chem.*, **2022**, 22(01), 11-30.
43. D. Tewari, O. Samoila, D. Gocan, A. Mocan, C. Moldovan, H.P. Devkota, A.G. Atanasov, G. Zengin, J. Echeverria, D. Vodnar, B. Szabo, G. Crisan, *Front. in Pharmacology*, **2019**, 10.
44. I. Sher-Rosenthal, E. Bubis, Z. Goldberg, M. Samara, A. Elmann, Y. Rotenstreich, *Invest. Ophth. Vis. Sci.*, **2021**, 62(8).
45. A.K. Ghosh, R. Thapa, H.N. Hariani, M. Volyanyuk, S.D. Ogle, K.A. Orloff, S. Ankireddy, K.R. Lai, A. Ziniauskaite, E.B. Stubbs, G. Kalesnykas, J.J. Hakkarainen, K.A. Langert, S. Kaja, *Pharmaceutics*, **2021**, 13(9).
46. S. Davinelli, S. Ali, G. Scapagnini, C. Costagliola, *Front. Nutr.*, **2021**, 8.
47. H. Matsuda, T. Wang, H. Managi, M. Yoshikawa, *Bioorgan. Med. Chem.*, **2003**, 11(24), 5317-5323.

48. H. Matsuda, T. Morikawa, I. Toguchida, M. Yoshikawa, *Chem. Pharm. Bull.*, **2002**, 50(6), 788-795.
49. B.S. Patil, G.K. Jayaprakasha, K.N.C. Murthy, A. Vikram, *J. Agr. Food. Chem.*, **2009**, 57(18), 8142-8160.
50. S. Majumdar, R. Srirangam, *J. Pharm. Pharmacol.*, **2010**, 62(8), 951-965.
51. W. Kalt, A. Hanneken, P. Milbury, F. Tremblay, *J. Agr. Food Chem.*, **2010**, 58(7), 4001-4007.
52. M. Stefek, *Interdiscipl. Toxicol.*, **2011**, 4(2), 69-77.
53. J.K. Song, D.D. Guo, H.S. Bi, *Int. J. Mol. Med.*, **2018**, 41(2), 765-772.
54. B.P. Mohanty, T. Mitra, S. Ganguly, S. Das Sarkar, A. Mahanty, *Biol. Trace Elem. Res.*, **2021**, 199(9), 3354-3359.
55. J.I. Choi, J. Kim, S.Y. Choung, *Mol. Vis.*, **2019**, 25, 118-128.
56. J. Cao, T. Wang, M. Wang, *BMC Ophthalmol.*, **2018**, 18, 48.
57. X.F. Liu, J.L. Hao, T. Xie, N.J. Mukhtar, W. Zhang, T.H. Malik, C.W. Lu, D.D. Zhou, *Front. in Pharmacol.*, **2017**, 8, 66.
58. J.H. Liao, Y.S. Huang, Y.C. Lin, F.Y. Huang, S.H. Wu, T.H. Wu, *J. Agr. Food Chem.*, **2016**, 64(10), 2080-2086.
59. C.G. Wang, L. Xu, F. Cheng, H.Q. Wang, L.Y. Jia, *RSC Adv.*, **2015**, 5(38), 30197-30205.
60. C.N. Grama, P. Suryanarayana, M.A. Patil, G. Raghu, N. Balakrishna, M.N.V.R. Kumar, G.B. Reddy, *Plos One*, **2013**, 8(10), 78217.
61. J.W.R. Wu, C.Y. Kao, L.T.W. Lin, W.S. Wen, J.T. Lai, S.S.S. Wang, *Biochem. Eng. J.*, **2013**, 78, 189-197.
62. A. Dawn, V. Goswami, S. Sapra, S. Deep, *Langmuir*, **2023**, 39(3), 1330-1344.
63. H. Nagashima, N. Sasaki, S. Amano, S. Nakamura, M. Hayano, K. Tsubota, *Sci. Rep.*, **2021**, 11(1), 2174.
64. B. Neha, R. Jannavi, P. Sukumaran, *J. Pharm. Res. Int.*, **2021**, 33(29a), 17-32.
65. J. Jeevanandam, R. Madhumitha, N.T. Saraswathi, *J. Mol. Struct.*, **2021**, 1226, 129428.
66. M. Sakthivel, P. Geraldine, P.A. Thomas, *Graef Arch. Clin. Exp. Ophthalmol.*, **2011**, 249(8), 1201-1210.
67. M.L. Broide, C.R. Berland, J. Pande, O.O. Ogun, G.B. Benedek, *Proc. Natl. Acad. Sci. USA*, **1991**, 88(13), 5660-5664.
68. E. Matei, A. Zheng, W. Furey, J. Rose, C. Aiken, A.M. Gronenborn, *J. Biol. Chem.*, **2010**, 285(17), 13057-13065.
69. P.A. Ravindranath, S. Forli, D.S. Goodsell, A.J. Olson, M.F. Sanner, *Plos Comput. Biol.*, **2015**, 11(12), e1004586.
70. S. Forli, A.J. Olson, *J. Med. Chem.*, **2012**, 55(2), 623-638.
71. L. El Khoury, D. Santos-Martins, S. Sasmal, J. Eberhardt, G. Bianco, F.A. Ambrosio, L. Solis-Vasquez, A. Koch, S. Forli, D.L. Mobley, *J. Comput. Aid. Mol. Des.*, **2019**, 33(12), 1011-1020.
72. X.B. He, S.H. Liu, T.S. Lee, B.H. Ji, V.H. Man, D.M. York, J.M. Wang, *ACS Omega*, **2020**, 5(9), 4611-4619.
73. D. Santos-Martins, L. Solis-Vasquez, A.F. Tillack, M.F. Sanner, A. Koch, S. Forli, *J. Chem. Theor. Comput.*, **2021**, 17(2), 1060-1073.

AN EXPLORATION OF HUMAN  $\gamma$ D-CRYSTALLIN AFFINITY FOR POTENTIAL AGGREGATION  
INHIBITORS: A MOLECULAR DOCKING INVESTIGATION

74. S. Brudar, B. Hribar-Lee, *J. Mol. Liq.*, **2023**, 386, 122461.
75. P. Das, J.A. King, R.H. Zhou, *Proc. Natl. Acad. Sci. USA*, **2011**, 108(26), 10514-10519.
76. J. Gasteiger, M. Marsili, *Tetrahedron*, **1980**, 36(22), 3219-3228.
77. G.M. Morris, D.S. Goodsell, R.S. Halliday, R. Huey, W.E. Hart, R.K. Belew, A.J. Olson, *J. Comput. Chem.*, **1998**, 19(14), 1639-1662.
78. J. Fuhrmann, A. Rurainski, H.P. Lenhof, D. Neumann, *J. Comput. Chem.*, **2010**, 31(9), 1911-1918.
79. C.G. Floare, M. Bogdan, M. Tomoaia-Cotisel, A. Mocanu, *J. Mol. Struct.*, **2022**, 1248, 131477.
80. M. Mic, A. Pîrnau, C.G. Floare, M. Bogdan, *Int. J. Biol. Macromol.*, **2020**, 147, 326-332.
81. M. Mic, A. Pîrnau, C.G. Floare, G. Marc, A.H. Franchini, O. Oniga, L. Vlase, M. Bogdan, *J. Mol. Struct.*, **2021**, 1244, 131278.
82. E.F. Pettersen, T.D. Goddard, C.C. Huang, G.S. Couch, D.M. Greenblatt, E.C. Meng, T.E. Ferrin, *J. Comput. Chem.*, **2004**, 25(13), 1605-1612.



## ESSENTIAL OIL FROM *KNEMA ELEGANS* WARB.: CHEMICAL COMPOSITION, ANTIOXIDANT AND ANTI-ACETYLCHOLINESTERASE ACTIVITIES

Dau B. THIN<sup>a\*</sup>, Truong T. V. HOA<sup>b</sup>, Bui B. THINH<sup>c\*</sup>

**ABSTRACT.** *Knema elegans* Warb. is an evergreen tree belonging to the Myristicaceae family, primarily native to Southeast Asia. This study examined the chemical composition and assessed the antioxidant and anti-acetylcholinesterase properties of the essential oil from the leaves of *K. elegans* in Vietnam. Gas chromatography/mass spectrometry analysis revealed the main compounds in the essential oil, including bicyclogermacrene (23.8%), germacrene D (17.1%),  $\beta$ -caryophyllene (15.4%),  $\delta$ -cadinene (8.2%), and  $\alpha$ -cadinol (7.9%). Antioxidant activity was assessed using 2,2-diphenyl-1-picrylhydrazyl (DPPH) and 2,2'-azino-bis(3-ethylbenzothiazoline-6-sulfonic acid) (ABTS) methods, with half-maximum inhibitory concentration (IC<sub>50</sub>) values of  $93.11 \pm 1.95 \mu\text{g/mL}$  and  $114.95 \pm 2.41 \mu\text{g/mL}$ , respectively, indicating moderate antioxidant potential. Additionally, the essential oil exhibited significant anti-acetylcholinesterase effects, with an IC<sub>50</sub> value of  $87.44 \pm 2.52 \mu\text{g/mL}$ . These findings highlight the biological significance of *K. elegans* essential oil and suggest avenues for further investigation, particularly in elucidating its mechanisms of action in antioxidant and anti-acetylcholinesterase activities. Notably, this research represents the first comprehensive exploration of the chemical composition, antioxidant activity, and acetylcholinesterase inhibition effects of *K. elegans* essential oil from its leaves.

**Keywords:** *Knema elegans*, sesquiterpenes, Myristicaceae, DPPH, ABTS, AChE

<sup>a</sup> Hong Duc University, 565 Quang Trung Str, Thanh Hoa, 40130, Vietnam.

<sup>b</sup> VNU University of Science, Vietnam National University - Hanoi, Hanoi, 11400, Vietnam.

<sup>c</sup> Biotechnology Center of Ho Chi Minh City, Ho Chi Minh City, 70000, Vietnam.

\* Corresponding authors: daubathin@hdu.edu.vn; buibaothinh9595@gmail.com



## INTRODUCTION

Myristicaceae is a prominent family of flowering plants, commonly known as the nutmeg family, comprising approximately 20 genera and over 500 species [1]. These plants are primarily distributed in tropical regions around the world, with a significant presence in Africa, Asia, Pacific islands, and the Americas [2]. Among the genera within Myristicaceae, *Knema* stands out as a significant representative. This genus comprises approximately 60 species of small-medium trees distributed primarily in tropical regions of Asia, Africa, and Australia [3, 4]. Across various cultures in its native range, *Knema* species have been utilized for their medicinal properties, serving as essential components in traditional herbal remedies [5]. The plants are often harvested for their bark, leaves, fruits, and even roots, which contain bioactive compounds believed to have therapeutic effects such as alleviating fevers, digestive issues, and respiratory problems [4, 5]. Furthermore, scientific research has begun to explore the biological activities and potential therapeutic applications of *Knema* compounds. Studies have identified bioactive constituents such as phenolic lipids, flavonoids, and lignans in *Knema* extracts, exhibiting a range of pharmacological properties including antioxidative, antidiabetic, antimicrobial, anti-inflammatory, antimalarial, neuroprotective, and hepatoprotective activities [3-5]. These findings suggest the promising potential of *Knema* plants in modern pharmacology and drug discovery.

Essential oils, derived from various plants, have garnered significant attention due to their diverse therapeutic properties, including antioxidant and anti-acetylcholinesterase (anti-AChE) activities [6-8]. Antioxidants play a crucial role in neutralizing harmful free radicals, thus protecting cells from oxidative stress and reducing the risk of chronic diseases such as cancer, cardiovascular disorders, and neurodegenerative conditions [7]. Furthermore, anti-AChE activity is vital in the context of cognitive health, as it inhibits the breakdown of acetylcholine, a neurotransmitter essential for memory and cognitive function [9]. With the increasing interest in natural remedies and the demand for effective therapeutic agents, there is a burgeoning curiosity in exploring the potential applications of essential oils. These oils not only hold promising therapeutic potential but also offer sustainable alternatives to synthetic pharmaceuticals with fewer adverse effects [8]. Therefore, comprehending the biological activity of essential oils becomes paramount, propelling the quest for oils with heightened efficacy across various therapeutic applications.

*Knema elegans* Warb. is a flowering plant species belonging to the Myristicaceae family, originating from tropical regions of Southeast Asia [10]. To date, ethnobotanical information regarding *K. elegans* is somewhat

limited. However, several studies have demonstrated the presence of flavane derivatives and flavonoids in extracts of *K. elegans*, exhibiting antioxidant activity,  $\alpha$ -glycosidase inhibition, DNA polymerase  $\beta$  inhibition, and DNA damage [11-13]. Furthermore, researchers have explored the chemical composition and biological activities of essential oils from various *Knema* species. Specifically, essential oils from *K. hookeriana* [14], *K. kunstleri* [15], *K. intermedia* [16], *K. malayana* [17], *K. angustifolia* [18], *K. pierrei* [19], and *K. globularia* [20], along with their antioxidant [15, 19, 20], antimicrobial [19], anti-AchE [14], anti-tyrosinase [16, 17], and lipoxygenase inhibition [15] activities, were evaluated. Despite the increasing interest in *Knema* plants, comprehensive information regarding the chemical composition and biological activities of *K. elegans* essential oil is still lacking. Motivated by this gap in knowledge, our study focuses on the chemical composition and evaluation of antioxidant and AChE inhibitory activities of essential oil extracted from *K. elegans* leaves collected in Vietnam. By conducting thorough analyses, we aim to contribute to a deeper understanding of the medicinal and pharmacological properties of *K. elegans*, shedding light on its potential applications in healthcare and beyond.

## RESULTS AND DISCUSSION

### Chemical composition of essential oil

The leaves of *K. elegans* were hydrodistilled to successfully obtain pure essential oil with a yield of 0.11% (v/w). *K. elegans* essential oil revealed a chemical composition with 30 constituents identified, rich in sesquiterpene hydrocarbons (77.8%) and oxygenated sesquiterpenes (16.3%) by GC/MS analyses. As presented in Table 1, bicyclogermacrene (23.8%), germacrene D (17.1%),  $\beta$ -caryophyllene (15.4%),  $\delta$ -cadinene (8.2%), and  $\alpha$ -cadinol (7.9%) were the major compounds of *K. elegans* essential oil. The structures of these major compounds are illustrated in Fig. 1. In addition, considerable amounts of  $\alpha$ -humulene (4.2%), germacrene B (3.4%), caryophyllene oxide (2.6%), epi- $\alpha$ -cadinol (1.7%), and  $\gamma$ -muurolene (1.3%) were detected.

This research marks the initial exploration into the chemical composition of essential oil derived from *K. elegans*, thereby precluding direct comparisons with analogous samples from the same species. However, an extensive examination of essential oils from other *Knema* species, including *K. hookeriana* [14], *K. kunstleri* [15], *K. intermedia* [16], *K. malayana* [17], *K. angustifolia* [18], *K. pierrei* [19], and *K. globularia* [20], has been documented.

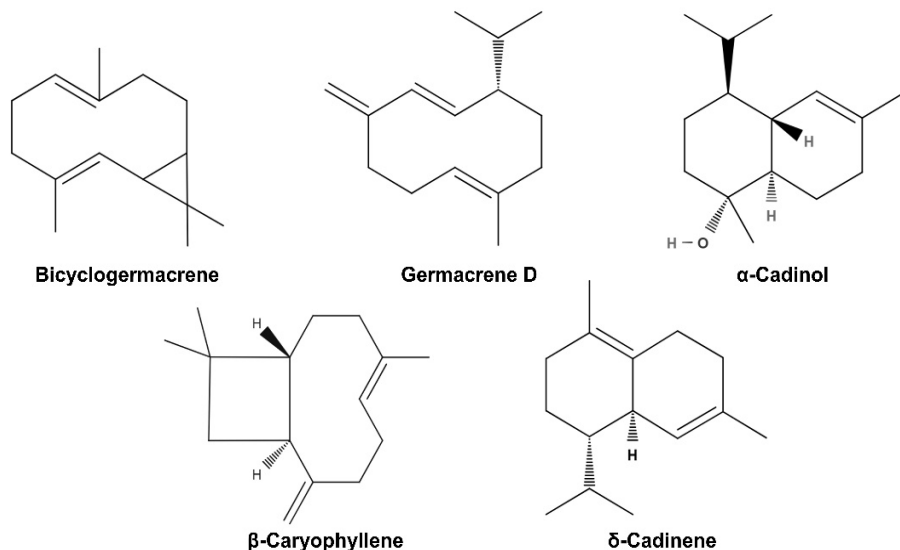


**Table 1.** Chemical compositions of *Knema elegans* essential oil

No.	Compound <sup>a</sup>	RT <sup>b</sup>	RI <sup>c</sup>	RI <sup>d</sup>	Area (%)
1	$\delta$ -Elemene	23.56	1338	1335	0.5
2	$\alpha$ -Copaene	24.94	1377	1374	0.2
3	$\beta$ -Cubebene	25.50	1386	1387	0.7
4	$\beta$ -Elemene	25.98	1393	1389	0.1
5	$\beta$ -Caryophyllene	26.54	1421	1417	15.4
6	$\gamma$ -Elemene	26.97	1435	1434	0.2
7	Aromadendrene	27.08	1440	1439	0.1
8	$\alpha$ -Humulene	27.55	1455	1452	4.2
9	9- <i>epi</i> -( <i>E</i> )-Caryophyllene	27.78	1465	1464	0.6
10	$\gamma$ -Muurolene	28.17	1476	1478	1.3
11	Germacrene D	28.43	1480	1484	17.1
12	$\beta$ -Selinene	28.59	1488	1489	0.8
13	Bicyclogermacrene	28.85	1498	1500	23.8
14	( <i>E,E</i> )- $\alpha$ -Farnesene	28.89	1504	1505	0.2
15	$\beta$ -Bisabolene	28.98	1506	1505	0.1
16	$\gamma$ -Cadinene	29.34	1514	1513	0.9
17	$\delta$ -Cadinene	29.55	1525	1522	8.2
18	Germacrene B	30.75	1559	1559	3.4
19	Spathulenol	31.36	1579	1577	0.6
20	Caryophyllene oxide	31.57	1583	1582	2.6
21	Globulol	31.62	1587	1590	0.5
22	Viridiflorol	31.67	1594	1592	0.7
23	Guaiol	31.83	1600	1600	0.9
24	Ledol	32.25	1605	1602	0.2
25	Humulene epoxide II	32.31	1612	1608	0.3
26	<i>epi</i> - $\alpha$ -Cadinol	33.11	1639	1638	1.7
27	<i>epi</i> - $\alpha$ -Muurolol	33.15	1645	1640	0.6
28	$\beta$ -Eudesmol	33.47	1650	1649	0.1
29	$\alpha$ -Cadinol	33.53	1659	1652	7.9
30	Intermedeol	34.31	1667	1665	0.2
	Sesquiterpene hydrocarbons (No. 1-18)				77.8
	Oxygenated sesquiterpenes (No. 19-30)				16.3
	Total % of compounds identified				94.1

<sup>a</sup>Elution order on Equity-5 column; <sup>b</sup>Retention time (min); <sup>c</sup>Retention indices on Equity-5 column; <sup>d</sup>Literature retention indices.

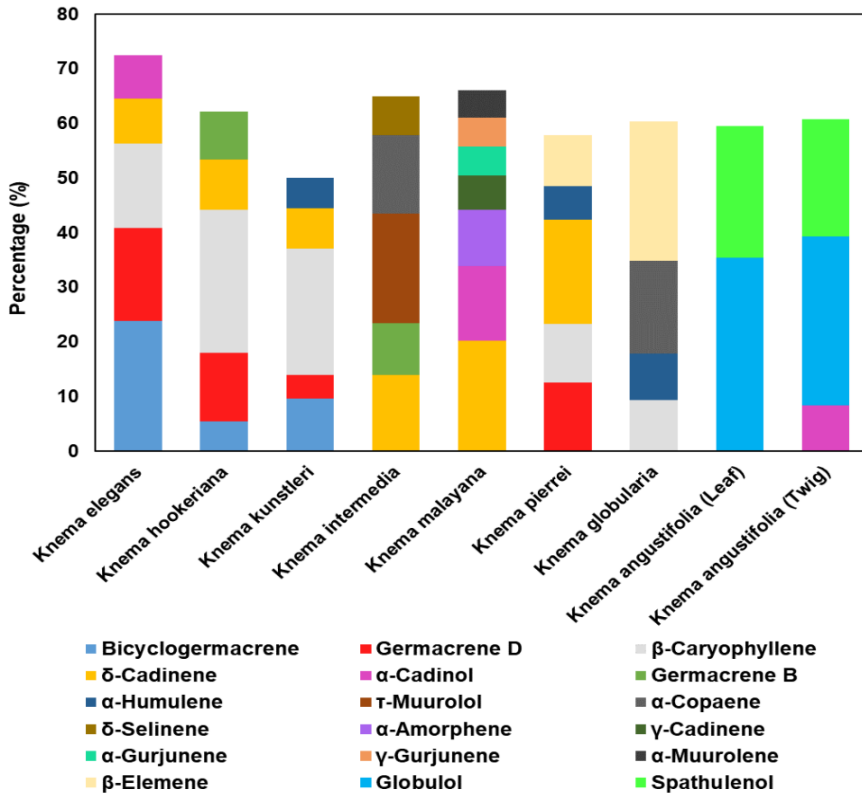
ESSENTIAL OIL FROM *KNEMA ELEGANS* WARB.: CHEMICAL COMPOSITION,  
ANTIOXIDANT AND ANTI-ACETYLCHOLINESTERASE ACTIVITIES



**Figure 1.** Chemical structures of main compounds in the essential oil of *Knema elegans*.

Previous studies have identified distinctive volatile compounds within these species, shedding light on the unique aromatic profiles of each. The major components of *K. elegans* essential oil compared with other *Knema* species are presented in Fig. 2. For instance, the essential oil from *K. hookeriana* displayed a predominant presence of  $\beta$ -caryophyllene (26.2%), germacrene D (12.5%),  $\delta$ -cadinene (9.2%), germacrene B (8.8%), and bicyclogermacrene (5.5%) [14]. On the other hand, *K. kunstleri* essential oil exhibited  $\beta$ -caryophyllene (23.2%), bicyclogermacrene (9.6%),  $\delta$ -cadinene (7.3%),  $\alpha$ -humulene (5.7%), and germacrene D (4.3%) as major constituents [15]. Notably,  $\beta$ -elemene (25.48%) emerged as an abundant compound in *K. globularia* essential oil [20]. Further distinctions were observed in the major compounds of *K. malayana* and *K. pierrei* essential oils, where  $\delta$ -cadinene (20.2% and 19.04%) took precedence [17, 19]. A significant amount of globulol was found in essential oils from the leaves (35.46%) and twigs (30.83%) of *K. angustifolia* [18], while  $\tau$ -muurolol (20.1%) was demonstrated to be the major compound in *K. intermedia* essential oil [16]. Despite acknowledging sesquiterpene compounds as predominant in *Knema* genus essential oils from Vietnam and other regions globally, our findings reveal distinct differences in the main compounds present in *K. elegans* essential oil compared to other *Knema* species. The observed variations in essential oil chemical compositions may stem from factors such as plant age, climatic and environmental

conditions, selection of plant organs, and harvest timing [21, 22]. These factors potentially influence plant biosynthesis pathways, leading to diverse chemical compositions and content, thereby contributing to the development of distinct chemotypes [23].



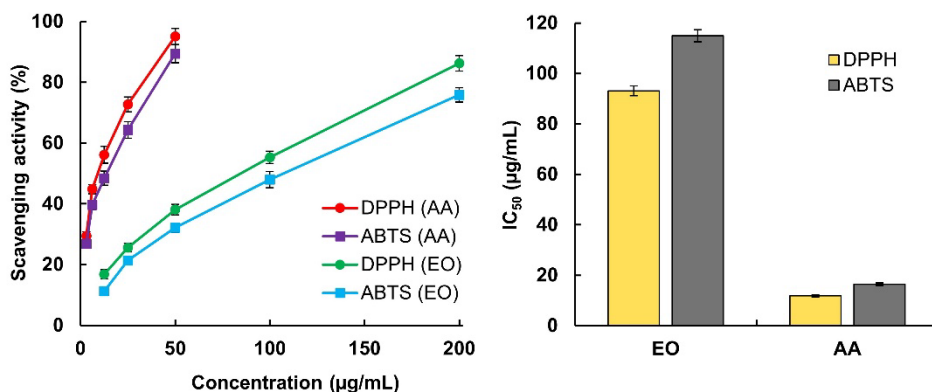
**Figure 2.** Comparison of major components in essential oils from different *Knema* species.

### Antioxidant activity of essential oil

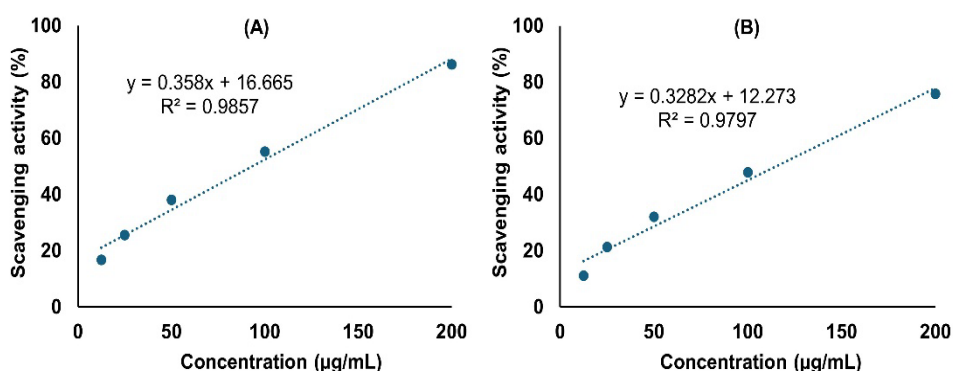
The essential oil of *K. elegans* showed moderate antioxidant activity based on both DPPH and ABTS methods compared to the ascorbic acid as a standard synthetic antioxidant (Fig. 3). The scavenging activity increased with the increment of essential oil concentration. At a concentration of 50  $\mu\text{g/mL}$  of *K. elegans* essential oil, the DPPH and ABTS colors were reduced by  $38.09\% \pm 1.74$  and  $32.14\% \pm 1.52$ , respectively, while ascorbic acid

ESSENTIAL OIL FROM *KNEMA ELEGANS* WARB.: CHEMICAL COMPOSITION,  
ANTIOXIDANT AND ANTI-ACETYLCHOLINESTERASE ACTIVITIES

showed a reduction of  $95.05\% \pm 2.62$  and  $89.37\% \pm 2.95$ , respectively, at the same concentration. To calculate  $IC_{50}$ , standard curves of antioxidant activity in DPPH and ABTS assays were constructed (Fig. 4). According to the  $IC_{50}$  data, the *K. elegans* essential oil revealed  $IC_{50}$  values of  $93.11 \pm 1.95 \mu\text{g/mL}$  and  $114.95 \pm 2.41 \mu\text{g/mL}$  for DPPH and ABTS, respectively. The standard antioxidant, ascorbic acid, showed  $IC_{50}$  values of  $11.86 \pm 0.45 \mu\text{g/mL}$  and  $16.40 \pm 0.51 \mu\text{g/mL}$ , regarding DPPH and ABTS, respectively.



**Figure 3.** Antioxidant activity at different concentrations and half-maximum inhibitory concentration ( $IC_{50}$ ) of *Knema elegans* essential oil (EO) and ascorbic acid (AA) based on the scavenging of DPPH and ABTS. Values are means ( $n = 3$ )  $\pm$  standard deviation.



**Figure 4.** Standard curves of antioxidant activity in DPPH (A) and ABTS (B) assays for *Knema elegans* essential oil.

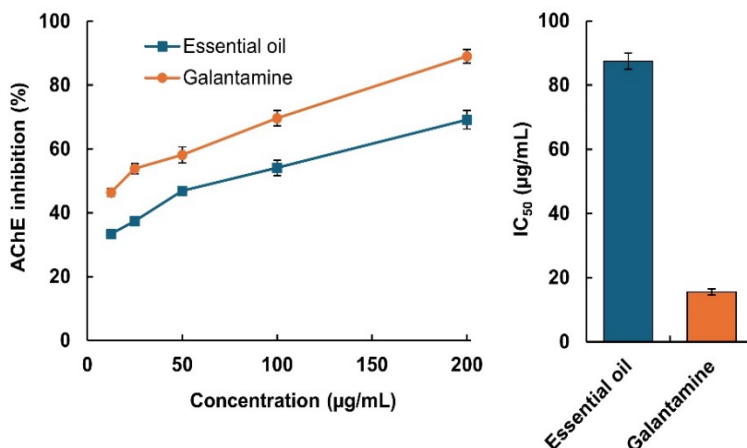
There are no reports in the literature regarding the antioxidant capacity of *K. elegans* essential oil. However, there are reports of this activity for essential oils obtained from other species of the genus *Knema*. For instance, the essential oil of *K. kunstleri*, composed mainly of  $\beta$ -caryophyllene (23.2%), bicyclogermacrene (9.6%),  $\delta$ -cadinene (7.3%),  $\alpha$ -humulene (5.7%), and germacrene D (4.3%), which presented potential antioxidant activity by the DPPH method, with an  $IC_{50}$  value of 80.5  $\mu\text{g/mL}$  [15]. Similarly, the essential oil from the leaves of *K. pierreii*, mainly consisting of  $\delta$ -cadinene (19.04%), germacrene D (12.57%),  $\beta$ -caryophyllene (10.74%),  $\beta$ -elemene (9.32%), and  $\alpha$ -humulene (6.18%), showed antioxidant activity with  $IC_{50}$  values of 152.17  $\mu\text{g/mL}$  by the DPPH method and 173.62  $\mu\text{mol Trolox/g}$  by the FRAP method [19]. In another study by Thinh et al. [20], the essential oil of *K. globularia*, characterized by major compounds like  $\beta$ -elemene (25.48%),  $\alpha$ -copaene (17.05%),  $\beta$ -caryophyllene (9.37%), and  $\alpha$ -humulene (8.42%), exhibited antioxidant activity with  $IC_{50}$  values of 198.13  $\mu\text{g/mL}$  by the DPPH method and 143.61  $\mu\text{g/mL}$  by the ABTS method. It can be seen that *K. elegans* essential oil in this study demonstrated stronger antioxidant activity than *K. globularia* and *K. pierreii* essential oils. However, *K. elegans* essential oil showed weaker antioxidant activity than *K. kunstleri* essential oil. These variations can be attributed to differences in the content and presence of compounds in essential oils, as demonstrated earlier [24, 25].

The remarkable antioxidant activity exhibited by *K. elegans* essential oil can be attributed to its key sesquiterpene components, notably bicyclogermacrene, germacrene D,  $\beta$ -caryophyllene, and  $\delta$ -cadinene. This assertion was supported by various studies focusing on essential oils from different plant sources [26, 27]. For instance, an investigation involved *Marrubium peregrinum* essential oil sourced from three distinct locations in Serbia and revealed robust antioxidant capabilities, with the primary constituents  $\beta$ -caryophyllene, bicyclogermacrene, and germacrene D demonstrating potent activity in neutralizing DPPH $\cdot$ , NO $\cdot$ , and O $_2\cdot^-$  radicals, as evidenced by  $IC_{50}$  values that ranged from 8.81 to 16.41  $\mu\text{g/mL}$  [28]. Similarly, the essential oil derived from the female leaf sample of *Baccharis punctulata*, featuring bicyclogermacrene, germacrene D, and  $\beta$ -caryophyllene as predominant components, exhibited noteworthy antioxidant efficacy, reaching 0.328 mg AAE/g in the DPPH test [29]. In another study, *Kundmannia sicula* essential oil, enriched in the sesquiterpene hydrocarbon germacrene D, showcased commendable ABTS free radical scavenging activity, with an  $IC_{50}$  value of 14.5  $\mu\text{g/mL}$  [30]. Moreover, an independent study highlighted the antioxidant potential of  $\delta$ -cadinene, the predominant compound in *Jatropha curcas* essential oil, with an  $IC_{50}$  value of 314  $\mu\text{g/mL}$  in the DPPH test [31]. It is essential to underscore that the observed antioxidant activities in essential

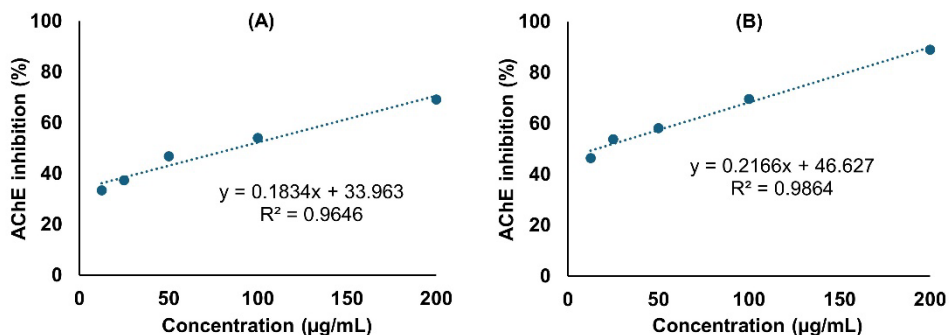
oil may have arisen from the synergistic interactions among both major and minor components [24, 32, 33]. Overall, the diverse compositions of this essential oil contributed to its collective antioxidant efficacy.

### Anti-acetylcholinesterase activity of essential oil

AChE is an enzyme crucial for terminating nerve impulses by catalyzing the breakdown of acetylcholine, a neurotransmitter [6, 9]. Dysregulation of AChE activity is associated with various neurological disorders, including Alzheimer's disease [6, 9]. In this study, we assessed the potential AChE inhibition of *K. elegans* essential oil by measuring its rate at five different concentrations, as presented in Fig. 5. The AChE inhibition activity increased with the increasing concentration of essential oil. At a concentration of 200  $\mu\text{g/mL}$ , *K. elegans* essential oil and galantamine achieved AChE inhibition rates of  $69.16\% \pm 2.14$  and  $89.05\% \pm 2.87$ , respectively. To calculate  $\text{IC}_{50}$ , standard curves of anti-AChE activity were constructed (Fig. 6). According to the  $\text{IC}_{50}$  data, the *K. elegans* essential oil exhibited significant inhibitory activity with an  $\text{IC}_{50}$  value of  $87.44 \pm 2.52 \mu\text{g/mL}$ , while galantamine showed an  $\text{IC}_{50}$  value of  $15.57 \pm 0.89 \mu\text{g/mL}$ . To date, there are no reports in the literature regarding the anti-AChE activity of *K. elegans* essential oil. However, there is one report on this activity for essential oil obtained from the genus *Knema*. Our findings are supported by Salihu et al., who reported that *K. hookeriana* essential oil showed high AChE inhibitory activity with an  $\text{IC}_{50}$  value of  $70.5 \mu\text{g/mL}$  [14].



**Figure 5.** Anti-acetylcholinesterase activity at different concentrations and half-maximum inhibitory concentration ( $\text{IC}_{50}$ ) of *Knema elegans* essential oil and galantamine. Values are means ( $n = 3$ )  $\pm$  standard deviation.



**Figure 6.** Standard curves of anti-acetylcholinesterase activity for *Knema elegans* essential oil (A) and galantamine (B).

Previous research has established that essential oils rich in sesquiterpenes possess anti-cholinesterase properties [34-36]. The anti-AChE activity of *K. elegans* essential oil, as indicated in the study, can be attributed to its main sesquiterpene compounds. This is consistent with findings from other studies, such as the one involving essential oil from *Psychotria poeppigiana* leaves, where germacrene D and bicyclogermacrene, the two main compounds, exhibited significant AChE inhibition [37]. Similarly, *Gynura bicolor* leaf essential oil, known for its richness in (*E*)- $\beta$ -caryophyllene, demonstrated substantial AChE inhibition, reaching 53% at a concentration of 0.50  $\mu\text{g/mL}$ , with an  $\text{ID}_{50}$  (50% inhibitory dose) value of 85  $\mu\text{g/mL}$  [38]. The anti-AChE activity of essential oils is commonly associated with competitive inhibition of the enzyme. This inhibition occurs when bioactive molecules within the essential oil bind to the active site of the AChE enzyme [39]. While AChE inhibition is of particular interest in the context of studying treatments or interventions for Alzheimer's disease and other neurodegenerative conditions, it is difficult to attribute the anti-AChE activity of *K. elegans* essential oil only to one or several active compounds. This implies that the overall effect on AChE activity may be a result of the combined actions of various constituents in the essential oil, working together in a synergistic manner [39].

## Conclusions

In summary, this research delved into the chemical composition of essential oil from *K. elegans* leaves in Vietnam and its antioxidant and anti-AChE properties. The moderate antioxidant activity and significant anti-AChE

effects suggest that this essential oil could be explored for its neuroprotective and cognitive-enhancing properties. Further studies could focus on elucidating the mechanisms behind these observed effects, exploring potential applications in neurodegenerative diseases, and optimizing extraction techniques to enhance the oil's bioactivity. Additionally, clinical trials may be warranted to validate the oil's safety and efficacy for potential pharmaceutical or nutraceutical use. Overall, these findings open avenues for continued research into the medicinal properties of *K. elegans* essential oil.

## EXPERIMENTAL SECTION

### Plant material

Leaves of *K. elegans* were collected at the Ba Vi National Park in Hanoi, Vietnam in August 2022. The identification and authentication of plant samples was performed by author Dau B. Thin from Hong Duc University, Vietnam. A voucher specimen was deposited in the herbarium of that university with code BV106. Fresh leaves were transported to the laboratory, chopped, and air-dried under shade for a week before essential oil extraction.

### Extraction of essential oil

The essential oil of *K. elegans* was collected by hydrodistillation method. For this purpose, the air-dried leaves were submitted to hydrodistillation using a Clevenger-type apparatus for 4 h as described previously [40]. The resultant essential oil was collected in clean glass vials, dried with anhydrous sodium sulfate, and stored at 4°C until analyses.

### Essential oil chemical analysis

The essential oil of *K. elegans* was analyzed using gas chromatography coupled to mass spectrometry (GC-MS) with a GCMS-QP2010 Plus apparatus from Shimadzu, Japan. The analysis employed a fused silica Equity-5 capillary column (30 m × 0.25 mm i.d., film thickness 0.25 µm). Helium, flowing at a rate of 1.5 mL/min, served as the carrier gas. The column temperature program was initiated at 60°C for 2 min, followed by a 3°C/min increase to 240°C, and then a 5°C/min increase to 280°C, maintained for 40 min. The sample was injected with a split ratio of 10:1, and the injector and interface temperatures were set at 280°C. The mass spectrometer operated in electron impact mode at 70 eV, and the detector voltage was fixed at 0.82 kV. Mass spectra were



acquired through automatic scanning every 0.5 s, covering mass fragments in the 40–500  $m/z$  range. Identifications relied on comparisons between the obtained spectra and those stored in the MS library and the retention index (RI) compared with literature data [41, 42]. The RI was calculated using the Van Den Dool and Kratz equation [43], determined by co-injecting a homologous series of linear  $n$ -alkanes. A semi-quantitative analysis was conducted to determine the relative amounts of each component in the essential oil. For quantitative data on essential oil constituents, the GC2010 equipment from Shimadzu, coupled with a flame ionization detector (FID), was used under conditions similar to the GC-MS system.

### Antioxidant assay

The 2,2-diphenyl-1-picrylhydrazyl (DPPH) assay of *K. elegans* essential oil was conducted following previously established procedures [44]. Briefly, a 0.1 mM DPPH solution in methanol was prepared. Subsequently, 2 mL of this solution was added to 0.1 mL of various concentrations of essential oil dissolved in methanol for testing. The reaction mixture was thoroughly vortexed, placed in the dark at 25°C for 30 min, and then measured at 517 nm. The essential oil's ability to scavenge the DPPH radical was calculated as % inhibition using the following equation: % inhibition =  $(A_c - A_s) / A_c \times 100$ , where  $A_c$  is the absorbance of the control, and  $A_s$  is the absorbance in the presence of essential oil. Ascorbic acid served as a positive control. The experiment was performed in triplicate. The inhibitory concentration ( $IC_{50}$ ) of the essential oil, required to inhibit 50% of the DPPH radicals, was determined from the standard curve and compared to that of ascorbic acid.

The 2,2'-azino-bis(3-ethylbenzothiazoline-6-sulfonic acid) (ABTS) assay of *K. elegans* essential oil was conducted following previously established procedures [44]. Briefly, the ABTS radical was generated by mixing 7 mM ABTS and 2.45 mM potassium persulphate through incubation at room temperature in the dark for 16 h. The ABTS solution was then diluted with distilled water to an absorbance of  $0.70 \pm 0.02$  at 734 nm. The ABTS reaction mixture comprised 2.6 mL of a diluted ABTS radical solution and 0.1 mL of essential oil at various concentrations, dissolved in methanol for testing. After incubation at 25°C for 6 min, the absorbance of the mixture solution was measured at 734 nm. Ascorbic acid served as a positive control. The experiment was performed in triplicate, and the percentage inhibition of the ABTS radical and the  $IC_{50}$  value by the essential oil were calculated, as described in the DPPH assay.

### Anti-acetylcholinesterase assay

The anti-AChE assay of *K. elegans* essential oil was conducted following previously established procedures [45]. Briefly, the total reaction volume (200  $\mu$ L) consisted of 150  $\mu$ L of 0.1 M sodium phosphate buffer (pH 8.0), 20  $\mu$ L of AChE (0.45 U/mL), 10  $\mu$ L of different concentrations of essential oil dissolved in methanol, 10  $\mu$ L of 5,5'-dithio-bis-[2-nitrobenzoic acid] (DTNB) (0.03 mM), and 10  $\mu$ L of acetylthiocholine iodide (0.68 mM). This reaction mixture was incubated at room temperature for 20 min. Following incubation, the optical density was measured immediately at 412 nm. Galantamine was used as a positive control. The experiment was performed in triplicate. The inhibition rate (%) of AChE activity was calculated using the following equation: % inhibition =  $(Ac - As) / Ac \times 100$ , where Ac is the absorbance of the control, and As is the absorbance of the test sample. An extract concentration providing 50% inhibition ( $IC_{50}$ ) was obtained by plotting the inhibition percentage against extract solution concentrations.

### Statistical analysis

All the experiments were performed in triplicate and results were given as the mean  $\pm$  standard deviation (SD). Statistical analysis was performed using Microsoft Excel 2016 for Windows (Microsoft, USA).

## REFERENCES

1. M. J. Christenhusz; J. W. Byng; *Phytotaxa*, **2016**, 261(3), 201-217.
2. B. Li; T. K. Wilson; Myristicaceae. In: Flora of China Online, Vol. 7, Science Press, Beijing, China, **2008**.
3. W. M. N. H. W. Salleh; F. Ahmad; *Pharm. Sci.*, **2017**, 23(4), 249-255.
4. A. S. Salihu; W. M. N. H. W. Salleh; *Vietnam J. Chem.*, **2023**, 61(4), 397-411.
5. N. Q. Hop; N. T. Son; *Curr. Pharm. Biotechnol.*, **2023**, 24, 1524-1553.
6. A. Maggio; S. Rosselli; M. Bruno; *Curr. Pharm. Des.*, **2016**, 22(26), 4011-4027.
7. M. G. Miguel; *Molecules*, **2010**, 15(12), 9252-9287.
8. F. Bakkali; S. Averbeck; D. Averbeck; M. Idaomar; *Food Chem. Toxicol.*, **2008**, 46(2), 446-475.
9. T. C. D. Santos; T. M. Gomes; B. A. S. Pinto; A. L. Camara; A. M. D. A. Paes; *Front. Pharmacol.*, **2018**, 9, 1192.
10. P. H. Ho; An Illustrated the Flora of Vietnam, Vol. 1. Tre Publishing House, Ho Chi Minh, Vietnam, **1999**.
11. Y. X. Zhang; Z. Lu; W. C. Wu; Y. G. Chen; R. Zhan; *Phytochem. Lett.*, **2021**, 42, 121-124.

- 12.Z. Lu; W. C. Wu; M. Wang; J. Q. Zhang; Y. G. Chen; R. Zhan; L. D. Shao; *Biochem. Syst. Ecol.*, **2020**, *88*, 103991.
- 13.J. Z. Deng; S. R. Starck; S. Li; S. M. Hecht; *J. Nat. Prod.*, **2005**, *68*(11), 1625-1628.
- 14.A. S. Salihu; W. M. N. H. W. Salleh; T. H. Ogunwa; *Nat. Prod. Res.*, **2024**, *14*, 2516-2521.
- 15.W. M. N. H. W. Salleh; M. Z. A. Anuar; S. Khamis; M. A. Nafiah; M. D. Sul'ain; *Nat. Prod. Res.*, **2021**, *35*(13), 2279-2284.
- 16.A. S. Salihu; W. M. N. H. W. Salleh; W. N. Setzer; *Z. Naturforsch. C.*, **2023**, *78*, 293-298.
- 17.A. S. Salihu; W. M. N. H. W. Salleh; *J. Essent. Oil Bearing Plants*, **2023**, *26*(2), 253-260.
- 18.R. Barman; J. Saikia; P. Sarmah; P. Konwar; M. Kumar; P. K. Bora; P. Bhattacharyya; S. P. Saikia; S. Haldar; D. Banik; *S. Afr. J. Bot.*, **2023**, *159*, 617-626.
- 19.D. B. Thin; B. B. Thinh; J. O. Igoli; *Chem. Nat. Compd.*, **2023**, *59*: 584-586.
- 20.B. B. Thinh; N. T. Khoi; R. V. Doudkin; D. B. Thin; I. A. Ogunwande; *Nat. Prod. Res.*, **2023**, *37*(10), 1625-1631.
- 21.A. Barra; *Nat. Prod. Commun.*, **2009**, *4*(8), 1147-1154.
- 22.A. C. Figueiredo; J. G. Barroso; L. G. Pedro; J. J. Scheffer; *Flavour Fragr. J.*, **2008**, *23*(4), 213-226.
- 23.N. Verma; S. Shukla; *J. Appl. Res. Med. Aromat. Plants*, **2015**, *2*(4), 105-113.
- 24.R. Amorati; M. C. Foti; L. Valgimigli; *J. Agric. Food Chem.*, **2013**, *61*(46), 10835-10847.
- 25.T. A. Misharina; E. S. Alinkina; L. D. Fatkulina; A. K. Vorobyova; I. B. Medvedeva; E. B. Burlakova; *Appl. Biochem. Microbiol.*, **2012**, *48*, 102-107.
- 26.H. Bartikova; V. Hanusova; L. Skalova; M. Ambroz; I. Bousova; *Curr. Top. Med. Chem.*, **2014**, *14*(22), 2478-2494.
- 27.H. Khan; A. L. Khan; J. Hussain; M. Adnan; I. Hussain; T. Khan; A. R. Khan; *Pak. J. Sci. Ind. Res. B: Biol. Sci.*, **2008**, *51*(6), 343-350.
- 28.B. Kaurinovic; S. Vlaisavljevic; M. Popovic; D. Vastag; M. Djurendic-Brenesel; *Molecules*, **2010**, *15*(9), 5943-5955.
- 29.J. Ascari; M. S. de Oliveira; D. S. Nunes; D. Granato; D. R. Scharf; E. Simionatto; M. Otuki; B. Soley; G. Heiden; *J. Ethnopharmacol.*, **2019**, *234*, 1-7.
- 30.S. Casiglia; M. Bruno; M. Bramucci; L. Quassinti; G. Lupidi; D. Fiorini; F. Maggi; *J. Essent. Oil Res.*, **2017**, *29*(6), 437-442.
- 31.R. A. Babahmad; A. Aghraz; A. Boutafda; E. G. Papazoglou; P. A. Tarantilis; C. Kanakis; M. Hafidi; Y. Ouhdouch; A. Outzourhit; A. Ouhammou; *Ind. Crops Prod.*, **2018**, *121*, 405-410.
- 32.L. D. do Nascimento; A. A. B. de Moraes; K. S. da Costa; J. M. P. Galúcio; P. S. Taube; C. M. L. Costa; J. D. Cruz; E. H. D. A. Andrade; L. J. G. de Faria; *Biomolecules*, **2020**, *10*(7), 988.
- 33.B. B. Thinh; D. B. Thin; I. A. Ogunwande; *Nat. Prod. Commun.*, **2024**, *19*(3), 1934578X241239477.
- 34.A. Arya; R. Chahal; R. Rao; M. H. Rahman; D. Kaushik; M. F. Akhtar; A. Saleem; S. M. A. Khalifa; H. R. El-Seedi; M. Kamel; G. M. Albadrani; M. M. Abdel-Daim; V. Mittal; *Biomolecules*, **2021**, *11*(3), 350.

ESSENTIAL OIL FROM *KNEMA ELEGANS* WARB.: CHEMICAL COMPOSITION,  
ANTIOXIDANT AND ANTI-ACETYLCHOLINESTERASE ACTIVITIES

- 35.H. Hajimehdipoor; M. Mosaddegh; F. Naghibi; A. Haeri; M. Hamzeloo-Moghadam; *An. Acad. Bras. Cienc.*, **2014**, *86*, 801-806.
- 36.B. B. Thinh; L. D. Chac; *J. Essent. Oil Bearing Plants*, **2024**, *27*(2), 574-583.
- 37.A. S. N. Formagio; W. Vilegas; C. R. F. Volobuff; C. A. L. Kassuya; C. A. L. Cardoso; Z. V. Pereira; R. M. M. F. Silva; D. A. D. S. Yamazaki; G. D. F. Gauze; J. Manfron; J. A. Marangoni; *J. Ethnopharmacol*, **2022**, *296*, 115220.
- 38.M. Miyazawa; H. Nakahashi; A. Usami; N. Matsuda; *J. Nat. Med.*, **2016**, *70*, 282-289.
- 39.J. Calva; M. Silva; V. Morocho; *Molecules*, **2023**, *28*(24), 8112.
- 40.B. B. Thinh; D. B. Thin; *J. Essent. Oil Bearing Plants*, **2023**, *26*(3), 653-663.
- 41.R. P. Adams; Identification of essential oil components by gas chromatography-mass spectrometry. 4th ed. Carol Stream (IL): Allured Publishing Corporation, **2007**.
- 42.NIST; Mass Spectral Library (NIST/EPA/NIH). National Institute of Standards and Technology, Gaithersburg, USA, **2018**.
- 43.H. Van Den Dool; P. Kratz; *J. Chromatogr. A.*, **1963**, *11*, 463-471.
- 44.D. B. Thin; A. A. Korneeva; B. B. Thinh; I. A. Ogunwande, *Russ. J. Bioorg. Chem.*, **2023**, *49*(4), 815-822.
- 45.S. Bendjabeur; O. Benchabane; C. Bensouici; M. Hazzit; A. Baaliouamer; A. Bitam; *J. Food Meas. Charact.*, **2018**, *12*, 2278-2288.



# CATALYTIC AND SOLVENT HYDROTHERMAL LIQUEFACTION OF MICROALGAE: A STRATEGY FOR RECOVERING FINE CHEMICALS

Sathish Raam RAVICHANDRAN<sup>a</sup> ,  
Chitra Devi VENKATACHALAM<sup>b\*</sup> , Mothil SENGOTTIAN<sup>a</sup> 

**ABSTRACT.** The study investigates the influence of various catalysts (Ni/TiO<sub>2</sub>, Co/TiO<sub>2</sub>, and Zeolite) on the hydrothermal liquefaction of microalgae and explores the effect of co-solvents (acetone, methanol, and toluene) on biocrude yield from different microalgae three species namely *Nannochloropsis oculata*, *Chlorella vulgaris*, and *Spirulina maxima*. Catalyst characterization using FE-SEM, XRD, and BET analysis revealed distinct properties. Under Co-TiO<sub>2</sub>, *Nannochloropsis oculata* and *Chlorella vulgaris* yield 56.21% and 57.6% biocrude at 5% loading; *Spirulina maxima* yields 45.3% at 2.5% loading. With Ni-TiO<sub>2</sub>, *Nannochloropsis oculata* yields 52.4% at 2.5% loading; *Chlorella vulgaris* yields 44.7% at 5%; *Spirulina maxima* yields 44% at 2.5% loading. Zeolite yields: *Spirulina maxima* and *Chlorella vulgaris* yield 53.8% and 52.1% at 2.5%; *Nannochloropsis oculata* yields 48.3% at 7.5% loading. Co-solvent addition significantly boosts biocrude yield; methanol and toluene yield 53.7% and 49.2% for *Chlorella vulgaris* and *Spirulina maxima*, respectively, while acetone yields 57.6% for *Nannochloropsis oculata*. Different solvents extract diverse functional groups such as alkanes, halides, aromatics, and aldehydes which has wide industrial applications.

**Keywords:** Biocrude, Catalysts, Co-Solvents, Hydrothermal Liquefaction, Microalgae

---

<sup>a</sup> Department of Chemical Engineering, Kongu Engineering College, Perundurai, Erode – 638060, Tamil Nadu, India.

<sup>b</sup> Department of Food Technology, Kongu Engineering College, Perundurai, Erode – 638060, Tamil Nadu, India.

\* Corresponding author: [erchitrasuresh@gmail.com](mailto:erchitrasuresh@gmail.com)



## INTRODUCTION

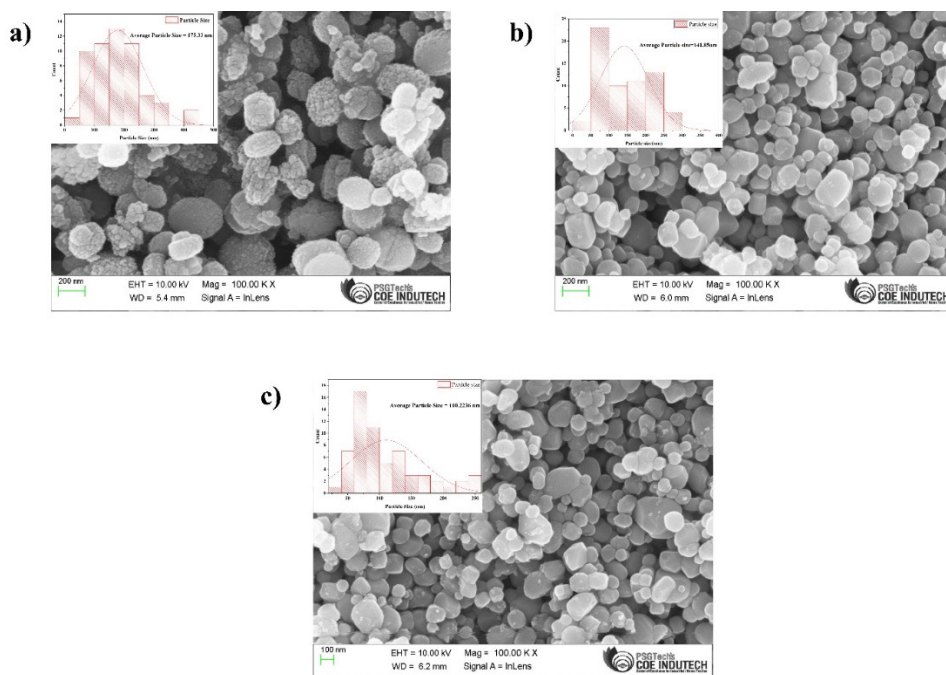
The escalating global demand for fossil fuels, driven by population growth, has exacerbated energy scarcity issues and contributed to a rise in atmospheric CO<sub>2</sub> concentrations, reaching 407 ppm by 2017 due to human activities [1]. This has underscored the urgency of transitioning towards renewable energy sources, particularly biofuels derived from thermochemical conversion of abundant biomass. Hydrothermal liquefaction (HTL) has emerged as a promising technology in this context, capable of converting biomass into biofuels and valuable chemicals sustainably [2]. Unlike pyrolysis and gasification, HTL operates at mild temperatures (250-350°C) and moderate to high pressures (10-25 MPa), minimizing energy input [3]. Microalgae have gained prominence as an ideal feedstock for HTL due to their efficient photosynthesis, rapid growth rates, high energy content, adaptability to various environments, and high biomass productivity per unit area [4, 5], making them suitable for producing biofuels and fine chemicals essential for applications such as medicines, cosmetics, pesticides, paints, and food additives [6-10]. HTL deconstructs complex organic compounds through depolymerization, dehydrogenation, deoxygenation, and repolymerization processes, yielding simple hydrocarbons and organic functional groups such as ketones, furals, and esters [11]. It distinguishes itself among thermochemical methods by operating without the need for biomass drying [12, 13], with biocrude, biochar, biogas, and an aqueous phase as its primary products [14]. The addition of catalysts and co-solvents enhances the yield of fine chemicals within biocrude [15-19], enhancing its potential for diverse applications.

Catalytic hydrothermal liquefaction (C-HTL) enhances biocrude production by modifying water's properties under elevated temperatures, facilitating biomass dissolution [20, 21]. Lipids undergo hydrolysis, yielding methanol, acetaldehyde, and ethanol, while proteins undergo decarboxylation and deamination reactions producing ammonia and organic acids [22]. Carbohydrates decompose into water-soluble organic compounds like organic acids and aldehydes [23], underscoring C-HTL as a sustainable pathway for converting biomass into valuable products aligned with green energy initiatives. Co-Solvent Hydrothermal Liquefaction (Co-HTL) represents an advanced variant where additional solvents enhance efficiency by improving the solubility of less soluble compounds in water [24]. This approach addresses traditional HTL limitations, resulting in increased biomass conversion efficiency. Through optimization of catalysts and organic solvents in HTL, this study aims to enhance the yield and chemical characteristics of bioproducts derived from microalgae, contributing insights into biomass conversion for fuels, adsorbents, catalysts, fertilizers, and fine chemical synthesis.

## RESULTS AND DISCUSSIONS

### Catalyst Characterization

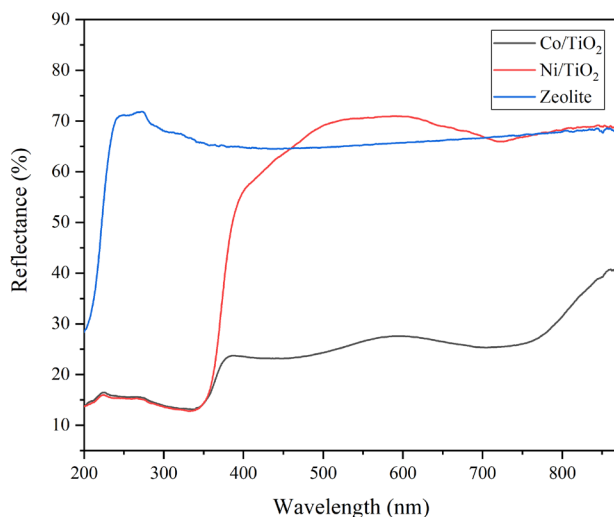
The examination of the surface structures of the synthesized catalysts was conducted using the Field Emission Scanning Electron Microscope (FE-SEM) method, providing insights into the microstructures present in the catalyst. Fig 1 illustrates the FE-SEM results along with particle size distribution as an inset. Fig 1a) shows that the zeolite synthesized showed the presence of rough surfaces and non-uniform structures, additionally, there are visible pores within the catalyst structure showcasing the porosity, the particle size analysis shows that the zeolite catalyst synthesized had an average particle size of 173.33 nm. The analysis of Co/TiO<sub>2</sub> & Ni/TiO<sub>2</sub> shows that both catalysts had similar structures with the combination of tetragonal and hexagonal shapes. This was further confirmed with XRD analysis. The particle size analyzed through FE-SEM results showed that the catalysts had 141.82 nm and 110.226 nm respectively can be seen in Fig 1b) and 1c).



**Figure 1.** (a) FE-SEM image and particle size distribution of Zeolite, (b) FE-SEM image and particle size distribution of Co/TiO<sub>2</sub>, (c) FE-SEM image and particle size distribution of Ni/TiO<sub>2</sub>.



The UV-Vis diffuse reflectance spectroscopy (Fig 2) spectrum of Co/TiO<sub>2</sub> shows distinct peaks and valleys typical of both cobalt and titanium dioxide components. For cobalt, the observed peaks at approximately 535 nm (1.19%) and 623 nm (1.31%) suggest absorption bands related to its electronic transitions, possibly indicative of its oxidation states or coordination environment in the catalyst. Meanwhile, titanium dioxide, known for its wide bandgap, exhibits high reflectance in the UV region, as evidenced by peaks around 869 nm (40.84%), reflecting its efficient scattering and reflection of UV light. This behaviour underscores its potential as a catalyst TiO<sub>2</sub> [23]. Additionally, regions of lower reflectance in the spectrum may correspond to absorption bands where titanium dioxide absorbs UV light, revealing insights into its electronic band structure and potential catalytic activity.



**Figure 2.** UV-visible diffuse reflectance spectra (DRS) of Co/TiO<sub>2</sub>, Ni/TiO<sub>2</sub> and Zeolite.

The UV-Vis diffuse reflectance spectroscopy spectrum of the nickel over titanium dioxide (Ni/TiO<sub>2</sub>) catalyst reveals distinct absorption features and reflectance patterns across the measured range of 870 to 200 nm (Fig. 2). The spectrum exhibits a broad absorption band extending from approximately 300 to 600 nm, characteristic of surface plasmon resonance (SPR) phenomena typically observed in nickel nanoparticles. This absorption band indicates the presence of nickel nanoparticles on the TiO<sub>2</sub> support, which is crucial for catalytic applications. The shoulder observed around 400 nm further supports the presence of Ni nanoparticles, indicating their uniform dispersion, which is favourable for enhanced catalytic performance. The overall

high reflectance in the UV region (200-300 nm) and the gradual decrease towards longer wavelengths are indicative of the TiO<sub>2</sub> support, confirming its role in stabilizing the Ni nanoparticles and possibly influencing the catalyst's electronic structure Ni [24].

The UV-Vis diffuse reflectance spectroscopy was also employed to characterize the zeolite catalyst (Fig 2). Upon analysis of the spectrum, distinct absorption features are observed, notably a broad absorption band spanning from approximately 300 to 500 nm. The peak reflectance values vary within this range, with a maximum reflectance of 71.854% observed at around 870 nm and a minimum reflectance of 28.362% at approximately 200 nm. These absorption bands are indicative of electronic transitions within the catalyst structure, likely arising from transitions involving the d-orbitals of the metal centers incorporated into the zeolite framework. The observed absorbance at shorter wavelengths suggests the presence of ligand-to-metal charge transfer (LMCT) transitions, whereas the absorption at longer wavelengths may be associated with metal-to-ligand charge transfer (MLCT) transitions Zeolite [25].

The catalysts (zeolite, Ni/TiO<sub>2</sub>, and Co/TiO<sub>2</sub>) were subjected to X-ray diffraction (XRD) to determine the crystallinity and peak patterns. The obtained XRD data revealed specific peak positions for each catalyst as shown in Fig 3, which were compared to patterns in JCPDS. The zeolite catalyst exhibited peak positions at 9.83°, 24.34°, and 26.41°, closely resembling those in JCPDS Card No. 29-1257, indicating its moderate zeolite nature. The Ni/TiO<sub>2</sub> catalyst displayed peaks at 42.41° and 65.79° for nickel and 24.78° and 33.93° for TiO<sub>2</sub>, consistent with JCPDS Card No. 01-078-07533, confirming the presence of nickel and TiO<sub>2</sub>. Similarly, the Co/TiO<sub>2</sub> catalyst exhibited peaks at 27.8° and 39.21° for cobalt and 23.76° and 32.89° for TiO<sub>2</sub>, resembling JCPDS Card No. 00-042-1467, indicating the presence of cobalt and TiO<sub>2</sub>. These results underscore the conformity of the catalyst's crystalline phases with the reference database, providing essential insights into their structural properties and their behavior in catalytic reactions.

The catalysts employed in this study exhibit distinct surface area and pore volume characteristics, reflecting their unique properties as shown in Fig 4. Co/TiO<sub>2</sub> presents a pore volume of 0.020 cc/g and a surface area of 6.901 m<sup>2</sup>/g, highlighting its specific attributes as shown in Fig 4a. While Ni/TiO<sub>2</sub> on the other hand, demonstrates a slightly higher surface area of 8.485 m<sup>2</sup>/g and a corresponding pore volume of 0.026 cc/g as shown in Fig 4b. In stark contrast, Zeolite stands out with a significantly larger surface area, measuring 132.174 m<sup>2</sup>/g, and a substantial pore volume of 0.111 cc/g as shown in Fig 4c, underscoring its remarkable porosity and potential for catalytic applications.

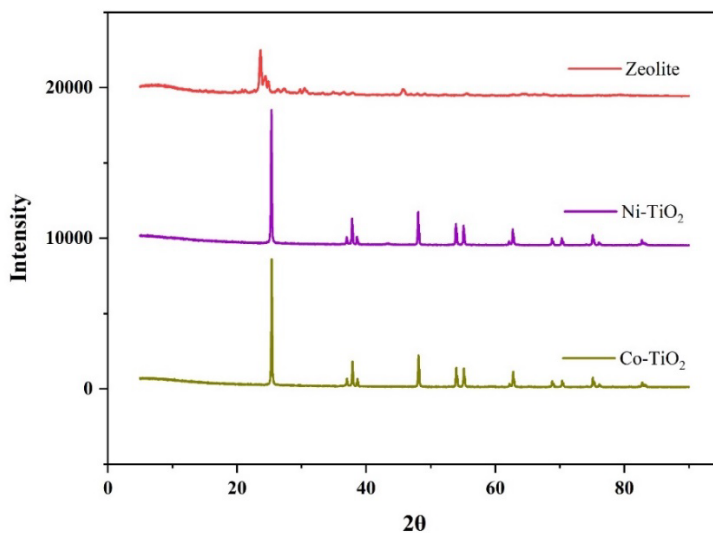


Figure 3. XRD patterns for Zeolite, Ni/TiO<sub>2</sub>, and Co/TiO<sub>2</sub> catalysts.

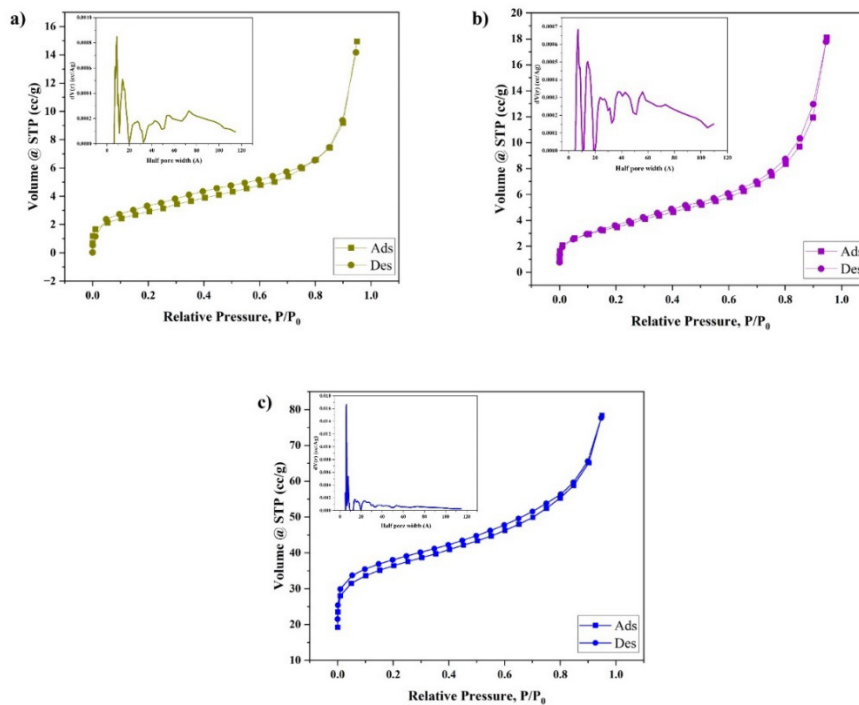
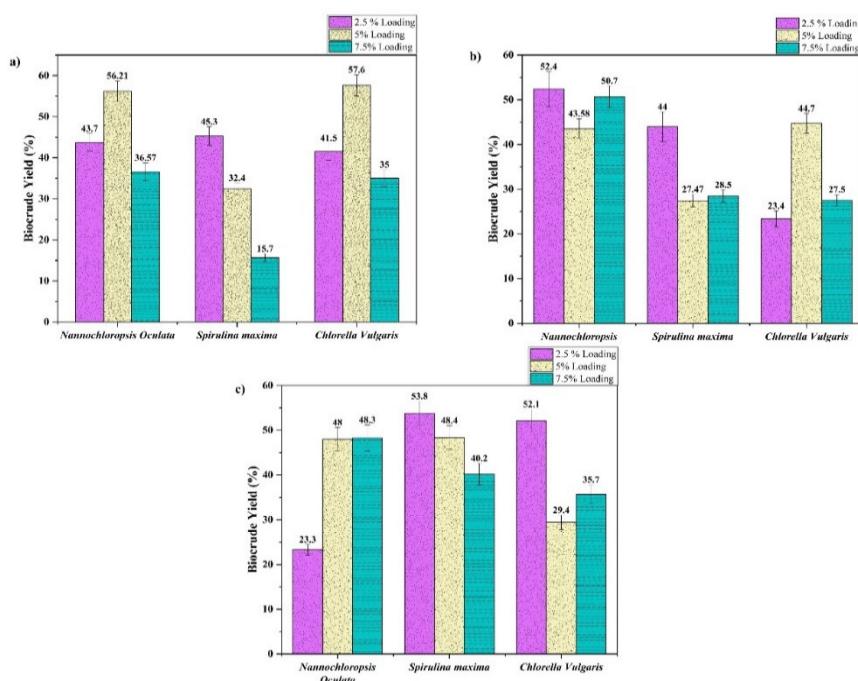


Figure 4. BET Isotherm graphs for (a) Co/TiO<sub>2</sub>, (b) Ni/TiO<sub>2</sub>, (c) Zeolite.

### Effect of catalyst on biocrude yield

The efficiency of bio-crude production varies significantly among different microalgae species and catalyst loading concentrations as shown in Fig 5. In the case of the Co-TiO<sub>2</sub> catalyst, *Nannochloropsis oculata* exhibited the highest bio-crude yield at a 5% loading (56.21%), followed by 2.5% (43.7%) and 7.5% (36.57%) loadings. Similarly, *Chlorella vulgaris* displayed a similar trend, with the maximum bio-crude yield obtained at 5% loading (57.6%), followed by 2.5% (41.5%) and 7.5% (35%) loadings. *Spirulina maxima* exhibited a unique trend, with the highest bio-crude yield recorded at 2.5% loading (45.3%), followed by 5% (32.4%) and 7.5% (15.7%) loadings as shown in Fig 5a. These findings underscore the importance of understanding the impact of Co-TiO<sub>2</sub> loading on each microalgae species individually to optimize biocrude production efficiency.



**Figure 5.** (a) Effect of Co/TiO<sub>2</sub> catalyst on biocrude yield, (b) Effect of Ni/TiO<sub>2</sub> catalyst on biocrude yield, (c) Effect of Zeolite catalyst on biocrude yield.

Similarly, significant variations were observed in bio-crude yields among different microalgae species and Ni-TiO<sub>2</sub> loading concentrations. For *Nannochloropsis oculata*, the highest bio-crude yield was achieved at a 2.5%

loading concentration (52.4%), followed by 7.5% (50.7%) and 5% (43.58%) loadings. Conversely, *Chlorella vulgaris* exhibited the maximum bio-crude yield at a 5% loading concentration (44.7%), followed by 2.5% (23.4%) and 7.5% (27.5%) loadings. *Spirulina maxima* showed different patterns, with the highest bio-crude yield achieved at a 2.5% loading concentration (44%), followed by 7.5% (28.5%) and 5% (27.47%) loadings as shown in Fig 5b. These results highlight the species-specific response to Ni-TiO<sub>2</sub> loading.

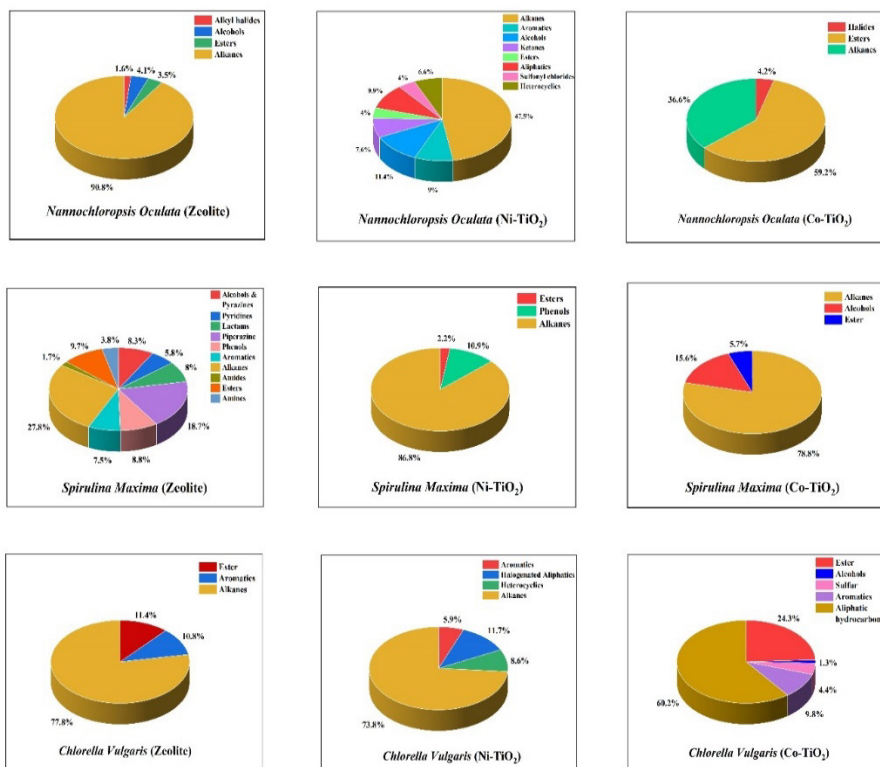
Furthermore, significant variations were observed in bio-crude yields among different microalgae species and zeolite loading concentrations. For *Nannochloropsis oculata*, the highest bio-crude yield was achieved at 7.5% loading (48.3%), followed by 5% (48%) and 2.5% (23.3%) loadings. *Chlorella vulgaris* displayed contrasting behavior, with the maximum bio-crude yield recorded at 2.5% loading (52.1%), followed by 7.5% (35.7%) and 5% (29.4%) loadings. *Spirulina maxima* exhibited a similar trend to *Nannochloropsis oculata*, with the highest bio-crude yield obtained at 7.5% loading (40.2%), followed by 5% (48.4%) and 2.5% (53.4%) loadings as shown in Fig 5c. These results highlight the importance of considering species-specific responses to zeolite loading for effective catalyst optimization strategies. The present study results were compared to previous studies and found to have an improvement on the biocrude yield in some cases, these are shown in Table 1.

**Table 1.** Biocrude yield of C-HTL of microalgae

Si. no	Species	Temperature °C	Catalyst	Biocrude Yield %	Ref
1	<i>Nannochloropsis sp.</i>	210, 230, 250	nano-Ni/SiO <sub>2</sub> zeolite, Na <sub>2</sub> CO <sub>3</sub>	11 -30	[26]
2	<i>Nannochloropsis</i>	250	Na <sub>2</sub> CO <sub>3</sub>	47.05	[27]
3	<b>ENTEROMORPHA PROLIFERA</b>	230	H <sub>2</sub> SO <sub>4</sub>	28.43	[28]
4	<b>DUNALIELLA TERTIOLECTA</b>	360	Na <sub>2</sub> CO <sub>3</sub>	25.8	[29]
5	<i>Spirulina platensis</i>	350	Na <sub>2</sub> CO <sub>3</sub>	51.6	[30]
6	<i>Nannochloropsis sp.</i>	390	Ni/TiO <sub>2</sub>	69.70	[31]
7	<i>Scenedesmus almeriensis</i>	400	Pt/Al <sub>2</sub> O <sub>3</sub>	53.1	[32]
8	<i>Nannochloropsis oculata</i>	280	Co/TiO <sub>2</sub>	56.21	Present study
9	<i>Spirulina maxima</i>	278	Zeolite	53.8	Present study
10	<i>Chlorella vulgaris</i>	290	Co/TiO <sub>2</sub>	57.6	Present study

CATALYTIC AND SOLVENT HYDROTHERMAL LIQUEFACTION OF MICROALGAE:  
A STRATEGY FOR RECOVERING FINE CHEMICALS

The GC-MS results of the C-HTL shown in Fig 6 indicate that when zeolite was used as a catalyst the composition of the biocrude had larger amounts of alkanes with *Nannochloropsis oculata* having around 90%. However, the overall composition of the biocrude of *Spirulina maxima* had larger varieties of organic compounds suggesting that the zeolite catalyst had indeed helped in breaking down complex volatile compounds. On the other hand, *Nannochloropsis oculata* biocrude had more varieties of organics when coupled with Ni catalysts. Alkane compounds dominated the composition of the biocrudes with above 40% on all three microalgae, this shows that Ni-based catalyst can be used to produce a biocrude that can be easily processed further into biofuels.



**Figure 6.** GC/MS results for the effect of different catalysts on the bio-crude composition.

The Co-based catalyst though showed similar results with *Nannochloropsis oculata* and *Spirulina maxima* on the presence of alkanes, there was a significant change in the rest of the compounds with ester dominating

*Nannochloropsis oculata* while it was alcohols that had a major percentage in *Spirulina maxima*. When compared to the previous study [33] in which the hydrothermal liquefaction was performed without any catalyst, the GC-MS results showed an increased aromatic compound in the likes of benzene, and phenols. etc., which has a drastic change when catalysts were included, this shows the involvement of catalysts in the reaction process helping in the breaking of complex organic compounds [34, 35].

### **Effect of co-solvent on biocrude yield**

For *Chlorella vulgaris*, *Nannochloropsis oculata*, and *Spirulina maxima* species three different co-solvents (acetone, methanol, toluene) were used to enhance the biocrude yield as shown in Fig 7. For *Chlorella Vulgaris*, three different co-solvents were used to enhance the biocrude yield. Acetone as a co-solvent plays a significant role in the HTL process, significantly impacting the yields obtained. Specifically, In addition to acetone in a ratio of (25:75) the increased biocrude yield of 52.1 % was achieved at the ratio of 75% water and 25% acetone, water becomes the primary solvent. Water's polar nature promotes the dissolution of polar compounds, while the presence of acetone as a co-solvent enhances the extraction of lipids. This ratio aims to maintain the advantages of water as a solvent while benefiting from the enhanced lipid extraction efficiency of acetone compared to other ratios such as 0:100, 50:50, 75:25, 100:0.

This enhancement can be attributed to acetone's unique ability to enhance the solubility of biomass components, thereby increasing the overall conversion efficiency of the process and the product quality. Methanol at the ratio of (100:0), the increased bio-crude yield of 53.7 % was achieved at the ratio of 0% water and 100% Methanol. Pure methanol as the solvent Methanol, being less polar than water may favor the dissolution of certain hydrophobic components from the algae biomass leading to a higher yield of bio-crude the absence of water might hinder hydrolysis reactions compared to other ratios (0:100, 25:75, 50:50, 75:25). Toluene in a ratio of (100:0) this ratio, pure toluene is used as the solvent. The increase in bio-crude yield (54%) compared to other ratios (0:100, 25:75, 50:50, 75:25) Toluene as a solvent in this ratio yields promising results in terms of increasing the extraction process's efficiency and showing its ability to obtain a higher yield of biocrude from *Chlorella vulgaris*.

**Table 2.** Various biocrude yields of microalgae during hydrothermal liquefaction using different co-solvents

Si. no	Species	Temperature °C	Solvent	Solvent to Water ratio	Biocrude Yield %	Ref
1	<i>Tetraselmis sp.</i>	275-350	Ethylene glycol Isopropyl alcohol	1:8	31.5-35.4 29-30.4	[36]
2	<i>Chlorella pyrenoidosa</i>	280	Ethanol	5:2	57.3	[37]
3	<i>Galdieria sulphuraria</i>	350	Glycerol	1:2.5	73.2	[38]
4	<i>Galdieria sulphuraria</i>	310	Ethanol	1:2.5	23.7	[38]
5	<i>Tetraselmis sp.</i>	350	Isopropyl alcohol	1:8	35.4	[39]
6	<i>Spirulina platensis</i>	300	Methanol Ethanol Formic acid	1:10	36.2-59	[40]
7	<i>Nannochloopsis gladina</i>	272	Methanol	0.75:0.25	57.8	[41]
8	<i>Nannochloropsis oculata</i>	280	Methanol	3:1	58.8	Present study
9	<i>Spirulina maxima</i>	278	Toluene	1:0	50.8	Present study
10	<i>Chlorella vulgaris</i>	290	Toluene	1:0	54	Present study

For *Spirulina maxima* the addition of methanol at the ratio (75:25) of 25% water and 75% methanol, methanol becomes the dominant solvent. This higher concentration of methanol results in an increased biocrude yield (49.2%) compared to ratios with other ratios (0:100, 25:75, 50:50, 100:0). Methanol, being a polar solvent with some ability to dissolve nonpolar compounds, enhances the extraction of a wider range of compounds from the biomass compared to water alone. For acetone at the ratio (100:0) of 100% Acetone and 0% water results in an increased biocrude yield (49.2%). The higher extraction properties of acetone may lead to higher biocrude yields (49.6%) compared to other ratios (0:100, 25:75, 50:50, 75:25). For toluene at the ratio (100:0) of 100% Toluene and 0% water. The effective extraction properties of toluene may lead to higher biocrude yields (50.8%) compared to other ratios (0:100, 25:75, 50:50, 75:25).

For *Nannochloropsis oculata* the addition of toluene at the ratio (25:75) of 75% water and 25% toluene shows a higher yield (59.6%) compared to other ratios (0:100, 50:50, 75:25, 100:0), water becomes the primary solvent.



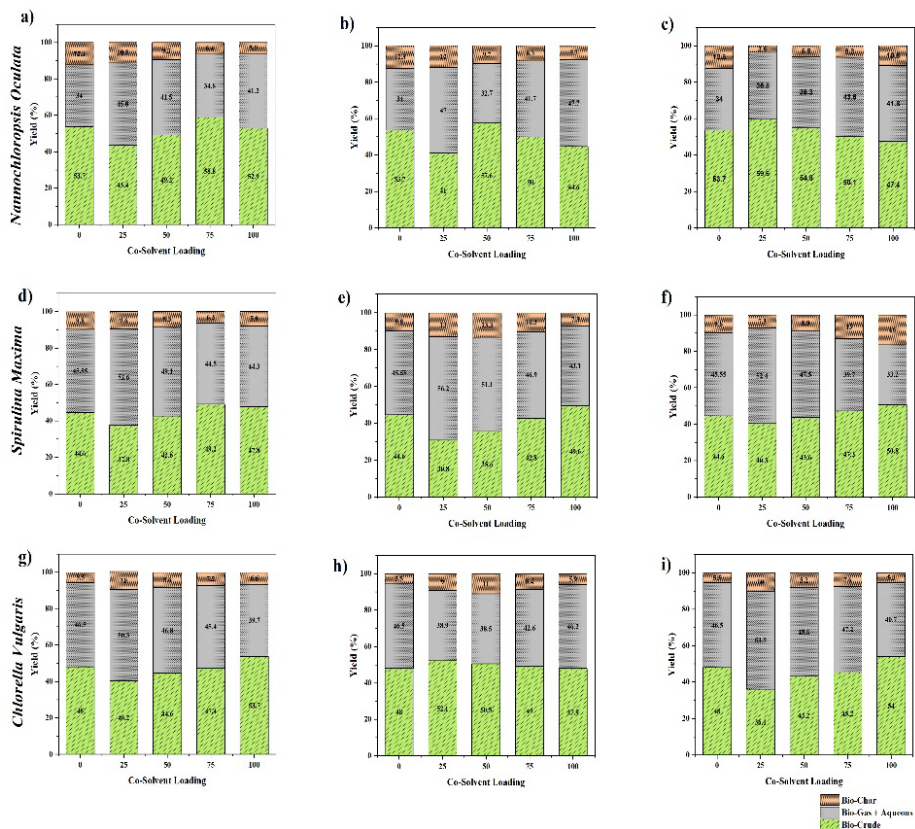
Water's polar nature promotes the dissolution of polar compounds, while the presence of toluene is a co-solvent. In addition of acetone at the ratio (50:50) of 50% water and 50 % acetone results in a higher yield of (57.6%) compared to other ratios (0:100, 25:75, 75:25,100:0). In this balanced ratio, water and acetone are present in equal proportions. This combination aims to capitalize on the advantages of both solvents. Water facilitates the hydrothermal breakdown of organic molecules, while acetone enhances the extraction efficiency of lipids. Methanol at the ratio (75:25) of 25% water and 75% methanol, shows higher biocrude yield (58.8%) due to its improved solubility of nonpolar compounds compared to other ratios (0:100, 25:75, 50:50,100:0).

Comparing the results obtained from this study with similar works as shown in Table 2, shows that addition of solvents during the hydrothermal liquefaction process indeed help in increasing the yield but also enhances the quality of biocrude produced influencing the chemical composition of the biocrude which further found using GC-MS analysis.

When methanol is utilized as a co-solvent, the primary functional groups obtained include amines, alkanes, and carboxyl groups. These functional groups are very important in the chemical makeup derived from *Nannochloropsis oculata*. While using acetone as a co-solvent, the major fine chemical functional groups obtained are halides, alkanes, and carboxyl groups. Halides are particularly notable in this composition, alongside alkanes and carboxyl groups. The change in the chemical composition compared to when methanol is used highlights the impacts of co-solvent. When toluene is used as a co-solvent, the main types of chemical groups obtained are alkanes and halides. This highlights the significance of alkanes in the chemical composition derived from *Nannochloropsis oculata*. The presence of halides alongside alkanes indicates a distinct chemical profile when toluene is the co-solvent, different from when methanol or acetone is used.

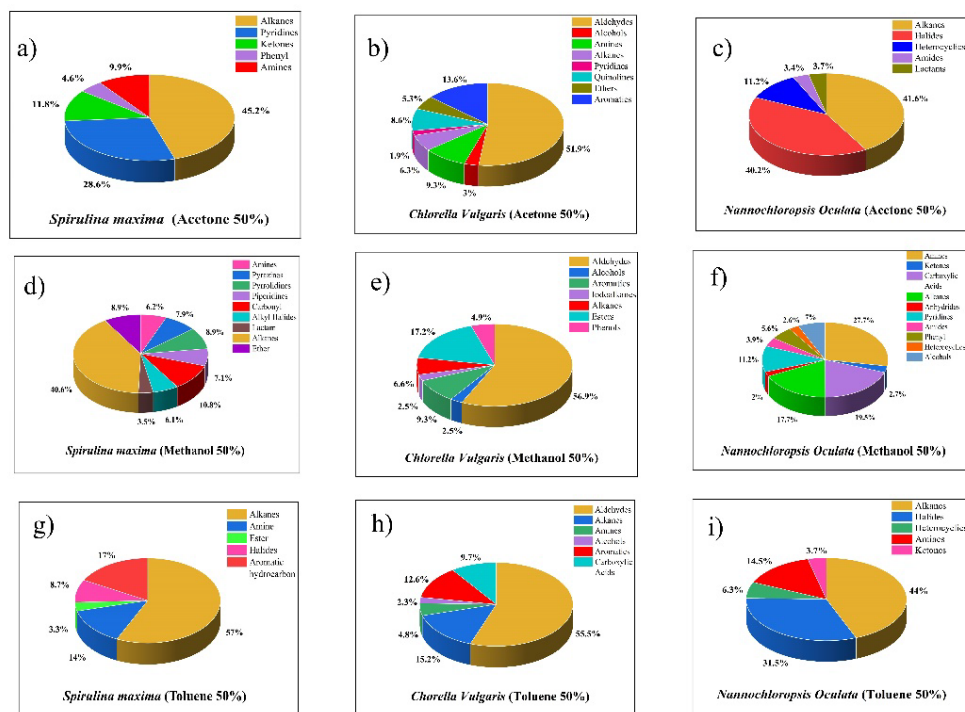
The consistent presence of alkanes across all three cases highlights their significance in the chemical composition derived from *Nannochloropsis oculata*. These highlighted alkanes are essential substances taken from the biomass of algae, depending on the co-solvent used. Furthermore, consistently find amines, halides, and carboxyl groups, although their amounts differ depending on the co-solvent used. This indicates that the choice of co-solvent not only impacts which functional groups are extracted but also influences how much of each is present in the end chemical mixture. The types and amounts of fine chemicals we get from *Nannochloropsis oculata* depend on which co-solvents we use in the hydrothermal liquefaction process. The presence and quantity of certain chemical groups change depending on which co-solvent is utilized.

CATALYTIC AND SOLVENT HYDROTHERMAL LIQUEFACTION OF MICROALGAE:  
A STRATEGY FOR RECOVERING FINE CHEMICALS



**Figure 7.** (a)(d)(g) Effect of methanol on different species bio-crude yield, (b)(c)(h) Effect of acetone on different species bio-crude yield, (c)(f)(i) Effect of toluene on different species bio-crude yield.

The composition of fine chemicals obtained from *Nannochloropsis Oculata* is depicted in detail varies significantly depending on the choice of co-solvent during hydrothermal liquefaction. Methanol yields prominent functional groups like amines, alkanes, and carboxyl groups, contributing to a diverse range of compounds. In contrast, acetone shifts the major functional groups towards halides, alkanes, and carboxyl groups, diverging from the profile observed with methanol. Toluene as a co-solvent results in major functional groups of alkanes and halides, indicating a distinct chemical profile compared to both methanol and acetone. The consistent presence of alkanes highlights their importance across all cases, while variations in amines, halides, and carboxyl groups reflect differences in co-solvent composition.



**Figure 8.** GCMS results for the effect of co-solvents at 50% ratio on the bio-crude composition.

The composition of fine chemicals obtained from *Spirulina maxima* is depicted in a detailed Fig 8, revealing a variety of functional groups. When methanol is used as a co-solvent, the primary functional groups observed include alkanes, pyrrolopyrazine, and carbonyl groups. when acetone is used as a co-solvent, the major functional groups obtained are alkanes, pyridines, and amines. This alteration in the chemical profile highlights the significant influence of the choice of co-solvent in the final composition. Similarly, when toluene is employed as a co-solvent, the major functional groups are alkanes, halides, and aromatic hydrocarbons. This emphasizes the diverse range of compounds that can be obtained by varying the co-solvent used during extraction. The presence of alkanes in all three cases underscores their importance in the chemical derived from *Spirulina maxima*. Additionally, other fine chemical groups like pyrrolopyrazine, carbonyl, pyridines, and halides are also present based on the composition of co-solvent

The composition of fine chemicals obtained from *Chlorella Vulgaris* is depicted in a detailed Fig 8. When methanol is employed as a co-solvent, the primary functional groups observed are aldehyde and ester groups. When acetone is used as a co-solvent, the major functional groups shift to aldehyde, aromatics, and alkenes. Similarly, when toluene serves as a co-solvent, the major functional groups obtained are aldehydes and alkanes. This variation in functional groups highlights the significant impact of co-solvent selection on the chemical composition of the fine chemicals. The consistent presence of aldehyde groups across all three cases demonstrates their importance in the fine chemical derived from *Chlorella Vulgaris*. Additionally, the ester, aromatics, and alkenes further highlight the diverse range of compounds that can be obtained from *Chlorella Vulgaris*, the choice of co-solvent plays a crucial role in determining the final composition of fine chemicals from *Chlorella Vulgaris*, highlighting the importance of optimizing co-solvent ratios

### **Biocrude elemental analysis**

The another important aspect of biocrude to be processed into different applications is the elemental analysis where the composition of Carbon, Hydrogen, Nitrogen, Oxygen and Sulfur are measured to check improvements in their composition. The elemental composition of biocrude from both catalytic and co-solvent HTL is given in Table 3.

The analysis results of biocrude without any catalyst or co-solvent present in Table 3 is taken from our previous study [33] and the rest corresponds to the biocrude with highest yield under their respective category. The results shows that there is a decrease in the wt% of carbon on *Nannochloropsis oculata* during the addition of catalysts or co-solvents which has a small effect on the higher heating value (HHV) of that particular microalgae species with other two species having similar results. When compared to the feedstock results there is a definite increase in HHV of the species stating that HTL under catalytic or co-solvent condition is very much crucial in obtaining a better quality crude. This results indicate that HTL process either with catalyst or co-solvent can improve the characteristics of the oil as seen in the GC-MS analysis and also help in improving the biocrude to enable it to be further processed to be used as alternate fuels or as an additives.

**Table 3.** Ultimate analysis of biocrude produced HTL using catalysts and Co-Solvents

Species	Catalyst/ Co-Solvent	C (wt%)	H (wt%)	N (wt%)	S (wt%)	O (wt%)	HHV (MJ/Kg)
<i>Nannochloropsis oculata</i>	-	73.56	12.06	8.89	1.15	4.34	39.85
<i>Spirulina maxima</i>	-	65.72	9.85	7.79	0.82	15.82	32.47
<i>Chlorella vulgaris</i>	-	65.83	10.72	7.19	0.80	15.46	33.88
<i>Nannochloropsis oculata</i>	Ni/TiO <sub>2</sub>	65.36	7.40	7.02	0.32	19.9	28.34
<i>Spirulina maxima</i>	Ni/TiO <sub>2</sub>	68.69	7.50	7.32	0.22	16.27	30.12
<i>Chlorella vulgaris</i>	Ni/TiO <sub>2</sub>	69.54	5.58	7.05	0.45	17.38	27.54
<i>Nannochloropsis oculata</i>	Co/TiO <sub>2</sub>	67.50	7.97	6.68	0.26	17.59	30.28
<i>Spirulina maxima</i>	Co/TiO <sub>2</sub>	69.48	8.08	7.65	0.34	14.45	31.44
<i>Chlorella vulgaris</i>	Co/TiO <sub>2</sub>	68.65	7.86	7.32	0.45	15.72	30.70
<i>Nannochloropsis oculata</i>	Zeolite	66.94	7.79	7.51	0.22	17.54	29.72
<i>Spirulina maxima</i>	Zeolite	67.74	8.08	6.83	0.42	16.93	30.59
<i>Chlorella vulgaris</i>	Zeolite	69.50	7.94	6.60	0.41	15.55	31.23
<i>Nannochloropsis oculata</i>	Methanol	68.35	7.66	8.12	0.33	15.54	30.23
<i>Spirulina maxima</i>	Methanol	67.85	7.70	7.35	0.51	16.59	30.07
<i>Chlorella vulgaris</i>	Methanol	67.12	7.03	6.84	0.41	18.6	28.63
<i>Nannochloropsis oculata</i>	Acetone	68.65	8.32	6.43	0.56	16.04	31.43
<i>Spirulina maxima</i>	Acetone	68.23	8.03	6.57	0.51	16.66	30.77
<i>Chlorella vulgaris</i>	Acetone	69.02	7.78	6.32	0.48	16.4	30.75
<i>Nannochloropsis oculata</i>	Toluene	68.33	8.12	7.03	0.50	16.02	30.96
<i>Spirulina maxima</i>	Toluene	68.71	8.31	6.85	0.53	15.6	31.45
<i>Chlorella vulgaris</i>	Toluene	69.03	8.22	6.98	0.54	15.23	31.46

## CONCLUSIONS

This study explored the catalytic and co-solvent effects on hydrothermal liquefaction (HTL) of microalgae for bio-crude production. Three catalysts (Co/TiO<sub>2</sub>, Ni/TiO<sub>2</sub>, and Zeolite) were synthesized and characterized, demonstrating varying bio-crude yields across different microalgae species. Co/TiO<sub>2</sub> and Ni/TiO<sub>2</sub> catalysts significantly enhanced bio-crude yields, with increases of up to 25% and 20%, respectively, compared to non-catalytic HTL. Zeolite, characterized by its high surface area (over 200 m<sup>2</sup>/g) and pore volume (0.5 cm<sup>3</sup>/g), also showed promising bio-crude yields, particularly with *Spirulina maxima*, where a yield increase of 18% was observed. The influence of co-solvents (acetone, methanol, and toluene) on bio-crude yields and composition was investigated. Methanol and acetone enhanced bio-crude yields by 15% and 12%, respectively, through efficient extraction of lipids and carbohydrates. Toluene, while less effective in yield enhancement, enriched bio-crude with aromatics and halides, suggesting potential applications in specialty biofuel formulations. Elemental analysis revealed that catalytic HTL processes with Co/TiO<sub>2</sub> and Ni/TiO<sub>2</sub> increased bio-crude carbon content by 10% and 8%, respectively, compared to non-catalytic HTL. Heating values of bio-crude derived from Co/TiO<sub>2</sub> and Ni/TiO<sub>2</sub> catalytic HTL were measured at approximately 40 MJ/kg, indicating improved fuel properties suitable for biofuel applications. Overall, this study underscores the synergistic benefits of catalysts and co-solvents in enhancing bio-crude yields and quality from microalgae HTL. The findings highlight the potential of Co/TiO<sub>2</sub>, Ni/TiO<sub>2</sub>, and Zeolite catalysts in improving biofuel production efficiency, with implications for sustainable energy development. Future research directions include optimizing catalyst formulations, exploring novel co-solvent systems, and scaling up processes to advance the commercial viability of microalgae-based biofuel production.

## EXPERIMENTAL SECTION

### Materials

The algal species *Nannochloropsis oculata* (Jemmax Nutraceuticals Pvt. Ltd, Tamil Nadu), *Chlorella vulgaris* (Cleanergis Biosciences, Bangalore), and *Spirulina maxima* (Evergreen Agro Creations, Dindigul) were used after sieving to get a uniform size. Dichloromethane (CH<sub>2</sub>Cl<sub>2</sub>), Methanol (CH<sub>3</sub>OH), Toluene (C<sub>7</sub>H<sub>8</sub>), Acetone (CH<sub>3</sub>COCH<sub>3</sub>), Tetra Propyl Ammonium Hydroxide - TPAOH ((C<sub>3</sub>H<sub>7</sub>)<sub>4</sub>NOH), Tetra Ethyl Ortho Silicate - TEOS (Si(OC<sub>2</sub>H<sub>5</sub>)<sub>4</sub>),

Aluminium Nitrate ( $\text{Al}(\text{NO}_3)_3$ ), Sodium Hydroxide ( $\text{NaOH}$ ), Nickel nitrate ( $\text{Ni}(\text{NO}_3)_2 \cdot 6\text{H}_2\text{O}$ ), Cobalt nitrate ( $\text{Co}(\text{NO}_3)_2 \cdot 6\text{H}_2\text{O}$ ) and Titanium dioxide ( $\text{TiO}_2$ ) were purchased from Chemico Glass & Scientific Company – Erode and are of laboratory grade. Also deionized water was used for the study.

### **Preparation of Metal Catalyst over $\text{TiO}_2$**

The metal-supported catalyst was synthesized by dissolving  $\text{Ni}(\text{NO}_3)_2 \cdot 6\text{H}_2\text{O}$  &  $\text{Co}(\text{NO}_3)_2 \cdot 6\text{H}_2\text{O}$  in deionized water to reach a targeted theoretical concentration of 0.75 mol/L. Subsequently, 100 ml of this impregnation solution was blended with 20 g of  $\text{TiO}_2$  and mixed continuously in a 250 ml beaker at ambient temperature (25 °C) for 24 hours, allowing for the effective permeation of metal ions into the  $\text{TiO}_2$  matrix. Once the permeation process was complete, the impregnation liquid was carefully separated through decantation. The impregnation product was then dried at 110°C in an oven to remove residual solvents and moisture for about 12 hours, followed by a controlled calcination procedure in a muffle furnace at 600°C for 4 h. The resulting calcinated catalyst was powdered using mortar and pestle, sieved through an 80-mesh sieve, and securely stored in an air-tight vessel for further characterization and application. This resulting catalyst was labeled as M/ $\text{TiO}_2$ , where the M represents the metal ions.

### **Preparation of Zeolite Catalyst**

The Zeolite catalyst was synthesized using a blend of essential materials such as tetra propylammonium hydroxide (TPAOH), Tetraethyl orthosilicate (TEOS), deionized water, Aluminium Nitrate, and Sodium Hydroxide ( $\text{NaOH}$ ). 6 grams of TPAOH and 22 g of water taken in a beaker and thoroughly mix using a magnetic stirrer. 6.5 g of TEOS was incrementally introduced into the mixture with continuous stirring maintained at a speed from 300 to 400 rpm for 24 h under a consistent temperature range of 70°C to 80°C. A second solution was prepared, composed of 2 g of water, 0.5 g of Aluminium Nitrate, and 0.15 g of  $\text{NaOH}$ . The first solution was cooled to room temperature and the second solution was added in drops with continuous stirring and homogenization for an additional 30 to 45 min. This mixture was then placed in a muffle furnace at 175°C for 4 to 6 h. The resulting zeolite catalyst was allowed to cool to room temperature, desiccated, and stored in an air-tight container for further characterization and application.

### **Catalytic Hydrothermal Liquefaction**

C-HTL process was performed on different catalyst loading (2.5, 5 and 7 wt%) for the three feedstocks. The process condition for the three feedstocks was already optimized in the previous study, hence those conditions were unchanged [33]. The process was performed in a stainless steel autoclave with a capacity of 600 ml. Once, the reactor cooled down to room temperature the contents were emptied into a beaker and DCM was added as the solvent to extract the biocrude. After the specified time, the contents were filtered to remove the biochar, with liquid products transferred to a separating funnel to individually remove the aqueous phase and organic phase. The solvent was recovered using a vacuum separator and the generated biocrude was stored in a closed environment for further processing.

### **Hydrothermal Liquefaction with Co-solvent**

The solvents (methanol, acetone, and toluene) were added along with water at different ratios of 0:100, 25:75, 50:50, 75:25, and 100:0 while keeping the same optimized process conditions of the feedstock as earlier. After the HTL process, a similar procedure was followed to extract biocrude as in section 2.4 with additional care being taken in separating the solvents added along with water. Once, the biocrude was separated through vacuum evaporation it was stored in a closed environment for further processing.

### **Characterization and Quantitative analysis**

Surface characteristics of the catalysts were performed in Zeiss Sigma FE-SEM coupled with EDAX to find the surface structure and the surface chemistry of the catalysts, while the pore analysis was performed using Quantachrome autosorb – IQ-C-XR to identify the pore size distribution and the surface area of the catalysts. The crystallinity and the lattice matrix were identified using an X'Pert<sup>3</sup> x-ray diffraction spectrometer with  $2\theta$  between  $5-90^\circ$  and a scan speed of  $1.8^\circ/\text{min}$ . Agilent Model 8890 GC System with Single Quadrupole Mass Spectrometer (5977B MSD) analyzer was used in identifying the complex organic compounds present in the biocrude. CHNS elemental analysis was done to for the produced biocrude to calculate the higher heating value (HHV) and its suitability to be used as a biofuel.



## ACKNOWLEDGMENTS

The authors would like to emphasize their gratitude towards SAIF, IIT Madras, and PSG COE Indutech, Coimbatore for their support in the material characterization and analysis. Additionally, the authors also express their sincere thanks to the Department of Chemical Engineering and the Department of Food Technology, Kongu Engineering College, Perundurai, Erode for providing the necessary infrastructure and support for the conduct of experiments.

## REFERENCES

1. Agarwala, N. and S. Polinov *J. Adv. Humanit. Soc. Sci.*, **2021**, 2, 1-24.
2. De Caprariis, B., P. De Filippis, A. Petruccio, and M. Scarsella *Fuel*, **2017**, 208, 618-625.
3. Hu, Y., M. Gong, S. Feng, C. Xu, and A. Bassi **2019**, 101, 476-492.
4. López Barreiro, D., W. Prins, F. Ronsse, and W. Brilman **2013**, 53, 113-127.
5. Ravichandran, S.R., C.D. Venkatachalam, M. Sengottian, S. Sekar, S. Kandasamy, K.P.R. Subramanian, K. Purushothaman, A.L. Chandrasekaran, and M. Narayanan *Fuel*, **2022**, 313, 122679.
6. Levasseur, W., P. Perré, and V. Pozzobon *Biotechnol. Adv.*, **2020**, 41, 107545.
7. Sathasivam, R., R. Radhakrishnan, A. Hashem, and E.F. Abd\_Allah *Saudi J. Biol. Sci.*, **2019**, 26, 709-722.
8. Vaz, B.d.S., J.B. Moreira, M.G.d. Morais, and J.A.V. Costa **2016**, 7, 73-77.
9. Osman, A.I., N. Mehta, A.M. Elgarahy, A. Al-Hinai, A.a.H. Al-Muhtaseb, and D.W. Rooney *Environ. Chem. Lett.*, **2021**, 19, 4075-4118.
10. Zhuang, X., J. Liu, C. Wang, Q. Zhang, and L. Ma *Fuel*, **2022**, 313, 122671.
11. SENGOTTIAN, M., C.D. VENKATACHALAM, S.R. RAVICHANDRAN, and S. SEKAR *Studia UBB Chemia.*, **2024**, 69,
12. Gollakota, A., N. Kishore, and S. Gu *Renew. Sust. Energ. Rev.*, **2018**, 81, 1378-1392.
13. Ong, H.C., W.-H. Chen, A. Farooq, Y.Y. Gan, K.T. Lee, and V. Ashokkumar *Renew. Sust. Energ. Rev.*, **2019**, 113, 109266.
14. Hietala, D.C., C.M. Godwin, B.J. Cardinale, and P.E. Savage *Appl. Energ.*, **2019**, 235, 714-728.
15. Biller, P. and A. Ross *Bioresource technol.*, **2011**, 102, 215-225.
16. Biswas, B., A. Arun Kumar, Y. Bisht, R. Singh, J. Kumar, and T. Bhaskar **2017**, 242, 344-350.
17. Chen, Y., Y. Wu, P. Zhang, D. Hua, M. Yang, C. Li, Z. Chen, and J. Liu *Bioresource technol.*, **2012**, 124, 190-198.
18. Cheng, S., C. Wilks, Z. Yuan, M. Leitch, and C.C. Xu *Polym. Degrad. Stabil.*, **2012**, 97, 839-848.

CATALYTIC AND SOLVENT HYDROTHERMAL LIQUEFACTION OF MICROALGAE:  
A STRATEGY FOR RECOVERING FINE CHEMICALS

19. Ross, A., P. Biller, M. Kubacki, H. Li, A. Lea-Langton, and J. Jones *Fuel*, **2010**, 89, 2234-2243.
20. Dong, S., Z. Liu, and X. Yang *Chinese Chem. Lett.*, **2023**, 109142.
21. Zhang, W. and Y. Liang *J. Environ. Chem. Eng.*, **2022**, 10, 107092.
22. LeClerc, H.O., G.A. Tompsett, A.D. Paulsen, A.M. McKenna, S.F. Niles, C.M. Reddy, R.K. Nelson, F. Cheng, A.R. Teixeira, and M.T. Timko *Isience*, **2022**, 25,
23. Toro, R.G., M. Diab, T. de Caro, M. Al-Shemy, A. Adel, and D. Caschera *Materials*, **2020**, 13, 1326.
24. Ganesh, I., A. Gupta, P. Kumar, P. Sekhar, K. Radha, G. Padmanabham, and G. Sundararajan *The Scientific World Jo.*, **2012**, 2012, 127326.
25. Mitta, H., P.K. Seelam, S. Ojala, R.L. Keiski, and P. Balla *Appl. Catal. A-Gen.*, **2018**, 550, 308-319.
26. Saber, M., A. Golzary, M. Hosseinpour, F. Takahashi, and K. Yoshikawa *Appl. Energ.*, **2016**, 183, 566-576.
27. Shakya, R., J. Whelen, S. Adhikari, R. Mahadevan, and S. Neupane *Algal Res.*, **2015**, 12, 80-90.
28. Yang, W., X. Li, S. Liu, and L. Feng *Energ. Convers. Manage.*, **2014**, 87, 938-945.
29. Shuping, Z., W. Yulong, Y. Mingde, I. Kaleem, L. Chun, and J. Tong *Energy*, **2010**, 35, 5406-5411.
30. Jena, U., K.C. Das, and J.R. Kastner *Appl. Energ.*, **2012**, 98, 368-375.
31. Wang, W., Y. Xu, X. Wang, B. Zhang, W. Tian, and J. Zhang *Bioresource Technol.*, **2018**, 250, 474-480.
32. López Barreiro, D., B.R. Gómez, F. Ronsse, U. Hornung, A. Kruse, and W. Prins **2016**, 148, 117-127.
33. Ravichandran, S.R., C.D. Venkatachalam, and M. Sengottian **2023**,
34. Huang, Y., Y. Chen, J. Xie, H. Liu, X. Yin, and C. Wu *Fuel*, **2016**, 183, 9-19.
35. Xu, D., G. Lin, S. Guo, S. Wang, Y. Guo, and Z. Jing *Renew. Sust. Energ. Rev.*, **2018**, 97, 103-118.
36. Han, Y., S.K. Hoekman, Z. Cui, U. Jena, and P. Das **2019**, 38, 101421.
37. Zhang, J. and Y. Zhang *Energ. Fuel*, **2014**, 28, 5178-5183.
38. Cui, Z., F. Cheng, J.M. Jarvis, C.E. Brewer, and U. Jena *Bioresource Technol.*, **2020**, 310, 123454.
39. Han, Y., K. Hoekman, U. Jena, and P. Das **2020**, 13,
40. Jena, U., B.E. Eboibi, and K.C. Das **2022**, 3, 326-341.
41. Masoumi, S., P.E. Boahene, and A.K. Dalai **2021**, 217, 119344.



## CONTRIBUTIONS TO ASSESSMENT AND REMEDICATION OF ACID TARS LAGOONS

Mihaela NICOLAE (TITA)<sup>a</sup>, Ion ONUTU<sup>b</sup>, Daniel TITA<sup>c</sup>,  
Timur CHIS<sup>d</sup>, Bogdan DOICIN<sup>e\*</sup>

**ABSTRACT.** Acid tars, a waste unique to the oil processing industry, pose a significant toxicity risk. These by-products originate from refining certain petroleum fractions, such as oil and paraffin, and are commonly found in the waste streams of crude oil processing. In Romania, particularly in the post-war period, acid tars were predominantly managed through storage. Although advancements in catalytic processes have considerably reduced the generation of acid tars in the Romanian refining industry, an efficient treatment method is still required to address the existing acid tars lagoons. The present research refers to a case study carried out on a laboratory scale for the physico-chemical stabilization/encapsulation of acid tars from a lagoon belonging to a refinery in Prahova-Romania county.

The experimental program aimed at formulating and applying optimal stabilization recipes for acid tar from the selected lagoon was conducted to reduce the total hydrocarbon and toxic metal content, in compliance with Order No. 95 of 12.02.2005 from Romanian legislation. The leaching data showed that the recipes that stabilize and encapsulate acid tar provide a good immobilization capacity for the five heavy metals (Pb, Cd, Cu, total Cr, Ni)

---

<sup>a</sup> Faculty of Petroleum Processing and Petrochemistry, Petroleum-Gas University, Bulevardul București 39, 100680 Ploiesti, Romania; mihaela.tita@upg.ploiesti.ro; Eurototal, Bucharest, Romania; eurototalcomp@eurototal.eu

<sup>b</sup> Faculty of Petroleum Processing and Petrochemistry, Petroleum-Gas University, Bulevardul București 39, 100680 Ploiești, Romania; ionutu@upg-ploiesti.ro

<sup>c</sup> Faculty of Petroleum Processing and Petrochemistry, Petroleum-Gas University, Bulevardul București 39, 100680 Ploiești, Romania; daniel.tita@eurototal.eu

<sup>d</sup> Faculty of Petroleum and Gas Engineering, Petroleum-Gas University, Bulevardul București 39, 100680 Ploiești, Romania; timur-vasile@upg-ploiesti.ro

<sup>e</sup> Faculty of Petroleum Processing and Petrochemistry, Petroleum-Gas University, Bulevardul București 39, 100680 Ploiești, Romania; bogdan.doicin@upg-ploiesti.ro

\* Corresponding author: bogdan.doicin@upg-ploiesti.ro



and As, while their releases are dependent on the pH- and varies with the total hydrocarbon content of the treated tar. The laboratory study carried out and presented in this work, as well as the results obtained after performing the leaching test, allow the extrapolation and application of this stabilization - encapsulation procedure on a macro-in situ scale and the remediation of the lagoon where the acid tar was stored.

**Keywords:** *refinery waste, acid tars, lagoon, encapsulation, stabilization, total petroleum hydrocarbons (TPH), heavy metals and As, leaching test.*

## INTRODUCTION

The oil industry as a whole generates waste from both extraction and refining operations, including drilling fluids, hydrocarbon- and salt-contaminated wastewater, sludge from oil effluent treatment plants, tank cleaning sludge, acid tars, spent catalysts, and bleaching earth. [1,2].

In Romania, in 2014, there were 861 potentially contaminated sites due to petroleum operations (drilling, extraction, transport, processing) [3].

In line with the European Commission's initiatives to remediate hydrocarbon-polluted environments, an area of 1,054,549 square meters was decontaminated, accounting for 84% of the total area recorded at the national level. [4,5].

Among the wastes specific to the oil processing industry, acid tars present a particular *toxicity hazard* [6]. Acid tars were obtained in the late 1800s, by the treatment of refining products with sulfuric acid in synthesis processes [7].

Acid tars also result from the refining of specialty oils, including those used in alternating current transformers, hydraulic systems, medicinal and cosmetic applications, as well as from the production of flotation reagents and the sulfonation of specific hydrocarbons and petroleum fractions. [8, 9, 10, 11, 12].

Romania, like countries such as the USA, UK, the Netherlands, Belgium, Germany, Latvia, Slovenia, Slovakia, China, Zimbabwe, and Ukraine, also stores acid tar in the open air, in spent pits, storage ponds, lagoons, or near landfills. [3,5,6].

The research on the waste lagoons fields in Romania confirms the impossibility of treating acid tars by classical methods (due to their aging), incineration, thermal decomposition, or neutralization, which are techniques with high costs and low economic results [4,13].

In this paper, an experimental study was carried out regarding the selection, evaluation and application of a original variant of treating acid tars from a refinery lagoon in Prahova, Romania. The **stabilization/ encapsulation (S/E)** technology was chosen and applied, which does not destroy the tracked contaminants but keeps them from “leaching” at lower concentrations, safe for the environment [11]. Leaching occurs when water from rain or other sources dissolves and carries away contaminants. We achieved the validation of the process applied by S/E of acid tars by performing the leaching test, a useful method for assessing and evaluating the potential mobility of different contaminants in acid tars and soil.

## RESULTS AND DISCUSSION

### Results

Before applying an in situ remediation technology, it is necessary to know the degree of contamination of the lagoon that will be treated.

Therefore, in the present work it was necessary to provide a rapid but robust characterization of the acidity, the degree of hydrocarbons and heavy metals and As contamination in acid tar, so that appropriate treatment/remediation techniques could then be used.

The characterization of fresh acid tar was conducted by determining key indicators such as pH, total petroleum hydrocarbons (TPH), heavy metals (Pb, Cd, Cu, total Cr, Ni), and As. For the treated tar, additional parameters such as sulfate content and dissolved organic compounds (DOC) were also measured.

The obtained experimental data were analyzed, evaluated and then validated. The samples taken and analyzed from the site of selected lagoon, belonging to a refinery in Romania, confirmed the inhomogeneous composition of the stored acid tar, the values of the main indicators considered and analyzed varying as follows (Figures 1-8):

- pH value between 0.20 and 5.28
- THP content between 48 333 and 477 062 mg/kg dry substance (d.s.)
- Metals content:
  - Lead between 42 and 2235 mg/kg d.s.
  - Cadmium content between 1 and 126 mg/kg d.s.
  - Copper between 2.6 and 789 mg/kg d.s.
  - Nickel between 2 and 859 mg/kg d.s.
  - Total chromium between 3 and 452 mg/kg d.s.
- Arsenic content: between 1.4 and 589 mg/kg d.s.
- Cyanides content between 0.013 and 0.380 mg/kg d.s.

- Chlorides content between 9.08 and 844 mg/kg d.s.
- Sulphate content between 54.01 and 618.9 mg/kg d.s.
- DOC between 108 and 2047 mg/kg d.s.

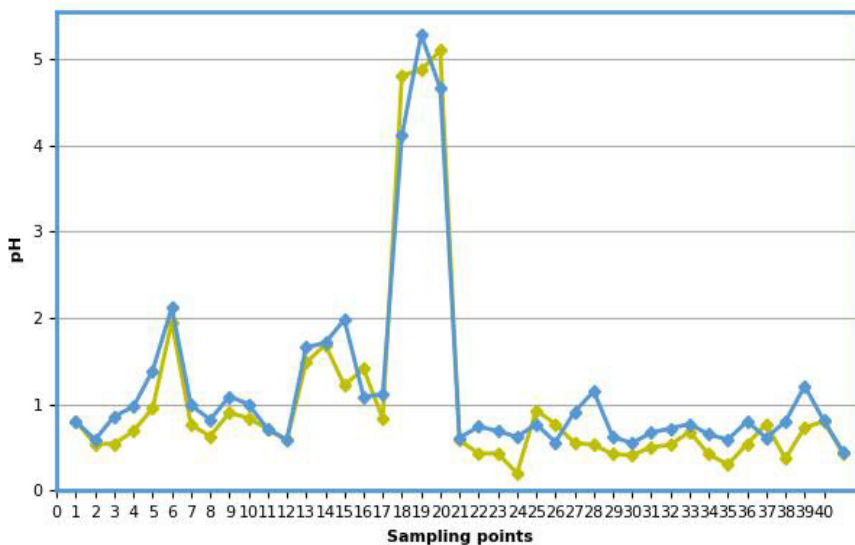


Figure 1. pH values of untreated acid tar samples.

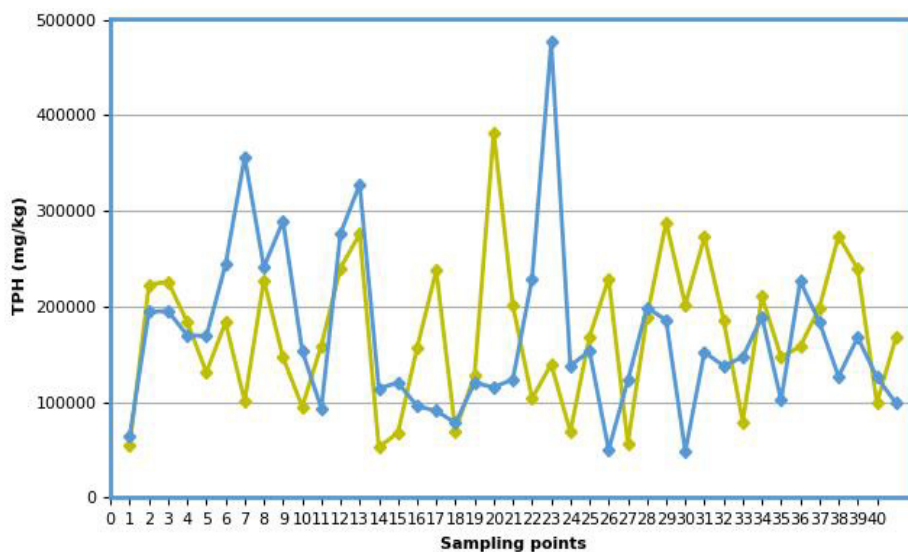


Figure 2. TPH content of untreated acid tar samples.

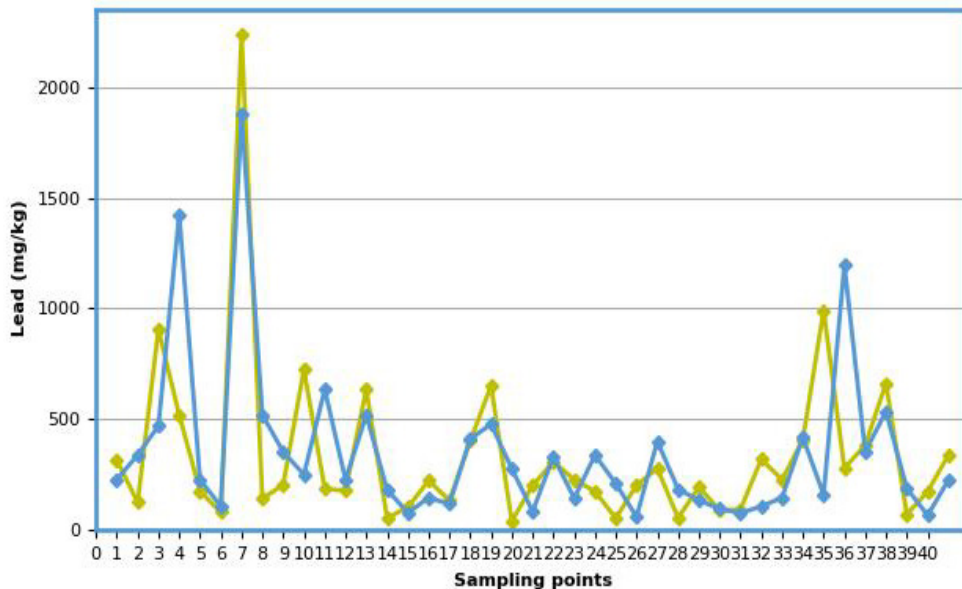


Figure 3. Lead content of untreated acid tar samples.

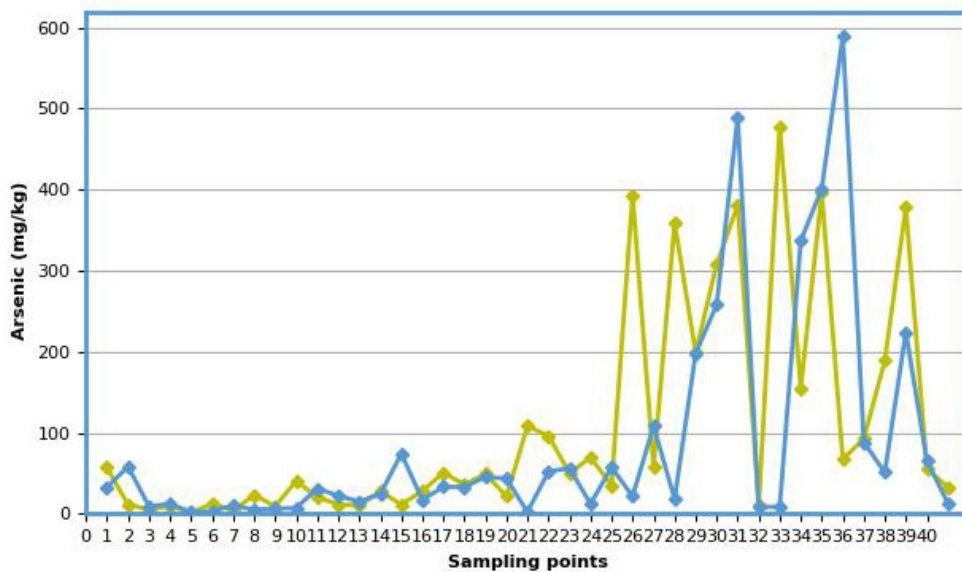


Figure 4. Cadmium content of untreated acid tar samples.



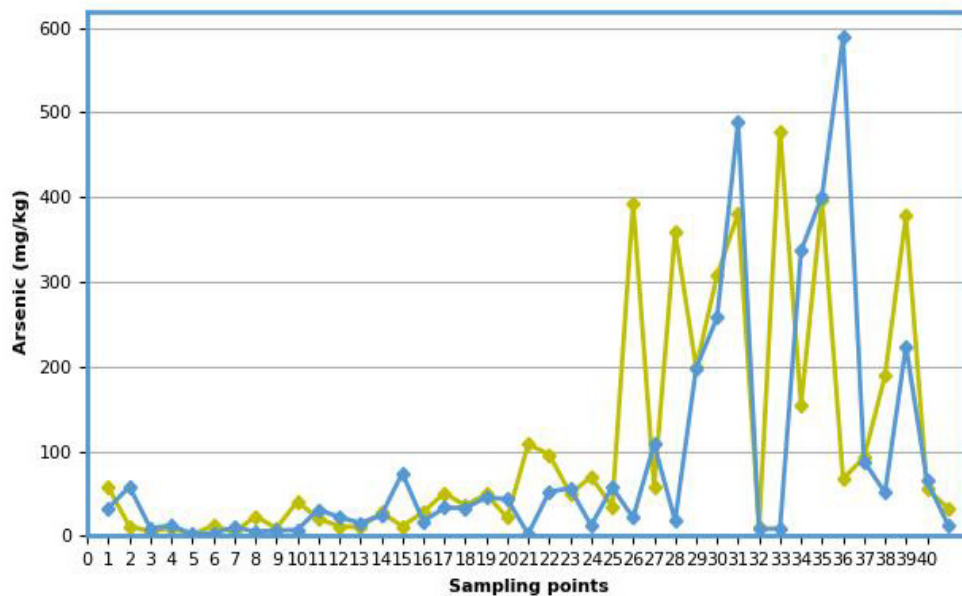


Figure 5. Copper content of untreated acid tar samples.

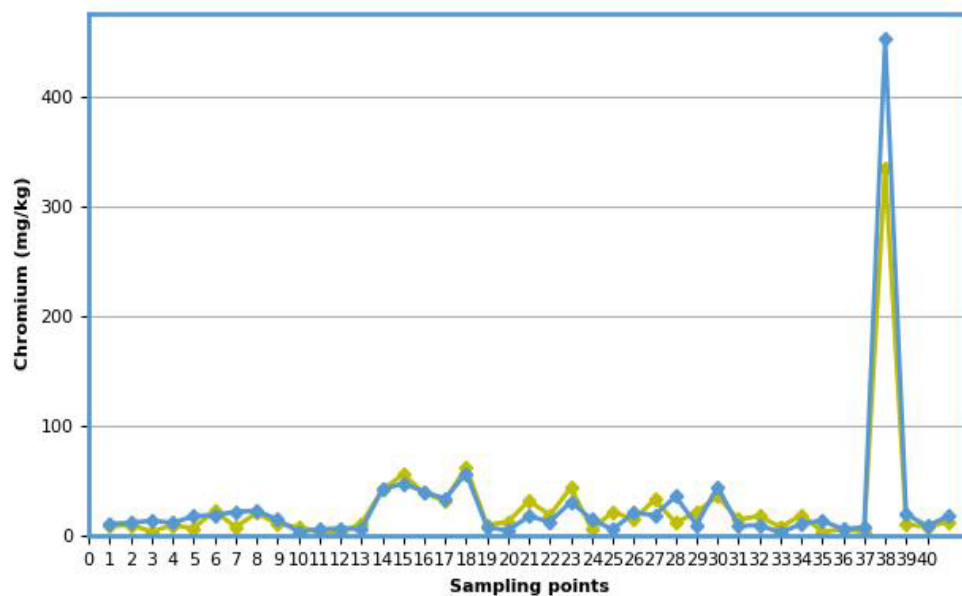


Figure 6. Chromium content of untreated acid tar samples.

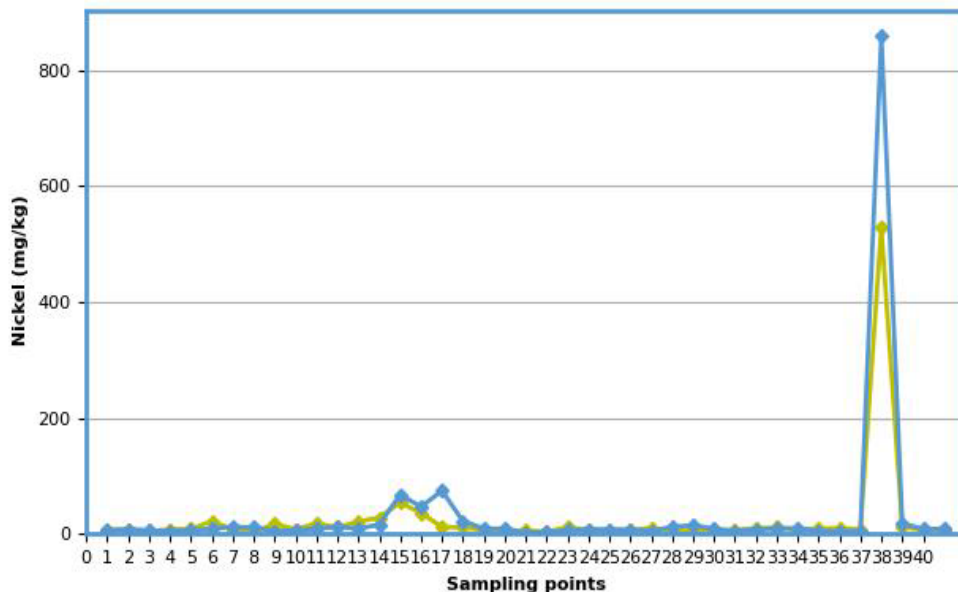


Figure 7. Nickel content of untreated acid tar samples.

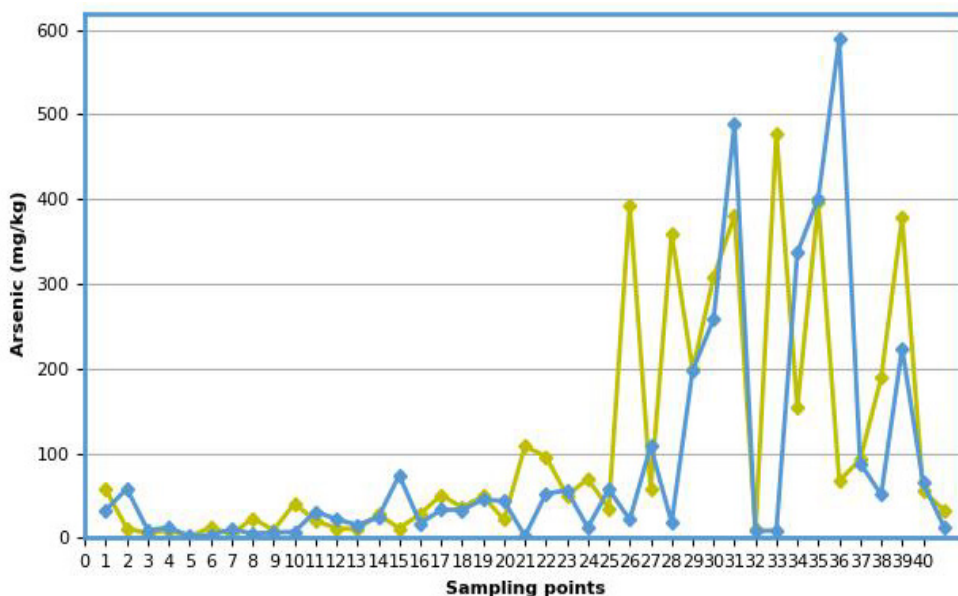


Figure 8. Arsenic content of untreated acid tar samples.

In the stabilization/encapsulation treatment applied to acid tars, the following substances were used as additives and filler materials: cement, sand, calcium oxide, sodium hydroxide, bentonite, emulsifiers, strengthening additives, absorbents, and sodium metasilicate (Table 1). The remainder, up to 100%, was composed of the acid tar undergoing stabilization.

The identification and selection of reagents used in the experiment were based on a review of technical literature from the theoretical research, as well as the author's experience in implementing stabilization and encapsulation projects.

**Table 1.** The composition for the neutralization, stabilization and encapsulation of acid tar

<b>Ingredient</b>	<b>(%)</b>
Cement	3-20%
Sand	2-5%
Calcium oxide	3-8%
Sodium hydroxide	1% - 10%
Bentonite	1-2,8%
Emulsifier	1-2%
Strengthening additives	1%

Finally, three recipes were established for treating acid tars, according to Table 2.

The first recipe was applied for tars with high pH values and low TPH values (acid pH value is 10.3).

The third recipe was used for tars with low pH values and high TPH values (acid pH value is 8.5).

For tars with medium TPH values, the second recipe gave the best results (acid pH value is 9.4).

It was observed that the TPH content, pH values, and other indicators, including the concentrations of various metals in the initial tar, affect the efficiency of the stabilization recipe applied. All these efforts culminated in the acquisition of two patents: one international and one national. [15,16].

The literature suggests that the effectiveness of stabilization/encapsulation technologies largely depends on the quality and intrinsic properties of the additives and binders used in the treatment recipes. This highlights the importance of selecting appropriate materials to achieve optimal performance in these technologies. [17-21].

**Table 2.** Encapsulation tar acid recipes

Ingredient	recipe 1	recipe 2	recipe 3
Sodium metasilicate, %	0.30	0.50	0.80
Emulsifier	1.00	3.50	4.00
Calcium oxide	8.00	3.00	7.00
Magnesium oxide	0.10	0.20	0.30
Bentonite	1.00	2.00	2.80
Sand	2.00	5.00	3.00
Cement	3.00	5.00	8.00
Reinforcing additives	1.00	1.00	1.00
Absorbent (oil absorbent)	1.00	1.00	1.00
Sodium hydroxide	1.00	1.00	1.00

## Discussions

The laboratory-scale application of the encapsulation stabilization technology of the acid tar and analysis of the experimental results may lead to the following conclusions:

- Increasing the pH from values between 0.2 and 5.28 (in untreated acid tar) to values between 8.7 and 10 (in the leachate) positively impacted leaching performance, including the speciation of metal contaminants.

The highest concentration of TPH was detected in all acid tar samples, and at a depth of 30 cm, this concentration decreased by approximately fourfold. In the present study, Portland cement played a significant role in immobilizing Cr, Cu, and Pb. The degree of immobilization improved with increased curing time of the hardened material. The high pH of the cement facilitates the retention of metals as insoluble hydroxide or carbonate salts within the hardened structure. Additionally, calcium oxide and the emulsifier contributed to the transition of metals from a volatile phase to a stable phase. Specifically, the calcium oxide enhanced the immobilization of Cd, Cu, Ni, and Pb.

- The stabilization/encapsulation technology applied significantly reduced the mobility of cadmium, copper, chromium, lead, nickel, and arsenic in the acid tar, achieving a concentration decrease of over 95% for the target metals group (Pb, Cd, Cu, Cr, Ni).
- As observed in the published literature, the leaching of some heavy metals is largely influenced by the pH of the leachate. [14].

- Lead (Pb) concentrations ranged from 0.0003 to 0.0056 mg/kg in all stabilized samples.
- The pH of the samples from which metals were determined ranged from 8.7 (with a Pb content of 0.008 mg/kg) to 10.0 (with a Pb content of 0.002 mg/kg).
- Cadmium (Cd) concentrations in the eluate/leachate samples ranged between 0.0001 and 0.005 mg/kg.
- As mentioned in the literature, cement benefits Cd immobilization in all conditions [25].
- Copper (Cu) concentrations were found to vary from 0.00083 to 0.0161 mg/kg.
- Chromium (Cr), one of the most toxic metals, was measured in the eluate collected after acid tar treatment, with concentrations ranging from 0.0010 to 0.084 mg/kg.
- The immobilization of Cr<sup>6+</sup> by the cement-based encapsulation/stabilization technology was achieved through the formation of a complex calcium chromate (CaCrO<sub>4</sub>), which has low solubility.

Nickel (Ni) concentrations in the eluate ranged from 0.0015 to 0.091 mg/kg dry substances. It was observed that Ni and Cd hydroxides are incorporated into the hydrated cement matrices, which provides effective immobilization for Ni.

- Arsenic (As) was distributed across a wide range of values in untreated tar, from 1.4 to 589 mg/kg dry substances, and in the eluate, from below 0.001 to 0.402 mg/kg.
- Cyanide concentrations in untreated acid tar ranged from 0.013 to 0.368 mg/kg dry substances, but in the leachate, they decreased to below 0.001, falling below the detection limit.
- There was a reduction in the concentration of chlorides, sulfates, and dissolved organic compounds (DOC) in the leachate.
- The DOC content ranged from 108 to 2047 mg/kg, with three values exceeding 1000 mg/kg.
- This research suggests that applying the stabilization and encapsulation process on a macro scale to acid tar with TPH values below 200,000 mg/kg would reduce the heavy metal content (Pb, Cd, Cu, Cr, Ni) and arsenic (As) to below the imposed limits and lower DOC to below 1000 mg/kg dry substance.

**Table 3.** Acid tar stabilization/encapsulation results

Acid tar	Leachate
<ul style="list-style-type: none"> <li>• pH: between 0,2 and 5,28</li> <li>• TPH between 48 333 and 477 062 mg/kg s.u.</li> <li>• Metals with values above the permitted limits: <ul style="list-style-type: none"> <li>- Lead between 42 and 2235 mg/kg d.s.</li> <li>- Cadmium between 1 and 126 mg/kg d.s.</li> <li>- Copper between 2.6 and 789 mg/kg d.s.</li> <li>- Total chromium between 3 and 452 mg/kg d.s.</li> <li>- Nickel between 2 and 859 mg/kg d.s.</li> <li>- Arsenic between 1.4 and 589 mg/kg d.s.</li> </ul> </li> <li>• Cyanides with values between 0.013-0.368 mg/kg d.s.</li> </ul>	<ul style="list-style-type: none"> <li>• pH: between 8.7 and 10.0</li> <li>• THP between 263 and 3009 mg/kg</li> <li>• Metals with values above the permitted limits: <ul style="list-style-type: none"> <li>- Lead between 0.0003 and 0.0056mg/kg</li> <li>- Cadmium between 0.0001-0.0050 mg/kg</li> <li>- Copper between 0.00083 and 0.0161 mg/kg</li> <li>- Total chromium between 0.0010 and 0.084 mg/kg</li> <li>- Nickel between 0.0015-0.091 mg/kg d.s.</li> <li>- Arsenic between LQ and 0.402 mg/kg d.s.</li> </ul> </li> <li>• Cyanides with values &lt;0.001 (LQ)</li> <li>• Chloride content between 9.08 and 844 mg/kg</li> <li>• Sulphate content between 54.01 and 618.9 mg/kg</li> <li>• DOC between 108 and 2047 (with 3 values above 1000 mg/kg)</li> </ul>

In conclusion, the effectiveness of the treatment for the studied acid tar is evident from the fact that the initial acid tar contained levels of representative contaminants above the maximum allowed limits. In the stabilized leachate, however, these values were significantly reduced, with some even falling below the quantification limits of the determination methods (Table 3).

## CONCLUSIONS

In the literature, there are partial data on the pH, the content of hydrocarbons and heavy metals in the contaminated soil in the area of oil refineries, and even less in the acid tars.

There are no data available on the level of hydrocarbon and heavy metal concentrations in the acid tar lagoons, before the remedial treatment, and these data are almost completely missing for the lagoons subjected to the remedial processes.

Additionally, there is limited information on organic leaching from acid tars following the application of stabilization/encapsulation technology, as well as on the effects of organics on complex setting reactions that may alter the cement matrix. In this article, all these previously mentioned aspects are

covered, associated with data regarding the application of original recipes for the stabilization/encapsulation of acid tars from refinery lagoons.

The article presents scientific information published for the first time regarding the correlation of pH values with the concentrations of TPH and heavy metals (Pb+Cd+Cu+Cr+Ni) and As following the application of a complex process of neutralization, stabilization and encapsulation of acid tar from lagoon from a refinery in Romania.

To emphasize that the correlation of the pH, of the TPH content with the level of heavy metals and As in a lagoon allow the extrapolation and application of this stabilization - encapsulation procedure on a macro-in situ scale and the remediation of the lagoon where the acid tar was stored.

## EXPERIMENTAL

In this paper, the experimental program involved the following steps:

- collection, codification and preparation of acid tar samples for testing (Figure 9);
- characterization of the initial samples;
- sample homogenization;
- performing chemical tests (determination of pH, TPH and heavy metal content);
- carrying out treatability tests;



**Figure 9.** Acid tar, (a) sampling area; (b) acid tar sample analysis, evaluation and validation of treatability test results by performing leaching tests.

- Conducting tests by mixing reactants with acid tar samples and preparing formulations for subsequent testing;
- optimization of the mix design and selection of the mix design verification phase (from three recipes);
- preparation of the final mix design and performing treatability testing.

Considering the area of the site (a lagoon surface area of about 100 000 m<sup>2</sup>), a number of 82 sampling points were chosen for the 2 depths (41 samples each for the two depths of 5 and 30 cm, respectively), which corresponds to the need for proper characterization of the acid tar on site. The acid tar samples were collected in boxes on which the sampling depth and the sample number were noted (Figure 9).

For the collection of acid tar samples from the depth of 5-30 cm, sampling probes was used a standard *auger set (with bayonet connection)*. Once the samples were collected, proper homogenization were performed prior to initial (baseline) characterization.

In this phase, the experimental data were statistically analyzed using artificial intelligence (Data Science) to accurately predict the properties of acid tars from waste lagoons and their associated leachate. Additionally, the authors developed a software program employing Machine Learning to estimate key properties of acid tars, such as pH, total petroleum hydrocarbons (TPH), metals, and cyanides. The program evaluates five Machine Learning models (Linear Regression, Ridge, Lasso, Elastic Net, and Decision Tree) and selects the one with the best accuracy, as indicated by the Mean Absolute Error [24]. Given the high values of the mentioned indicators (pH, TPH, metals, and As) exceeding legal limits, several recipes were formulated, prepared, and tested. Ultimately, three representative recipes were selected (Table 2). After each recipe was applied, the acid tar samples were homogenized, mixed, and tested. Based on the values of TPH, pH, and metal concentrations, one of the recipes listed in Table 2 will be applied. The three formulated recipes are distinguished by:

- Constant concentrations of strengthening additives, absorbent, and sodium hydroxide (approximately 1% each)
- Variable amounts of emulsifier, synthesized at 1%, 3.5%, and 4%
- Increasing cement concentration, ranging from 3% in recipe 1 to 8% in recipe 3
- Variable concentrations of calcium oxide, from 8% in recipe 1 to 7% in recipe 3



- Increasing concentration of bentonite, from 1% in recipe 1 to 2.8% in recipe 3
- a relatively constant increase is noted for sodium metasilicate (0.30%, 0.50% and 0.80% respectively - recipe 3).

*Batch leaching test: The validation of the proposed recipes for acid tar was conducted by ensuring that the indicators of the leachate/eluate from the treated acid tar met the maximum values allowed for leachate as specified by Order 95/2005. The leaching test was performed according to SR EN 12457-2/2003 – Waste Characterization: Leaching – Compliance Verification Test for Granular Waste and Sludge Leaching. This test involved contacting the waste sample with a leaching agent (water) at a mass ratio of waste/leaching agent (L/S) = 10 l/kg, maintaining this contact for 24 hours, separating the leachate, and analyzing the eluate to determine the relevant indicators.*

Analytical determinations on the collected samples were carried out according to the following standardized methods:

- SR EN ISO16703:2011 – Soil quality. Determination of the hydrocarbon content in the C10–C40 range by gas chromatography,
- SR EN 16192:2012 – Characterization of waste. Leachate analysis,
- SR ISO 11465:1998 – Soil quality. Determination of dry matter and water content relative to mass. gravimetric method,
- SR EN ISO 9377-2-2002 – Water quality. Determination of the hydrocarbon index,
- SR ISO 10523:2009- Determination of pH,
- Method EPA413.2 and 418.1 ASTM, method D7066-04-Total content of hydrocarbons C10-C40 HP by IIR spectrometry with the INFRACAL 2 analyzer,
- SR EN ISO 15586:2004-Determination of trace metals by atomic absorption spectrometry with a graphite furnace,
- SR ISO 11047/1999-Determination of lead with flame atomic absorption spectrophotometer Xplor AA Dual GBS Scientific,
- Determination of the content of heavy metals with a mobile EDXRF spectrometer with X-ray detection for the rapid detection of trace elements from Mg (Z = 12) to U (Z = 92),
- ASTM D 516-2016-Determination of sulphates with UV-VIS spectrometer DR 3900 Hach,
- SR ISO 9297: 2001-Determination of chlorides with UV- VIS spectrometer DR 3900 Hach
- Determination of cyanides content with UV - VIS spectrometer DR 3900 Hach.

## REFERENCES

1. M.R. Riazi; *Characterization and Properties of Petroleum Fractions*, Publisher: ASTM International, USA, **2005**; pp. 20-25
2. J.S. Alshammari; F.K. Gad; A.M., Elgibaly; A.R., Khan; *Am. J. Environ. Sci.* **2008**; 4, 353-361.
3. S. Kuppusamy; T. Palanisami; T. Megharaj; M. Naidu; K. Venkateswarlu; In-Situ Remediation Approaches for the Management of Contaminated Sites: A Comprehensive Overview, *Rev. Environ. Contam. T.*, **2016**; 236, 1-115.
4. <https://apmnt.anpm.ro/-/situri-potential-contaminate>, (potential site contained by oil) (accessed on 3.12.2023).
5. [https://ec.europa.eu/eurostat/statistics-explained/index.php?title=Waste\\_statistics#Total\\_waste\\_generation](https://ec.europa.eu/eurostat/statistics-explained/index.php?title=Waste_statistics#Total_waste_generation), (accessed on 3.12.2023).
6. T. Chis; A.E Sterpu; O.V. Săpunaru; *Chem. Eng.* **2022**, 6(3), 41.
7. V.A. Kolmakov; D.F. Grishin; A.D. Zorin; V.F. Zanozina; *Pet. Chem.* 47 (6), 379-388.
8. X. Hao; C. Smith; Physical and chemical properties of acid tars. *Consoil 2005*, 9th International FZK / TNO Conference on Soil-Water Systems, Bordeaux Convention Center, Bordeaux France, 2005.
9. P. Catney; P. Lawson; P. Palaseanu-Lovejoy; S. Shaw; T. Smith; T. Stafford; T. Talbot; X. Hao; Acid tars lagoon: risks and sustainable remediation in an urban context, in: SUBR: IM Public Conference on Regeneration and Renewal, London, UK, **2005**.
10. A.F. Frolov; A.N., Aminov; S.D., Timrot; *Chem. Tech. Fuels Oils*, **1981**; 17 284–288.
11. D.J. Nancarrow; N.J. Slade; J.E. Steeds; Land Contamination: Technical Guidance on Special Sites: Acid Tar Lagoons, *R&D Technical Report P5-042/TR/04, WS Atkins Consultants Limited*, **2001**.
12. I. Onuțu; M. Tita; *Scientific Papers. Series E. Land Reclamation, Earth Observation & Surveying, Environmental Engineering*, Vol. VII, **2018**, pp. 140-145.
13. X. Zeng; U. Ichiro; I. Naruse; F. Wang; H. Zhennan; X. Guangwen; *Carbon Resour. Convers.*, 3, **2020**, 1-18.
14. <https://legislatie.just.ro/Public/DetaliuDocumentAfis/59751>, (accessed on 3.12.2023).
15. WO/2021/221524 Composition and process for in situ treatment of acid tar and contaminated soil WO - 04.11.2021, Int. Class B09C 1/00 Appl. No PCT/RO2021/000002 Applicant TITA, Mihaela Inventor TITA, Mihaela, <https://patents.google.com/patent/WO2021221524A1/en> (accessed on 3.12.2023). RO134684 Compoziția și procesul de stabilizare și încapsulare a gudronului acid și a solului contaminat situ, <https://patentimages.storage.googleapis.com/fd/d6/92/c3b1247266e173/RO134684A0.pdf>, (accessed on 3.12.2023).
16. D.D. Milne; Acid tar: production, treatment and disposal. MSc thesis, Department of Civil Engineering, Imperial College of Science and Technology, University of London, **1985**, 75pp.

17. D. McNeil; Coal Carbonisation Products, in: D.D. Milne, A.I. Clark, R. Perry; *Waste Manag. Res.*, 1986, 4, 407–418.
18. M.N. Puring; A.V. Neyaglov; T.A. Kruglova; N.A., Bitulev; N.A. Gorbacheva; Y.V. Startsev; *Chem. Tech. Fuels Oils* **1990**, 26, 32–35.
19. D. Banks; N.L. Nesbit; N.L., T. Firth; S. Power; *Special Publication*, vol. 128, Geological Society, London, **1998**, 283–311.
20. Restoration of Acid Tar Lagoons,  
<http://www.acidtarlagoons.org.uk/ACIDTARS.htm>, (accessed on 3.12.2023).
21. E.I. Obiajunwa; D.A. Pelemo; S.A. Owalabi; M.K. Fasaii; A. Johnson-Fatokun; *Nucl Instrum Methods Phys Bull*, **2002**, 194, 61–64.
22. V. Rajaganapath; F. Xavier; D. Sreekumar; P.K. Mandal; *J. Environ. Sci. Technol.*, **2011**, 4 (3), 234–249.
23. M. Tita; I. Onuțu; B. Doicin; *Appl. Sci.* **2024**, 14, 3382.
24. D. Wang, Q. Wang; *Cem. Concr. Res.*, **2022**, 161 (11) 1-20.

# A PROCEDURE FOR THE GRAVIMETRIC QUANTIFICATION OF TOTAL ORGANIC CARBON AND CARBONATES IN NATURAL ROCKS FOCUSED ON MINERAL AND COAL PROCESSING

Javier E. VILASÓ-CADRE<sup>a\*</sup> ,  
Iván A. REYES-DOMÍNGUEZ<sup>a,b\*</sup> , Juan J. PIÑA<sup>c</sup> 

**ABSTRACT.** This paper presents a gravimetric method for the quantification of total organic carbon by ignition at 1100°C and carbonates by acid dissolution in rock samples containing coal. Two minerals (CM-1 and CM-2) and a sub-bituminous coal (SBC) were used in the study. The mineralogical characterization of the samples was performed by X-ray diffraction and scanning electron microscopy. This revealed the presence of calcite in samples CM-1 (20.4%) and CM-2 (74.7%), dolomite in CM-2 (0.7%), and graphite in sample SBC (42.6%). To eliminate carbonates, the samples were treated with 4 mol/L HCl, which allowed quantification. Results of the carbonate gravimetric quantification were compared with those obtained with a calcimeter. A significant difference was observed for the sample CM-2 (70.3% versus 63.4% by calcimetry,  $p$ -value = 0.0042). For the sample without carbonates, no differences were observed for loss on ignition without and with the acid treatment, so this is not necessary for this type of sample. A morphological study showed no significant surface change after acid treatment, but fracture of iron oxide particles was observed in CM-1 and CM-2 after heat treatment. In this study it was demonstrated that rock mineralogy is essential to correctly analyze organic and inorganic carbon content.

**Keywords:** *total organic carbon, gravimetry, carbonates, coal, mineralogy*

<sup>a</sup> *Institute of Metallurgy, Autonomous University of San Luis Potosí, San Luis Potosí 78210, Mexico*

<sup>b</sup> *National Council of Humanities, Sciences, and Technologies of Mexico (CONAHCYT), Mexico City 03940, Mexico*

<sup>c</sup> *Division of Molecular Biology, Instituto Potosino de Investigación Científica y Tecnológica, A.C. (IPICYT), San Luis Potosí 78216, Mexico*

\* *Corresponding authors: a321418@alumnos.uaslp.mx, alejandro.reyes@uaslp.mx*



## INTRODUCTION

Total organic carbon (TOC) and inorganic carbon, the latter mainly as carbonates, are important chemical parameters for the characterization of samples such as soils, rocks, biomass, minerals, and some artificial materials [1–3]. They are also interesting parameters in water samples, since TOC in particular is a measure of the amount of organic matter present, which can be a toxicological problem in high amounts [4,5].

Although coal is not technically a mineral, it is considered as such in the context of coal processing. TOC quantification is especially important in solid samples containing coal because it is related to the potential as a fuel or its use as a carbon source, among others [6,7]. TOC and carbonates are essential determinations for coal beneficiation.

There are many analytical methods for determining TOC, the most commonly used being the instrumental method, the gravimetric method, and the volumetric method. Even within these, there is a wide variety of techniques. The instrumental method, commonly referred to as a TOC analyzer, is based on the exhaustive oxidation of organic matter and the detection of the  $\text{CO}_2$  produced. When a catalyst is used, combustion requires a lower temperature. Chemical oxidation is commonly used with persulfate ion, which also occurs under heat-catalyzed conditions, radiation, or even both. While the instrumental method is preferable, such an analyzer is not always available in the laboratory. This forces the use of less expensive methods such as gravimetry, volumetry, or UV-vis molecular absorption spectrophotometry [8–10].

The gravimetric method for TOC is also a favorite, although it usually has some limitations. It is based on the oxidation of organic matter at an elevated temperature in a muffle, with quantification by the difference in weight before and after. It is therefore a gravimetric method by volatilization. The method actually measures the loss on ignition (LOI), which is related to the TOC by a proportionality factor. It is a method that looks simple, but in reality it is not, because the presence of carbonates and other volatile inorganic substances affects the result, so prior stages of removal of these are required. This brings up an important problem, which is that a unique procedure for the determination of TOC by gravimetry is not possible for all solid samples, but it is necessary to know the qualitative composition to establish a series of analytical steps to ensure a reliable TOC result. This is one of the main problems addressed in this work for natural samples with coal content [8–12]. Artificial intelligence has also reached TOC methods, for example, machine learning has been implemented for estimation based on mineralogical composition [2].

The volumetric redox method is based on wet oxidation with potassium dichromate and sulfuric acid. Part of the potassium dichromate is reduced to  $\text{Cr}^{3+}$ , while the excess is titrated with  $\text{Fe}^{2+}$ , usually from Mohr's salt or  $\text{FeSO}_4$ ,

using ferroin as an indicator. The volumetric method has been carried out in various ways. This is the same basis as the spectrophotometric method for TOC, but the quantification is done by measuring the absorbance at the wavelength of the  $\text{Cr}^{3+}$  ion, which is close to 600 nm [9–11].

Carbonates, on the other hand, are potential interferences in the ignition-based TOC determination. This occurs because carbonates volatilize at a temperature lower than that at which the combustion of organic matter is completed. Therefore, it is important to quantify and eliminate them when determining TOC in mineral samples, where they are usually abundant [9,10].

Establishing an analytical method for TOC in mineral samples containing coal can be complicated because existing techniques are highly dependent on the chemical characteristics of the rock and the composition of mineral matrices is highly variable. This work presents a simple procedure for the quantification of TOC by the loss-on-ignition gravimetric method in mineral samples containing coal. The method takes into account the effect of carbonates and assumes their quantification as part of a step before TOC quantification. This procedure is mainly focused on the determination of TOC and carbonates in mineral and coal processing as a quantitative parameter in stages such as froth flotation.

## RESULTS AND DISCUSSION

### Physicochemical and mineralogical characterization of the samples

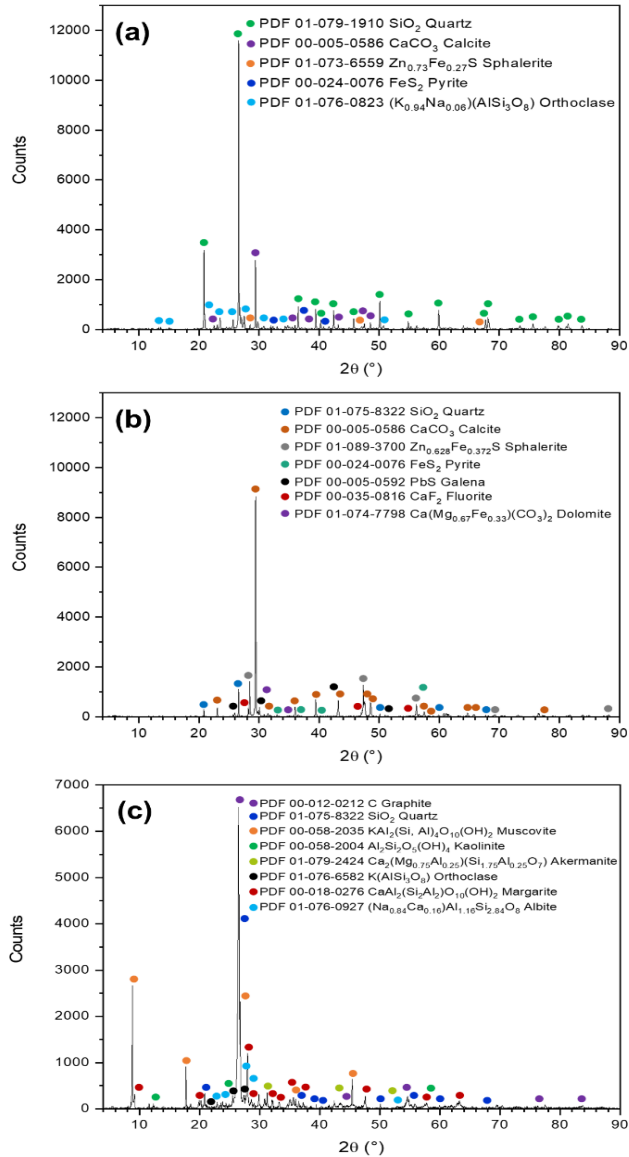
For this work, two carbonaceous mineral rocks (CM-1 and CM-2) from Mexican metallic sulfide processing mines were used. The third sample was a sub-bituminous coal (SBC) from a Mexican coal mine. The moisture and pH were determined for flotation studies and are presented in Table 1 [13,14].

**Table 1.** Properties of the mineral samples used in this work [13,14]

Sample	Moisture (%)	pH
CM-1	0.83	8.1
CM-2	0.33	7.8
SBC	0.58	7.0

CM: Mineral with coal content, SBC: Sub-bituminous coal

Figure 1a shows the XRD pattern of sample CM-1. It can be observed that the crystalline phases composing this sample are quartz, calcite, sphalerite, pyrite, and orthoclase. This means that this is a sample with a content of metallic sulfides and minerals of the silicate group. In addition, the presence of carbonate (calcite), which is the analytical objective of this work, is demonstrated by this



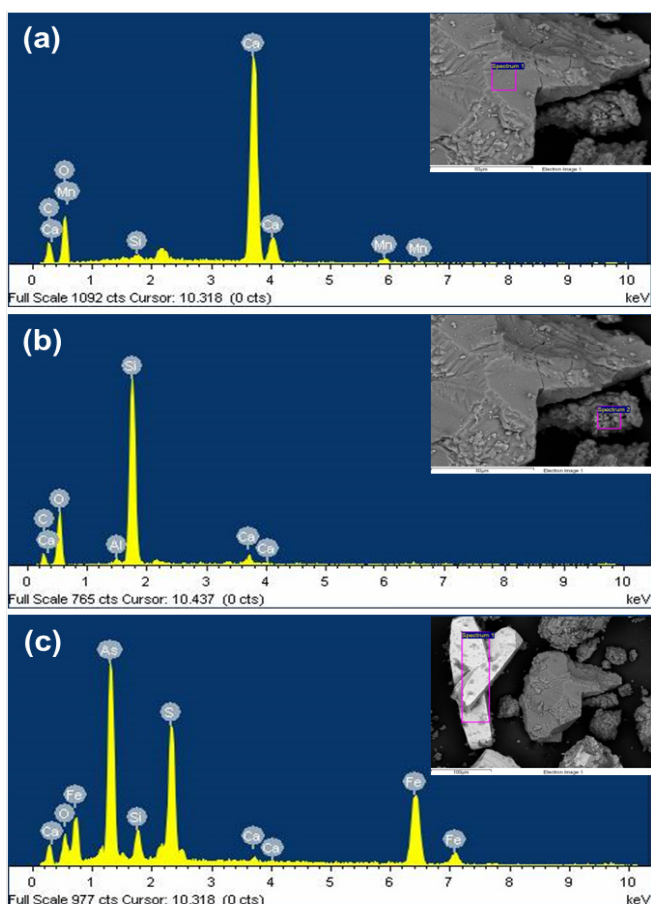
**Figure 1.** X-ray diffractograms: (a) Sample CM-1, (b) Sample CM-2, (c) Sample SBC.

technique. In the case of sample CM-2 (Figure 1b), something similar happens, but the variety of sulfide minerals is greater. Fluorite, calcite, and dolomite are also present. Calcite is the most common carbonate phase found in nature.

A PROCEDURE FOR THE GRAVIMETRIC QUANTIFICATION OF TOTAL ORGANIC CARBON AND CARBONATES IN NATURAL ROCKS FOCUSED ON MINERAL AND COAL PROCESSING

There are other  $\text{CaCO}_3$  phases such as aragonite and vaterite, but they are less stable. Dolomite is a carbonate of calcium and magnesium formed by substitution in the limestone rock. In this case, dolomite phase has iron in the composition. In the case of the sample SBC (Figure 1c), there is no calcite phase or other carbonate, and there is a greater variety of silicates than in the previous samples. A graphite phase is observed in this sample, which is consistent with the fact that it is a coal.

Figure 2 shows the EDS spectra of different particles from sample CM-1. The morphological aspects of the samples will be discussed later in this paper. The three spectra show chemical elements associated with metallic sulfides, calcite, and silicates, showing in principle some agreement with the XRD results, although this is not entirely the case since it should be noted in Figure 2c

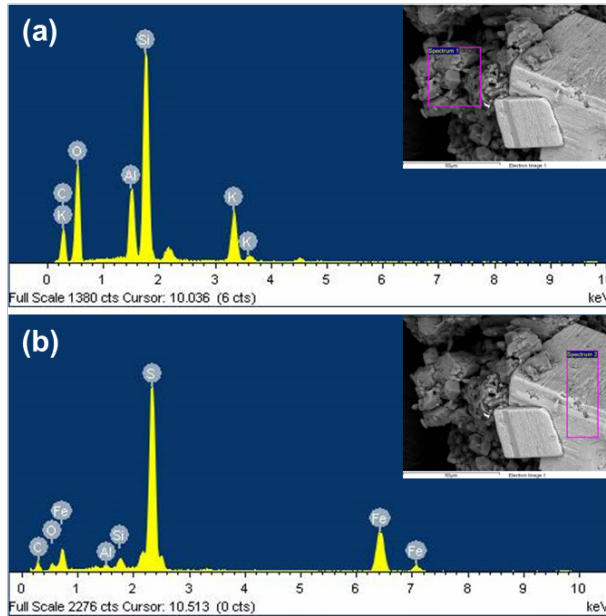


**Figure 2.** EDS spectra for different particles of sample CM-1 identified by SEM.



that the elemental composition of the particle corresponds to arsenopyrite, a mineralogical phase not detected by XRD. On the other hand, diffraction did not reveal any Mn-containing phase (Figure 2a), which is probably due to an amorphous component or an elemental substitution not identifiable by XRD.

Figure 3 shows the EDS spectra of two particles that, although appearing together, correspond to different minerals. In the case of Figure 3a, an elemental composition is observed which is consistent with the identification of silicates by XRD. In the case of Figure 3b, a composition mainly of sulfur and iron is observed, which can be associated with the pyrite content previously identified in the diffractogram. In general, the results of Figure 3 confirm the XRD identifications.



**Figure 3.** EDS spectra for different particles of sample CM-2 identified by SEM.

Figure 4 shows the EDS spectra of various particles from the sample SBC. In this case, more particles were analyzed because a greater variety was observed in the microscopic study. An elemental composition of the particles consistent mainly with silicates is observed. The calcium identified is associated with akermanite, margarite, and albite, unlike the previous samples, where this element was mainly associated with carbonates. Note that, in this sample, the presence of metallic sulfides is not identified by any method, but the presence of iron oxides can be inferred considering Figure 4e.

A PROCEDURE FOR THE GRAVIMETRIC QUANTIFICATION OF TOTAL ORGANIC CARBON AND CARBONATES IN NATURAL ROCKS FOCUSED ON MINERAL AND COAL PROCESSING

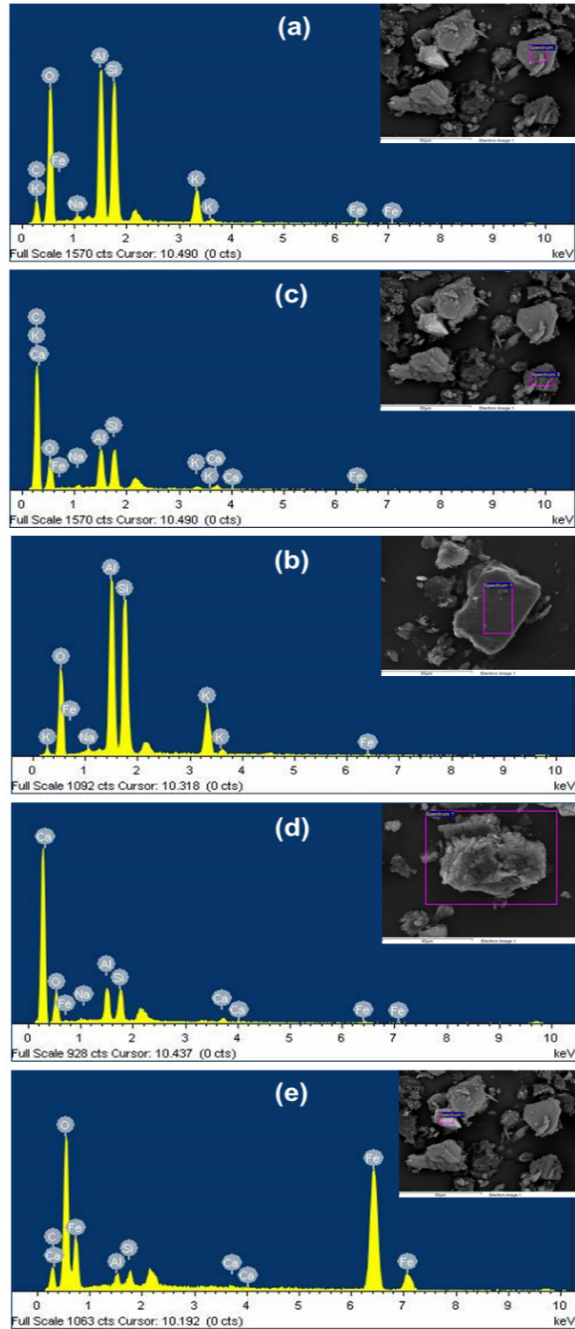


Figure 4. EDS spectra for different particles of sample SBC identified by SEM.

## Quantification of carbonates, LOI, and TOC

Existing methods for TOC quantification generally have drawbacks. This has to do with the fact that ensuring the complete oxidation of organic matter is not as easy as it might be thought. The very marked differences that exist between different soil types and minerals, as well as the mineralogical associations in which organic matter is sometimes involved are aspects that influence TOC results. In addition, organic matter is very diverse, ranging from microbial biomass to high molecular weight organic compounds. All of this generally results in incomplete oxidation even under the most oxidizing conditions. Therefore, there is usually a proportionality factor between oxidized organic matter and TOC that can vary from one method to another [10]. However, these are empirical factors and although widely used, as in this work, they are not fully generalizable because oxidation is more complete in some samples than in others. On the other hand, interferences often produce very important effects in these analytical methods, such as the presence of chlorides, clays, or carbonates [9]. Nevertheless, these are the methods available, and some are more available than others depending on the laboratory. Therefore, the best solution to these problems is to establish procedures according to the type of sample.

Table 2 shows the results of the semi-quantification of inorganic carbon by XRD. It was only possible to determine the carbonate content in samples CM-1 and CM-2, corresponding to calcite in both cases and additionally to dolomite in CM-2, as previously observed in the diffractograms (Figure 1). In the case of sample SBC, the graphite content was determined.

**Table 2.** Semi-quantification of inorganic carbon by XRD in mineral samples containing coal

Sample	Mineral phase	%
CM-1	Calcite	20.4
CM-2	Calcite, Dolomite	74.7, 0.7
SBC	Graphite	42.6

Table 3 shows the analytical results of the quantification of carbonates in the form of  $\text{CaCO}_3$  for samples CM-1 and CM-2 using the Bernard calcimeter. Five quantifications were performed for each sample. It can be observed that, for sample CM-1, the content ( $18.6 \pm 0.9\%$ ) is much lower than for sample CM-2 ( $63.4 \pm 2.0\%$ ). These results are quite coincident with those obtained in the semi-quantification by XRD, which is an indicator that the analytical procedure is adequate.

**Table 3.** Quantification of carbonates in mineral samples containing coal using the Bernard calcimeter

	<b>m (g)</b>	<b>V(CO<sub>2</sub>, mL)</b>	<b>CaCO<sub>3</sub> (%)</b>
<b>CM-1</b>	0.2002	6.1	18.7
	0.2007	6.5	19.9
	0.2010	6.1	18.7
	0.2005	5.7	17.5
	0.2011	5.9	18.0
<b>Mean</b>	<b>0.2007</b>	<b>6.1</b>	<b>18.6</b>
<b>SD</b>	<b>0.0004</b>	<b>0.3</b>	<b>0.9</b>
<b>CM-2</b>	0.2029	21.8	66.1
	0.2024	20.1	61.1
	0.2026	20.5	62.2
	0.2021	21.2	64.5
	0.2023	20.8	63.2
<b>Mean</b>	<b>0.2025</b>	<b>20.9</b>	<b>63.4</b>
<b>SD</b>	<b>0.0003</b>	<b>0.7</b>	<b>2.0</b>

CaCO<sub>3</sub> standard: m = 0.2002±0.0001 g, V(CO<sub>2</sub>) = 32.55±0.21 mL

The gravimetric quantification of TOC is not new, however, the procedure and the temperatures at which the sample is treated vary greatly from one literature to another, and this is because it is highly dependent on the type of sample [9–11]. Table 4 shows the results of the quantification of carbonates, LOI, and TOC in samples CM-1 and CM-2 by the proposed gravimetric method. Each quantification was performed in triplicate. First, the carbonate content should be analyzed. For sample CM-1 it is 19.2±0.4%, while for sample CM-2 it is 70.3±2.4%. These values are similar to those obtained by XRD and Bernard calcimetry. However, a more rigorous criterion is the t-test for the comparison of the means obtained by gravimetry and calcimetry, shown in Table 5. The p-value for sample CM-1 is higher than the 0.05 significance level (95% confidence). This means that there are no statistically significant differences between the results obtained for this sample by the gravimetric method with acid treatment and the Bernard calcimetric method. However, this is not the case for sample CM-2, where the p-value is less than 0.05 and less than 0.01, which means that there are statistically significant differences at both the 95% and 99% confidence levels. This may be related to incomplete dissolution of carbonates during the acid treatment in the Bernard calcimeter, since the carbonate content in this sample is much higher than in sample CM-1. This can be inferred if it is considered that the result by gravimetry is higher than that obtained with the calcimeter. However, some acid dissolution effects of components other than carbonates, including organic matter, cannot be ruled out, which may also

overestimate the carbonate result by the gravimetric method. Note how the relative standard deviation (RSD) increases dramatically for the analysis of sample CM-2 compared to CM-1, especially for LOI and TOC. In addition to the acid dissolution mentioned above, incomplete dissolution of carbonates may also occur, leading overall to less homogeneous volatilization from one replicate to another during the combustion treatment at 1100°C. A more intensive treatment of the sample, i.e., using time longer than 2 h and a higher amount of acid may solve the problem of incomplete dissolution; even slightly increasing the temperature can help. However, if dissolution of other components occurs, its effect on the analytical result can be increased by applying more intensive conditions. In any case, it should be considered by the analyst as a possible source of error depending on the mineralogy of the sample and the carbonate content.

**Table 4.** Quantification of carbonates, LOI, and TOC by gravimetry in mineral samples containing coal

	CaCO <sub>3</sub> (%)	LOI (%)	TOC (%)
<b>CM-1</b>	19.1	3.3	1.9
	18.8	3.6	2.1
	19.6	3.7	2.1
<b>Mean</b>	<b>19.2</b>	<b>3.5</b>	<b>2.1</b>
<b>SD</b>	<b>0.4</b>	<b>0.2</b>	<b>0.1</b>
<b>RSD (%)</b>	<b>2.1</b>	<b>5.7</b>	<b>4.8</b>
<b>CM-2</b>	72.7	1.9	1.1
	70.1	2.5	1.4
	68.0	3.1	1.8
<b>Mean</b>	<b>70.3</b>	<b>2.5</b>	<b>1.4</b>
<b>SD</b>	<b>2.4</b>	<b>0.6</b>	<b>0.3</b>
<b>RSD (%)</b>	<b>3.4</b>	<b>24.0</b>	<b>21.4</b>

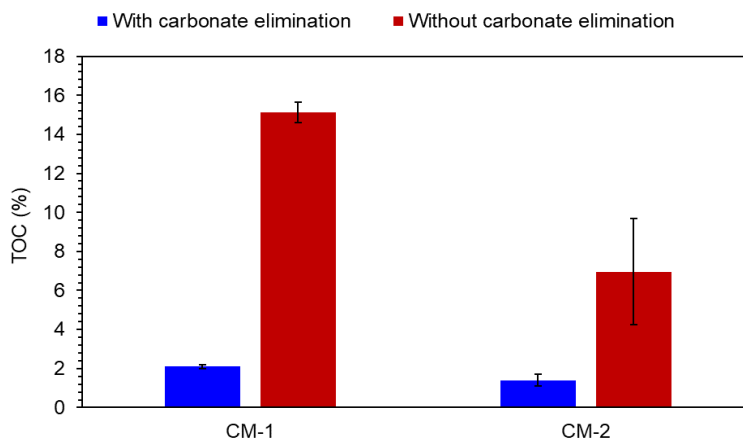
**Table 5.** T-test for the comparison between the carbonate results obtained by the Bernard calcimeter and the gravimetric method

Sample	t-statistic	p-value
CM-1	-1.07264	0.3247
CM-2	-4.4733	0.0042

In the case of TOC, it has been observed that the accuracy of the method can be lower depending on the type of sample, e.g., in sandy soils the RSD tends to be much higher than in forest floor samples when using the LOI method [12]. Furthermore, De Vos et al. [12] point out that the LOI-based

method is the most convenient but that its accuracy is questionable. In fact, Li et al. [11] show that the LOI method has the highest error and variability of results compared to wet oxidation with potassium dichromate and sulfuric acid. This allows to understand that the difference in precision for TOC observed in this work is common. Furthermore, this shows that the mineralogical and organic matter composition is the key to explain the variability of the LOI method. This is because the composition of the sample matrix defines the occurrence or not of interfering effects or incomplete volatilization effects. Nevertheless, the results obtained in this work are adequate for application in mineral and coal processing.

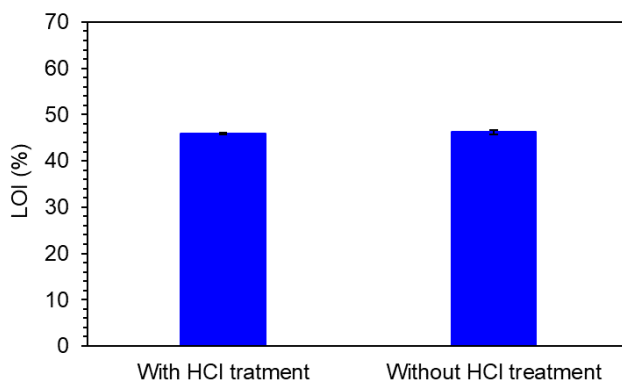
Figure 5 compares TOC determination for samples CM-1 and CM-2 with and without carbonate removal by acid treatment. This is to check the effect of incorrect processing of a carbonated sample. It is observed that when proper treatment is not performed on carbonates, the TOC results are incorrect, and the variability of the results is greatly increased. This supports the above discussion of how necessary the complete removal of carbonates in mineral samples is for accurate TOC quantification.



**Figure 5.** TOC values of samples CM-1 and CM-2 with and without carbonate elimination.

Figure 6 shows that, in samples with absence of carbonates, such as the sub-bituminous coal analyzed, it is not necessary to perform acid treatment with HCl, clearly observing how the result with and without treatment is practically the same. In fact, a t-test revealed a p-value greater than 0.05 (t-statistic = 1.4321, p-value = 0.2254), which allows affirming that there are no statistically significant differences for 95% confidence.

The conversion factor of 0.58 between TOC and organic matter was not applied to the LOI determined for the SBC sample because the content lost after ignition at 1100°C closely matches the percentage of graphite obtained by XRD (42.6%), indicating that the substance combusted was mainly graphite. Graphite normally ignites at temperatures below 800°C and combustion is complete before 1000°C [15–17], so it is to be expected that at 1100°C this material would be lost. A t-test showed that the LOI quantified without acid treatment ( $46.2 \pm 0.4\%$ ) is not statistically equal to the graphite content obtained by XRD for either 95% or 99% confidence (t-statistic = 14.5815, p-value = 0.0047). This indicates that probably, the 3.6% difference between both values corresponds to organic matter, whose TOC would be 2.1% ( $3.6 \times 0.58$ ). However, the XRD method is semi-quantitative, so this analysis is not analytically reliable. Since the graphite content is in the major part anyway (44.1%, 21 times higher than 2.1%), it is preferable in this case to assume LOI as a measure of carbon content other than carbonates. To be more rigorous, it is necessary to apply a refinement method for XRD to quantify the graphite phase. However, the application of carbon quantification in mineral and coal processing does not require these levels of analytical performance. Nevertheless, this demonstrates the importance of knowing the mineralogy of the sample before applying an analytical procedure to determine TOC and carbonates.



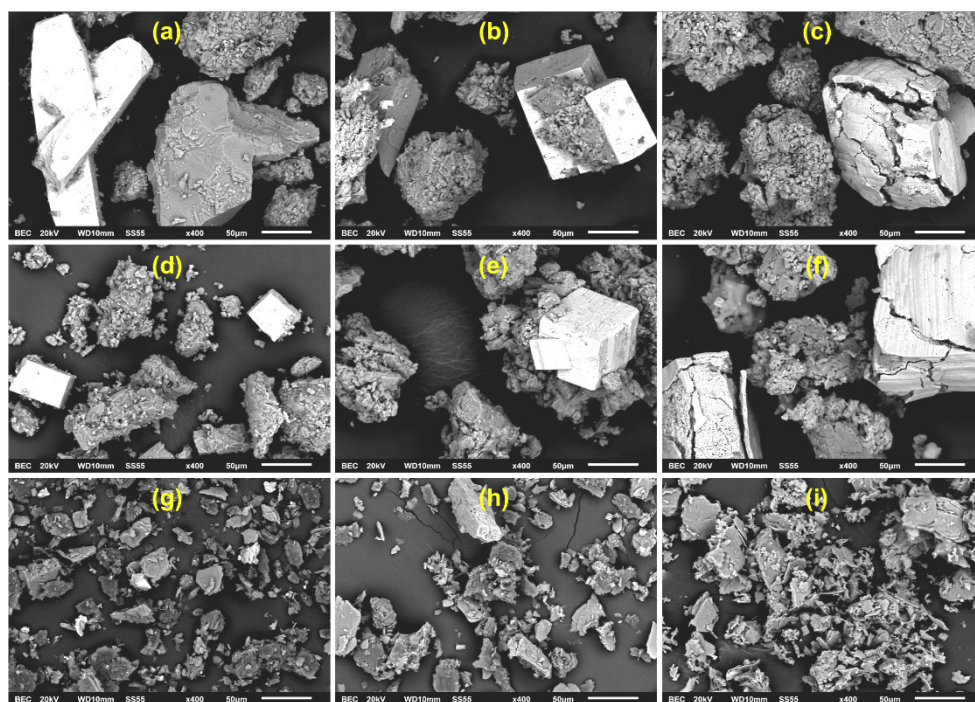
**Figure 6.** LOI values for the sample SBC without and with HCl treatment to remove carbonates.

### Morphological study

Figure 7 shows the backscattered electron micrographs of the three samples before any treatment, after acid treatment, and after heat treatment at 1100°C. In the case of sample CM-1, Figure 7a shows particles with different

A PROCEDURE FOR THE GRAVIMETRIC QUANTIFICATION OF TOTAL ORGANIC CARBON AND CARBONATES IN NATURAL ROCKS FOCUSED ON MINERAL AND COAL PROCESSING

morphologies and brightnesses associated with different minerals released as a result of the grinding process to which each sample was subjected. After the acid treatment, no significant change in morphology is observed (Figure 7b), but after the high temperature treatment, some fractured particles are observed due to the heat effect (Figure 7c). The same behavior is observed for sample CM-2 (Figures 7d-f). In an EDS analysis, these fractured particles were identified as iron oxides. In the case of sample SBC, Figures 7g-i do not show marked differences in brightness and morphology as in the case of the two previous samples. This is because this sample has a less varied composition in terms of mineral type (only silicates and graphite), as observed by XRD.



**Figure 7.** Scanning electron micrographs: (a-c) Sample CM-1 before any treatment, after acid treatment, and after heat treatment at 1100°C, respectively. (d-f) Sample CM-2 before any treatment, after acid treatment, and after heat treatment at 1100°C, respectively. (g-i) Sample SBC before any treatment, after acid treatment, and after heat treatment at 1100°C, respectively.



## **Conclusions**

Quantification of TOC and carbonates is possible in the same gravimetric procedure for mineral samples containing coal. Carbonates play a fundamental role in the accuracy of the gravimetric loss-on-ignition method for TOC determination. They must be identified prior to analysis and, if found, must be removed by acid treatment, the extent and intensity of which will depend on the amount present. It is necessary to consider the incomplete dissolution of carbonates as well as the dissolution of other components as possible sources of error in the gravimetric method. Samples free of carbonates do not require acid treatment for TOC quantification. Knowing the mineralogy of the rock is essential to accurately analyze both the organic and inorganic carbon content in samples containing coal and other minerals.

## **EXPERIMENTAL SECTION**

### **Mineralogical and morphological characterization of the samples**

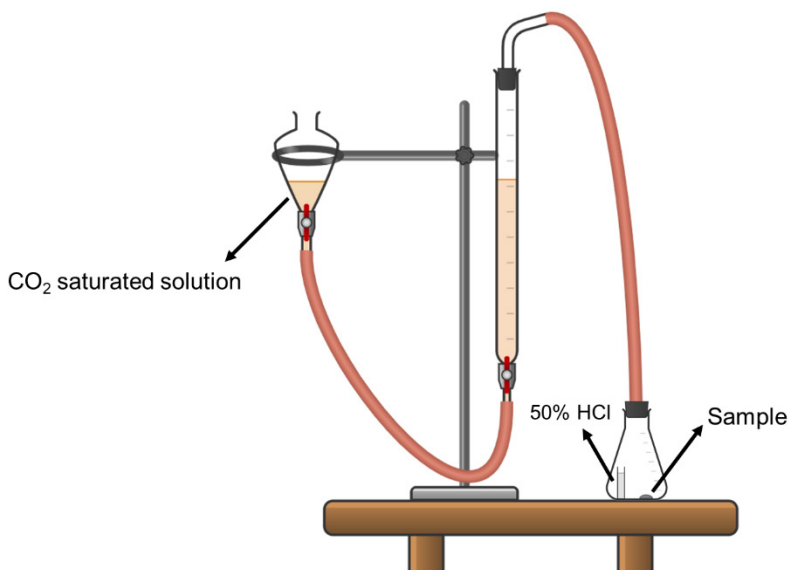
The mineralogical composition of the samples was studied by X-ray diffraction (XRD) and scanning electron microscopy (SEM) with an energy dispersive X-ray spectroscopy (EDS) analyzer. The XRD method was performed with a Bruker D8-Advance diffractometer operated at 30 kV using a wavelength of 1.5406 Å. For the electron microscopy, a JEOL JSM-6610LV scanning microscope operated at 20 kV was used. The morphology of the samples was studied using this microscope with a backscattered electron detector. For all samples, grinding and milling was performed to a particle size of less than 100 µm.

### **Identification and quantification of carbonates as CaCO<sub>3</sub>**

Quantification of carbonates as CaCO<sub>3</sub> was performed using a Bernard calcimeter (Figure 8). This apparatus consists of a hermetically sealed vessel containing the sample and a small glass or stainless-steel vessel containing 50% HCl. This vessel or chamber is connected by a hose to the top of a column with a scale (it can be a burette) that allows the gas volume to be measured using a liquid column consisting of a CO<sub>2</sub> saturated solution stained with methyl orange. The saturated solution prevents some of the carbon dioxide from dissolving in the water. When the containing chamber is agitated enough to spill the HCl over the sample, a reaction occurs that releases CO<sub>2</sub>. The gas displaces the colored liquid column, allowing a liquid

A PROCEDURE FOR THE GRAVIMETRIC QUANTIFICATION OF TOTAL ORGANIC CARBON AND CARBONATES IN NATURAL ROCKS FOCUSED ON MINERAL AND COAL PROCESSING

level equivalent to the gas volume to be measured. The displacement of the liquid column is related to the carbonate concentration using a substance as a standard, usually calcium carbonate [18,19].



**Figure 8.** Schematic of the Bernard calcimeter used for the determination of carbonates in mineral samples containing coal.

Prior to the determination, a saturated CO<sub>2</sub> solution was prepared by mixing 350 mL of deionized water with 1 g NaHCO<sub>3</sub> and 100 g NaCl. Subsequently, a 1 mol/L H<sub>2</sub>SO<sub>4</sub> solution was added until a slight acid reaction with CO<sub>2</sub> release was provoked. Then, a few drops of methyl orange were added to facilitate the visualization of the CO<sub>2</sub> volume on the measuring scale. For quantification with the calcimeter, 0.2 g of mineral was used, and as carbonate standard, 0.2 g of dry CaCO<sub>3</sub> (105°C for 2 h). Equation 1 was used to calculate the calcium carbonate content in the samples.

$$CaCO_3(\%) = \frac{V(CO_2)_{\text{mineral}} \times m(CaCO_3)}{V(CO_2)_{CaCO_3} \times m(\text{mineral})} \times 100 \quad (1)$$

Where V is the volume of liquid displaced (mL), m is the mass (g).

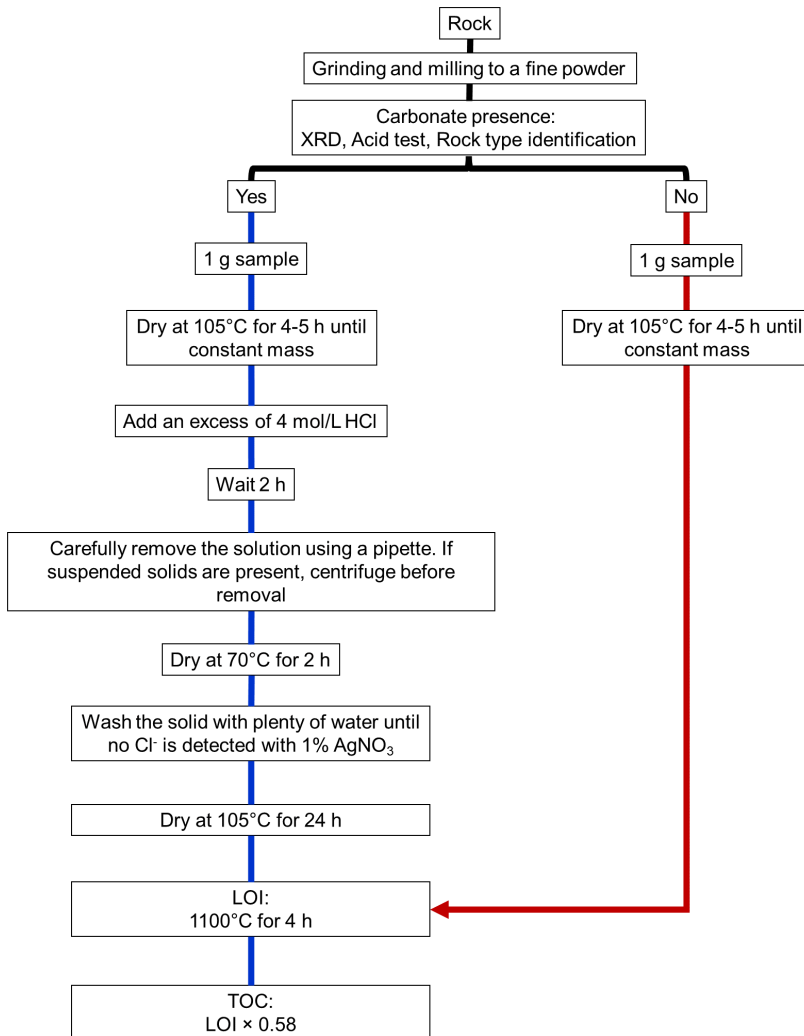
## **Gravimetric procedure for TOC and carbonate quantification in mineral samples with coal content**

The procedure established for the determination of TOC and carbonates by gravimetry in the sample types used in this work is shown in Figure 9. First, the rock is ground and milled to a fine powder ( $< 100 \mu\text{m}$ ). Before proceeding with the analytical determination, it is important to know whether carbonates are present, which can be done by XRD, acid test with concentrated HCl, or prior mineralogical identification by optical or electron microscopy. The qualitative acid test is based on the reaction of carbonates with hydrogen ions to release  $\text{CO}_2$ , which causes bubbling. However, it is important to note that this test may lack sensitivity when the amount of carbonates is very small. If there is any uncertainty about the absence of carbonates, it is preferable to perform the procedure as if carbonates were present.

For both carbonate and non-carbonate containing samples, the first analytical step is the removal of moisture. To do this, 1 g of sample is weighed into a porcelain capsule and heat treated at  $105^\circ\text{C}$  for 4 h, then allowed to cool to room temperature in a desiccator and the capsule is weighed. It is placed again for 1 h in the oven, and after cooling in the desiccator, it is weighed again. This is done as many times as necessary until constant weight.

If carbonates are present, after removing the moisture, the sample is treated with an excess of 4 mol/L HCl;  $\text{CO}_2$  bubbling will be observed, whose intensity and duration depend on the amount of carbonates. When the bubbling stops, it is necessary to wait 2 h for the decomposition reaction to complete. The solution is then carefully removed with a Pasteur pipette. This step may be problematic if suspended solids remain after the 2 h rest period. In this case, it is advisable to centrifuge the mixture to avoid the loss of solids. It is important to note that it is not necessary to remove all of the solution, but to remove a sufficient amount until, due to the small amount of solution, there is a risk of extracting solids with the pipette. After removing as much of the solution as possible, the solid is dried at  $70^\circ\text{C}$  for 2 h. This step does not require complete drying of the solid, but it is necessary to evaporate all the liquid, so if 2 h is not sufficient, the treatment should be extended. After the treatment at  $70^\circ\text{C}$ , the chlorides remaining from the acid elimination of the carbonates are removed. This is done by washing the solid with a sufficient amount of water until no chloride is detected in the qualitative analysis with 1% silver nitrate, which gives a white solid as a positive result. When all chloride has been removed, the moisture in the sample is eliminated by heat treatment at  $105^\circ\text{C}$  for 24 h.

A PROCEDURE FOR THE GRAVIMETRIC QUANTIFICATION OF TOTAL ORGANIC CARBON AND CARBONATES IN NATURAL ROCKS FOCUSED ON MINERAL AND COAL PROCESSING



**Figure 9.** Step-by-step diagram of the analytical procedure for the gravimetric determination of TOC and carbonates in mineral samples containing coal.

Subsequently, heat treatment is carried out at 1100°C for 4 h to ignite the organic matter. This allows the LOI to be calculated as the difference in mass before and after the calcination treatment. Equation 2 shows how to calculate the TOC after the procedure. Dividing the LOI by the sample mass and then multiplying by 100 allows the percentage LOI to be calculated, which is related to the TOC by a factor of 0.58 (1/1.724) [11].

For a carbonate-free sample, 1 g of sample is weighed, and the moisture is removed as above. After this step, the LOI is determined gravimetrically as described previously.

$$TOC(\%) = \frac{m_{105^{\circ}C(24h)} - m_{1100^{\circ}C}}{m_{sample}} \times 100 \times 0.58 \quad (2)$$

Where  $m_{105^{\circ}C(24h)}$  is the sample mass (g) after acid treatment and drying at  $105^{\circ}C$  for 24 h,  $m_{1100^{\circ}C}$  is the sample mass (g) after calcination at  $1100^{\circ}C$  for 4 h,  $m_{sample}$  is the sample mass (g) weighed initially.

The quantification of carbonates is implicit in the procedure shown in Figure 9. These are calculated as the difference between the sample mass before acid treatment with 4 mol/L HCl (after moisture removal) and the sample mass after acid treatment (after drying at  $105^{\circ}C$  for 24 h). The gravimetric calculation is performed according to Equation 3.

$$CaCO_3(\%) = \frac{m_{105^{\circ}C(4h)} - m_{105^{\circ}C(24h)}}{m_{sample}} \times 100 \quad (3)$$

Where  $m_{105^{\circ}C(4h)}$  is the sample mass (g) after removal of moisture at  $105^{\circ}C$  for at least 4 h,  $m_{105^{\circ}C(24h)}$  is the sample mass (g) after acid treatment and drying at  $105^{\circ}C$  for 24 h,  $m_{sample}$  is the sample mass (g) weighed initially.

## ACKNOWLEDGMENTS

Javier E. Vilasó-Cadre thanks CONAHCYT for the PhD scholarship assigned to the Postgraduate Program in Minerals Engineering at the Institute of Metallurgy of the Autonomous University of San Luis Potosí. Iván A. Reyes-Domínguez thanks CONAHCYT for the professorship assigned at the same Institute. The authors thank Rosa Lina Tovar-Tovar and Martha Franco-Vásquez for technical support for this work.

## REFERENCES






1. S. Hussain, V. Sharma, V.M. Arya, K.R. Sharma, S. Rao, *CATENA*, **2019**, *182*, 104104.
2. S. Asante-Okyere, S.A. Marfo, Y.Y. Ziggah, *Upstream Oil and Gas Technology*, **2023**, *11*, 100089.
3. D.N. Benoit, H. Zhu, M.H. Lillierose, R.A. Verm, N. Ali, A.N. Morrison, J.D. Fortner, C. Avendano, V.L. Colvin, *Anal. Chem.*, **2012**, *84*, 9238–9245.

A PROCEDURE FOR THE GRAVIMETRIC QUANTIFICATION OF TOTAL ORGANIC CARBON AND CARBONATES IN NATURAL ROCKS FOCUSED ON MINERAL AND COAL PROCESSING

4. Z. Mohd Hanafiah, W.H.M. Wan Mohtar, W.A.A.Q.I. Wan-Mohtar, A.S. Bithi, R. Rohani, A. Indarto, Z.M. Yaseen, S. Sharil, T.S. Binti Abdul Manan, *Chemosphere*, **2024**, *358*, 142209.
5. M. Ghoochani, N. Rastkari, R.N. Nodehi, A.H. Mahvi, S. Nasser, S. Nazmara, *J. Environ. Health Sci. Eng.*, **2013**, *11*, 28.
6. M.H. Hakimi, W.H. Abdullah, S.G. Sia, Y.M. Makeen, *Mar. Pet. Geol.*, **2013**, *48*, 31–46.
7. D.S. Panwar, V.K. Saxena, S. Suman, V. Kumar, A.K. Singh, *Eneg. Sources Part A*, **2017**, *39*, 1182–1189.
8. I. Bisutti, I. Hilke, M. Raessler, *TrAC, Trends Anal. Chem.*, **2004**, *23*, 716–726.
9. D.W. Nelson, L.E. Sommers, Total Carbon, Organic Carbon, and Organic Matter, in *Methods of Soil Analysis, Part 3: Chemical Methods*, D.L. Sparks, A.L. Page, P.A. Helmke, R.H. Loeppert, P.N. Soltanpour, M.A. Tabatabai, C.T. Johnston, M.E. Sumner Eds.; John Wiley & Sons Ltd, New Jersey, USA, **1996**, Chapter 34, pp. 961–1010.
10. M. Eyherabide, H. Sainz Rozas, P. Barbieri, H.E. Echeverría, *Ciencia Del Suelo*, **2014**, *32*, 13–19.
11. N. Li, D. Sack, J. Sun, S. Liu, B. Liu, J. Wang, G. Gao, D. Li, Z. Song, D. Jie, *CATENA*, **2020**, *185*, 104276.
12. B. De Vos, B. Vandecasteele, J. Deckers, B. Muys, *Commun. Soil Sci. Plant Anal.*, **2005**, *36*, 2899–2921.
13. J.E. Vilasó-Cadre, D.M. Ávila-Márquez, I.A. Reyes-Domínguez, A. Blanco-Flores, E.J. Gutiérrez-Castañeda, *Fuel*, **2021**, *304*, 121363.
14. J.E. Vilasó-Cadre, D.M. Ávila-Márquez, I.A. Reyes-Domínguez, A. Blanco-Flores, H.P. Toledo-Jaldin, E.J. Gutiérrez-Castañeda, J.A.C. de Albornoz, *IJCT*, **2023**, *30*, 103–110.
15. W. Jiang, G. Nadeau, K. Zaghib, K. Kinoshita, *Thermochim. Acta*, **2000**, *351*, 85–93.
16. I.T. Kim, J. Lee, J.C. An, E. Jung, H.K. Lee, M. Morita, J. Shim, *Int. J. Electrochem. Sci.*, **2016**, *11*, 5807–5818.
17. L.A. Gomez-Moreno, A. Klemettinen, R. Serna-Guerrero, *IScience*, **2023**, *26*, 107782.
18. A. Carranza-Edwards, G. Bocanegra-García, L. Rosales-Hoz, L. De Pablo Galán, *Sediment. Geol.*, **1998**, *119*, 263–274.
19. P. Pereira, X. Úbeda, D.A. Martin, *Geoderma*, **2012**, *191*, 105–114.



## EFFECTS OF AUDIO FREQUENCY ELECTRIC FIELDS ON THE ESTERIFICATION REACTIONS OF ACETIC ACID WITH C4-C8 BRANCHED ALCOHOLS

Ioan-Alexandru UDREA<sup>a</sup>, Valentin ORDODI<sup>a\*</sup>, Cristina PAUL<sup>a</sup>,  
Mircea DAN<sup>a</sup>, Ana-Maria PANĂ<sup>a</sup>, Cristian STĂNESE<sup>b</sup>,  
Dumitru Daniel BONCIOG<sup>c</sup>, Luca DORU-ALEXANDRU<sup>d</sup>,  
Narcis-Grațian CRĂCIUN<sup>d</sup>, Nicolae VASZILCSIN<sup>a</sup>

**ABSTRACT.** The esterification reactions, which lead to esters with a big diversity of uses across numerous industries, is one of the most important reactions in organic synthesis. Within these esterification reactions, a variety of strategies have been used to improve conversion, reaction rate, and equilibrium. This paper investigated the effects of the audio frequency electric fields on the esterification reactions of acetic acid with C4-C8 branched aliphatic alcohols. The aim of these studies was to synthesize a few acetic acid esters in an environmentally and friendly manner utilizing a new method. The only raw materials used were acetic acid, C4–C8 branched aliphatic alcohols and an audio frequency electric field acting as an accelerator. In order to determine the efficacy of the suggested approach, these esters were also synthesized without applying the audio frequency electric field. Analysis using gas chromatography technique revealed that the audio frequency electric field significantly increased esterification yields. The highest yields of ester were obtained for 2-octyl acetate, exhibiting a notable increase in comparison to the synthesis that did not employ the application of an audio

<sup>a</sup> Politehnica University Timisoara, Faculty of Industrial Chemistry and Environmental Engineering, 6 V. Pârvan Bd., RO-300223, Timisoara, Romania

<sup>b</sup> Politehnica University Timisoara, Faculty of Electrical and Power Engineering, 2 V. Pârvan Bd., RO-300223, Timisoara, Romania

<sup>c</sup> Politehnica University Timisoara, Faculty of Electronics, Telecommunications and Information Technologies, 2 V. Pârvan Bd., RO-300223, Timisoara, Romania

<sup>d</sup> Politehnica University Timisoara, Faculty of Mechanics, 1 Mihai Viteazu Bd., RO-300222, Timisoara, Romania

\* Corresponding author: valentin.ordodi@upt.ro





frequency electric field as an enhancer of the reaction rate. The proposed new method, as well as the employing of raw materials of natural origin, allows the production of esters in an environmentally friendly manner and with reduced costs. These esters can be used without any restrictions in a variety of industries, including food, pharmaceuticals, and cosmetics.

**Keywords:** *audio frequency electric field, esterification reactions, natural esters, food and pharmaceutical industry, green method*

## INTRODUCTION

A wide range of flavors and fragrances are used in the pharmaceutical, food and drink industries. [1]. The most utilized substances in these industries are esters, which are typically obtained through Fischer esterification. However, there are numerous alternative methods, including Tishchenko condensation and the addition of a carboxylic acid to an alkene, which are less prevalent. [2, 3]. Also, the most recent techniques of ester synthesis are transesterification reaction, assisted by microwaves, pulsed electric fields or visible light [4 - 9].

If the esters should be utilized within the food or pharmaceutical industries, it is imperative that they are derived from natural sources. Two main methods exist for the synthesis of natural esters, the first one employing chemical reaction, typically utilizing enzymes (especially lipases) as catalysts, and the second one conducted in the presence of an electromagnetic field which serves as catalyst [10-11].

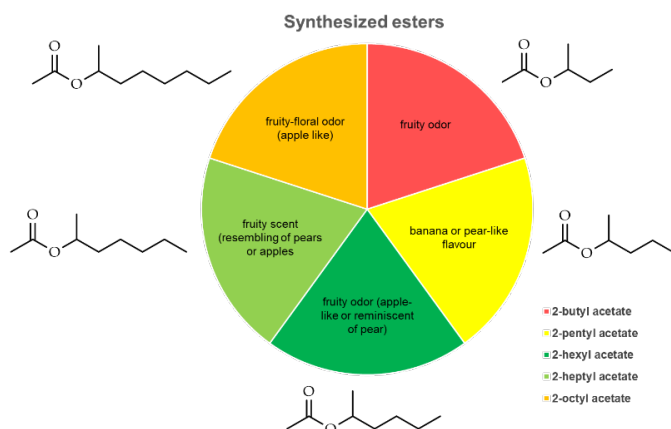
The most utilized enzymes used in the synthesis of esters belong to the *Candida*, *Hanseniaspora*, *Kluyveromyces* or *Pichia* families.

Although the use of enzymes in esterification reactions is a natural process, allowing the resulting esters to be classified as “natural” (and thus eligible for unrestricted use in food), the high cost of these enzymatic biocatalysts will inevitably result in elevated final production costs [10].

In the light of these findings, a novel synthesis method was proposed that employs an audio frequency electric field as a catalyst. This method enables the classification of the resulting esters as “natural,” provided that the raw materials are of natural origin, as the audio frequency electric field has been found to have no adverse effects. The esterification process in the presence of an electric field has the advantage of requiring only the necessary reactants, such as alcohol and acid. If these are obtained by fermentation, the resulting esters would be 100% natural, devoid of any synthetic by-products and are suitable for the use in the food industry or in the manufacture of

## EFFECTS OF AUDIO FREQUENCY ELECTRIC FIELDS ON THE ESTERIFICATION REACTIONS OF ACETIC ACID WITH C4-C8 BRANCHED ALCOHOLS

pharmaceutical products [12]. Within this study, the synthesized esters were: 2-butyl acetate, 2-pentyl acetate, 2-hexyl acetate, 2-heptyl acetate and 2-octyl acetate (Figure 1). The selection of these esters was based on their potential applications in the pharmaceutical, food, and cosmetic industries [13-22].



**Figure 1.** The esters obtained in this study and their flavoring characteristics.

## RESULTS AND DISCUSSIONS

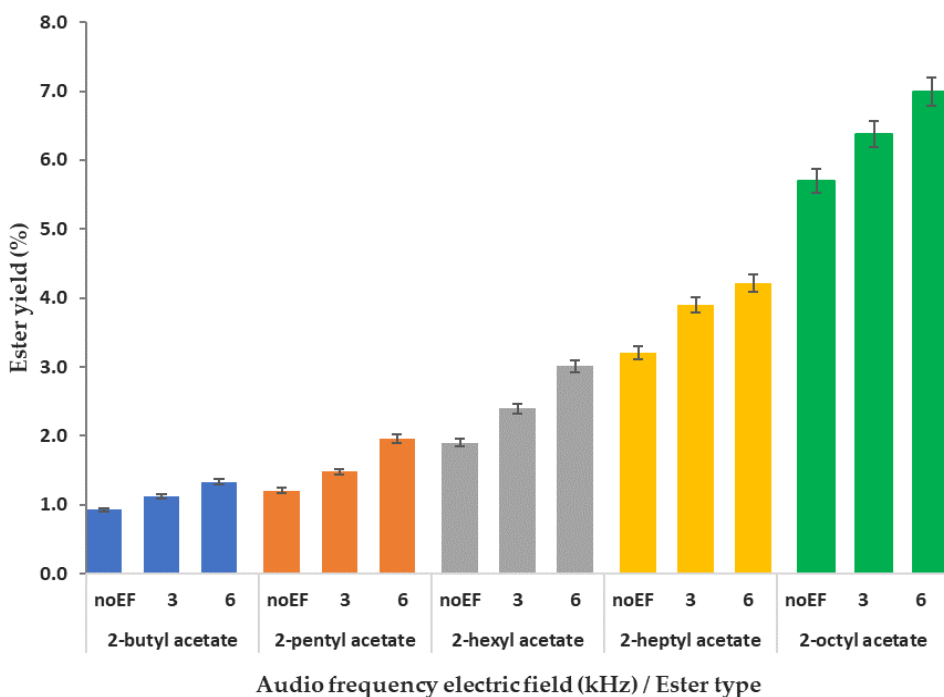
In these investigations, two frequencies (3 kHz and 6 kHz) and two temperatures (20°C and 50°C) were used to synthesize five acetic acid esters with branched aliphatic C4–C8 alcohols in the presence of an audio frequency electric field. The results are expressed as yields of esters obtained after 24 hours at the 2 frequencies used, compared to the ones obtained without applying the audio frequency electric field.

According to the experimental determinations, the esterification reaction of acetic acid with branched alcohols was positively impacted by the audio frequency electric field. The application of the audio frequency electric field leads to a better orientation of the molecular dipoles of acetic acid and alcohols increasing the probability of effective collisions, which raises the yields of ester.

It is already well known that the temperature has a big impact on the esterification reactions. In particular, the yields of ester are diminished when lower temperatures are employed in the esterification reaction in comparison to the yields obtained when higher temperatures are utilized. As a result, the yields of esters obtained when the reactions were performed at 20°C were lower than those obtained when the syntheses were performed at 50°C.

The optimal frequency that produced the highest yields of ester was 6 kHz for both scenarios (when the syntheses were conducted at 20°C and 50°C). This phenomenon can be attributed to the fact that the effect of the applied audio frequency electric field is more pronounced when a higher frequency is employed, orienting the alcohol molecules in favorable positions for efficient collisions with the acid molecule, which ultimately results in the attainment of higher yields of ester at the two used temperatures.

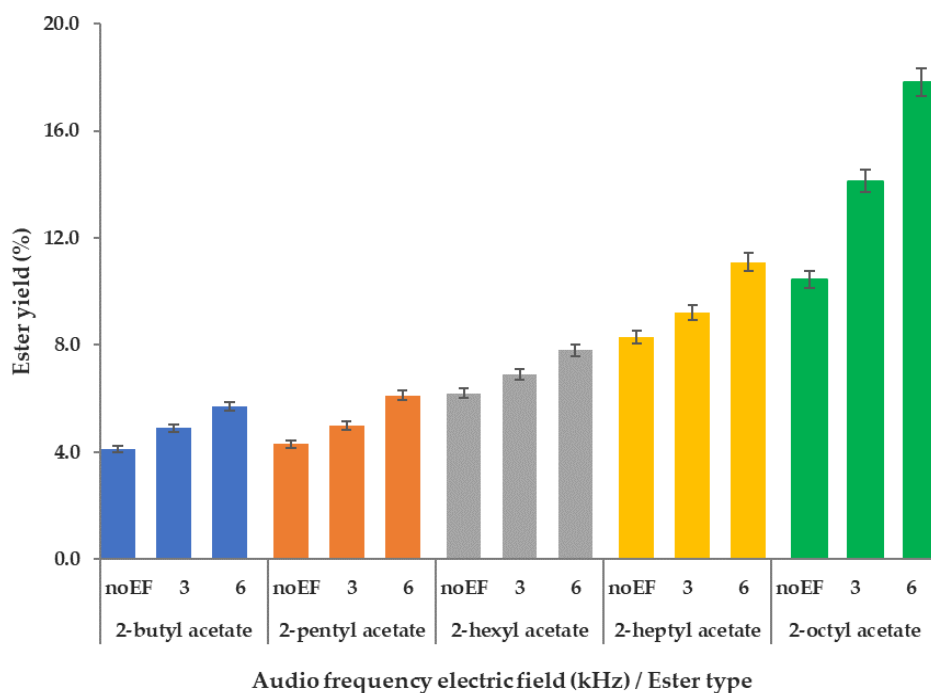
When the reactions were carried out at 20°C (Figure 2) and 3 kHz, the yields of ester varied in the range 1.1% - 6.4%, the highest one registering for 2-octyl acetate, while in the case of using 6 kHz, the yields of esters varied in the range 1.3% - 7.0%, the highest one registering also for 2-octyl acetate. In the case of the reactions conducted without applying the audio frequency electric field, it was observed that the yields of ester were lower than in the case of using it, more precisely, they varied in the range 0.9% - 5.7%.



**Figure 2.** Effect of the audio frequency electric field (kHz) on the ester yield in esterification reactions operated at 20°C. (noEF—in the absence of an electric field).

EFFECTS OF AUDIO FREQUENCY ELECTRIC FIELDS ON THE ESTERIFICATION REACTIONS OF ACETIC ACID WITH C4-C8 BRANCHED ALCOHOLS

The reactions performed at 50°C (Figure 3) and 3 kHz showed that the yields of ester varied in the range 4.9% - 14.1%, the highest one registering for 2-octyl acetate. When 6 kHz was used, the yields of ester varied in the range 5.7% - 17.8%, the highest one registering also for 2-octyl acetate. The reactions performed without applying the audio frequency electric field showed that the yields of ester were lower than in the case of using it, more precisely, they varied in the range 4.1% - 10.5%.



**Figure 3.** Effect of the audio frequency electric field (kHz) on the ester yield in esterification reactions operated at 50°C. (noEF—in the absence of an electric field).

In comparison to the yields of esters obtained in the case of standard esterification (the electric field has not been applied), it can be concluded that the application of an audio frequency electric field resulted in higher ester yields for all reactions, irrespective of temperature or frequency.

It can also be concluded that the optimum frequency (within this study) was 6 kHz for all the reactions carried out and that the highest yields of ester were obtained for 2-octyl acetate.

### **Mechanism of esterification using the audio frequency electric field as catalyst**

The esterification reaction typically requires the use of a catalyst, usually an acid, in order to increase the yield of the reaction. However, in the presence of an audio frequency electric field, the reaction can be positively influenced by polarizing the reactant molecules, reducing the activation energy and favoring molecular orientation.

The proposed mechanism of the esterification reaction using an audio frequency electric field as a catalyst can be divided into six steps as follows:

1. Polarization of the reactants: the application of an audio frequency electric field has the effect of polarizing the reactant molecules, making the carboxylic acid more electrophilic and the alcohol more nucleophilic due to the alignment of their dipole moments.

2. Nucleophilic attack: the polarized alcohols are easier to attack the carbonyl carbon of the carboxylic acid, with the formation of tetrahedral intermediates, more specifically, the audio frequency electric field increases the electrophilicity of the carboxylic acid and the nucleophilicity of the alcohol, which makes nucleophilic attack more favorable and simpler.

3. The formation of a tetrahedral intermediate is a subsequent consequence of the nucleophilic attack. This intermediate is stabilized by the audio frequency electric field, which aligns the dipoles and reduces the activation energy.

4. A proton transfer occurs within the tetrahedral intermediate, leading to the formation of a more stable intermediate. The audio frequency electric field plays a stabilizing role in this process, facilitating the transfer of protons.

5. Dehydration: The application of an audio frequency electric field serves to facilitate the elimination of a molecule of water from the tetrahedral intermediate. This is achieved by stabilizing the transition state and thereby reducing the activation energy that is required in this instance.

6. The final stage is the ester formation and the release of water. Throughout this process, the audio frequency electric field orients and stabilizes the molecules, enhancing the reaction yield even in the absence of a catalyst.

The effect of the audio frequency electric field can be summarized as follows: the polarization of the reactant molecules is achieved, increasing their reactivity; this is accomplished by making the carbonyl carbon more electrophilic and the alcohol's oxygen more nucleophilic. Furthermore, the stabilization of intermediates and transition states is facilitated, reducing the activation energy and additionally, orienting the reactant molecules in such a way that makes the reaction more favorable and efficient [11], [23].

## CONCLUSIONS

The results of experimental syntheses demonstrated that the audio frequency electric field has a beneficial effect on the esterification reactions of acetic acid with branched alcohols.

Within these studies, five esters of acetic acid with C4-C8 branched aliphatic alcohols were synthesized for the first time using an audio frequency electric field as enhancer of the reaction yields, the proposed method being a sustainable way in the synthesis of “green” esters.

The highest yields of ester were obtained for 2-octyl acetate in the case of the synthesis using the audio frequency electric field, which were significantly higher than within the synthesis without applying it. Although the synthesis of the other esters proceeded with lower yields of esters, in all situations the yields were higher than in the standard esterification case (without the application of an audio frequency electric field).

The methodology outlined in this study demonstrated efficacy in the production of natural esters which can be used in a variety of industries, including food, pharmaceuticals, and cosmetics, without any restrictions due to the non-harmful effect of the catalyst, which is an audio frequency electric field.

## EXPERIMENTAL SECTION

### Materials

The reagents used for the below mentioned synthesis are commercial and they had been used without further purification: acetic acid (99%, Merck), 2-butanol (99%, Merck), 2-pentanol (99%, Merck), 2-hexanol (99%, Merck), 2-heptanol (99%, Merck), 2-octanol (99%, Merck), acetone (99%, Merck) and nitrobenzene (99%, Merck).

### *Synthesis using the audio frequency electric field as catalyst*

The experimental setup for the synthesis was reported in our previous work [24].

The device used during this study consists of a reaction vessel represented by a cylindrical capacitor connected to the secondary coil (with high number of turns) of a resonant transformer with an open ferrite core. The capacitor has a capacity of 100 pF, as determined by the LCR-meter 880 BK Precision. This capacitor is provided with external copper thermostatic jacket

as armature which is also the external cylindrical electrode connected to the ground of the device. The dielectric medium comprises the reaction mass and the glass vessel in which the physical-chemical phenomenon occurs.

The reaction vessel/reactor is made of glass and is provided with a stainless-steel central electrode. An electric field is established between this central electrode and the external thermostatic coil, which will be maintained at a constant intensity of 13.5 kV/cm throughout the experiments by adjusting the amplitude of the input signal. The electric capacity of the reactor and the inductance of the transformer's secondary coil combine to create a parallel LC circuit that can be adjusted to a desired frequency of 1–10 kHz by adjusting the ferrite core. The electrostatic voltmeter with very high impedance is used to measure the intensity of electric field (of the order of kV/cm). A sinusoidal signal generator with adjustable frequency (1 – 10 kHz) and amplitude (0 – 1 V) provides the amplifier's input signal.

The primary coil of this resonant transformer consists in a low number of turns connected in series with an equivalent capacitor made by the connection in parallel of 1 to 19 fixed condensers of 0.1  $\mu\text{F}$  each one. The working capacity of this equivalent capacitor depends on the number of fixed capacitors connected, and each fixed capacitor can be individually inserted into the circuit by manipulating 19 ON-OFF contacts. This creates a series LC circuit that is adjusted at resonance of the working frequency by varying the above-discussed equivalent capacity and it is the load of the power amplifier built using TDA2003 integrated circuit. The correct tuning of this resonant circuit on the working frequency is estimated by ensuring that the filament lamp connected in series has the maximum illumination.

Predetermined volumes of alcohol and acetic acid in a 1:1 molar ratio were added to the 30 mL glass mini-reactor to create a total volume of 20 mL reaction mass. The reactions were incubated at 20°C and 50°C, with stirring and samples were collected, for each reaction, 24 hours later. All the esterification experiments were carried out in duplicate, and the mean values were taken into consideration.

The obtained esters were subjected to gas chromatography (data not shown), using a Varian 450 Chromatograph (Varian Inc., Utrecht, The Netherlands) equipped with a flame ionization detector (FID), and a 15 m x 0.25 mm VF-1ms non-polar capillary column with a 0.25  $\mu\text{m}$  film thickness.

The GC analysis conditions were: oven temperature 50°C (0.5 min) – 75°C (1 min), with a heating rate of 3°C/min, injector temperature 300°C, detector temperature 350°C, and carrier gas flow (hydrogen) 2.0 mL/min. Samples were diluted with acetone and a quantitative analysis was performed using nitrobenzene as an internal standard, and the ester yield was determined based on GC data. All gas chromatographic analyses of the samples were performed in triplicate.

The structure of the esters was validated by GC-MS using a Hewlett-Packard HP6890 gas chromatograph and HP5973 mass spectrometer (Agilent Technologies, Santa Clara, California, USA) with electron ionization (EI) of 70 eV. Prior to analysis, the ester samples were diluted 1:10 in acetone. A DB-WAX high-polarity, polyethylene glycol (PEG) capillary column (30 m\*0.25 mm\*0.25 µm film thickness) (Agilent Technologies J&W Scientific INC.) was used. The analysis conditions were: oven temperature from 50°C to 250°C with a rate of 5°C/minute, a final hold of 5 min, and a flow rate of 1 mL/min. The MS conditions were: source temperature was set at 230°C, quadrupole detector temperature was set at 150°C. The MS detector was set in scan mode and the mass range of compounds was from 50 to 600 amu and started to register after 3 minutes of solvent delay. MS software used was: Chemstation Data Analysis (Agilent Technologies, Santa Clara, California, USA) and AMDIS (NIST, Gaithersburg, MD, USA).

## ACKNOWLEDGEMENTS

The financial support and research facilities were offered by Doctoral School of Politehnica University Timișoara.

## REFERENCES

1. D. Baines; N.C. Da Costa; M.L. Dewis; S. Eri; J. Grigor; S.J. Herman; S.B. Jameson; J. Knights; P. Kraft; J. Margetts; L. O'Hare; D.J. Rowe; L. Turin; C. Winkel; M. Zviely; *Chemistry and Technology of Flavors and Fragrances*, D.Rowe, Blackwell Publishing, Oxford, UK, **2004**, pp. 56-82.
2. V.V. Rekha; M.V. Ramani; A. Ratnamala; V. Rupakalpana; G.V. Subbaraju; C. Satyanarayana; C.S. Rao; *Org Process Res & Dev*, **2009**, *13*, 769–773.
3. T. Seki; T. Nakajo; M. Onaka; *Chem. Lett.*, **2006**, *35* (8), 824-829.
4. M. Salaheldeen; A.A. Mariod; M.K. Aroua; S.M.A. Rahman; M.E.M. Soudagar; I.M.R. Fattah; *Catal.*, **2021**, *11*(9), 1121.
5. N.R. Khan; V.K. Rathod; *Process Biochem*, **2018**, *75*, 89-98.
6. H. Wang; J. Ni; Y. Zhang; *Tetrahedron Lett.*, **2022**, *104*, 154021.
7. D.C. Cubides-Roman; V.H. Pérez; H.F. de Castro; C E. Orrego; O. H. Giraldo; E.G. Silveira; G.F. David; *Fuel*, **2017**, *196*, 481-487.
8. H. Ligong; D. Xuebao; *JSCUT*, **2011**, *39*(12),127-131.
9. Y. Feng; T. Yang; Y. Zhang; A. Zhang; L. Gai; D. Niu; *Front Nutr.*, **2022**, *9*, 1048632.



10. M. Salaheldeen; A.A. Mariod; M.K. Aroua; S.M.A. Rahman; M.E.M. Soudagar; I.M.R. Fattah; *Catal.*, **2021**, *11*(9), 1121.
11. Z.R. Lin; X.A. Zeng; S.J. Yu; D-W. Sun; *Food Bioprocess Tech*, **2011**, *5*, 2637–2645.
12. I-A. Udrea; V. Ordodi; C. Paul; C. Stănese; N. Vaszilcsin; *Studia UBB Chemia*, **2023**, *1*, 49–58.
13. P. Mahapatra; A. Kumari.; V. Kumar Garlapati; R. Banerjee; A. Nag; *J Mol Catal*, **2009**, *60*, 57–63.
14. R.G. Berger, *Biotechnol Lett*, **2009**, *31*, 1651–1659.
15. A.B. Martins; N.G. Graebin; A.S.G Lorenzoni; R. Fernandez-Lafuente; M.A.Z. Ayub; *Process Biochem*, **2011**, *46*, 2311–2316.
16. I. Calinescu; A. Vartolomei; I-A. Gavriila; M. Vinatoru; T.J. Mason; *Ultrason. Sonochem*, **2019**, *54*, 32–38.
17. N.T.C. Duong; A. Uthairatanakij; N. Laohakunjit; P. Jitareerat; N. Kaisangsri; *Food Biosci*, **2023**, *52*, 102410.
18. A.R. Deshmukh; V.K. Rathod, *Green Process Synth*, **2017**, *6*, 55–62.
19. R. Lanciotti; N. Belletti; F. Patrignani; A. Gianotti; F. Gardini; M.E. Guerzoni *J Agric Food Chem*, **2003**, *51*, 2958–2963.
20. A.G.A. Sá; A.C.D. Meneses; P.H.H.D. Araújo; D.D. Oliveira; *Trends Food Sci*, **2017**, *69*, 95–105.
21. HEPTYL ACETATE NATURAL 1233, Advanced Biotech, **2015**.
22. K. Fahlbusch; F. Hammerschmid; J. Panten; W. Pickenhagen; D. Schatkowski; K. Bauer; D. Garbe; H. Surburg; Flavors and Fragrances. In *Ullmann's Encyclopedia of Industrial Chemistry*; Wiley-VCH, Ed.; Wiley, **2003** ISBN 978-3-527-30385-4.
23. W. Schmickler, E. Santos, Electrocatalysis, In *Interfacial Electrochemistry*, 2<sup>nd</sup> ed., Springer, Heidelberg, Germany, **2010**, ISBN: 978-3-642-04929-8.
24. I-A. Udrea; A.T. Lukinich-Gruia; C. Paul; M-A. Pricop; M. Dan; V. Păunescu; A. Băloi; C.A. Tatu; N. Vaszilcsin; V. Ordodi, *Processes*, **2024**, *12* (9), 1-17.

# USE OF ELECTRODIALYSIS TO PRODUCE AND RECYCLE ON-SITE RAW MATERIALS FOR WASTE PRINTED CIRCUIT BOARD RECYCLING PROCESS. I. HBr AND KOH ELECTROSYNTHESIS

Gabriele-Mario BOGDAN<sup>a</sup>, Marian Iosif FRÎNCU<sup>a,b</sup> ,  
Sorin-Aurel DORNEANU<sup>a,b\*</sup> 

**ABSTRACT.** The technological progress and consumerism trend stimulate electric and electronic equipment replacing, inducing the generation of huge amounts of wastes, many of them containing dangerous (but valuable) waste printed circuit boards (WPCBs). A promising technology for their recycling is based on the electrochemically regenerable Br<sup>-</sup>/Br<sub>2</sub> leaching system, for which the raw materials can be produced and recycled by electrochemical ways. In this context, the present work presents our research concerning the feasibility to produce by electrodialysis, on-site, HBr and KOH, which are required for the electro-hydrometallurgical recovery of metals from WPCBs. For this purpose, a four-compartment filter-press electrochemical reactor, divided by two cation and one anion exchange membranes, was used. The obtained results demonstrate that the proposed process can produce, at a current density of 4 kA/m<sup>2</sup>, target solutions with concentrations over 73% and 82%, and average current efficiencies over 73% and 82%, and average specific energy consumptions around 40 and 25 kWh/kg for HBr and KOH, respectively. Moreover, several preliminary measurements performed simultaneously with the electrodialysis tests revealed that, by acquiring rigorous temperature data, the concentrations of the target solutions

---

<sup>a</sup> Department of Chemical Engineering, Faculty of Chemistry and Chemical Engineering, Babeş-Bolyai University, 11 Arany Janos Street, RO-40028, Cluj-Napoca, Romania

<sup>b</sup> Interdisciplinary Research Institute on Bio Nano Sciences, Babeş-Bolyai University, 42 Treboniu Laurian Street, RO-400271, Cluj-Napoca, Romania

\* Corresponding author: sorin.dorneanu@ubbcluj.ro



can be easily and rapidly evaluated and monitored on-line using simple electrochemical sensors for pH and conductivity, but more accurate and exhaustive calibration data is required.

**Keywords:** *WPCBs recycling, on-site KOH and HBr electrosynthesis, electro dialysis, filter-press electrochemical reactor, electrochemical concentrations monitoring*

## INTRODUCTION

Today, worldwide, the technological progress and consumerism trends [1, 2] accelerate the replacement of electric and electronic equipment (EEE). This tendency leads to the generation of large quantities of waste EEE (WEEE), many of which contain dangerous waste printed circuit boards (WPCBs). Concretely, from the resulting 62 Mt of WEEE in 2022, only 20% were properly recycled and in 2024 the amount of WEEE increased to 74 Mt, being estimated to reach up to 82 Mt by 2030.[3] Due to their high content of valuable materials (especially, base and noble metals), complexity and diversity, a unitary strategy for WPCBs recycling cannot be applied, being used for this purpose combinations of consecrated (industrial) technologies and innovative experimental ones.[4,5]

More recently, several electro-hydrometallurgical WPCBs recycling processes based on electrochemically regenerable leaching systems such as  $\text{Cl}_2/\text{Cl}^-$ [6],  $\text{Fe}^{3+}/\text{Fe}^{2+}$ [7,8] or  $\text{Cu}^{2+}/\text{Cu}^+$ [9] were successfully tested. Between these alternatives, our already published results indicate that our innovative process, based on the electrochemically recyclable  $\text{Br}^-/\text{Br}_2$  leaching system, promises to be a feasible and advantageous solution.[10-14] In this context, it is important to note that the experimental result presented in this work were obtained by authors during the elaboration of the bachelor thesis of Mr. Eng. Gabriele-Mario Bogdan.[15] In this framework, to increase the profitability of the proposed process, to significantly reduce the environmental impact, and, more importantly, to consolidate its circular economy character, we concluded that this innovative technology can be started and operated continuously, in a quasi-closed loop, using only 3 main raw materials: (i) a solution of 2 M KBr + 0.5 M HBr used as fresh (primary) leaching agent and primary washing flow of final products, (ii) a KOH solution with concentration over 0.5 M required for the precipitation of trace metals unrecovered by electrodeposition, and (iii) demineralized water, used for the final decontamination of the final products and recovered materials.[15]

Consequently, during the present work, we evaluated and confirmed the feasibility of producing and recycling, on-site, the fresh leaching solution and the KOH one. To do this, accepting the performance limitations of the ion exchange membranes (IEM)[16-19], we built and tested a computer controlled complex experimental setup based on a filter-press electrochemical reactor (FPER), divided in four compartments (named C1 to C4) by two cation exchange membranes (CEM1 and CEM2) and an anion one (AEM), able to produce HBr and KOH by electrodialysis.

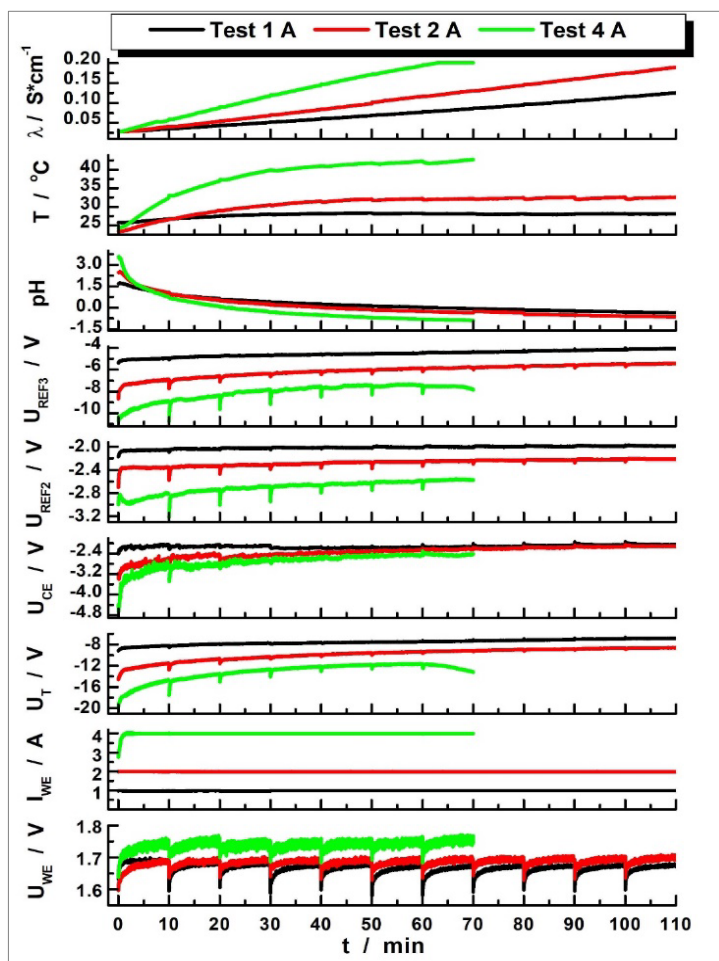
Moreover, inspired by literature data[20,21], synchronously with the electrodialysis tests, we recorded and treated pH, conductivity and temperature data, proving that the concentrations of the target solutions can be easily, accurately and rapidly evaluated and monitored on-line using simple and inexpensive electrochemical sensors.

## RESULTS AND DISCUSSION

The main measurements performed during the present study consist of 3 complex experiments, all divided in steps with equal duration, of 10 minutes each one. The tests were performed galvanostatically at imposed currents through the FPER of 1, 2 and 4 A, corresponding to current densities (i) of 1, 2 and 4 kA/m<sup>2</sup>. The tests done at 1 and 2 A lasted 110 min., whereas the one performed at 4 A was terminated prematurely, at 70 min., due to the saturation of the conductivity measurement system. To rigorously evaluate the quantities of HBr and KOH produced throughout each 10 min. stage, 2 samples of 5 mL were extracted from the tanks connected to C2 and C4 of the FPER and analyzed by automatic titration using KOH and (COOH)<sub>2</sub>, both of 0.1 N concentration, respectively.

During each experiment, complex sets of data were recorded on-line using the data acquisition system and a dedicated LabView application, and were used to evaluate the main operational parameters presented in Figure 1, where  $U_{WE}/V$  (in V) represents the potential of the working electrode (WE, anode in this case) in respect to the reference electrode 1 (Ref.1),  $I_{WE}/A$  is the current (in A) imposed through the WE,  $U_T/V$  stands for the voltage (in V) at the FPER's terminals,  $U_{CE}/V$  is the potential (in V) of the counter electrode (CE, cathode in this case) in respect to Ref.4,  $U_{REF3}$  and  $U_{REF2}$  represent the potentials measured using Ref.2 and Ref.3, in the second and third compartments of the FPER, respectively, pH is the pH value measured in the tank connected to C2, and, finally,  $T/^\circ C$  and  $\lambda/S^*cm^{-1}$  represent the temperature (in  $^\circ C$ ) and the conductivity ( $\lambda$ , in  $S^*cm^{-1}$ ) of the KOH solution stored in the tank connected to the C4 of FPER.

As it can be seen in Figure 1, each doubling of the imposed current ( $I_{WE}$ ) through FPER has a small influence over the  $U_{WE}$  value (of less than 50 mV), indicating that, fortunately, the use of a dimensionally stable anode for  $O_2$  evolution (DSA- $O_2$ ) and a concentrated anolyte (2 M  $H_2SO_4$ ) lead to a small overpotential for  $O_2$  evolution. Contrarily, the use of a Ni cathode and a relatively diluted KOH solution (0.1 N at start) as catholyte lead to significant  $U_{CE}$  increases, differences that becomes neglectable after the solution's alkalization, revealing that the major component of the  $U_{CE}$  is the ohmic drop over the catholyte and not the overpotential for hydrogen evolution.



**Figure 1.** Evolution of the main operational parameters during the experiments of HBr and KOH electrosynthesis by electro dialysis.

Studying the evolution of  $U_{REF2}$ , which represents, practically, the sum of the ohmic drops over the anolyte, CEM1 and half of the solution from the C2 of FPER, we conclude that CEM1 presents a good proton conductivity, and that these components play a minor role in the global budget of electrical energy consumption. Contrarily, the evolution of  $U_{REF3}$ , which is the sum of  $U_{REF2}$  with the ohmic drops over the AEM and half of the solutions from C2 and C3 of the FPER, suggests that the AEM presents a poor conductivity for bromide.

Concerning the evolution of the KOH solutions conductivities, quasi-linear increases can also be observed in Figure 1, but, for an accurate evaluation of the real concentrations, data must be corrected against the temperature evolution. More interestingly, for all performed tests, the recorded pH values, at each experiment's end, dropped significantly close to -1, suggesting a theoretical proton activity of around 10 M, fact which seems absurd in reality. In a first attempt, we tried to associate this anomaly to an abnormal proton activity in the concentrated KBr solution or to a failure of the pH measurement system in the studied conditions.

Noticeably, due to the Joule effect on electrolytes and CEM2, the temperatures of the recirculated KOH solutions increased constantly, the highest growth being recorded for the maximum tested current density ( $4 \text{ kA/m}^2$ ). Basically, this fact may be benefic for the process efficiency, diminishing the  $U_T$  values due to the increase of electrolytes' conductivity, but, if a high productivity is required, the resulted extra-heat must be carefully managed and smartly valorized to avoid damaging the setup components (FPER elements, pumps, tubes, etc.) and to diminish the process' costs.

Finally, comparing the evolution of the  $U_T$  parameter during the three experiments, we concluded that the imposed current through FPER, the concentration, conductivity and temperature of the electrolytes and also the membranes conductivity all together play essential roles on the  $U_T$  global values. Consequently, to increase the global process efficiency, an optimal compromise between the production rate and the global energy consumption must be found and applied.

Next, based on data presented in Figure 1 and those obtained by the automatic titration of the extracted samples, we evaluated the values of the major process performance indicators, represented by the current efficiency ( $C_{Eff,XXX,t}$ ), specific electrical energy consumption ( $W_{S,XXX,t}$ ), productivity ( $PR_{XXX,t}$ ) and the solutions molar concentrations ( $C_{M,XXX,t}$ ) at the sampling time ( $t$ , in s), the supplementary indexes "XXX" indicating the monitored product (HBr or KOH). Firstly, we evaluated the remaining volume ( $V_{T,XXX,t}$ ) in the corresponding tanks at the sampling moment  $t$ , using the equation:

$$V_{T,XXX,t} = V_{T,XXX,t-1} - 2 * V_S + \frac{\int_{t-1}^t I_{WE} \cdot dt}{F * 1000} * M_{H_2O} * \sum h_i \quad [\text{mL}] \quad (1)$$

where  $V_{T,XXX,t-1}$  is the remaining volume at the previous sampling time (t-1),  $V_S$  is the samples' volume (5 mL),  $F$  is the Faraday constant ( $F = 96485 \text{ A}\cdot\text{s}/\text{E.g.}$ ),  $M_{H_2O}$  is the molar mass of water, and  $h_i$  are the hydration numbers of the ions that migrate through the membranes. In our case,  $h_i$  values of 3, 6 and 7 were considered for  $H^+$ ,  $K^+$  and  $Br^-$ , respectively.

On the next step, using the  $C_{M,XXX,t}$  data (calculated as the mean of the values obtained by the automatic titration of each extracted samples pair), we calculated the amounts ( $m_{XXX,t}$ ) of the target compounds accumulated until the t moment, according with the next equation:

$$m_{XXX,t} = C_{M,XXX,t} * V_{T,XXX,t} * 10^{-3} \quad [\text{g}] \quad (2)$$

Having this data, the values of the  $C.\text{Eff.}_{XXX,t}$ ,  $W_{S,XXX,t}$  and  $PR_{XXX,t}$  parameters were calculated using the following equations:

$$C.\text{Eff.}_{XXX,t} = \frac{m_{XXX,t} - m_{XXX,t-1}}{M_{XXX} * \frac{\int_{t-1}^t I_{WE} \cdot dt}{F}} * 100 \quad [\%] \quad (3)$$

$$W_{S,XXX,t} = \frac{\int_{t-1}^t (U_T * I_{WE}) \cdot dt}{m_{XXX,t} - m_{XXX,t-1}} * \frac{10^{-3}}{3600} \quad [\text{kWh/kg}] \quad (4)$$

$$PR_{XXX,t} = \frac{m_{XXX,t} - m_{XXX,t-1}}{1000} * \frac{3600}{t - (t-1)} * \frac{10000}{S_{AE}} \quad \text{kg}/(\text{m}^2 \cdot \text{h}) \quad (5)$$

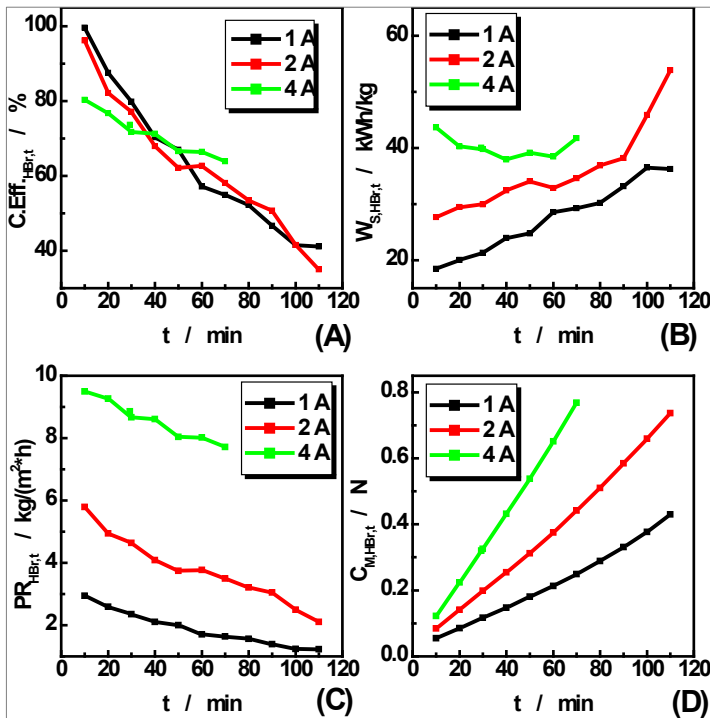
where  $m_{XXX,t-1}$  is the accumulated mass until (t-1),  $M_{XXX}$  are the molar masses of the products, and  $S_{AE}$  is the active surface of the electrodes (in  $\text{cm}^2$ ).

Using the previously presented equations, we calculated, by turn, the values of the performance parameters for the electrosynthesis of HBr and KOH by electrodialysis. The first data sets, evaluated for HBr, are presented in Table 1 and Figure 2, where, supplementarily to the already defined parameters, the indexes "A" and "F" indicate that the corresponding terms represent the averaged or final values, calculated for the whole experiment or at its end, respectively.

**Table 1.** Averaged or final values of the performance parameters for the electrosynthesis of HBr by electrodialysis using the FPER with 4 compartments

Test	$i$ kA/m <sup>2</sup>	C.Eff. <sub>HBr,A</sub> %	W <sub>S,HBr,A</sub> kWh/kg	PR <sub>HBr,A</sub> kg/(m <sup>2</sup> ·h)	C <sub>M,HBr,f</sub> M	pH <sub>f</sub> -
1 A	1	63.4	27.5	1.89	0.43	-0.81
2 A	2	62.4	36.0	3.76	0.74	-1.25
4 A	4	71.0	40.1	8.55	0.77	-1.20
4 A @ 46.5 min.	4	73.7	40.0	8.86	0.50	-0.70

As it can be seen from Table 1 and Figure 2, unexpectedly and fortunately, the four time increase of the current density ( $i$ ) leads to a more than 4.5-times larger average productivity ( $PR_{HBr,A}$ ) and a gentle improvement of the averaged current efficiency ( $C.Eff._{HBr,A}$ ), whereas the averaged specific energy consumption ( $W_{S,HBr,A}$ ) increased by only 31.5%. This benefic behavior can be explained by the fact that, at high  $i$  values, the undesirable mass transport through membranes

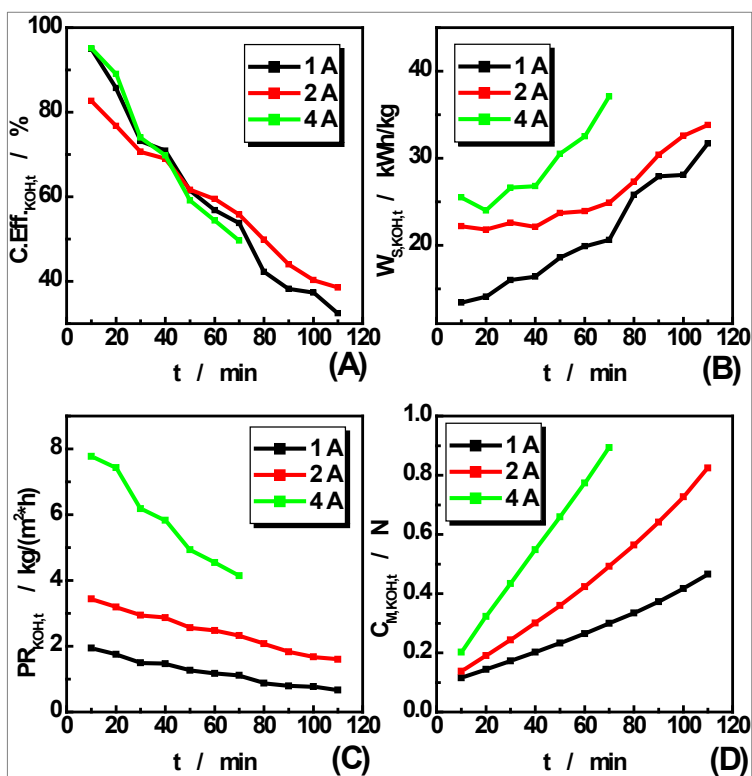


**Figure 2.** Time evolution of C.Eff.<sub>HBr,t</sub> (A), W<sub>S,HBr,t</sub> (B), PR<sub>HBr,t</sub> (C) and C<sub>M,HBr,t</sub> (D) for HBr electrosynthesis by electrodialysis using the FPER with 4 compartments.



due to the diffusion phenomenon (in the unwanted direction) becomes eclipsed by the ions' forced migration under the effect of the applied electric field. The competition between these two processes, combined with the inherent imperfections of the ion exchange membranes [16-19], lead to a small and constant degradation of the performance parameters, but their averaged values can be improved, as indicated in the last row of Table 1, by limiting the process duration until the target concentration is attained (0.5 M at approx. 46.4 min.).

Similar sets of data were recorded and treated to evaluate the performance parameters for the KOH electrolysis by electrodiagnosis using the FPER with 4 compartments, the obtained results being presented in Figure 3 and Table 2.



**Figure 3.** Evolution of C.Eff.<sub>KOH,t</sub> (A),  $W_{S,KOH,t}$  (B),  $PR_{KOH,t}$  (C) and  $C_{M,KOH,t}$  (D) for KOH electrolysis by electrodiagnosis using the FPER with 4 compartments.

**Table 2.** Averaged or final values of the performance parameters for the electrosynthesis of KOH by electrodialysis using the FPER with 4 compartments

Test	$i$ A/m <sup>2</sup>	C.Eff. <sub>KOH,A</sub> %	W <sub>S,KOH,A</sub> kWh/kg	PR <sub>KOH,A</sub> kg/(m <sup>2</sup> *h)	C <sub>M,KOH,f</sub> M	$\lambda_f$ mS/cm	T <sub>f</sub> °C
1 A	1000	58.82	21.15	1.210	0.466	125.3	28.09
2 A	2000	58.97	25.94	2.453	0.824	189.5	32.58
4 A	4000	70.16	28.99	5.834	0.893	200.8	42.70
4 A @ 24 min.	4000	82.44	25.70	6.840	0.500	104.0	38.40

As it can be seen from Figure 3 and Table 2, the evolution of the performance parameters for KOH electrosynthesis by electrodialysis in the FPER with 4 compartments is very similar to those observed in the case of HBr, the best results being obtained at the highest tested current density (4 kA/m<sup>2</sup>). Noticeably, due to the better selectivity of the CEM in rapport with the AEM one and the reduced number of water molecules remaining in the cathodic compartment (C4), the target concentration of KOH (0.5 M) can be attained, as pointed in the last row of Table 2, after only 24 min. Also, excellent values for C.Eff.<sub>KOH,A</sub> and PR<sub>KOH,A</sub> were obtained, whereas the 4 time increase of the current density raises the value of W<sub>S,KOH,t</sub> by only 17.7%, but multiplies 5.7 times the PR<sub>KOH,A</sub> value.

From another point of view, it is important to note that the essential raw materials (KBr, KOH and demineralized water) are recycled in the proposed process and that the moderate concentrations of the recirculated electrolytes diminish the equipment degradation. In these conditions, we concluded that the main production expenses can be associated with the cost of electricity. Consequently, based on this assumption and using global market data, we tried to evaluate the profitability of the proposed technical solution, the essential information being summarized in Table 3.

**Table 3.** Basic data for economical analysis of proposed process

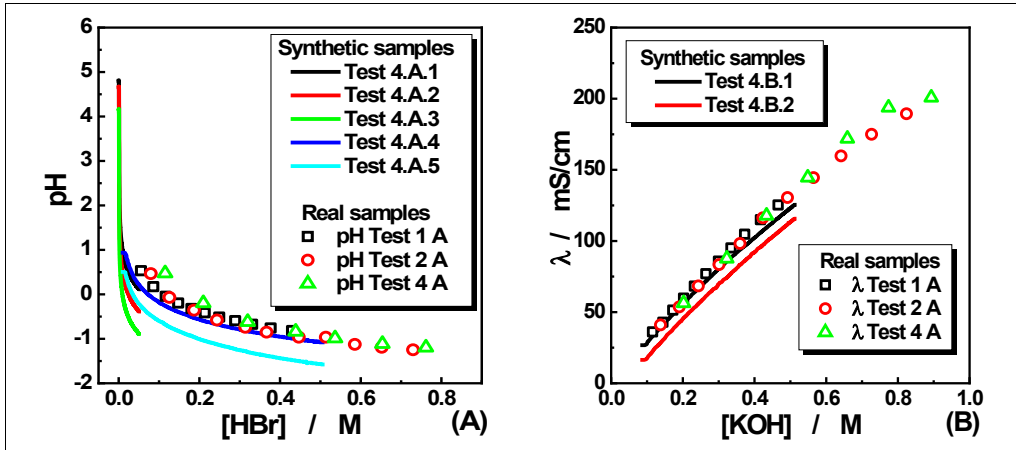
Reagent	W <sub>S,A</sub>	Electricity cost	Market Price	Difference
	(MWh/t)	USD/t	USD/t	(%)
HBr	40.0	8685	2480 [22]	+350
KOH	25.7	5580	900 [23]	+620

For the calculations presented in Table 3, an average electricity price (for the 2023 second half) of 0.2008 Euro/kWh[24] and an US Dollar (USD) to Euro (EUR) exchange rate of 0.9248[25] were considered, revealing that

our process is able to produce, at an optimal compromise between the operational parameters, the essential reagents (HBr and KOH) at a price, apparently, 3.5 and 6.2 times larger in comparison with those available on the free market, respectively. In practice, the situation looks much better, because the market prices indicated in Table 3 represent the FOB-Shanghai values[26] and, for HBr, the offered product is a 48% solution and not the pure reagent, meaning that, the on-site production of main raw materials probably starts becoming profitable by eliminating the high import, shipping, storage and handling costs. Moreover, the process profitability may still be improved considering that: (i) both reagents are produced simultaneously, using the same amount of electricity; (ii) supplementary energy (as electricity and heat) can be recovered by valorizing the produced hydrogen in a  $H_2/O_2$  combustion fuel cell; (iii) the produced extra-heat can be valorized properly and smartly in the interest of the process. Finally, considering that the proposed process can be fully automated, and the required reagents are produced only on-demand, we conclude that the obtained economies will be sufficient to cover the amortization, operation and maintenance costs. Also, the global carbon fingerprint of the proposed technology will be significantly reduced, and the process can be considered as a substantial component in the framework of the circular economy concept.

The second goal of our research was to evaluate the possibilities to monitor, simply and efficiently, on-site, in-situ and on-line, the concentrations of the produced reagents. The tested solution consisted in using simple, reliable and cheap pH and  $\lambda$  electrochemical sensors assisted by temperature ones. Firstly, to observe, in the interest range, the pH and  $\lambda$  evolution in respect to HBr and KOH concentrations, synthetic samples were prepared by additions of concentrated acid and base solutions in 2 M KBr of pH of 5 and 1, and 0.1 M KOH, respectively. For these measurements we used the same experimental setup and dedicated LabView software as for automated titration, the obtained results for the repeated experiments being presented in Figure 4.

As it can be seen from Figure 4, the data recorded during the repeated measurements performed in the synthetic samples are quasi-identical, the individual observation of the obtained curves being possible only after an artificial down-shifting. In these conditions, we conclude that the evolutions of pH and  $\lambda$  in respect to the concentrations of the samples are highly reproducible, creating the premises to use these parameters to monitor rapidly and accurately the process evolution. Interestingly and unexplainedly, as already pointed in the comments for the Figure 1, the pH values, recorded in the mixtures of 2 M KBr with HBr of concentrations higher than  $10^{-3}$  M, indicate a proton activity 10 times larger than those evaluated by calculation. The elucidation of this abnormal behavior will be one of the main goals of the upcoming research activity.



**Figure 4.** Comparison between: (A) pH values recorded in synthetic samples prepared by addition of 0.1 M HBr in 2 M KBr (Test 4.A.1÷4.A.3) or HBr 1 M in 2 M KBr + 0.01 M HBr (Test 4.A.4÷4.A.5) with those resulting after the automatic titrations of samples extracted during the electro dialysis experiments; (B)  $\lambda$  values recorded in synthetic samples prepared by addition of 0.886 M KOH (Test 4.B.1÷4.B.2) in 0.1 M KOH with those resulting after the automatic titrations of samples extracted during the electro dialysis experiments. For better visibility, the curves corresponding to the Test 4.A.2, 4.A.3, 4.A.5 and 4.B.2 were artificially shifted down by 0.5, 1.0 and 0.5 pH units and 10 mS/cm, respectively.

On the next step, the data recorded in the synthetic samples were compared with the pairs of values resulted by correlating the concentration data evaluated by automatic titration (see Figures 2.D and 3.D) with the time evolution of pH and  $\lambda$  values (see Figure 1). The good correlation between these data allowed us to conclude that, by evaluating rigorously and compensating the inherent experimental, calibration and calculation errors, and using an appropriate temperature compensation, the pH and conductivity measurements for the obtained solutions offer a powerful tool to convert these electrochemical data into the corresponding instant concentration values, assuring a reliable, accurate and unexpensive, on-site, in-situ and on-line monitoring of the proposed process functioning. Noticeably, the successful implementation of this monitoring solution requires a large data base concerning the correlations between pH,  $\lambda$ , concentration and temperature, which must be gathered using accurate equipment and pure reagents.

## CONCLUSIONS

Our already published results allow us to conclude that the proposed innovative process, based on the electrochemically recyclable Br/Br<sub>2</sub> leaching system can be started and operated continuously, in a quasi-closed loop, using only 3 main and simple raw materials. Consequently, during the present work, we evaluated and confirmed the feasibility of producing and recycling, on-site, the fresh leaching solution and the KOH one. For this purpose, we built and tested a complex experimental setup designed around a four compartments FPER, divided using two cation exchange membranes and an anion one, able to produce KOH and HBr through electrodialysis. Using this equipment, we performed 3 sets of experiments at 3 different current densities allowing us to conclude that the best compromise between the operational parameters corresponds at the current density of 4 kA/m<sup>2</sup>. In these conditions, running the process until the target concentrations were attained, current efficiencies over 73% and 82%, and specific electricity consumption around 40 and 27 kWh/kg were obtained for HBr and KOH electrosynthesis by electrodialysis, respectively.

Additionally, a preliminary economic analysis performed using our results and market data allow us to conclude that the proposed process is profitable, and, by optimizing it, we can improve the rentability.

Finally, completing additional experiments, we proved that, using simple, reliable and inexpensive pH and conductivity electrochemical sensors, the concentrations of the target products can be easily, rapidly and accurately monitored on-site, in-situ and on-line.

As a perspective, these researches will continue with several studies concerning the recovery of KBr and regeneration of demineralized water by electrodialysis. Moreover, substantial researches will be performed to elucidate the observed discrepancy between pH and the real proton concentration, to acquire and treat data to find empirical or analytical correlations between the solutions' concentration and temperature, and their pH and conductivity, respectively. Additionally, consistent efforts will be focused on the optimization of the experimental parameters.

## EXPERIMENTAL SECTION

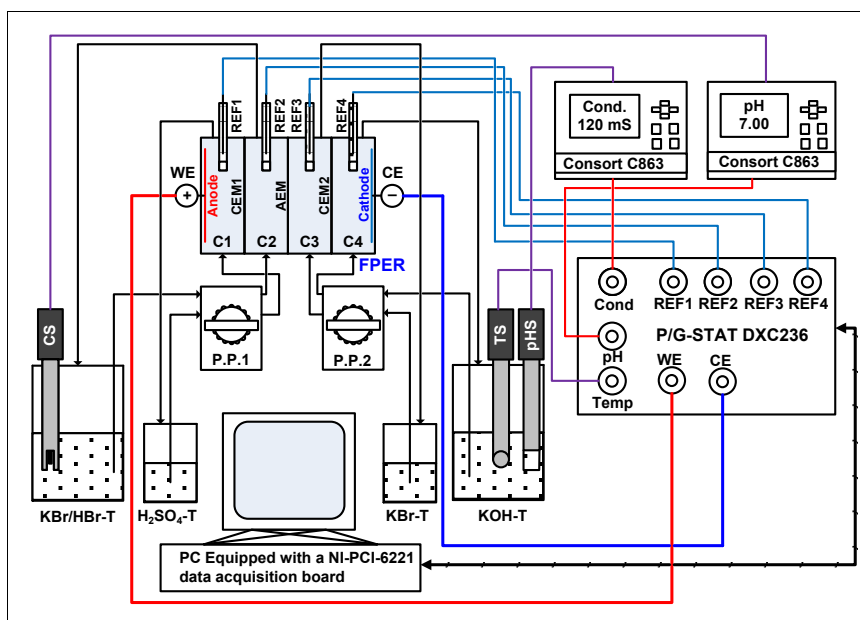
### Chemicals

Pure solids of KBr and KOH and 48% HBr solution of p.a. grade (Merck) were used to prepare the required solutions. Unless specified otherwise, 2 M KBr solutions were used, especially as starting solutions in the flow circuit associated

with C2 and C3 of the FPER. Additionally, 7.01 and 1.68 pH, and 111.8 mS/cm standards (Hanna Instruments, Romania) were used to calibrate the pH-meter and conductometer, respectively.

### Equipment and methods

The simplified schematic of the experimental setup used for the electro dialysis tests is presented in Figure 5. The presented schematic reveals that the main experimental setup was built around a four compartments FPER of MicroFlowCell® type, equipped with two CEM of NAFION 423 type (DuPont, France), a DSA-O<sub>2</sub> and a Ni cathode, all from Electrocell (Denmark), and one AEM of Fumasep FAB-PK-130 type (FUMATECH BWT GmbH, Germany). The effective surface of both electrodes and membranes was 10 cm<sup>2</sup>. For the electro dialysis experiments, the electrolyte flows, at a volume flow rate of 40 mL/min, were assured by 2 peristaltic pumps model Reglo Digital MS-2/08-160 (ISMATEC, Switzerland), whereas, for the automatic titrations, a Reglo Analog MS2/8 peristaltic pump (ISMATEC, Switzerland) was used. Additionally, to measure the WE and CE potentials and those in the FPER's intermediary compartments, 4 liquid junctions and 4 home-made reference electrodes of Ag/AgCl/KCl<sub>SAT</sub> type were used.



**Figure 5.** Simplified scheme of the experimental setup used to produce HBr and KOH by electro dialysis.

To impose the required current through the FPER, a computer-controlled power source of DXC236 type (Datronix Computer SRL, Romania) was used for chrono-potentiometric measurements in galvanostatic mode. For the pH,  $\lambda$  and temperature measurements, a SP10T pH/T combined electrode (Consort, Belgium), a conductometric cell of CM 02/88G type (Tacussel, France) and a Pt-100 sensor (Radiometer, France) were used, respectively. The power source and the peristaltic pumps were computer-controlled using a NI-PCI-6221 data acquisition board (National Instruments, USA). LabVIEW 2015 applications were used to control the equipment and to acquire, treat and save the data. For pH and  $\lambda$  measurements, two Consort C863 multi-parameter analyzers (Consort, Belgium) were additionally used.

## REFERENCES

1. A. Hayes, "Consumerism: Definition, Economic Impact, Pros & Cons", **2024**, [www.investopedia.com/terms/c/consumerism.asp](http://www.investopedia.com/terms/c/consumerism.asp), Accessed 15.07.2024.
2. P. I. Tantawi, *Int. Rev. Public. Nonprofit Mark.*, **2024**, *21*, 1-25.
3. C. P. Baldé, R. Kuehr, T. Yamamoto, R. McDonald, E. D'Angelo, S. Althaf, G. Bel, D. Otmar, E. Fernandez-Cubillo, V. Forti, V. Gray, H. Sunil, S. Honda, G. lattoni, D. S. Khetriwal, V. Luda Di Cotremiglia, Y. Lobuntsova, I. Nnorom, N. Pralat, M. Wagner, "The Global E-waste Monitor 2024", UNITAR-SCYCLE Programme, ITU, Geneva/Bonn, **2024**.
4. J. Fazari, M. Z. Hossain, P. Charpentier, *J. Mater. Sci.*, **2024**, <https://doi.org/10.1007/s10853-024-09941-6>.
5. R. Jha, M. Agrawal, A. Jena, G. Mishra, H. R. Verma, A. Meshram, K. K. Singh, *Can. Metall. Q.*, **2024**, 1-17. <https://doi.org/10.1080/00084433.2024.2310348>.
6. E. Y. Kim, M. S. Kim, J. C. Lee, J. Jeong, and B. D. Pandey, *Hydrometallurgy*, **2011**, *107(3-4)*, 124-132.
7. L. A. Diaz and T. E. Lister, *Waste Manag.*, **2018**, *74*, 384-392.
8. S. Fogarasi, F. Imre-Lucaci, A. Egedy, Á. Imre-Lucaci, P. Ilea, *Waste Manag.*, **2015**, *40*, 136-143.
9. C. Cocchiara, S. A. Dorneanu, R. Inguanta, C. Sunseri, P. Ilea, *J. Clean. Prod.*, **2019**, *230*, 170-179.
10. S. A. Dorneanu, *Studia UBB Chemia*, **2017**, *LXII(3)*, 177-186.
11. S. A. Dorneanu, A. A. Avram, A. H. Mărincaș, N. Cotolan, T. Frențiu, P. Ilea, *Studia UBB Chemia*, **2018**, *LXIII(4)*, 147-158.
12. S. Varvara, S. A. Dorneanu, A. Okos, L. M. Muresan, R. Bostan, M. Popa, D. Marconi, P. Ilea, *Materials*, **2020**, *13*, 3630.
13. M. I. Frîncu, E. Covaci, S. A. Dorneanu, P. Ilea, *Studia UBB Chemia*, **2020**, *LXV(3)*, 33-44.

USE OF ELECTRODIALYSIS TO PRODUCE AND RECYCLE ON-SITE RAW MATERIALS FOR  
WASTE PRINTED CIRCUIT BOARD RECYCLING PROCESS

14. M. I. Frîncu, E. Covaci, S. A. Dorneanu, P. Ilea, *Studia UBB Chemia*, **2020**, LXVI(2), 137-149.
15. G. M. Bogdan, "Production by electrodialysis od materials and raw materials for WPCBs recycling", *Batchelor Thesis*, FCIC-UBB, Cluj Napoca, Romania, **2024**.
16. H. Deng, H. Wang, Y. Hao, S. Chen, W. Zhang, *Sep. Purif. Technol.*, **2024**, 340, 126774.
17. T. Luo, S. Abdu, M. Wessling, *J. Memb. Sci.*, **2018**, 555, 429-454.
18. J. Ran, L. Wu, Y. He, Z. Yang, Y. Wang, C. Jiang, L. Ge, E. Bakangura, T. Xu., *J. Memb. Sci.*, **2017**, 522, 267-291.
19. C. Jiang, M. M. Hossain, Y. Li, Y. Wang, and T. Xu, *J. Memb. Separ. Tech.*, **2014**, 3(4), 185-205.
20. R. J. Giliam, J. W. Graydon, D. W. Kirk, S. J. Thorpe, *Int. J. Hydrogen Energy*, **2007**, 32, 359-364.
21. E.S. Shahid, S.H. Afzali, N. Talebbeydokhti, M. Rastegar, *Desalin. Water Treat.*, **2020**, 175, 255-262.
22. <https://www.chemanalyst.com/Pricing-data/hydrobromic-acid-1135>, Accessed 16.07.2024.
23. <https://www.chemanalyst.com/Pricing-data/caustic-potash-1212>, Accessed 16.07.2024.
24. [https://ec.europa.eu/eurostat/statistics-explained/index.php?title=Electricity\\_price\\_statistics](https://ec.europa.eu/eurostat/statistics-explained/index.php?title=Electricity_price_statistics), Accessed 15.07.2024.
25. <https://www.poundsterlinglive.com/history/USD-EUR-2023>, Accessed 15.07.2024.
26. <https://www.shippo.co.uk/glossary/fob-free-on-board/>, Accessed 16.07.2024.





# ANTIOXIDANT ACTIVITY ENHANCEMENT OF ICARISIDE II THROUGH COMPLEXATION WITH WHEY PROTEIN CONCENTRATE

Róbert SZABÓ<sup>a</sup>, Csaba Pál RÁCZ<sup>b</sup>, Norbert MUNTEAN<sup>b</sup>,  
Francisc Vasile DULF<sup>a\*</sup>

**ABSTRACT.** Various food supplements provide antioxidant benefits by neutralizing free radicals, thus preventing diseases associated with oxidative stress. The antioxidant properties of pure icaraside II (ICS), icaraside II whey protein concentrate complex (ICS-WPC), and surfactant-based icaraside II whey protein complexes (S-ICS-WPC) were evaluated. The assessment was conducted using the Briggs-Rauscher oscillating system and the 1,1-diphenyl-2-picrylhydrazyl (DPPH·) radical scavenging assay, with the latter providing a quantitative analysis of antioxidant capacity. The complexation procedure successfully increased the antioxidant activity of ICS.

Additionally, the inclusion of various surfactants such as Tween 80 and lecithin in the ICS-WPC complex led to further significant advancements.

**Keywords:** *icaraside II, antioxidant activity, whey protein complexes, Briggs-Rauscher oscillating reaction, DPPH· radical scavenging*

## INTRODUCTION

Free radicals are formed during regular physiological functions like metabolism, as well as by external factors such as tobacco smoke, UV radiation, chemicals, etc. [1]. The accumulation of free radicals can result in oxidative

<sup>a</sup> *Department of Environmental and Plant Protection, University of Agricultural Sciences and Veterinary Medicine Cluj-Napoca, 3-5 Calea Mănăştur, 400372 Cluj-Napoca, Romania*

<sup>b</sup> *Babeş-Bolyai University, Faculty of Chemistry and Chemical Engineering, Department of Chemistry and Chemical Engineering, Hungarian Line of Study, 11 Arany János str., RO400028, Cluj-Napoca, Romania*

\* *Corresponding author: francisc.dulf@usamvcluj.ro*



stress, which can damage cells, proteins, and DNA. Thus, antioxidants play an important role in our health by preventing the harmful activity of those free radicals. Antioxidants, based on their origin, can be categorized into synthetic and natural forms. Natural antioxidants have fewer negative effects on the human body, consequently, their demand by the general population has increased in the last decade [2]. Natural flavonoids, such as icaraside II (ICS), are essential for various biological processes and responses to environmental factors in plants. These compounds are frequently found in human consumption patterns and exhibit significant antioxidant properties alongside a range of other bioactive functions, including antimicrobial and anti-inflammatory effects, which contribute to the prevention of diseases [3].

Icaraside II, also called Baohuoside I, serves as the primary pharmacological metabolite derived from icariin, the principal active ingredient found in the botanical species *Herba Epimedii sp.* [4]. Historically, in ancient China, these plants were utilized as herbal remedies known for their aphrodisiac and antirheumatic properties [5]. Recent investigations have brought to light various other health-enhancing properties of icaraside II. Among these, the most noteworthy include its potential as an anticancer agent [6], its efficacy in treating cardiovascular diseases [7], its ability to halt the progression of neurodegenerative disorders [8], and its effectiveness in addressing erectile [9] and testicular dysfunction [10]. ICS exhibits antioxidant effects by effectively reducing the levels of reactive oxygen species. Additionally, it enhances the activities of antioxidant enzymes, thereby demonstrating its great ability to combat oxidative stress [11]. Because of the properties mentioned above, ICS demonstrates considerable promise for utilization as a dietary supplement. Its distinct qualities position it as a favorable choice for integration into dietary regimens to enhance nutritional and wellness advantages.

For the determination of antioxidant activity, numerous tests are documented in the literature: Oxygen radical absorbance capacity (ORAC), Trolox equivalent antioxidant capacity (TEAC), 1,1-diphenyl-2-picrylhydrazil (DPPH·), Total oxidant scavenging capacity (TOSC), and Total radical trapping parameter (TRAP) [12]. These methods produce different radicals, using different solvents and different pH values ranging from 3.3 to 10.5. Moreover, a limitation of each assay is their suitability for only hydrophilic or lipophilic substances according to the solvent they use [13].

Another method to determine the antioxidant properties of different natural compounds is the Briggs-Rauscher (BR) oscillating system. It was observed by R. Cervellati et al. that the addition of antioxidants to the system caused an immediate halt of the oscillations, however, over time, the oscillatory pattern is restored [14]. The duration in which the oscillations cease is referred to as the inhibition time. A linear correlation was found between the duration of inhibition and the quantity of antioxidants incorporated into a BR mixture [15].

This discovery [14] has paved the way for the development of a straightforward, consistent, swift, and cost-effective analytical method for assessing the efficiency of antioxidant agents in neutralizing free radicals. The greatest advantage of this method is that it operates at  $\text{pH} \approx 2$ , which is in the vicinity of the acidic environment of stomach fluids [16]. Given that ICS food supplements are ingested orally, it is plausible that they demonstrate a significant portion of their antioxidant properties in combating the free radicals generated within the stomach. Additionally, certain antioxidants exhibit higher levels of activity and stability in an acidic solution as opposed to an alkaline one [17]. It is important to note that the free radicals found in the BR system, hydroperoxyl ( $\text{HOO}\cdot$ ) and hydroxyl ( $\text{HO}\cdot$ ) are identical to those naturally produced in the human body [18]. Providing an advanced representation of physiological processes in terms of antioxidant activity, the BR method is particularly valuable in assessing the *in vivo* effects of digested antioxidants.

The DPPH $\cdot$  radical scavenging assay is the most widely recognized, popular, and commonly used method to quantitatively determine antioxidant activity [19]. The mechanism of this approach lies in the modification of the solution's color as it interacts with the antioxidant substances. The antioxidants cause a hydrogen atom transfer, leading to the reduction of DPPH $\cdot$  to DPPH-H, resulting in the solution changing color from violet to pale yellow [20]. This color shift can be easily monitored with UV-VIS spectroscopy. Consequently, the DPPH $\cdot$  radical scavenging assay is commonly employed to evaluate the antioxidant capabilities of various substances, including pure antioxidant compounds, herbal extracts, and phenolic compounds such as icaraside II. While this technique may not be as accurate in representing the physiological processes as the BR, but it offers improved quantitative analysis capabilities.

The main objective of this research was to assess the changes in antioxidant properties of the products in relation to the pure material, demonstrating that the production process improved antioxidant activity. The Briggs-Rauscher oscillation technique provided qualitative insights into the antioxidant activity occurring in the human digestive system, especially in the stomach, whereas the DPPH $\cdot$  method facilitated a quantitative evaluation.

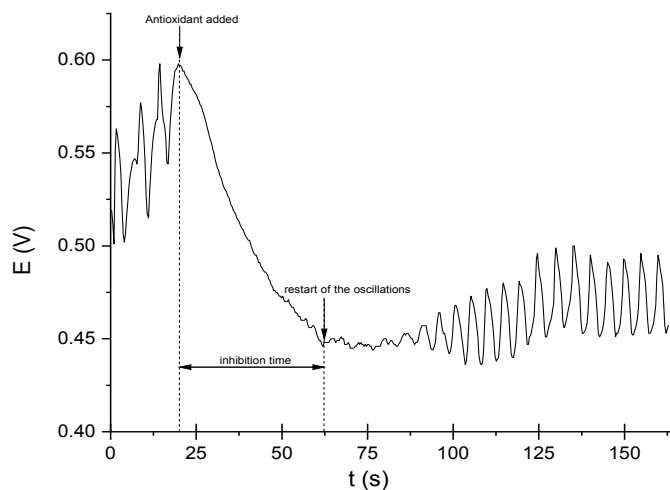
## RESULTS AND DISCUSSION

### **Antioxidant activity measurements with Briggs-Rauscher oscillating system**

The Briggs-Rauscher oscillation method provided a close insight into the antioxidant activity in the human digestive system, specifically the stomach.

Distilled water was employed in this setup to closely mimic the circumstances of the orally consumed ICS food supplements. From each sample, based on their molecular ratio, an equal amount of active agent was measured.

At the 3<sup>rd</sup> oscillation, the antioxidants were added to the system, which led to the immediate halt of the oscillations. The measurement data were acquired, and analyzed by utilizing the OriginPro 2019b software. The obtained result is given in Figure 1.



**Figure 1.** The effect of 2-1-3-3 molar ratio ICS-WPC-Tween 80-Lecitin on the BR mixture. The addition of antioxidant, and the restoration of the oscillations are marked with arrows.

The interval between the cessation and resumption of the oscillations, known as the inhibition time, was calculated and resumed in Table 1.

**Table 1.** Inhibition time of the different samples

Sample		Inhibition time (s)
Pure ICS		3
Molecular ratio of ICS-WPC-Tween 80-Lecithin	2-1-0-0	20
	2-1-3-0	22
	2-1-0-3	25
	2-1-3-3	42

It can be observed that the pure ICS displayed a negligible to non-existent antioxidant impact. This result can be attributed to the fact that this material is insoluble in water [21]. The complexation with whey protein

concentrate led to a significant enhancement in antioxidant activity. This outcome can be attributed to the antioxidant capacity of the  $\beta$ -lactoglobulin [22], which is the main component of the whey protein. Also, the complexation results in a higher water solubility which contributes to enhancing antioxidant activity. Furthermore, it can be observed that the addition of one of the surfactants didn't result in a significant antioxidant increment. In case when both surfactants were added to the mixture a synergetic effect took place and significantly increased the antioxidant activity of the final product.

### Antioxidant activity measurements with DPPH• free radical scavenging

To quantitatively determine the antioxidant activity of the samples the value of  $IC_{50}$  was calculated. By definition, the  $IC_{50}$  value represents the concentration of antioxidants needed to decrease the initial free radicals found in the DPPH• solution by 50% [23]. Therefore, this signifies that the value of  $IC_{50}$  is inversely proportional to the antioxidant activity. The measured data can be interpreted with the following equation:

$$C_{sample} = a \times A + b$$

where the  $C_{sample}$  represents the concentration of the sample,  $A$  the measured decrease in absorption, while  $a$  and  $b$  are the slope of the line and its y-intercept. From those values, the  $IC_{50}$  can be calculated with the following equation:

$$IC_{50} = \frac{(50 - b)}{a}$$

The obtained  $IC_{50}$  values are presented in Table 2.

**Table 2.** Half-maximal inhibitory concentrations ( $IC_{50}$ ) and standard error of the mean

Sample	$IC_{50}$ ( $\mu\text{g/mL}$ )	
Ascorbic acid	$5.0 \pm 1.1$	
Pure ICS	$3567 \pm 300$	
Molecular ratio of ICS-WPC-Tween 80-Lecithin	2-1-0-0	$2650 \pm 615$
	2-1-3-0	$1635 \pm 353$
	2-1-0-3	$1210 \pm 63$
	2-1-3-3	$856 \pm 178$

As can be observed, the antioxidant activity of pure ICS is exceedingly low compared to the ascorbic acid. However, the complexation with WPC led to an increase in antioxidant capacity. Furthermore, the addition of both surfactants (Tween 80 and lecithin) resulted in a 4.16-fold antioxidant activity increase. The progression of each product demonstrated a rise in antioxidant activity. The initial formation of complexes between ICS and WPC led to a 1.34-fold increase, possibly due to the antioxidant capabilities of  $\beta$ -lactoglobulin [22] and the increased solubility of the complexes in comparison to pure ICS. Subsequently, the incorporation of surfactants, such as Tween 80 and lecithin, further enhanced the final products' antioxidant activity.

## CONCLUSIONS

The primary aim of this study was to investigate the impact of complexation and the addition of surfactants on the antioxidant activity of icaraside II. Two methods were employed for this purpose: the BR technique and the DPPH $\cdot$  method. The first was applied for qualitative studies, replicating the antioxidant effects of the samples within the human gastric environment using distilled water as a solvent. Secondly, the DPPH $\cdot$  method was utilized for quantitative measurements of antioxidant properties. The BR method closely imitates antioxidant reactions related to free radicals in the human body, while the DPPH $\cdot$  method provides a more precise quantitative evaluation of antioxidant activity, especially given the limited solubility of the samples in water.

The results from these measurements demonstrated that the antioxidant activity of pure ICS was significantly enhanced through complexation with whey protein concentrate. Furthermore, the addition of surfactants resulted in additional increases in antioxidant activity. The similarity in trends between the two measurement methods is evident in how various preparation methods impacted antioxidant activity.

The BR method revealed that orally administered pure ICS would not exhibit antioxidant effects in the human body due to its insolubility in water. To address this limitation, complexation with WPC and the addition of surfactants were necessary.

Quantitatively, the final product, 2-1-3-3 ICS-WPC-Tween 80-Lecithin, showed the most significant improvement, with a remarkable 4.16-fold increase in antioxidant activity compared to pure ICS.

## EXPERIMENTAL SECTION

### *Materials and methods*

Icaraside II of analytical grade purity was acquired from Xi'an Day Natural Inc., located in China. The whey protein concentrate (80%) was purchased from

Foodcom S.A., a company based in Warsaw, Poland. Additionally, Tween 80 and lecithin were obtained from Sigma-Aldrich, Germany. All other reagents used in the experiments were of analytical grade.

### **Antioxidant activity measurements with Briggs-Rauscher oscillating system**

The antioxidant activity of pure ICS and the complexes with different molar ratio ICS-WPC-Tween 80-Lecithin (2-1-0-0, 2-1-3-3, 2-1-3-0, 2-1-0-3) was observed. An equivalent quantity of ICS (4 mg) from the different samples was diluted in 50 mL distilled water. To maintain consistency and reliability in the results for the BR antioxidant measurements the protocol described by Szabó et al. was closely followed [18]. The temperature was regulated at a constant level by employing a double-walled vessel with a 50 mL capacity connected to a thermostat. Continuous water circulation within the temperature jacket ensured a stable temperature of 37°C to simulate the physiological body conditions. The oscillations were electrochemically observed using an Ag/AgI indicator electrode and a Pt-wire counter electrode. The setup was linked to a computer via a PCI 6036 E data acquisition interface.

Using double distilled water, stock solutions of the following concentration were prepared for the oscillation reaction:  $[\text{H}_2\text{SO}_4]_0=0.27\text{ M}$ ,  $[\text{KIO}_3]_0=0.125\text{ M}$ ,  $[\text{MA}]_0=0.25\text{ M}$ ,  $[\text{MnSO}_4]_0=0.032\text{ M}$ , and  $[\text{H}_2\text{O}_2]_0=6.6\text{ M}$ . From each solution 5 mL was added, the mixing order was as follows: malonic acid,  $\text{MnSO}_4$ ,  $\text{H}_2\text{SO}_4$  and  $\text{KIO}_3$  and finally using  $\text{H}_2\text{O}_2$  the oscillation reactions were initiated.

### **Antioxidant activity measurements with DPPH• free radical scavenging**

Similarly, as above, the antioxidant activity of pure ICS and the complexes with different molar ratio ICS-WPC-Tween 80-Lecithin (2-1-0-0, 2-1-3-3, 2-1-3-0, 2-1-0-3) was analyzed. As standard the antioxidant capacity of ascorbic acid was used. From each complex, according to their molecular ratio, an equal amount of ICS (4 mg) was diluted in 10 mL of methanol. A methanol stock solution of  $1.01 \times 10^{-4}\text{ M}$  DPPH• was prepared and stored in an amber volumetric flask as a prevention from decomposition. Various concentrations of antioxidant solution were prepared with the addition of different volumes (ranging from 0 to 800  $\mu\text{L}$ ) of stock solution (4000  $\mu\text{g}/\text{mL}$ ) to 3 mL of the DPPH• stock solution, followed by the dilution with methanol to achieve a final volume of 5 mL. This process resulted in the preparation of a range of solutions. The acquired solutions were placed in the dark for 20 minutes for the reaction to take place. The addition of antioxidants to the DPPH• solution resulted in a color change that was observed with a UV-VIS spectroscope at 517 nm wavelength [24].



### Statistical analysis

All the measurements were conducted in triplicate and the results are reported as the mean value  $\pm$  the standard error of the mean. A one-factor ANOVA test was performed and statistical significance was established for  $p < 0.05$ .

### ACKNOWLEDGMENTS

This work was supported by a grant of the Ministry of Research, Innovation and Digitization, CNCS-UEFISCDI, project number PN-III-P4-PCE-2021-0750, within PNCDI III.

This work was supported by the Collegium Talentum Programme of Hungary.

### REFERENCES

1. H. T. Hoang; J.-Y. Moon, Y.-C. Lee; *Cosmetics*, **2021**, *8*, 106
2. S. H. Hassanpour, A. Doroudi; *Avicenna J. Phytomed.*, **2023**, *13*, 354
3. N. Shen; T. Wang; Q. Gan; S. Liu; L. Wang, B. Jin; *Food Chem.*, **2022**, *383*, 132531
4. R. Szabó; C. P. Rácz, F. V. Dulf; *Int. J. Mol. Sci.*, **2022**, *23*, 7519
5. X. Jin; Z.-h. Zhang; E. Sun; Q. Qian; X.-b. Tan, X.-b. Jia; *Int. J. Nanomed.*, **2012**, *4907-4916*
6. K. He; J. Wang; Y. Zhou; Z. Huang; N. Xie; Y. Li; H. Hu; Z. Chen; Y. He, Y. Tang; *Eur. J. Pharmacol.*, **2023**, *955*, 175914
7. S. Fu; Y.-L. Li; Y.-T. Wu; Y. Yue; Z.-Q. Qian, D.-L. Yang; *Biomed. Pharmacother.*, **2018**, *100*, 64-71
8. W. Fan, J. Zhou; *Exp. Ther. Med.*, **2024**, *27*, 1-10
9. T. Zheng; T. Zhang; W. Zhang; K. Lv; D. Jia; F. Yang; Y. Sun; J. Lian, R. Wang; *Biomed. Pharmacother.*, **2020**, *125*, 109888
10. C.-S. Lu; C.-Y. Wu; Y.-H. Wang; Q.-Q. Hu; R.-Y. Sun; M.-J. Pan; X.-Y. Lu; T. Zhu; S. Luo; H.-J. Yang; D. Wang, H.-W. Wang; *Phytomedicine*, **2024**, *123*, 155217
11. Y. Li; L. Feng; D. Xie; Y. Luo; M. Lin; J. Gao; Y. Zhang; Z. He; Y. Z. Zhu, Q. Gong; *Eur. J. Pharmacol.*, **2023**, *956*, 175987
12. Y. R. Girish; K. S. Sharath Kumar; K. Prashantha; S. Rangappa, M. S. Sudhanva; *Mater. Chem. Horizons*, **2023**, *2*, 93-112
13. 1K. Höner, R. Cervellati; *Eur. Food Res. Technol.*, **2002**, *215*, 437-442
14. R. Cervellati; N. Crespi-Perellino; S. D. Furrow, A. Minghetti; *Helv. Chim. Acta*, **2000**, *83*, 3179-3190
15. N. Muntean, G. Szabo; *Studia UBB Chemia*, **2013**, *58*, 175-183

ANTIOXIDANT ACTIVITY ENHANCEMENT OF ICARISIDE II THROUGH COMPLEXATION  
WITH WHEY PROTEIN CONCENTRATE

16. R. Cervellati; C. Renzulli; M. C. Guerra, E. Speroni; *J. Agric. Food Chem.*, **2002**, *50*, 7504-7509
17. J. Gajdoš Kljusurić; S. Djaković; I. Kruhac; K. Kovačević Ganić; D. Komes, Ž. Kurtanjek; *Acta Aliment.*, **2005**, *34*, 483-492
18. G. Szabo; E. Csiki; Á.-F. Szőke, N. Muntean; *Studia UBB Chemia*, **2022**, *67*, 7-16
19. L. Varvari; G. Szabo, A. Nicoara; *Studia UBB Chemia*, **2010**, *55*, 189-197
20. Í. Gulcin, S. H. Alwasel; *Processes*, **2023**, *11*, 2248
21. J. Hou; J. Wang; E. Sun; L. Yang; H.-M. Yan; X.-B. Jia, Z.-H. Zhang; *Drug Deliv.*, **2016**, *23*, 3248-3256
22. M. Stobiecka; J. Król, A. Brodziak; *Anim.*, **2022**, *12*, 245
23. F. Martinez-Morales; A. J. Alonso-Castro; J. R. Zapata-Morales; C. Carranza-Álvarez, O. H. Aragon-Martinez; *Chem. Pap.*, **2020**, *74*, 3325-3334
24. G. Celiz; M. Renfige, M. Finetti; *Chem. Pap.*, **2020**, *74*, 3101-3109



# OBTAINING AND CHARACTERIZATION OF PROPANEDIOL PHYTOEXTRACTS FROM *ACMELLA OLERACEA*

Claudia MAXIM<sup>a</sup>, Adriana TRIFAN<sup>b</sup> ,  
Daniela SUTEU<sup>a\*</sup>

**ABSTRACT.** Plant extracts are becoming an increasingly important trend in phytocosmetic preparations, replacing chemical synthesis products and ensuring the quality of products in line with consumer requirements. Using propanediol as an extraction solvent, this paper characterizes *Acmella oleracea* extracts obtained by traditional or combined extraction methods. The evaluation of their antioxidant activity and their content of polyphenols and flavonoids served as a basis for their physico-chemical characterization. Based on the best extract of *Acmella oleracea*, an emulsion was prepared and its stability and homogeneity were preliminary evaluated.

**Keywords:** *Acmella oleracea*, antioxidant activity, oxidative stress, propanediol, vegetal extract

## INTRODUCTION

People's shift towards a healthy lifestyle and concern for the environment have led to a change in preferences and choice of personal care products, with phytocosmetics increasingly seen as healthy alternatives to conventional cosmetics.

---

<sup>a</sup> "Gheorghe Asachi" Technical University of Iasi, Faculty of Chemical Engineering and Environmental Protection "Cristofor Simionescu", 53 D. Mangeron Blvd., RO- 700050, Iasi, Romania

<sup>b</sup> "Grigore T. Popa" University of Medicine and Pharmacy, Faculty of Pharmacy, Iași, Romania

\* Corresponding author: [danasuteu67@yahoo.com](mailto:danasuteu67@yahoo.com)



Biologically active molecules from plants are increasingly being targeted by scientists as raw materials in various industries, in cosmetics, pharmaceuticals, the food industry or in pest control. Plants are an inexhaustible source of biologically active molecules suitable for cosmetic products *Acmella oleracea* (L.) R. K. Jansen is a plant with great potential, belonging to the Asteraceae family and cultivated as a medicinal plant in South America, particularly in Mexico, Peru, Bolivia and Brazil, where it is known by various names: jambu, paracress or electric plant [1]. The genus *Acmella* comprises over 30 species, with *Acmella oleracea* being the most commonly cultivated species. It is distinguished from the other species by its cylindrical, disk-shaped flower heads of a golden yellow color with a red tip [2] (Figure 1). In the literature, the names of the genus and species of *Acmella oleracea* are often confused and the genus *Acmella* is often taxonomically confused with the genus *Spilanthes* [3].

Due to numerous revisions, the plant is sometimes referred to as *Acmella oleracea* (L.) R. K. Jansen [4], *Spilanthes acmella* L. [5] or *Spilanthes oleracea* L. [6]. It is a medicinal plant, but also a food known above all for its local anesthetic effect, traditionally used in indigenous areas to treat toothache, which is why it has also been called the “toothache plant” or a substitute for pepper in various culinary preparations [7,8]. Although the plant has been known and used for centuries by the tribes of the Peruvian Amazon as an anesthetic for toothache, it was not until 1975 that Dr. Françoise Barbira-Freedman, an anthropologist at the College of Cambridge, brought the anesthetic effect of the plant, which she had discovered during studies on medicinal plants in the Amazon region, to the fore. Amazonas, came to the fore [9]. In various systems of traditional medicine, *Acmella oleracea* is used as an analgesic, antibiotic, anticonvulsant, antidiuretic, antifungal, anti-inflammatory, antipyretic, stomach ulcer remedy, antiviral, antifungal, anthelmintic and insecticide [10]. The chemical composition of the plant has been extensively studied in the literature, reporting a high content of biologically active compounds of interest for cosmetic products, including N-alkylamides, vanillic acid, scopoletin, trans-ferulic acid, trans-isoferulic acid, stigmasterol and sitosterone [11].

The biological properties of the plant are mainly due to the content of N-alkylamides, a group of molecules found in the genera *Spilanthes* and *Acmella*, represented by the main component spilanthol, the primary metabolite responsible for the anesthetic effect [12]. The biomedical interest in N-alkylamides (NAA) has grown enormously, as potential raw materials for various industrial sectors [13]. Spilanthol, the most important secondary metabolite of *Acmella oleracea* L., has aroused particular interest in the cosmetics industry due to its muscle-relaxing effect on the facial muscles and is regarded as a natural alternative to botulinum toxin [14].

In order to develop its effect, spilanthol must overcome the barrier function of the stratum corneum and penetrate deep into the skin. In a study, Veryser et al. [13] analyzed the transdermal pharmacokinetics of spilanthol using human skin in a Franz cell diffusion model. They showed that spilanthol, due to its lipophilicity and low molecular weight, readily penetrates the skin barrier, moves into the dermis and further into muscle tissue, suggesting that the rate of penetration of spilanthol through the epidermis is dependent on the delivery vehicle used. Furthermore, spilanthol is an enhancer of skin penetration of active ingredients from topical compositions [15]. In addition, Demarne and Passaro [14] have demonstrated that spilanthol has a reversible blocking effect on muscle contractions by blocking the activity of calcium and sodium-potassium channels in the cell membrane of neurons, a mechanism that delays the appearance of wrinkles.

*Acmella oleracea* (L.) R. K Jansen is usually native to tropical or subtropical regions as a perennial plant or in Mediterranean areas as an annual plant, but can be successfully acclimatized in temperate areas as an annual plant as it is sensitive to ice [16,17]. Recently, it was also acclimatized in Romania, in a small experimental culture in Iasi County, Popricani locality. The interest in this species lay in the wide range of biological activities on the skin described in the literature, including anti-wrinkle effect, antioxidant effect, antimicrobial effect and reduction of pigmentation spots. However, it is well known that the secondary metabolites of the same plant species vary according to the geographical area in which the plant grows and according to climatic and environmental conditions [18].

The purpose of this article is to investigate the antioxidant capacity of the extracts of *Acmella oleracea* grown in Romania in order to confirm the therapeutic value of the plant and to incorporate it as a biologically active substance in (dermato)cosmetic compositions. In this sense, the aim was to determine the optimal conditions for the application of the extraction methods by maceration (M), extraction by ultrasound (US - sonoextraction) and two combined methods: sonoextraction + maceration (USM) and maceration + sonoextraction (MUS) for obtaining extracts from the plant *Acmella oleracea*, using an aqueous propanediol solution as extraction agent and the aerial parts (stem, leaves, flowers) of the plant as solid phase.

## RESULTS AND DISCUSSION

Using solid-liquid extraction under specific experimental conditions (type and concentration of extraction solvent, solid/liquid ratio, extraction time), the protocol shown in figure 1 was followed in order to obtain vegetal extracts from *Acmella oleracea*, a cultivated plant acclimatized in Iasi, Romania.



**Figure 1.** The steps involved in collecting and obtaining extracts from *Acmella oleracea*.

The efficiency of the extraction methods was evaluated according to the amount of polyphenols and flavonoids obtained, depending on the work methodology and the established extraction conditions.

After filtration and centrifugation, the extracts were stored in cool rooms (refrigerator at 2-5°C) until further processing. The subsequent study aims to calculate the total content of polyphenols and flavonoids and determine the antioxidant activity of the extracts with the most representative content of polyphenols.

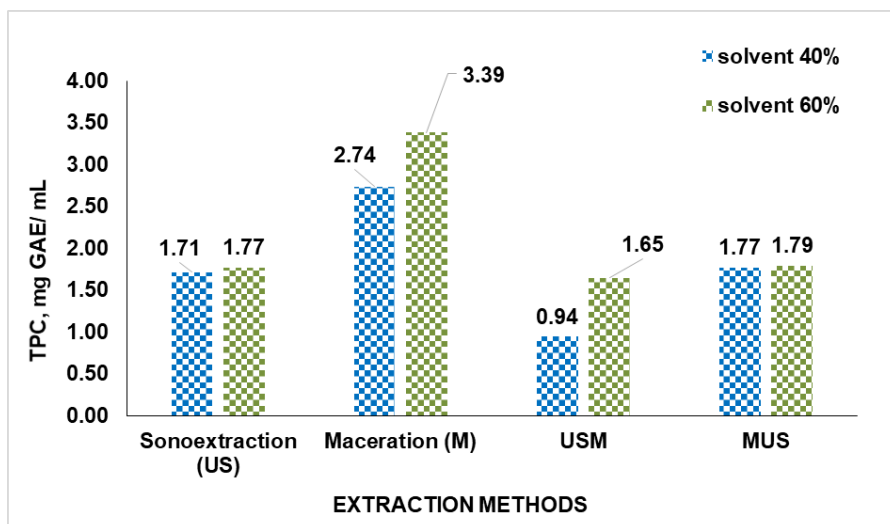
### Determination of the total content of polyphenols

The total content of polyphenols was determined spectrophotometrically, based on the Folin-Ciocalteu method [19] following a protocol used in a previous work [20] and applied to all plant extracts obtained depending on the extraction conditions. The results obtained were expressed as mg of Gallic acid equivalent (GAE) per mL extract and are presented in Figures 2-5.

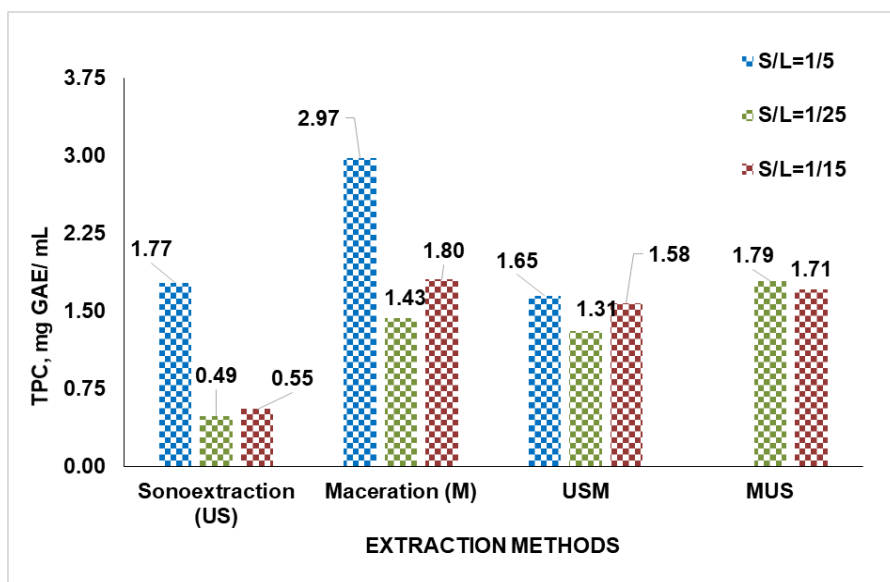
In the case of polyphenols, depending on the concentration of the extraction solvent (Figure 2), the best results were obtained through maceration (M)–3.39 mg GAE/mL (60%), also followed by maceration but with solvent of 40% concentration in propanediol with 2.74 mg GAE/mL (40%). Both variants were made using an S/L ratio of 1:5, an extraction time of 7 days.

If the assessment of the amount of extracted polyphenols is done according to the S/L ratio (Figures 3 and 4), it is observed that regardless of the concentration of the extraction reagent, the maceration (performed with a S/L ratio of 1:5 and a time of 7 days) is the method that provides the highest amounts of extracted polyphenols of 2.97 mg GAE/mL (60%), and respectively 2.74 mg GAE/mL (40%). It is followed by sonoextraction under S/L ratio conditions of 1: 5 and 5 minutes extraction time with a value of 1.77 mg GAE/mL (60%), respectively 1.71 mg GAE/mL (40%).

OBTAINING AND CHARACTERIZATION OF PROPANEDIOL PHYTOEXTRACTS  
FROM *ACMELLA OLERACEA*

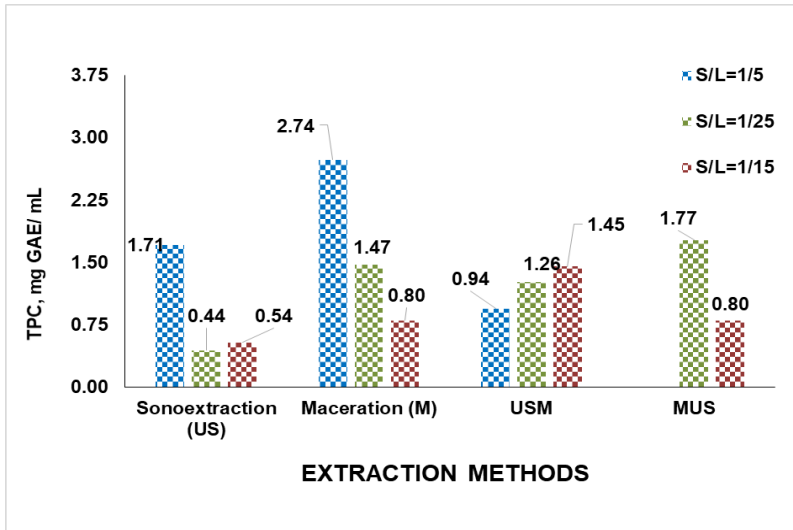


**Figure 2.** The total polyphenol content (TPC) in mg GAE/mL determined depending on the influence of solvent concentration. *Conditions:* (a) S/L= 1:5; M-7 days, US- 5 min., USM – 5 min+7 days; MUS : S/L= 1:20, 30 days +10 min.

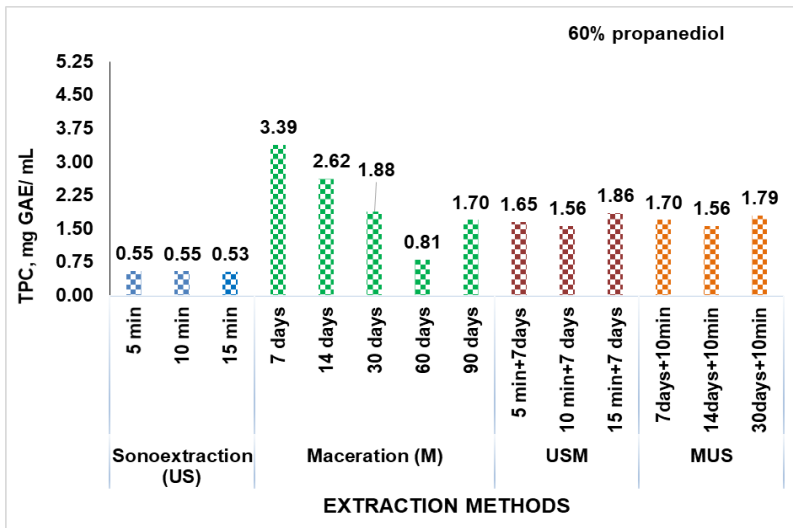


**Figure 3.** The total polyphenol content (TPC) in mg GAE/mL determined depending on the influence of ration solid (S)/liquid (L) when 60% propanediol was used as extraction agent . *Conditions:* M-7 days, US- 5 min., USM – 5 min+7 days; MUS- 30 days +10 min.



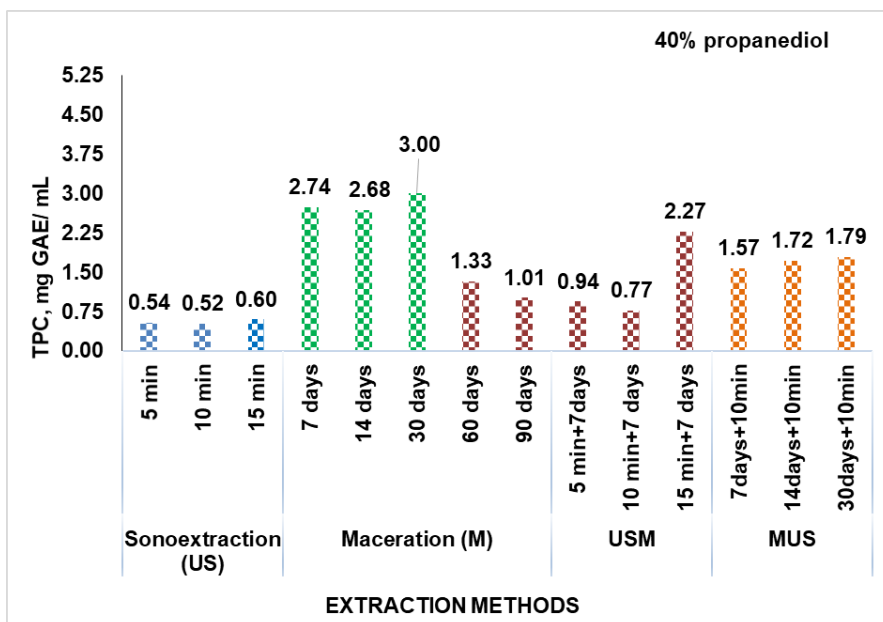


**Figure 4.** The total polyphenol content (TPC) in mg GAE/mL determined depending on the influence of ration solid (S)/liquid (L) when 40% propanediol was used as extraction agent . *Conditions:* M-7 days, US- 5 min., USM – 5 min+7 days; MUS- 30 days +10 min.



**Figure 5.** The total polyphenol content (TPC) in mg GAE/mL determined depending on the influence of extraction time, when 60% propanediol was used as extraction agent. *Conditions:* M, US, USM- S/L=1:5; MUS – S/L=1:20.

OBTAINING AND CHARACTERIZATION OF PROPANEDIOL PHYTOEXTRACTS  
FROM *ACMELLA OLERACEA*

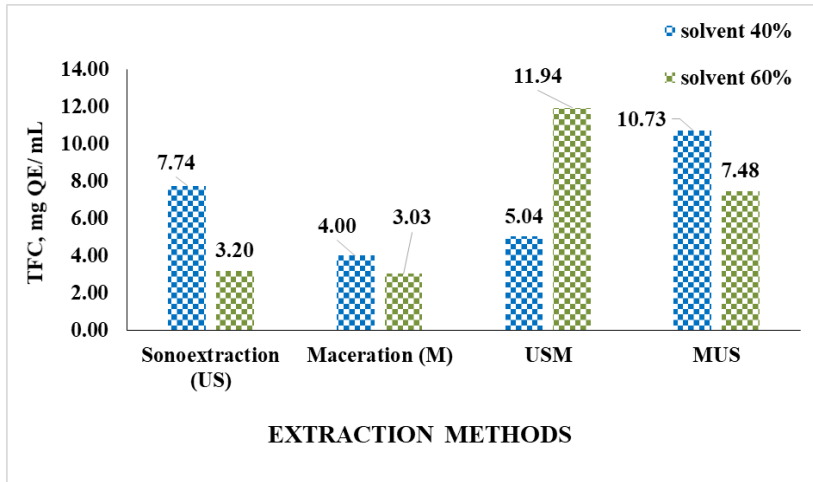


**Figure 6.** The total polyphenol content (TPC) in mg GAE/mL determined depending on the influence of extraction time, when 40% propanediol was used as extraction agent. *Conditions:* M, US, USM- S/L=1:5; MUS – S/L=1:20.

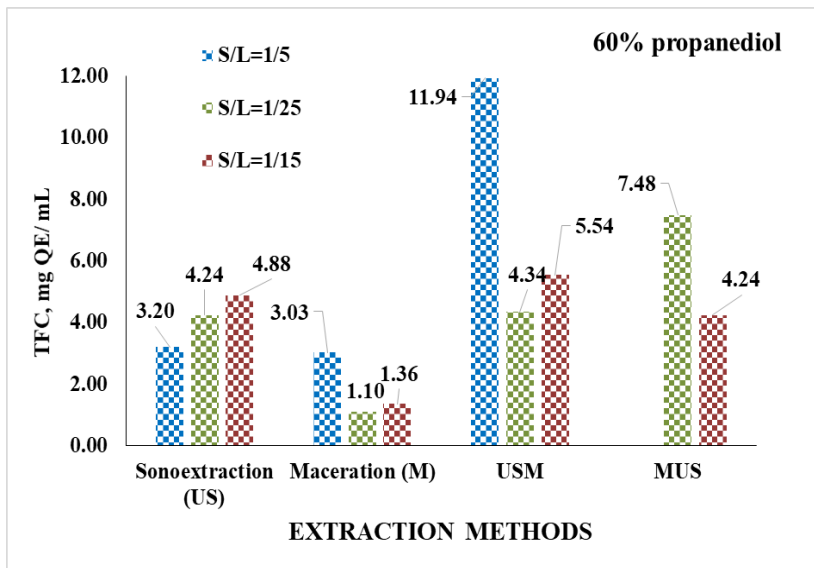
Analyzing the amount of polyphenols obtained according to the extraction time (Figures 5 and 6), the best values were obtained by maceration method (M) when working with an S/L ratio of 1:5, a time of extraction of 7 days and using as extraction solvent propanediol with 60% concentration.

The content of flavonoids (TFC) in all the plant extracts obtained was determined using the method involving treatment with a methanolic solution of 2%  $AlCl_3$ , following a protocol used in previous work [20]. The results obtained were expressed in mg quercetin equivalent (QE) per ml of extract and are shown in Figures 7-11.

The analysis of the amount of extracted flavonoids was similar to that of the polyphenols, as the factors influencing the extraction were the same. Thus, depending on the concentration of the extractant (Figure 37), the best results were obtained with the combined method: USM (11.91 mg QE/mL), under the working conditions: S/L=1:5, an extraction time of 5 min+7 days and 60% concentration of the extraction solvent propanediol, followed by the combined MUS method (10.73 mg QE/mL), performed under the working conditions: S/L=1:20, an extraction time of 30 days+10 min and an extraction solvent concentration of 40%.

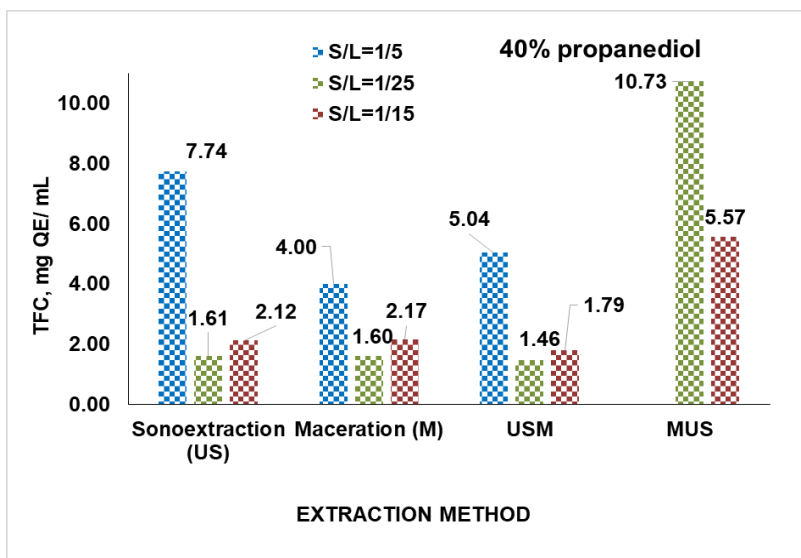


**Figure 7.** The flavonoids content (TFC) in mg QE/mL determined depending on the influence of solvent concentration. *Conditions:* S/L= 1:5; M-7 days, US- 5 min., USM – 5 min+7 days; MUS : S/L= 1:20, 30 days +10 min.

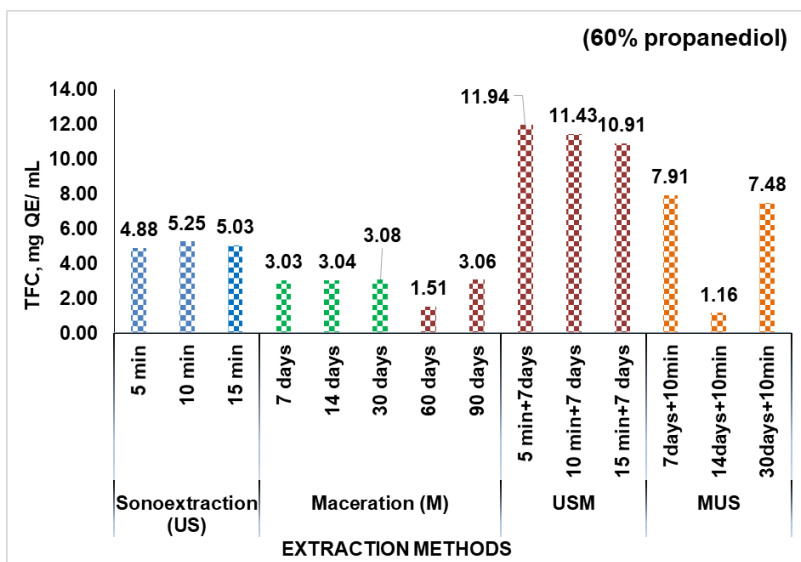


**Figure 8.** The flavonoids content (TFC) in mg QE/mL determined depending on the influence of ration solid (S)/liquid (L) when 60% propanediol was used as extraction agent. *Conditions:* M-7 days, US- 5 min., USM – 5 min.+7 days; MUS- 30 days +10 min.

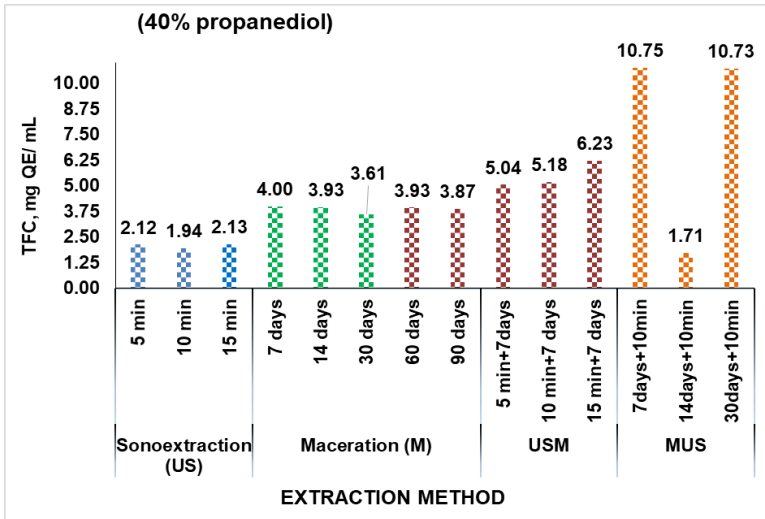
OBTAINING AND CHARACTERIZATION OF PROPANEDIOL PHYTOEXTRACTS FROM *ACMELLA OLERACEA*



**Figure 9.** The flavonoids content (TFC) in mg QE/mL determined depending on the influence of ration solid (S)/liquid (L) when 40% propanediol was used as extraction agent. *Conditions:* M-7 days, US- 5 min., USM – 5 min+7 days; MUS- 30 days +10 min.



**Figure 10.** The flavonoids content (TFC) in mg QE/mL determined depending on the influence of extraction time, when 60% propanediol was used as extraction agent. *Conditions:* M, US, USM- S/L=1:5; MUS – S/L=1:20.



**Figure 11.** The flavonoids content (TFC) in mg QE/mL determined depending on the influence of extraction time, when 40% propanediol was used as extraction agent. *Conditions:* M, US, USM- S/L=1:5; MUS – S/L=1:20.

When analyzing the results according to the S/L ratio (Figures 8 and 9), it can be seen that the best results were obtained with the combined MUS method (10.73 mg QE/mL) under the conditions S/L=1:20; propanediol at 40% concentration; an extraction time of 30 days+10 min. were obtained, followed by US (7.74 mg QE/mL) under the conditions S/L=1:5; propanediol at 40% concentration; an extraction time of 5 min. and the combined USM method (7.48 mg QE/mL) under the conditions: S/L=1:15 propanediol with 60% concentration and an extraction time of 5min.+7 days).

If the amount of extracted flavonoids is analyzed as a function of the extraction time, the best results for both concentrations of propanediol are obtained with the combined methods as follows: (■) 11.94 mg QE/mL or 11.43 mg QE/mL in the case of USM performed under the following conditions: S/L = 1:5; 60% propanediol concentration and an extraction time of 5 min+7 days and 10 min+7 days, respectively; (■) 10.75 mg QE/mL and 10.73 mg QE/mL, respectively, in the case of the MUS method performed under the following conditions: S/L = 1:20; 40% concentration of propanediol and an extraction time of 7 days + 10 min and 14 days + 10 min, respectively.

In conclusion:

- the best results in terms of polyphenol content were recorded in the case of the extracts obtained by maceration (3,386 mg GAE/mL) under working conditions of: S/L = 1:5, extraction time of 7 days and using 60% concentration propanediol as extraction solvent.

- the best results regarding the content of flavonoids were recorded in the case of the extracts resulting from the USM combined method (11.94 mg QE/mL) under conditions of S/L ratio of 1:5, an extraction time of 5 min. + 7 days and extraction solvent - popanediol with concentration 60%.

There are a number of studies in the specialized literature that stipulate that the use of organic solvents in the form of aqueous or alcoholic solutions to obtain plant extracts is much more beneficial than hydro alcoholic solutions [21-23]. One such organic solvent is propanediol, and recently attention is focused on the one of natural origin (propanediol 1,3).

Propanediol is increasingly used in cosmetic formulations as a texturing or humectant agent [24] or to stabilize and preserve the product [25]. Natural extracts in carrier solvents, such as glycerin or glycols, the most common being propylene glycol and 1,3 propanediol, are preferred to classic solvents, so that in the Coptis database, which includes over 15,000 cosmetic raw materials, one out of two extracts natural products sold on the market of cosmetic ingredients is diluted in glycerin or propanediol [26].

This type of extracts are much more combatable with the subsequent introduction in cosmetic formulations of the Oil in Water (O/W) or Water in Oil (W/O) type.

### Evaluation of antioxidant activity

The results obtained were reported as mean  $\pm$  standard deviation (SD) of three independent determinations in Table 1.

**Table 1.** DPPH and ABTS radicals scavenging activity of investigated extracts

Sample	DPPH (mg TE/mL)	ABTS (mg TE/mL)	TPC (mg GAE/ml)
<b>M</b> (S/L=1:5; propanediol 60%, extraction time of 7 days)	0.56 $\pm$ 0.03	2.18 $\pm$ 0.04	3.386
<b>US</b> (S/L=1:5; propanediol 60%, extraction time of 5 min.)	0.53 $\pm$ 0.02	2.22 $\pm$ 0.05	1.773
<b>USM</b> (S/L=1:5; propanediol 40%, extraction time of 15`+7days)	0.15 $\pm$ 0.04	2.05 $\pm$ 0.10	2.267
<b>MUS</b> (S/L=1:20; propanediol 60%, extraction time of 30 days+10 min.)	0.95 $\pm$ 0.01	2.41 $\pm$ 0.02	1.791

*Legend:* ABTS - 2,2'-azino-bis(3-ethylbenzothiazoline) 6-sulfonic acid; DPPH - 1,1-diphenyl-2-picrylhydrazyl; TE - Trolox equivalents.

The data presented in Table 1 made it possible to select the most suitable extract to proceed to the next phase of the formulation of a new dermatocosmetic product. Thus, the extract resulting from maceration (M in conditions: S/L=1:5; propanediol 60%, extraction time of 7 days) was chosen because it has the greatest amount of polyphenols (needed in the final product), although it is second in terms of antioxidant activity.

### **Preliminary analyses for emulsions based on *Acmella oleracea* extract**

Using the extract of *Acmella oleracea* obtained after extraction by maceration 7 days in following conditions: S/L=1:5, time of extraction = 7 days, solvent: 60% aqueous solution of propanediol, characterized by a total polyphenol content of 3.386 mg GAE/ml, we proceeded to obtain two types of emulsions using the same base. Their composition are presented in Table 4.




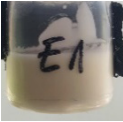
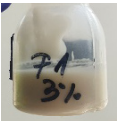
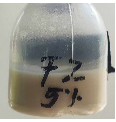



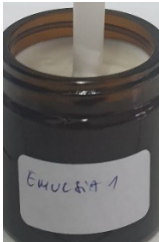

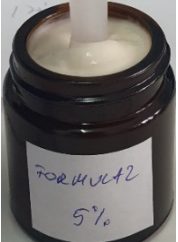
Before a product is placed on the market, it must undergo a series of analyzes according to quality standards to determine its stability and the best storage and conservation practices. With this in mind, a series of initial analyzes on the quality and stability of the manufactured preparations were taken into account. Based on the results obtained, the studies will continue with *in vitro* and *in vivo* evaluations.

An important aspect to consider when evaluating the quality of dermatocosmetic preparations is their stability in different environments and under different conditions. To evaluate the stability of the resulting dermatocosmetic emulsions, three physical evaluations were performed at two different time points: immediately after preparation at room temperature and 24 hours after formulation. Table 3 briefly summarises the results of the preliminary analyses that were performed, such as pH and conductivity measurements, sensory analysis, centrifugal and vibrational forces and microscopic image analysis.

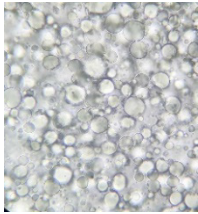
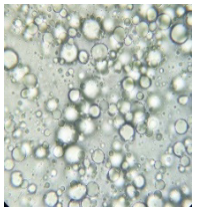
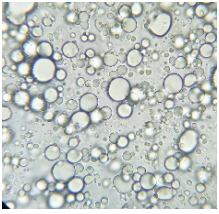



Table 3 presents the results of two stable products whose analysis will continue with investigations of structure morphology, rheological behavior, microbiological stability, diffusion through membranes, and *in vitro* and/or *in vivo* analyses.

OBTAINING AND CHARACTERIZATION OF PROPANEDIOL PHYTOEXTRACTS  
FROM *ACMELLA OLERACEA*

**Table 3.** Preliminary Characterization of Emulsions with *Acmella oleracea*

Parameters	Emulsions		
	Base emulsion	Formula 1 with 3% active	Formula 2 whis 5% active
Emulsion stability after the action of centrifugal force			
	The sample is stable, homogeneous, compact		The sample is stable, a thin layer of foam is observed due to the air incorporated when mixing the actives
Emulsion stability after the action of vibrational force			
	Homogeneous compact texture and appearance		
Measuring pH with a Hanna pH meter			
	Initial emulsion pH value: 6.01	The pH value 5.86 and 5.75 respectively, are compliant value and it does not require adjustment	
Organoleptic analysis			
	Compact, homogeneous texture. Characteristic, pleasant smell. Yellowish, glossy color, derived from the raw materials used		



Parameters	Emulsions		
	Base emulsion	Formula 1 with 3% active	Formula 2 whis 5% active
Microscopic images after 24 hours of emulsion preparation storage 25 °C			
Uniform particles of different sizes, without cremation, flocculation or sedimentation phenomena			
Conductivity measurement (mS) after 24 hours from emulsion preparation, storage at 25 °C			
		The conductivity value of 0.48 and 0.62 respectively, is a compliant value and it does not require adjustment	

## CONCLUSIONS

When the aqueous propanediol solution was used as an extractant, maceration (for a maximum content of polyphenols of 3.386 mg GAE/mL) and the combined sonoextraction-maceration method (for a maximum content of flavonoids of 11.94 mg QE/mL) proved to be the most effective methods for obtaining plant extracts from *Acmella oleracea*. Of the two concentrations of propanediol studied, the 60 % concentration proved to be the more efficient. The choice of working parameters leads to extracts rich in the desired biologically active compounds and with antioxidant activity. Due to the synergy of the compounds in the extracts, they can be used for the preparation of dermato-cosmetic emulsions to combat/treat oxidative stress

OBTAINING AND CHARACTERIZATION OF PROPANEDIOL PHYTOEXTRACTS  
FROM *ACMELLA OLERACEA*

on the skin. The stability of the two emulsions prepared with the propanediol extract of *Acmella oleracea* was preliminarily evaluated during preparation and during storage. The results were encouraging and suggest further in vivo and in vitro analysis to produce a market-ready topical preparation.

## EXPERIMENTAL SECTION

### Reagents

***Acmella oleracea*** (Regn Plantae, Order Asterales, Fam. Asteraceae, Gen. *Acmella*) plants come from a culture acclimatized in Romania by one of our team members, the culture located Popricani village, Iasi county, Romania (Figure 12). After harvesting the whole plant, its aerial parts were separated from the roots and dried in cool and shaded areas for six to seven weeks and then stored in brown glass containers to prevent moisture and UV light until needed.



**Figure 12.** Culture of *Acmella oleracea* from Popricani locality, Iasi county (Romania).

The **extraction solvent**, 1,3 propanediol, was obtained from the Elemental SRL company from Oradea (Romania). Obtained by fermentation of glucose, it is considered a natural and biodegradable solvent and is often studied as an alternative extraction solvent as a donor of hydrogen bonds in deep eutectic solvent, it is able to extract a large amount of polyphenols, compared to hydroethanolic extracts [26]. Due to the function of an ingredient in a cosmetic product, the incorporation of the solvent in the final formulation eliminates the subsequent processes of separating the solvent compounds [27].

## Extraction methods

The extraction methods used are: Maceration at room temperature (20 °C) - (M), ultrasound-assisted extraction (sonoextraction – US) and two combined methods: ultrasound-assisted extraction + maceration (USM) and maceration + ultrasound-assisted extraction (MUS) to obtain plant extracts from the *Acmella oleracea* plant with the highest content of active compounds. An aqueous solution of 40% and 60% propanediol was used as extracting agent. The variables whose effects on the extraction process were studied included the S/L ratio (1:5; 1:15 and 1:20), the concentration of the extractant (40% and 60%) and the extraction time (M= 60 min, 90 min and 120 min; US= 5 min, 10 min and 15 min; USM= 5 min+ 7 days, 10 min+ 7 days and 15 min+ 7 days; MUS= 7 days +10min; 14 days +10 min; and 30 days +10 min).

**The total polyphenol content** (TPC) was determined using the Folin-Ciocalteu method [19]. The results were presented as mg Gallic acid equivalent (GAE) per g (mg GAE/mL extract), taking into account the sample dilution. The analyses were performed twice. Using the same standard methods, the standard calibration curve ( $y=0.849x-0.01$ ) was constructed for different gallic acid concentrations.

**The amount of flavonoids** (TFC) was determined using a spectrophotometric technique with a 2%  $AlCl_3$  solution in methanol [20]. The results were expressed as mg quercetin equivalent (QE) per mL of extract (mg QE/mL). A spectrophotometric method was used in which the standard calibration curve ( $0.0005x-0.037$ ) was established for different quercetin concentrations.

For **antioxidant assays** were used two methods:

(a) *based on 2,2-diphenyl-1-picrylhydrazyl radical scavenging assay (DPPH)* conducted in accordance with a previously described method [17]. DPPH radical scavenging activity was calculated as milligrams of Trolox (TE) equivalents (mg TE/mL extract) based on spectrophotometric method ( $y = 0.0108x + 0.1167$ ,  $R^2 = 0.998$ ). Results were reported as the mean  $\pm$  standard deviation (SD) of three independent determinations;

(b) *based on 2,2'-azino-bis(3-ethylbenzothiazoline) 6-sulfonic acid radical scavenging assay (ABTS)* which followed a spectrophotometric methodology previously described in our research [28]. The ABTS radical scavenging activity was calculated as milligrams of Trolox equivalents (mg TE/mL extract) based on spectrophotometric method ( $y = 0.0082x + 0.0505$ ,  $R^2 = 0.9998$ ).

All the results were reported as the mean  $\pm$  standard deviation (SD) of three independent determinations.

### Formulation of emulsions based on *Acmella oleracea* extract

The extract with the highest polyphenol content was used to prepare two W/O emulsions that differed in the amount of extract used as an active ingredient with phytochemical properties to protect the skin from oxidative damage.

The base used to prepare the emulsions contains

- a lipophilic phase consisting of: *Amaranthus spinosus* seed oil, *Psoralea corylifolia* seed oil, *Malus domestica* seed oil and *Solanum lycopersicum* seed oil as emulsifier and the mixture: Cetearyl alcohol (and) glyceryl stearate (and) jojoba ester (and) *Helianthus annuus* (sunflower) seed wax (and) sodium stearoyl glutamate (and) water (and) polyglycerin-3 with the role of emulsifier;
- a hydrophilic phase consisting of: *Acmella oleracea* floral water as solvent and glycerol as conditioning agent;
- additives as viscosity agents: lecithin, sclerotium gum, pullulan, xanthan gum;
- preservatives such as: Benzyl alcohol, dehydroacetic acid.

The final W/O emulsions were prepared according to a method described in our previous work [29] and stored in cool rooms until analysis was completed, which can take up to ninety days. Samples were returned to room temperature before each analysis.

### REFERENCES

1. T. K. Lim; *Edible medicinal and non-medicinal plants* (Vol. 1), Springer: Dordrecht, The Netherlands, **2012**; pp. 285-292
2. T. G. G. Uthpala, S. B. Navaratne; *Food Rev. Int.*, **2021**, 37(4), 399-414.
3. J. Paulraj; R. Govindarajan; P. Palpu; *Advances in Pharmacological and Pharmaceutical Sciences*, **2013**, 2013 (1), Article ID 510298
4. N. K. Simas; E.D.C.L. Dellamora; J. Schripsema; C.L.S. Lage; A. M. de Oliveira Filho; L. Wessjohann; R. M. Kuster; *Phytochem. Lett.*, **2013**, 6(1), 67-72.
5. R. Sharma; N. Arumugam; *Future Foods*, **2021**, 3, 100022.
6. C. P. S. Martins; M. T. P. Melo; I. C. G. Honório; V. A. D'Ávila; W. G. O Carvalho Júnior; *Revista Brasileira de Plantas Mediciniais*, **2012**, 14, 410-413.
7. M. Rondanelli; F. Fossari; V. Vecchio; V. Braschi; A. Riva, P. Allegrini; G. Petrangolinid; G. Iannelloe; M. A. Falivac; G. Peronic; M. Nichettic; C. Gasparric; D. Spadaccinic; V. Infantinof; S. Mustafag; T. Alalwang; S. Perna; *Fitoterapia*, **2020**, 140, 104419.
8. E. Spinozzi; R. Pavela; G. Bonacucina; D. R. Perinelli; M. Cespi; R. Petrelli; L. Cappellacci; D. Fiorini; S. Scortichini, S. Garzoli, C. Angeloni, M. Freschi, S. Hrelia, L. Quassinti, M. Bramucci, G. Lupidi, S. Sut, S. Dall'Acqua, G. Benelli, A. Canale, E. Drenaggi, F. Maggi, *Ind. Crops Prod.*, **2021**, 172, 114027.

9. F. Barbira-Freedman; An Amazon Plant in Clinical Trial: Intersections of Knowledge and Practice. In *Collaborators Collaborating: Counterparts in Anthropological Knowledge and International Research Relations*, M.Konrad Ed.; Berghahn Books: Oxford, New York, **2012**, Chapter 2, pp. 40-58.
10. V. Prachayasittikul; S. Prachayasittikul; S. Ruchirawat; V. Prachayasittikul; *EXCLI* **2013**, *12*, 291.
11. A. F. Barbosa; M. G. D. Carvalho; R. E. Smith; A.U. Sabaa-Srur; *Revista Brasileira de Farmacognosia*, **2016**, *26*, 128-133.
12. E. Spinozzi; M. Ferrati; C. Baldassarri; L. Cappellacci; M. Marmugi; A. Caselli; G. Benelli; F. Maggi; R. Petrelli; *Plants*, **2022**, *11*(20), 2721.
13. L. Veryser; E. Wynendaele; L. Taevernier; F. Verbeke; T. Joshib; P. Tatke; B. De Spiegeleer; *Functional Foods in Health and Disease*, **2014**, *4*(6), 264-275.
14. F. Demarne; G. Passaro, U.S. Patent No. 7,531,193. Washington, DC: U.S. Patent and Trademark Office, **2009**.
15. B. De Spiegeleer; J. Boonen; L. Veryser; L. Taevernier; S. Malysheva; J.D. Di Mavungu; S. De Saeger; *In Stratum Corneum VII*, **2012**, *34*(4), 383-383.
16. R.K. Jansen; *Syst. Bot. Monogr.*, **1985**, *8*, 1–115.
17. P. B. Lalthanpuii; R. Lalawmpuii; K. Vanlaldinpuia; K. Lalchhandama, *Science Vision*, **2016**, *16*(4), 177-83.
18. R. Sulpice; P. C. McKeown; *Annual review of plant biology*, **2015**, *66*, 187-210.
19. L. Pavun; P. Đikanovic; M. Jelikic-Stankov; D. Đurdevic; S. Uskokovic-Markovic; *Czech J. Food Sci.*, **2018**, *36*, 233–238.
20. D. Turcov; A.S. Barna; A. Trifan; A.C. Blaga; A.M. Tanasa; D. Suteu; *Plants-Basel*, **2022**, *11*(19), Article Number 2454.
21. A. Apostolakis; S.Grigorakis; D.P. Makris; *Separation and Purification Technology*, **2014**, *128*, 89–95.
22. N.L. Huamán-Castilla; M.S. Mariotti-Celis; M. Martínez-Cifuentes; J.R. Pérez-Correa; *Biomolecules*, **2020**, *10*, 474.
23. J.R. Nastasi; V.D. Daygon; V. Kontogiorgos; M.A. Fitzgerald; *Metabolites*, **2023**, *13*, 566.
24. F. Chemat; M. Abert Vian; H. K. Ravi; B. Khadhraoui; S. Hilali; S. Perino; A. S. Fabiano Tixier; *Molecules*, **2019**, *24*(16), 3007.
25. A. Kerdudo; F. Fontaine-Vive; A. Dingas; C. Faure; X. Fernandez; *Int. J Cosmetic Sci.*, **2015**, *37*(1), 31-40.
26. V. Vieira; R. C. Calhelha; L. Barros; J. A. Coutinho; I.Cfr Ferreira; O. Ferreira; *Molecules*, **2020**, *25*(11), 2497.
27. M. Ruesgas-Ramón; M. C. Figueroa-Espinoza; E. Durand; *J. Agric. Food Chem.*, **2017**, *65*(18), 3591-3601.
28. S.V. Luca; L. Kulinowski; C. Ciobanu; G. Zengin; M.E. Czerwinska; S. Granica; J. Xiao; K. Skalicka-Woźniak; A. Trifan; *Ind. Crops Prod.*, **2022**, *178*, 114623.
29. C. Maxim; D. Turcov; A. Trifan; D. Suteu; A. S. Barna; *SCS-CICBIA*, **2024**, *25* (2), 1679-172.

## MICROENCAPSULATION OF *SALVIA OFFICINALIS* L. ESSENTIAL OIL BY COMPLEX COACERVATION TECHNOLOGY

István SZÉKELY-SZENTMIKLÓSI<sup>a</sup> , Emőke Margit RÉDAI<sup>b</sup>,  
Robert-Alexandru VLAD<sup>b</sup>, Zoltán SZABÓ<sup>a</sup> , Béla KOVÁCS<sup>c</sup> ,  
Attila-Levente GERGELY<sup>d</sup> , Csilla ALBERT<sup>e</sup> ,  
Blanka SZÉKELY-SZENTMIKLÓSI<sup>f\*</sup>, Emese SIPOS<sup>a</sup>

**ABSTRACT.** The essential oil of *Salvia officinalis* L. (sage) exhibits versatile biological properties. The high sensitivity of sage essential oil (SEO) to environmental conditions and limited processability represent important hurdles in its use, which, however, can be overcome by microencapsulation. The objective of the current study was to encapsulate sage essential oil into core-shell type microcapsules by complex coacervation technology and to transform it into solid form by freeze-drying. Arabic gum (GA) and three different type A gelatin (G)

<sup>a</sup> George Emil Palade University of Medicine, Pharmacy, Science, and Technology of Targu Mures, Faculty of Pharmacy, Department of Pharmaceutical Industry and Management, 38 Gheorghe Marinescu str., RO-540142, Targu Mures, Romania

<sup>b</sup> George Emil Palade University of Medicine, Pharmacy, Science, and Technology of Targu Mures, Faculty of Pharmacy, Department of Specialty Pharmaceutical Sciences, Pharmaceutical Technology, 38 Gheorghe Marinescu str., RO-540142, Targu Mures, Romania

<sup>c</sup> George Emil Palade University of Medicine, Pharmacy, Science, and Technology of Targu Mures, Faculty of Pharmacy, Department of Fundamental Pharmaceutical Sciences, Pharmaceutical Biochemistry and the Chemistry of Environmental Factors, 38 Gheorghe Marinescu str., RO-540142, Targu Mures, Romania

<sup>d</sup> Faculty of Economics, Socio-Human Sciences and Engineering, Sapientia Hungarian University of Transylvania, Department of Mechanical Engineering, 1 Piața Libertății str. 530104 Miercurea Ciuc, Romania

<sup>e</sup> Faculty of Economics, Socio-Human Sciences and Engineering, Sapientia Hungarian University of Transylvania, Department of Food Science, 1 Piața Libertății, RO-530104 Miercurea Ciuc, Romania

<sup>f</sup> George Emil Palade University of Medicine, Pharmacy, Science, and Technology of Targu Mures, Faculty of Pharmacy, Department of Specialty Pharmaceutical Sciences, Pharmaceutical Chemistry, 38 Gheorghe Marinescu str., RO-540142, Targu Mures, Romania

\* Corresponding author: [blanka.szekely-szentmiklosi@umfst.ro](mailto:blanka.szekely-szentmiklosi@umfst.ro)



grades were used to investigate the effect of the gel strength on microcapsule characteristics. The formation of essential oil containing microcapsules during complex coacervation was assessed by optical microscopy while SEM imaging was used to determine the morphology of the freeze-dried forms. Characterization of microcapsules was completed with FT-IR spectroscopy. Encapsulation efficiency was determined by UV-VIS spectrophotometry and the composition of essential oil by GC-MS technique. Results revealed that by the application of selected microencapsulation technology and freeze-drying method high encapsulation efficiency values could be achieved, the gel strength of gelatin has a decisive role in microcapsule particle size and the composition of essential oil is well preserved following the technological process.

**Keywords:** *microencapsulation, complex coacervation, essential oil, Salvia officinalis L.*

## INTRODUCTION

Sage (*Salvia officinalis* L., Figure 1) is a perennial evergreen subshrub, part of the Lamiaceae family. It is a well-known medicinal plant worldwide, which has been used since ancient times in traditional medicine. According to the European Union herbal monograph on *Salvia officinalis* L. - folium the well-established use could be considered as scientifically proven in mild dyspeptic complaints such as heartburn and bloating, relief of excessive sweating, inflammation in the mouth or the throat and minor skin inflammations [1,2]. But as the Latin name of the plant suggests (salvare = to save) and taking into account the extensive empirical experience, its healing effects might go beyond what has been proven so far which is still awaiting scientific confirmation.


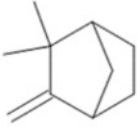
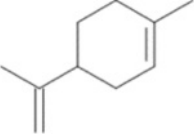
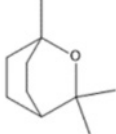
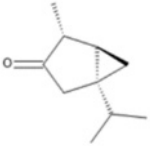
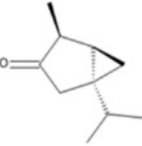
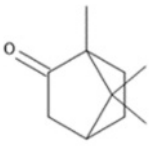
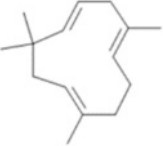
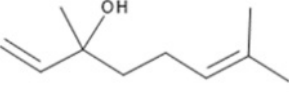
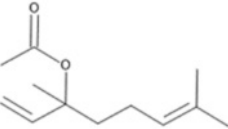
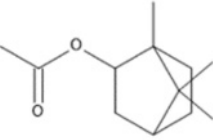


**Figure 1.** Different development stages of sage (*Salvia officinalis* L.)

MICROENCAPSULATION OF *SALVIA OFFICINALIS* L. ESSENTIAL OIL  
BY COMPLEX COACERVATION TECHNOLOGY

The major constituents of the essential oil are the terpenoids which are volatile and thermolabile in nature, prone to oxidation or hydrolysis depending on the structure. Thus, processing and storage conditions of plant material in the course of the extraction process and handling of obtained essential oil could greatly influence their chemical composition. On the other hand, the aging process of essential oils might be accompanied by the appearance of unpleasant flavors, a change of color or consistency, and even resinification. On the basis of these modifications could be oxidative damage, chemical transformations, or polymerization reactions [3].

The ISO standard 9909:1997 establishes the following acceptance criteria according to the chromatographic profile for compounds as presented in Figure 2 [4].

 <b><math>\alpha</math>-Pinene</b> Limit: 1 – 6.5 %	 <b>Camphene</b> Limit: 1.5 – 7 %	 <b>Limonene</b> Limit: 0.5 – 3 %	 <b>1,8 Cineole (Eucalyptol)</b> Limit: 5.5 – 13 %
 <b><math>\alpha</math>-Thujone</b> Limit: 18 – 43 %	 <b><math>\beta</math>-Thujone</b> Limit: 3 – 8.5 %	 <b>Camphor</b> Limit: 4.5 – 24.5 %	 <b><math>\alpha</math>-Humulene</b> Limit: max. 12 %
 <b>Linalool</b> Limit: max. 1 %	+	 <b>Linalyl acetate</b>	 <b>Bornyl acetate:</b> Limit: max. 2.5 %

**Figure 2.** Controlled components of *Salvia officinalis* L. essential oil and their acceptance criteria according to ISO standard 9909:1997



Apart from compounds listed in the ISO standard, the composition of Sage essential oil is more complex and depending on cultivar, soil type, pedoclimatic conditions, and harvesting period as well as post-harvest management might have a specific fingerprint [5].

Given the sensibility of several components of essential oil to the effect of environmental conditions [3] proper formulation and conditioning is required to prevent degradation and assure long-term preservation of the particular composition [6]. In many cases, the transformation of essential oil from a liquid state into free-flowing and easily manageable dry powders might be of fundamental importance to fit a specific application [7].

Microencapsulation is one of the most widely used techniques for these purposes. Although numerous microencapsulation techniques have been developed since then, due to its simplicity and cost-effectiveness, complex coacervation remained one of the most widely applied methods in the food and pharmaceutical industry [8].

The production process of core-shell type microcapsules by complex coacervation is composed of the following basic steps: dissolution of polymers, emulsification of essential oil, coacervation, gelation, hardening, rinsing, separation of microcapsules, and drying. The phenomenon takes place in a narrow pH range, between the pKa of anionic polysaccharide and the isoelectric point of the protein [9]. Due to its advantageous properties such as biodegradability, low immunogenicity, easy availability, and low cost, gelatin (G) remained one of the most widely applied shell components for microencapsulation. Besides its widespread utilization in the food sector, it is present also in the pharmaceutical industry not only in the composition of solid, semi-solid, and liquid dosage forms but also in the development of nano- and microscale carrier systems as well as in tissue engineering and regenerative medicine [10].

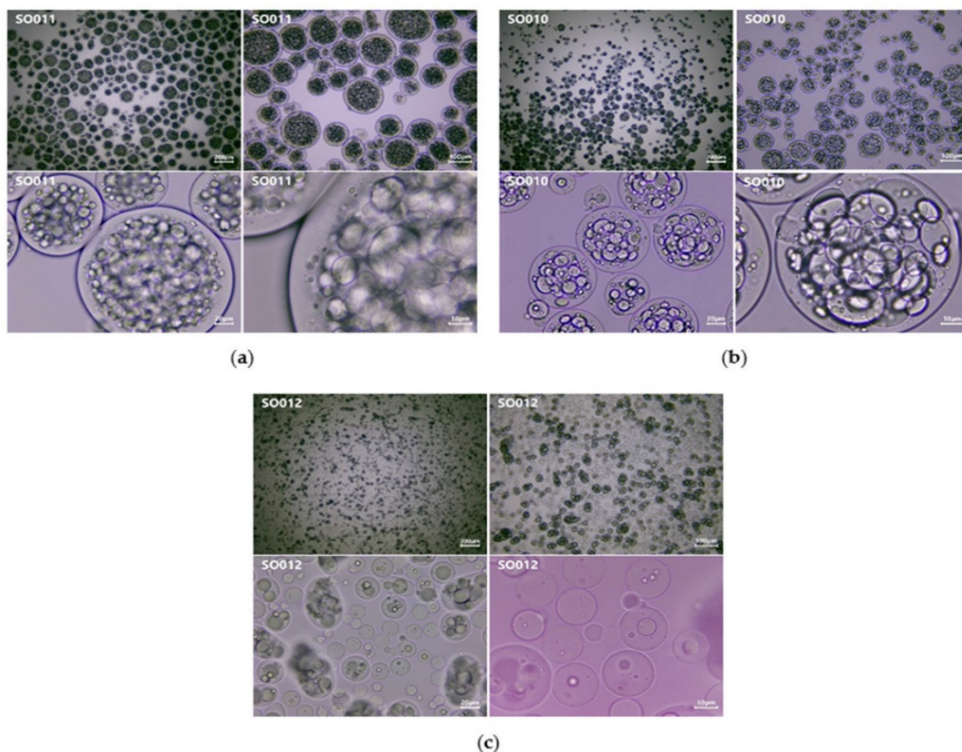
The current study intends to investigate the possibility of applying complex coacervation technology to encapsulate SEO by assessing the effect of three different gelatin grades and obtaining solid form material by freeze-drying for possible further processing and to evaluate the effect of microencapsulation on the composition of the essential oil.

## **RESULTS AND DISCUSSION**

### **Microscopic investigation of complex coacervate formation**

According to the optical microscopic investigation, microcapsules were successfully obtained in the case of each gelatin grade applied. The impact of gel strength on the particle size of microcapsules could be observed.

MICROENCAPSULATION OF *SALVIA OFFICINALIS* L. ESSENTIAL OIL  
BY COMPLEX COACERVATION TECHNOLOGY



**Figure 3.** Optical microscopic images of formed microcapsules at 40X, 100X, 400X, and 1000X magnifications: (a) experiment no. SO011 manufactured with GE  $\approx$ 300 Bloom; (b) experiment no. SO010 manufactured with GE  $\approx$ 175 Bloom; (c) experiment no. SO012 manufactured with GE 80-120 Bloom;

According to the optical microscopic images (Figure 3), spherical microcapsules were formed at each experiment. The largest particles resulted in the case of experiment no. SO011 when gelatin grade with the highest gel strength ( $\approx$  300 Bloom) was used. Contrarily, the smallest particles were formed in the case of microcapsules manufactured with gelatin grade having the lowest gel strength value of 80 – 120 Bloom (exp. no. SO012). Our results are in good alignment with conclusions drawn by Peters et al. during their study on the microencapsulation of theobromine that the diameter of microcapsules increased with increasing Bloom grade for type A gelatins [11]. Liu et al. tested five different grades of type B gelatins (140 Bloom, 180 Bloom, 200 Bloom, 220 Bloom, and 240 Bloom) in the complex coacervation of cinnamaldehyde with sodium carboxymethylcellulose. The authors found that the application of gelatin with 200 Bloom value resulted in microcapsules with the most uniform particle sizes [12].

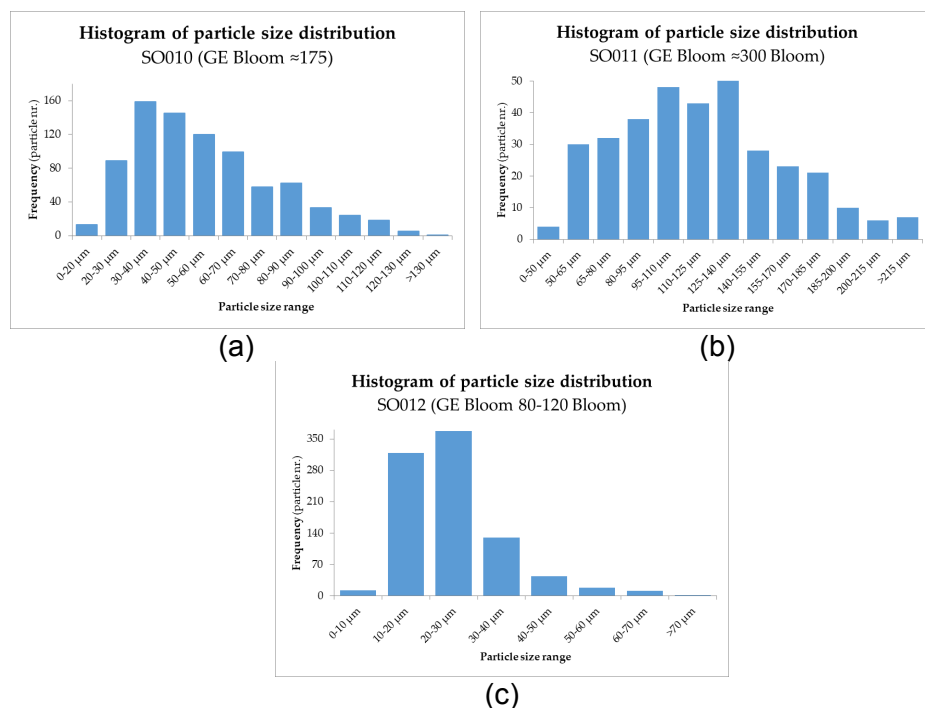
Particle size measurements performed by optical microscopy for the three experimental runs are presented in Table 1, as follows:

**Table 1.** Particle size characteristics of microcapsules containing SEO manufactured with different gelatin grades

Exp. no.	Particle size ( $\mu\text{m}$ )			SD	RSD %	Median ( $\mu\text{m}$ )	Polydispersity index
	Average	Min.	Max.				
SO010	<sup>1</sup> 55	16.2	135.3	23.85	43.31	52.60	0.19
SO011	<sup>2</sup> 119	43.0	227.7	40.85	34.29	116.95	0.12
SO012	<sup>3</sup> 25	8.2	93.3	10.58	42.80	23.90	0.18

<sup>1</sup> n = 826; <sup>2</sup> n = 340; <sup>3</sup> n = 903

The histograms of particle size distribution according to the microscopic measurements are presented in Figure 4.



**Figure 4.** Histogram of particle size distribution of SEO microcapsules (a) exp. no. SO010 with  $G \approx 175$  Bloom; (b) exp. no. SO011 with  $G \approx 300$  Bloom; (c) exp. no. SO012 with  $G = 80-120$  Bloom.

The histograms for experiment no. SO010 and SO011 manufactured with medium and high gel strength G grades exhibit a bimodal distribution tendency with peaks in the particle size ranges of 30-40  $\mu\text{m}$ , 80-90  $\mu\text{m}$  and 95-110  $\mu\text{m}$ , 125-140  $\mu\text{m}$  respectively. In the case of experimental run SO013 incorporating G 80-120 Bloom the vast majority of microcapsules are concentrated between 10-40  $\mu\text{m}$ .

In the case of the application of GA and G in a 1:1 ratio with gelatin type A with 175 Bloom gel strength, Rousi et al.[13] also reported a bimodal distribution and particle sizes somewhat lower in comparison to values obtained in the case of our experiment (SO010) incorporating G with the same Bloom value. Yang et al. [14] reported particle size values ranging from 5 to 12  $\mu\text{m}$  when gelatin with 100 Bloom was used. Literature data suggest that besides gel strength another decisive factor in microcapsule particle size in the case of G-GA systems is the ratio between the two polymers.

On the microscopic images captured at smaller magnifications (40X, 100X) the high polydispersity grade could be observed which is a characteristic of complex coacervation technique. At higher magnifications (400X, 1000X) the polynucleated nature of the microcapsule core is clearly visible in the case of experimental runs containing gelatin grades with intermediate (exp. no. SO010) respective high (exp. no. SO011) gel strength values. In this respect, presumably due to the relation of emulsion droplet size and microcapsule dimensions, in the case of experiment no. SO012 resulting smallest particle sizes, mono- and oligonucleated microcapsules were also present in a large amount.

### Assessment of freeze-dried microcapsules

- **Macroscopic aspect of freeze-dried form**

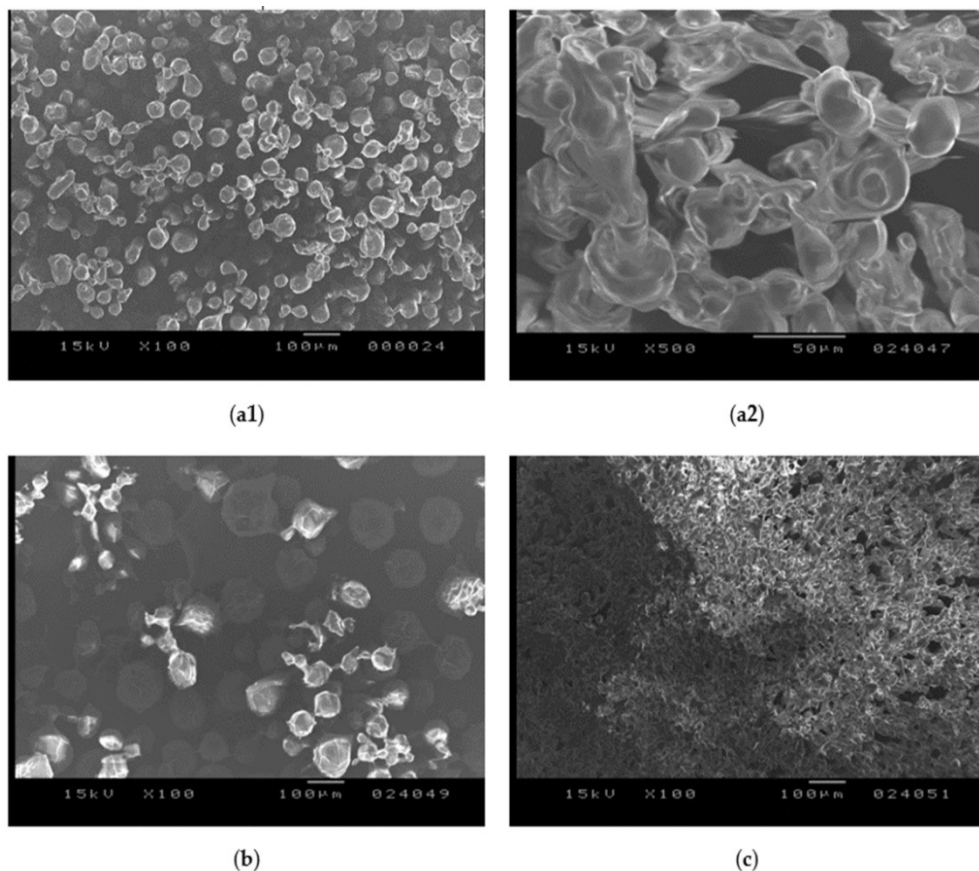
The effect of using different gelatin type A grades was reflected in the appearance of the lyophilized forms. Samples obtained by the application of gelatin with intermediate and high Bloom values (exp. no. SO010 and exp. no SO011) resulted in a lyophilized material with a looser structure and granular aspect. In case of exp. no. SO012 incorporating gelatin with low gel strength a more compact freeze-dried material was formed. (Figure 5)



**Figure 5.** Macroscopic aspect of the lyophilized samples obtained with different gelatin grades (exp. no. SO010 – G  $\approx$ 175 Bloom; exp. no. SO011 – G  $\approx$ 300 Bloom; exp. no. SO012 – G 80-120 Bloom).

• **Investigation of morphology by SEM**

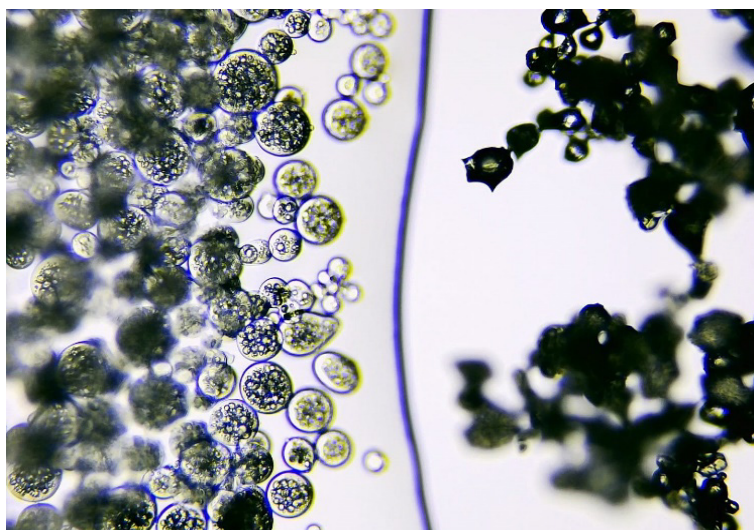
SEM images were recorded for the freeze-dried form of the three experimental runs. The particle size differences observed by optical microscopy in correlation with gelatin grades are well reflected on the SEM images as presented in Figure 6.



**Figure 6.** SEM images of freeze-dried microcapsules prepared with different gelatin grades: (a1) experiment no. SO010 manufactured with G  $\approx$ 175 Bloom at 100X magnification and (a2) 500X magnification; (b) experiment no. SO011 manufactured with G  $\approx$ 300 Bloom; (c) experiment no. SO012 manufactured G 80 - 120 Bloom.

The SEM images confirmed that the lower the gel strength of the G grade used, the smaller the resulting freeze-dried microcapsules are. A net-like structure is observed, which becomes denser as the particle size decreases. In experiment no. SO011, where gelatin with 300 Bloom gel strength was used, the individual spherical particles can be well distinguished with a specific wrinkled surface and only a few interconnections (Figure 6 - b). The application of gelatin with intermediate gel strength (175 Bloom – experiment no. SO010) resulted in the formation of a more interconnected structure, though the embedded spherical microcapsules remain easily distinguishable (Figure 6 – a1, a2). In experiment no. SO012 prepared with gelatin having the lowest gel strength, presumably due to the small size of formed microcapsules and associated high specific surface area, which facilitates the formation of interconnections, a denser, sponge-like structure was formed. In this case, individual microcapsules are hard to distinguish in the matrix that permeates the entire structure. Similar structures with interconnected particles following microencapsulation and subsequent freeze-drying were described by other authors [15–19].

The rehydration of lyophilized microcapsules could be easily performed. Upon the addition of water, the microcapsules regained almost instantly their original appearance (Figure 7). Our observation is in good alignment with that reported by Comunian et al. who described a similar phenomenon [20].



**Figure 7.** Lyophilized - (right) and rehydrated (left) microcapsules with water droplet propagation line in the middle captured by optical microscope for experiment no. SO010.

### **GC-MS investigation of essential oil composition**

Table 2 contains the GC-MS results obtained for free essential oil as well as the SEO composition obtained from the microcapsules.

**Table 2.** GC-MS results of free- and microencapsulated SEO. (exp. no. SO010 - with G Bloom approx. 175, exp. no. SO011 – with G Bloom approx. 300, exp. no. SO012 – with G 80-120 Bloom)

Nr.	Compound*	SEO	SO010	SO011	SO012
		peak, %			
1	alpha pinene**	2.31	3.62	2.74	3.15
2	3-hexanol	-	1.00	-	-
3	camphene**	3.40	4.37	3.12	3.58
4	beta-pinene	1.63	1.84	1.25	1.41
5	beta myrcene	0.56	-	-	-
6	p-cymene	0.93	0.48	-	-
7	limonene**	1.64	1.29	0.83	0.89
8	1,8 cineole**	10.34	5.48	3.05	2.39
9	gamma terpinene	1.17	0.99	0.77	0.87
10	terpinolene	0.60	0.45	-	-
11	linalool**	-	-	1.19	0.83
12	alpha-thujone**	23.76	19.30	24.29	22.66
13	beta-thujone**	5.45	3.88	6.79	6.59
14	camphor**	19.78	12.90	12.21	11.82
15	endo borneol	4.99	3.26	4.86	4.87
16	terpinen-4-ol	0.72	0.43	-	-
17	linalyl acetate**	-	-	0.99	-
18	bornyl acetate	2.53	2.19	4.65	5.09
19	caryophyllene	8.65	9.11	14.82	15.86
20	isocaryophyllene	-	0.71	-	-
21	humulene**	9.18	11.92	17.04	17.96
22	caryophyllene oxide	0.25	-	-	-
23	viridiflorol	0.78	1.58	1.4	2.02
<b>Total identified</b>		<b>98.67</b>	<b>84.80</b>	<b>100.00</b>	<b>99.99</b>

\*In the order of retention times, \*\* Components controlled by the ISO standard.

Commercial SEO purchased from the Romanian market fulfilled the requirements of ISO standards for the quantitative composition. 19 compounds were identified in the free essential oil. The order of the five major components was: alpha thujone > camphor > 1,8-cineole > humulene > caryophyllene. Similar results for *Salvia officinalis* L. essential oil composition were reported by Baj et al. [21].

A general conclusion is that the composition of SEO was well preserved following microencapsulation in the case of each experimental run, although the amount of 1,8 cineole and camphor encountered a significant decrease, while the relative ratio of some components with lower volatility (higher molecular mass and lower boiling point), as it is the case of caryophyllene and humulene, increased. Caryophyllene oxide and beta-myrcene, present already in the lowest amounts in the composition of the free SEO could not be detected in either of the microcapsules. However, other two highly volatile compounds (p-cymene and terpinolene: an aromatic monoterpene and an alkene monoterpene) were retained in the composition of SO010. The appearance of 3-hexanol (SO010), linalool (SO011 and SO012), linalyl acetate (SO011), and isocaryophyllene (SO010) might be explained by their relative increase in the composition due to the loss of high volatile components during the technological process. It should be emphasized that in the case of experiment no. SO010 the same five major components were present in the composition of the encapsulated essential oil in the order of alpha thujone > camphor > humulene > caryophyllene > 1,8-cineole. In the case of experiments SO011 and SO012, the order of the five major components was: alpha thujone > humulene > caryophyllene > camphor > beta thujone.

### **Determination of encapsulation efficiency and loading capacity by UV spectroscopy**

To determine the encapsulation efficiency, UV-visible spectroscopic measurements were undertaken at the absorption maximum of sage essential oil in ethanol, at wavelength 241 nm, and concentrations were determined by interpolation of the absorption of sage essential oil from microcapsules to a previously constructed calibration curve in ethanol. The blank microcapsules (PL) showed no absorption in this region, indicating that the presence of oil can be detected in the microcapsule solutions.

The calibration diagram was constructed using the concentrations and measured absorbances of six different alcoholic solutions of SEO, ranging from 25-65 µg/ml. The resulting equation,  $y = 0.0522 X - 0.0079$  with  $R^2 = 0.991$ , demonstrates a high linear correlation between SEO concentrations and absorbances at 241 nm.



The encapsulation efficiency (EE) and loading capacity (LC) are presented in Table 3 and should be taken into consideration to determine the efficiency of the microencapsulation process. A similar spectrophotometric method with the application of ethanol was applied by Gonçalves et al [22].

**Table 3.** Encapsulation efficiency and loading capacity for SEO microcapsules.

Sage essential oil in microcapsules SO010	SEO concentration (µg/ml) <sup>1</sup>	Concentration of microcapsule solution (µg/ml)	Theoretical (initial) oil content (µg/ml)	EE %	LC%
Total oil content	39.36	100	40.29	86.00	34.65
Surface oil content	4.71	100	40.29		

<sup>1</sup> Calculated based on the straight-line equation and the measured absorbance values.

Encapsulation efficiency refers to the proportion of core material successfully trapped within the microcapsules, serving as an important index for assessing the efficiency of microencapsulation [23,24].

Loading capacity, on the other hand, measures the amount of encapsulated core material relative to the total mass of the microcapsule.

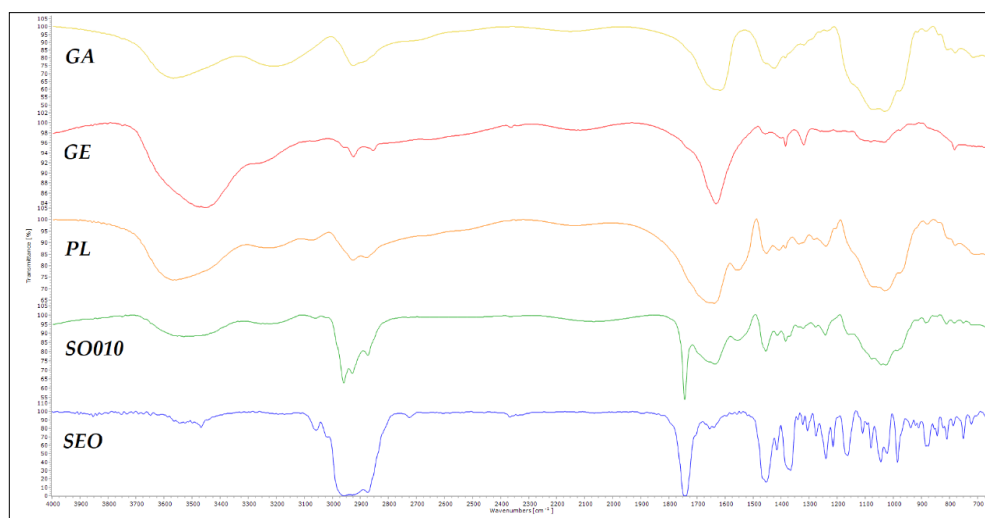
Due to the limited literature available on the microencapsulation of sage essential oil, the results were compared with the encapsulation of other substances and essential oils in a G-GA system, using similar parameters. For example, Xiao-Ying Qv et al. achieved an EE of 85-86 % when encapsulating lutein [25], while Glaucia A. Rocha-Selmi et al. reported EE values above 90% for lycopene microcapsules [26]. Ferreira S. and Nicoletti V.R. found EE values ranging from 89.7 to 98.7% for a ginger oil formulation prepared with the method of complex coacervation [27]. In a full factorial experimental design, Rungwasantisuk and Raibhu obtained EE values in the range of 67 - 85 % for complex coacervate of lavender oil using type A gelatin with 170-175 Bloom, gum arabic and glutaraldehyde as crosslinker, with freeze-drying [28]. Burhan et al. achieved a maximum EE of 77.9% for lavender oil microcapsules prepared with GA and maltodextrin, using spray drying. They applied also a UV-VIS spectrophotometric method for determination, the essential oil being extracted with 5 w/v% sodium lauryl sulfate solution [29]. Zhang et al. emphasized that the type and composition of wall materials, along with the drying process significantly influence EE values, which are typically high when gelatin is used alongside GA and sodium caseinate in complex coacervation [23]. Xiao et al. suggested that some essential oil loss might occur due to volatilization during emulsification and coacervation at around 50°C [30]. However, according to Napiórkowska et al., the type of oil has only a minor impact on EE [31].

The EE value obtained in our experiment is relatively high and aligns well with those reported in the literature for complex coacervation.

As for loading capacities, various ranges have been reported in the literature, attributed to differences in core materials, macromolecule types, and wall material ratios. Calderón-Oliver et al. reported the loading capacity of nisin and avocado peel extract ranging from 3.05 to 13.59 % and 4.58 to 20.54%, respectively [32], while the LC of coacervated black raspberry anthocyanin microcapsules prepared by Shaddel et al. ranged from 29.67 to 38 % [33].

### FT-IR spectroscopy

Figure 8 shows the FT-IR spectrum of the microcapsule from experiment SO010, compared with the spectra of the shell (PL) and core (SEO), as well as the spectra of the shell material components, namely 175-Bloom gelatin (GE) and gum arabic (GA).



**Figure 8.** The FT-IR spectra of gum arabic (GA), gelatin (GE), oil-free microcapsule (PL), microcapsules (SO010), and essential oil (SEO)

The FT-IR spectrum of gelatin polypeptide displays a broad peak at  $3453\text{ cm}^{-1}$ , and a smaller peak at  $3225\text{ cm}^{-1}$ , reflecting N-H stretching of amide bonds and  $-\text{NH}_2$  groups, as well as O-H stretching vibrations from hydroxyl groups in amino acid side chains [14,19]. The peak at  $2924\text{ cm}^{-1}$  is

due to the stretching vibrations of C-H bonds, while the peak at  $1385\text{ cm}^{-1}$  is associated with the bending vibrations of C-H bonds in the aliphatic chains of amino acid residues. A prominent peak at  $1632\text{ cm}^{-1}$  arises from C=O stretching vibrations in amide bonds in the polypeptide backbone, while the peak at  $1032\text{ cm}^{-1}$  indicates C-N stretching vibrations of amine groups or C-O stretching of hydroxyl groups [13,34].

Gum arabic is a complex mixture of polysaccharides and glycoproteins [35]. Its FT-IR spectrum (Figure 8) shows a strong absorption band at  $3567\text{ cm}^{-1}$ , due to the -OH stretching vibrations of free or hydrogen-bonded hydroxyl groups in polysaccharides, and a peak at  $3212\text{ cm}^{-1}$  linked to N-H stretching from glycoproteins [13]. The weaker peak at  $2925\text{ cm}^{-1}$  suggests C-H stretching vibrations in alkyl groups indicating hydrocarbon chains within the polysaccharides. Peaks at  $1617\text{ cm}^{-1}$  and  $1425\text{ cm}^{-1}$  correspond to carboxylate groups' (-COO-) asymmetrical and symmetrical stretching vibrations [31] mainly from glucuronic acid units, while the strong absorption band at  $1031\text{ cm}^{-1}$  indicates asymmetric stretching vibration of -C-O-C and -C-O in glycosidic linkages and hydroxyl groups in polysaccharides [34,36].

The FT-IR spectrum of SEO contains various peaks corresponding to the different functional groups present in its chemical constituents. It has a broad peak likely resulting from the overlap of three distinct peaks at  $2958\text{ cm}^{-1}$ ,  $2935\text{ cm}^{-1}$ , and  $2871\text{ cm}^{-1}$ , corresponding to C-H stretching vibrations of methyl (-CH<sub>3</sub>) and methylene (-CH<sub>2</sub>-) groups. The peak at  $1742\text{ cm}^{-1}$  is indicative of a C=O stretching vibration of carbonyl groups, which could be due to the presence of ketones like thujone and camphor. The peaks at  $1454\text{ cm}^{-1}$  and  $1367\text{ cm}^{-1}$  can be attributed to C-H bending (scissoring) vibrations in -CH<sub>2</sub>- groups, and C-H bending (deformation) vibrations of methyl groups (-CH<sub>3</sub>), respectively, characteristic to isoprenoid compounds. The peaks corresponding to single-bonded oxygen-containing components are also present in the spectrum. For example, the peak at  $1240\text{ cm}^{-1}$  due to C-O stretching vibrations indicates the presence of alcohols (e.g. linalool, borneol), esters (bornyl acetate), or ethers (1,8 cineole, caryophyllene oxide). Similarly, the peak at  $1166\text{ cm}^{-1}$ , which corresponds to C-O-C stretching vibrations suggests the presence of ethers and esters. The peak at  $1041\text{ cm}^{-1}$  related to C-O stretching vibrations is also characteristic of alcohols and ethers [37]. The peak at  $980\text{ cm}^{-1}$  could be associated with =C-H bending vibrations of alkene groups or out-of-plane bending vibrations of aromatic C-H. This indicates the presence of unsaturated terpenes (e.g. pinene, humulene, limonene) and aromatic compounds (p-cymene) in sage essential oil [36].

During complex coacervation, at pH below its isoelectric point (pH≈4) the positively charged amino groups of G will react with oppositely charged carboxylic groups of GA polysaccharides by electrostatic interaction forming

polyionic complexes [38]. The FT-IR spectrum of the blank coacervates (PL) shows characteristic peaks of both G and GA at  $3570\text{ cm}^{-1}$ ,  $2225\text{ cm}^{-1}$ ,  $2926\text{ cm}^{-1}$ , and  $1638\text{ cm}^{-1}$ . New peaks at  $1240\text{ cm}^{-1}$  and  $1029\text{ cm}^{-1}$  suggest N-H groups forming hydrogen bonds and participating in electrostatic interactions when protonated ( $\text{NH}_3^+$ ), as well as C-O stretching in GA, indicating the involvement of carboxylate groups ( $\text{COO}^-$ ) in electrostatic interactions [13,34].

To investigate the interactions between the wall and the core materials, the FT-IR spectra of the SEO-containing microcapsules were compared with the spectrum of essential oil (Figure 8 SEO) and the spectrum of the blank microcapsules (Figure 8 PL). In the oil-containing microcapsules, the characteristic peaks of PL are present at wavenumbers  $3570\text{ cm}^{-1}$  and  $1638\text{ cm}^{-1}$ , and the peak of SEO at  $2958\text{ cm}^{-1}$ . Some peaks of PL overlap with those of SEO in the wavenumber regions of  $2926\text{ cm}^{-1}$ - $2871\text{ cm}^{-1}$ , at  $1240\text{ cm}^{-1}$ , and between  $1030\text{ cm}^{-1}$  and  $1040\text{ cm}^{-1}$ .

The unchanged essential oil peaks within the microcapsule matrix, along with the absence of new peaks, indicate that the SEO was successfully encapsulated without significant interaction with the wall materials, confirming that the encapsulation involved physical rather than chemical interactions [23,29,30].

## CONCLUSIONS

Microencapsulation of SEO was successfully performed by the application of each G grade investigated using complex coacervation with GA along with glycerol as a crosslinker.

The particle size of SEO-containing microcapsules was determined by the gel strength of the G grade used. The incorporation of G with the highest Bloom value resulted in the largest particles, while the smallest microcapsules were obtained when G grade with the lowest gel strength was used. Average particle size values measured were  $25\text{ }\mu\text{m}$ ,  $55\text{ }\mu\text{m}$ , and  $119\text{ }\mu\text{m}$ , respectively. SEM investigation reflected the same trend regarding the correlation between gel strength and microcapsule particle size and revealed the net-like structure of lyophilized forms with different compactness.

According to the GC-MS analysis, the SEO composition was well preserved following the microencapsulation process. Most of the components identified in the free SEO were retained in the case of experimental run no. SO010 incorporating G with intermediate gel strength of approx. 175 Bloom where 17 compounds were identified out of 19 present in the free SEO.

EE determined by UV-VIS spectrophotometric method for experimental run proved to assure the best protection (SO010) was 86 %.

The FT-IR investigation confirmed that microcapsule shell formation is based on electrostatic interactions as the formation of new chemical bonds was not identified.

## EXPERIMENTAL SECTION

*Core material:* *Salvia officinalis* L. essential oil – was purchased from the Romanian market

*Shell materials:* Gelatin type A of porcine origin 80-120 Bloom, approx. 175 Bloom and approx. 300 Bloom value were purchased from Sigma Aldrich (St. Louis, USA). Gum arabic (GA) from acacia tree was purchased from Sigma Aldrich Chemie (Steinheim, Germany).

*pH adjustment:* 0.5 N HCl was used for pH adjustment. Hydrochloric acid was purchased from Silal Trading SRL (Romania, Bucharest).

*Crosslinker:* Glycerol was purchased from Chimreactiv SRL (Romania, Bucharest)

*Microencapsulation method:* Complex coacervation technology was applied according to the following major steps: 50 g of 3% w/w GA aqueous solution was prepared by dissolving gum arabic at room temperature under continuous stirring by the means of a magnetic stirrer (Arec, Velp Scientifica, Europe) at 800 rpm. 50 g of 3% G aqueous solution was prepared under continuous stirring and concomitant heating up to  $50 \pm 2^\circ\text{C}$  using a magnetic stirrer at 800 rpm. Three different gelatin type A grades were used with gel strength values as follows:  $\approx 175$  Bloom (for experiment no. SO010),  $\approx 300$  Bloom (for experiment no. SO011), and  $\approx 80 - 120$  Bloom (for experiment no. SO012). In each case 2.7 g of *Salvia officinalis* essential oil was emulsified into the formerly prepared 3% w/w G solution by using an IKA DI 18 B type ultraturrax (IKA®-Werke GmbH & Co. KG, Staufen, Germany) equipped with an IKA S 18 N – 19 G type dispersion tool (IKA®-Werke GmbH & Co. KG, Staufen, Germany) for 10 minutes at rotation speed of  $\approx 5,000$  rpm. This emulsion was added to the formerly prepared aqueous gum arabic solution under continuous stirring at approx.  $50^\circ\text{C}$ . HCl 0.5 N solution was used to adjust the pH of the obtained mixture to  $\text{pH}=4.0 \pm 0.05$ . After cooling to  $10^\circ\text{C}$  in an ice bath, the crosslinking agent glycerol (1 g) was added to harden the formed shell. Separation and purification of microcapsules were performed by decantation and washing with purified water (volume 3 x 50 mL): after decantation 50 mL of water was added to the microcapsule slurry and the mixture was stirred with a magnetic stirrer for 20 minutes. The washing procedure was repeated three times. Simultaneously, microcapsules without essential oil referred to as placebo were produced using the aforementioned method.

*Freeze drying* of microcapsules was performed in a Biobase BK FD10S (Biobase, Jinan, China) equipment by applying 4 hours of freezing at  $-55^{\circ}\text{C}$  followed by 20 hours of drying under a vacuum of 10 Pa.

*Optical microscopic investigation* was performed on an Optika B-150D-BRPL (Optika SRL, Ponteranica, Italy) brightfield microscope equipped with an integrated 3.1 MP camera at magnifications of 40X, 100X, 400X, and 1000X. For particle size measurement Optika Proview software (Optika SRL, Ponteranica, Italy) was used. Microscopic specimens were prepared by bringing from the last washing cycle one droplet of microcapsule dispersion on a glass slide after which a cover slip was gently applied. In the case of the 1000X magnification immersion oil was applied on the top of the cover slip.

*SEM investigation*: the morphology of the obtained products was investigated by scanning electron microscopic (SEM) imaging, with the use of a JEOL JSM-5200 scanning electron microscope (JEOL, Tokyo, Japan) at 10 kV potential. The samples were used as is (without sputter coating) and were fixed by conductive carbon adhesive tape.

*FT-IR spectroscopy* of solid samples was performed on a Bruker Tensor 27 IR spectrophotometer (Bruker Optics, Ettlingen, Germany) controlled by the Opus software (version 7.2). IR spectra of the solid components, the physical mixture, and the prepared products were recorded using KBr (Sigma Aldrich, Merck, Darmstadt, Germany) pellets, in transmittance mode over 400 – 4000  $\text{cm}^{-1}$  wavenumber range. The sample to KBr ratio was 1:100. Each sample was scanned 16 times, with a resolution of 2  $\text{cm}^{-1}$ .

FT-IR spectroscopy of essential oil was performed on a Nicolet 380 IR spectrophotometer (Thermo Electron Corporation, Madison, USA) controlled by the OMNIC software.

*UV-VIS spectroscopic* determinations were performed on a Shimadzu UV-1800 spectrophotometer (Shimadzu Co., Kyoto, Japan), controlled by UVProbe Software, using cuvettes made of special quartz glass with an optical path length of 10 mm (Hellma Analytics, Müllheim, Germany).

*SEO content* in the microcapsules was determined by UV-VIS spectroscopic method and quantified through the calculation of encapsulation efficiency and loading capacity.

The amount of essential oil in the microcapsules was measured through the following steps: first, 10 mg of microcapsules were powdered in a mortar, and 100 mL of absolute alcohol was added. The mixture was magnetically stirred for 15 minutes, to dissolve the total quantity of essential oil. Then, another 10 mg of microcapsules were stirred with 100 mL alcohol for 15 minutes, and the supernatant was collected, to recover the SEO on the surface of the microcapsules. The alcoholic solutions were filtered and analyzed spectrophotometrically at 241 nm after appropriate dilution. SEO concentrations were determined using a calibration curve built within the range of 25-65  $\mu\text{g}/\text{mL}$ .

The encapsulation efficiency (EE) and loading capacity (LC) were calculated using the following equations:

$$EE = \frac{m_m}{m_o} \times 100$$

where  $m_m$  represents the amount (mg) of oil contained in microcapsules, while  $m_o$  is the initial oil amount (mg) used. The amount of oil in microcapsules is determined by the difference between the total oil content ( $m_{to}$ ) and the surface oil content ( $m_{so}$ ):

$$m_m = m_{to} - m_{so}$$

$$LC = \frac{m_m}{M} \times 100$$

where M is the total amount (mg) of microcapsules.

*GC–MS analysis* of the essential oil was accomplished on an Agilent single-quadrupole mass spectrometer with an inert mass selective detector (MSD-5977 A, Agilent Technologies, USA). It was directly connected to an Agilent 7890B gas chromatograph with a split–splitless injector, a quick-swap assembly, an Agilent 7693 autosampler, and a HP-5MS fused silica capillary column (5% phenyl 95% dimethylpolysiloxane, 30 m × 0.25 mm internal diameter, 0.25 μm film thickness, Agilent Technologies, USA). The column was operated with an injector temperature of 250 °C. The oven temperature profile consisted of an isothermal hold at 50 °C for 4 minutes, a ramp of 4°C/min to 220°C, an isothermal hold for 2 minutes, followed by a second ramp to 280 °C at 20 °C/min, and a final isothermal hold for 15 minutes.

Before analysis, the essential oil was dissolved in hexane (1/100, v/v) and 1 μL of the solution was injected in 1:10 split mode. Extraction of essential oil from MC was performed from 250 mg freeze-dried material with 1 mL of hexane followed by filtration. As carrier gas helium was used at a flow rate of 1 ml/min. MSD ChemStation software, version F.01.01.2317 (Agilent) was used to obtain GC–TIC profiles and mass spectra. All mass spectra were acquired in the EI mode (scan range of m/z 45–600 and ionization energy of 70 eV). The electronic-impact ion source and the MS quadrupole temperatures were set at 230 °C and 150°C, respectively, with the MSD transfer line maintained at 280°C. For spectrum searching and identification NIST 14 MS spectrum library was used.

## REFERENCES

1. Committee on Herbal Medicinal Products (HMPC); *EMA Salvia Monograph*, 2016, 44.
2. Committee on Herbal Medicinal Products (HMPC); *Eur. Med. Agency - Comm. Herb. Med. Prod.*, 2016, 44.
3. M. Jakovljević; S. Jokić; M. Molnar; M. Jašić; J. Babić; H. Jukić; I. Banjari; *Plants*, 2019, 8, 55.
4. A. L. Lopresti; *Drugs R D*, 2017, 17, 53–64.
5. G. P. Eckert; *Front. Pharmacol.*, 2010, 1, 138.
6. M. Miroddi; M. Navarra; M. C. Quattropiani; F. Calapai; S. Gangemi; G. Calapai; *CNS Neurosci. Ther.*, 2014, 20, 485–495.
7. D. O. Kennedy; S. Pace; C. Haskell; E. J. Okello; A. Milne; A. B. Scholey; *Neuropsychopharmacology*, 2006, 31, 845–852.
8. T. Hase; S. Shishido; S. Yamamoto; R. Yamashita; H. Nukima; S. Taira; T. Toyoda; K. Abe; T. Hamaguchi; K. Ono et al.; *Sci. Rep.*, 2019, 9, 1–13.
9. S. Datta; S. Patil; *J. Alzheimer's Dis.*, 2020, 12, 131–143.
10. S. K. El Euch; D. B. Hassine; S. Cazaux; N. Bouzouita; J. Bouajila; *South African J. Bot.*, 2019, 120, 253–260.
11. R. Tundis; M. Leporini; M. Bonesi; S. Rovito; N. G. Passalacqua; *Molecules*, 2020, 25, 5826.
12. R. Bleiziffer; C. Mesaros; S. Suvar; P. Podea; A. Iordache; F.-D. Yudin; M. Culea; *Stud. Univ. Babeş-Bolyai Chem.*, 2017, 62, 373–385.
13. A. Russo; C. Formisano; D. Rigano; F. Senatore; S. Delfine; V. Cardile; S. Rosselli; M. Bruno; *Food Chem. Toxicol.*, 2013, 55, 42–47.
14. S. Sertel; T. Eichhorn; P. K. Plinkert; T. Efferth; *HNO*, 2011, 59, 1203–1208.
15. M. Yanagimichi; K. Nishino; A. Sakamoto; R. Kurodai; K. Kojima; N. Eto; H. Isoda; R. Ksouri; K. Irie; T. Kambe et al.; *Biochem. Biophys. Reports*, 2021, 25, 100882.
16. H. A. Mohammed; H. M. Eldeeb; R. A. Khan; M. S. Al-Omar; S. A. A. Mohammed; M. S. M. Sajid; M. S. A. Aly; A. M. Ahmad; A. A. H. Abdellatif; S. Y. Eid et al.; *Molecules*, 2021, 26, 5757.
17. C. Turek; F. C. Stintzing; *Compr. Rev. Food Sci. Food Saf.*, 2013, 12, 40–53.
18. International Organization for Standardization; *Oil of Dalmatian Sage (Salvia Officinalis L.)*; Geneva, Switzerland, 1997; Vol. ISO 9909:1.
19. G. Tibaldi; S. Hazrati; S. J. Hosseini; A. Ertani; R. Bulgari; S. Nicola; *Ind. Crops Prod.*, 2022, 183, 114923.
20. V. I. Sousa; J. F. Parente; J. F. Marques; M. A. Forte; C. J. Tavares; *Polymers (Basel)*, 2022, 14, 1730.
21. M. Arenas-Jal; J. M. Suñé-Negre; E. García-Montoya; *Eur. Food Res. Technol.*, 2020, 246, 1371–1382.
22. C. Thies; In *Encapsulation and Controlled Release Technologies in Food Systems*; J. M. Lakkis, Ed.; John Wiley & Sons Inc., 2016; pp. 41–77.



23. F. W. Tiebackx; *Zeitschrift für Chemie und Ind. der Kolloide*, 1911, 8, 198–201.
24. G. O. Fanger; In *Microencapsulation*; Springer US: Boston, MA, 1974; pp. 1–20.
25. Y. P. Timilsena; T. O. Akanbi; N. Khalid; B. Adhikari; C. J. Barrow; *Int. J. Biol. Macromol.*, 2019, 121, 1276–1286.
26. Z. Xiao; W. Liu; G. Zhu; R. Zhou; Y. Niu; *J. Sci. Food Agric.*, 2014, 94, 1482–1494.
27. F. Milano; A. Masi; M. Madaghiele; A. Sannino; L. Salvatore; N. Gallo; *Pharmaceutics*, 2023, 15, 1499.
28. C. E. Sing; S. L. Perry; *Soft Matter*, 2020, 16, 2885–2914.
29. L. Zhou; H. Shi; Z. Li; C. He; *Macromol. Rapid Commun.*, 2020, 41, 1–20.
30. H. J. W. Peters; E. M. G. van Bommel; J. G. F.; *Drug Dev. Ind. Pharm.*, 1992, 18, 123–134.
31. B. Liu; L. Lai; B. Muhoza; S. Xia; *Food Biosci.*, 2021, 44, 101403.
32. R. Shaddel; J. Hesari; S. Azadmard-Damirchi; H. Hamishehkar; B. Fathi-Achachlouei; Q. Huang; *Int. J. Biol. Macromol.*, 2018, 107, 1800–1810.
33. I. D. Alvim; C. R. F. Grosso; *Ciência e Tecnol. Aliment.*, 2010, 30, 1069–1076.
34. S. Leclercq; K. R. Harlander; G. A. Reineccius; *Flavour Fragr. J.*, 2009, 24, 17–24.
35. A. S. Prata; M. H. A. Zanin; M. I. Ré; C. R. F. Grosso; *Colloids Surfaces B Biointerfaces*, 2008, 67, 171–178.
36. A. S. Prata; C. R. F. Grosso; *J. Am. Oil Chem. Soc.*, 2015, 92, 1063–1072.
37. Y. P. Lemos; P. H. Mariano Marfil; V. R. Nicoletti; *Int. J. Food Prop.*, 2017, 20, 1–10.
38. B. Muhoza; S. Xia; J. Cai; X. Zhang; E. Duhoranimana; J. Su; *Food Hydrocoll.*, 2019, 87, 712–722.
39. B. Muhoza; S. Xia; X. Zhang; *Food Hydrocoll.*, 2019, 97, 105174.
40. Z. Rousi; C. Malhiac; D. G. Fatouros; A. Paraskevopoulou; *Food Hydrocoll.*, 2019, 96, 577–588.
41. W. Yang; Y. Gong; Y. Wang; C. Wu; X. Zhang; J. Li; D. Wu; *RSC Adv.*, 2024, 14, 4880–4889.
42. T. A. Comunian; J. Gomez-Estaca; R. Ferro-Furtado; G. J. A. Conceição; I. C. F. Moraes; I. A. De Castro; C. S. Favaro-Trindade; *Carbohydr. Polym.*, 2016, 150, 319–329.
43. P. H. M. Marfil; B. B. Paulo; I. D. Alvim; V. R. Nicoletti; *J. Food Process Eng.*, 2018, 41, 1–11.
44. G. A. Rocha-Selmi; F. T. Bozza; M. Thomazini; H. M. A. Bolini; C. S. Favaro-Trindade; *Food Chem.*, 2013, 139, 72–78.
45. M. G. Santos; F. T. Bozza; M. Thomazini; C. S. Favaro-Trindade; *Food Chem.*, 2015, 171, 32–39.
46. T. A. Comunian; M. Thomazini; A. J. G. Alves; F. E. De Matos Junior; J. C. De Carvalho Balieiro; C. S. Favaro-Trindade; *Food Res. Int.*, 2013, 52, 373–379.
47. T. Baj; A. Ludwiczuk; E. Sieniawska; K. Skalicka-Woźniak; J. Wideliski; K. Zieba; K. Główniak; *Acta Pol. Pharm.*, 2013, 70, 35–40.
48. N. D. Gonçalves; C. R. F. Grosso; R. S. Rabelo; M. D. Hubinger; A. S. Prata; *Carbohydr. Polym.*, 2018, 196, 427–432.

MICROENCAPSULATION OF *SALVIA OFFICINALIS* L. ESSENTIAL OIL  
BY COMPLEX COACERVATION TECHNOLOGY

49. R. Zhang; L. Huang; X. Xiong; M. C. Qian; H. Ji; *Flavour Fragr. J.*, 2020, 35, 157–166.
50. F. Baghi; S. Ghnimi; E. Dumas; A. Gharsallaoui; *Appl. Sci.*, 2023, 13, 6184.
51. X.-Y. Qv; Z.-P. Zeng; J.-G. Jiang; *Food Hydrocoll.*, 2011, 25, 1596–1603.
52. G. A. Rocha-Selmi; C. S. Favaro-Trindade; C. R. F. Grosso; *J. Chem.*, 2013, 2013, 982603.
53. S. Ferreira; V. R. Nicoletti; *J. Food Eng.*, 2021, 291, 110214.
54. A. Rungwasantisuk; S. Raibhu; *Prog. Org. Coatings*, 2020, 149, 105924.
55. A. M. Burhan; S. M. Abdel-Hamid; M. E. Soliman; O. A. Sammour; *J. Microencapsul.*, 2019, 36, 250–266.
56. Z. Xiao; W. Liu; G. Zhu; R. Zhou; Y. Niu; *Flavour Fragr. J.*, 2014, 29, 166–172.
57. A. Napiórkowska; A. Szpicer; I. Wojtasik-Kalinowska; M. D. T. Perez; H. D. González; M. A. Kurek; *Foods*, 2023, 12, 4345.
58. M. Calderón-Oliver; R. Pedroza-Islas; H. B. Escalona-Buendía; J. Pedraza-Chaverri; E. Ponce-Alquicira; *Food Hydrocoll.*, 2017, 62, 49–57.
59. P. J. Larkin; *Infrared Raman Spectrosc.*, 2018, 85–134.
60. H. H. Musa; A. A. Ahmed; T. H. Musa; In *Gum Arabic: Chemistry, Biological and Pharmacological Properties*; Springer, 2019; pp. 797–814.
61. B. H. Stuart; In *Infrared Spectroscopy: Fundamentals and Applications*; John Wiley & Sons Inc.: Hoboken, NJ, USA, 2004; pp. 71–80.
62. L. Ciko; A. Andoni; F. Ylli; E. Plaku; K. Taraj; A. Çomo; *Asian J. Chem.*, 2016, 28, 1401–1402.
63. L. Ang; Y. Darwis; L. Por; M. Yam; *Pharmaceutics*, 2019, 11, 451.